PHYSIK-DEPARTMENT

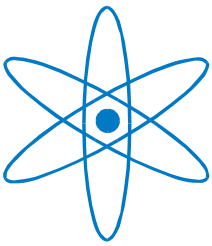

Fluid Flow Perception

Dissertation
von

Andreas N. Vollmayr

TECHNISCHE UNIVERSITÄT
MÜNCHEN

Physik Department

Lehrstuhl für theoretische Biophysik (T35)

Fluid Flow Perception

Andreas N. Vollmayr

Vollständiger Abdruck der von der Fakultät für Physik der Technischen Universität München zur Erlangung des akademischen Grades eines Doktors der Naturwissenschaften genehmigten Dissertation.

Vorsitzende(r): Univ.-Prof. Dr. Friedrich Simmel

Prüfer der Dissertation:

1. Univ.-Prof. Dr. J. Leo van Hemmen
2. Univ.-Prof. Dr. Folkmar Bornemann
3. Univ.-Prof. Dr. Roland Netz
   Freie Universität Berlin (nur schriftliche Beurteilung)

Die Dissertation wurde am 08.10.2014 bei der Technischen Universität München eingereicht und durch die Fakultät für Physik am 18.12.2014 angenommen.

Many theses have been written.
This is one of them.

Abstract

Flow-sensory systems are widespread in the animal kingdom. Some species, such as fish, primarily perceive their environment through the motion of the surrounding fluid. A theory for the reconstruction of the environment from the measured tangential velocities on the surface of a moving body is developed. Furthermore, the design and development of an artificial flow-sensory system is described. A model for the dynamics of an autonomous underwater vehicle (*Snookie*), that is capable of utilizing a flow-sensory system, is established.

Zusammenfassung

Strömungssensorsysteme sind im Tierreich weit verbreitet. Manche Arten nehmen ihre Umwelt hauptsächlich durch die Bewegung des sie umgebenden Fluids wahr. Eine Theorie zur Rekonstruktion der Umwelt aus Strömungsdaten, gemessen an der Oberfläche eines sich bewegenden Objektes, wird vorgestellt. Der Entwurf und die Entwicklung eines künstlichen Strömungssensorsystems wird beschrieben. Es wird ein Modell der Dynamik eines autonomen Unterwasserfahrzeuges (*Snookie*) aufgestellt, das in der Lage ist, ein Strömungssensorsystem sinnvoll zu nutzen.

Contents

Chapter 1

Introduction

Fluid-flow perception is very common in the animal kingdom. Many water-dwelling animals, e.g. fish [1], amphibians [2, 3], cephalopods [4, 5], and insects [6, ch. 7] are equipped with some kind of flow-sensory system. Most land-dwelling arthropods [7, 8] also possess flow sensors. It is known from behavioural experiments that information transmitted through the motion of the surrounding fluid is used for communication [9], hunting [10], escape from a predator [11], obstacle avoidance [12], object discrimination [13], map formation and self-localisation [14, 15]. Fluid-flow perception obviously enables these animals to cope with many vital tasks. One may ask the question, whether the ability of these animals and the solutions found for important tasks can be advantageous for technical applications.

This work considers the measurement, extraction, and analysis, summarised by the term *perception*, of signals transmitted through incompressible potential flow onto the surface of a smooth body $\mathcal{B}$. The questions addressed are: which information about the location, the motion, and the shape of bodies is transmitted by the fluid; which of the physical quantities related to the fluid motion can be measured; what do these physical quantities actually tell about the environment; how can fluid flow perception be used in technical systems; and finally, how must a technical system be designed to be able to make use of fluid flow perception?

The properties of the resulting flow fields on a flow-sensory system, induced by the motion of an object in the fluid, its length and time scales, and the physical quantities of fluid motion involved, are discussed with the help of simple examples in ch. 2. The question of how to retrieve information from a flow field measured on the surface of a body is covered in ch. 3. The analysis of fluid-flow perception is written in view of an application to an artificial flow-sensory system mounted on an autonomous underwater robot called *Snookie*. *Snookie* is specifically designed to be capable of sensing the fluid flow on its surface to perceive its environment. A model for the dynamics of *Snookie* used for the design and control of the robot is developed in ch. 4 and sec. 5.1.2. The hardware of the robot, and the development, the construction and the calibration of a flow-sensory system to be mounted on *Snookie* is described in sec. 5.2.

Although the discussion of the properties of fluid-flow perception and the mathematical methods developed might serve as a basis for the understanding of the neuronal information processing of a flow-sensory system, the analysis

forgoes a comparison with the morphological and electrophysiological studies. The purpose of the analysis of fluid-flow perception presented in this work is the development of theory and methods, which can be applied to an artificial flow-sensory system. It does not claim to explain the function or the neuronal information processing of a biological flow-sensory system. Nevertheless, artificial and biological flow-sensory systems have to solve similar problems. It is certainly worth thinking about how the results obtained in this works might affect the understanding of the neuronal information processing of a flow-sensory system. Where appropriate, it is marked during the course of the work, whenever a transfer of the acquired insight from theory back to the biological role models is possible.

1.1 Biological flow-sensory systems

Even if completely blind fish are able to locate obstacles and avoid them under poor visual conditions [16, 17]. Studies on the blind cave form of *Astyanax mexicanus* and the closely related *Astyanax jordani* (previously known as *Anoptichthys jordani*) show that these fish are able to detect and also discriminate objects, if gliding past or towards them at close distance. The objects are perceived by means of the *lateral-line system* (LLS), which is distributed along the body of the fish and responds to the movement of the water relative to the fish's skin [18, 19]. The term LLS, although originating from the visible line along the fish body, which marks the course of the lateral canal, also called trunk canal, is frequently used to denote the flow-sensory system (FSS) of fish as a whole. Besides a *superficial lateral-line system* (SLS) consisting of flow sensors on the surface of the body, many fish also possess flow sensors placed in canals, thin long tubes under the skin with regular pore openings through the skin to the surrounding fluid called *canal lateral-line system* (CLS). The presence of objects leads to an alteration of the flow field around the fish, which creates a "hydrodynamic image" [20] of the surroundings on the fish's body.

On the basis of behavioural experiments, some of the tasks, in which the lateral system is involved in, and some of the features of stimuli, which are reconstructed by the lateral-line system, have been identified. At some distance the flow field of most objects moving towards the lateral-line system may be approximated by that of a dipole – a moving sphere [21, p. 24 ff.] – since higher multipoles decrease much more rapidly with increasing distance. It has been shown that goldfish and mottled sculpin are able to determine the position of a dipole [22]. Moreover, mottled sculpins respond to the presentation of an oscillating sphere as the lowest-order representation of the flow field of prey with hunting behaviour and a strike towards the dipole source [23–26]. Experiments carried out on goldfish [27] suggest that fish are in principle also able to distinguish the direction of motion, speed, shape and size of solid objects. As an example, schooling can be achieved solely by perception of the flow fields of the neighbouring fish [28].

The blind cave form of *Astyanax mexicanus* was found to be able to detect, avoid, and also discriminate objects, when gliding past or towards them at a close distance [29–31]. For the blind Mexican cave fish, on the basis of behavioural experiments [12, 13, 30], there is no doubt about its elaborate capabilities in sensing its environment by means of the lateral-line system. The

limits of the flow-sensory system become apparent through its failure in case of a collision [31]. Teyke [29] explains a collision with a wall with tail movements disturbing the flow-sensory system while approaching an obstacle.

Although it is not quite clear what the capabilities of the lateral-line system really are and what tasks it can be used for, the example of the blind Mexican cave fish shows that it is obviously possible to make vital decisions based solely on information mediated by the surrounding fluid motion.

Flow sensing is usually split up in either the reception of a vortex structure or the reception of irrotational flow. Major objects moving in water normally produce a wake. In a large range of Reynolds numbers, the wake releases vortex structures, also called a von Kármán vortex street. Especially the strokes of the tail fin of fish leave behind prominent flow structures. These vortex structures mark the trace of swimming fish for quite a while [32, 33]. Because of the low viscosity and the high mass of water, vortices are quite stable and may remain up to several minutes. Catfish were shown to sense the vortex street with the lateral-line system during prey capture [34, 35]. Wake tracking can in principle also be achieved by other flow-sensory systems such as the whiskers of harbour seals [36, 37]. While the mapping of a vortex on the fish's lateral-line system is understood quite well [3], it is a non-trivial task to determine the properties of the vortex-producing hydrodynamic object [38].

The flow field of these vortex structures – seen from the perspective of extracting information – is completely different from the flow field produced for example by the blind Mexican cave fish [39–44] to sense its environment. The flow field in front of and besides the blind Mexican cave fish may be treated as irrotational as long as it is moving through nearly undisturbed water. The vorticity produced by the action of viscosity at the surface of the fish is convected to the rear with the incident flow. This is usually expressed by a high Reynolds number in front of the fish resulting in an inviscid and irrotational region of flow around the snout, well described by a velocity potential Φ for the incompressible Euler equations [45, 46]. Of course, the frequencies and the velocities involved in the problem guarantee incompressibility at any time.

Any object in the near surroundings disturbs the flow field on the surface of the fish, when compared to open water, resulting in a *hydrodynamic image*. The properties of a hydrodynamic image of a moving body mapped through an incompressible inviscid irrotational fluid are discussed in [47] by performing a multipole expansion of the flow field of varying shapes. The flow field is measured by a transparent artificial lateral line, meaning that the presence of the artificial lateral line does not disturb the flow field of the moving body. Then, from the estimated multipole moments basic information about the shape of the moving body is extracted. The conclusions are that – given a realistic resolution of the lateral-line sensors – the upper bounds for the range of localisation and shape reconstruction are roughly the size of the lateral-line system and the size of the moving object. The hydrodynamic image therefore only provides information about the environment in a very close range.

As mentioned in the introduction, FSSs are not unique to fish. Flow sensory systems are widespread in the land-dwelling arthropod world. Model systems for the study of flow-sensory systems in air are cockroaches [48], crickets [49, 50], and the wandering spider (*Cupiennius salei*) [8]. No matter if water or air, the physical description of the medium is the same. The interesting frequency range of the measured flow field produced by the motion of objects is in the

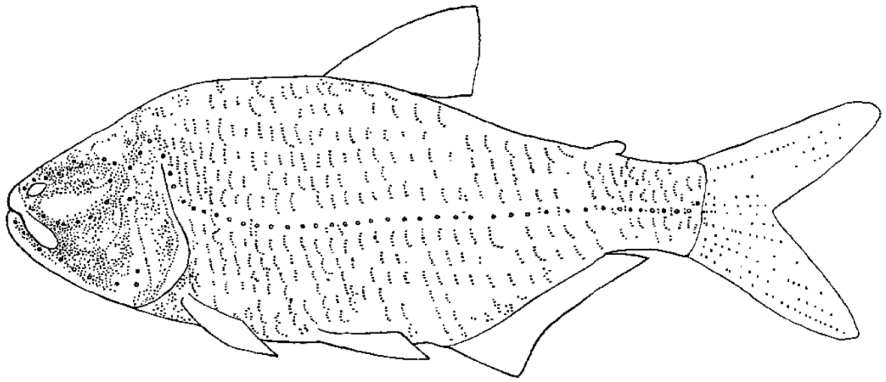

Figure 1.1: The lateral line system of the blind form of *Astyanax mexicanus*. Circles: pore openings of the *canal lateral-line system* (CLS). Dots: *superficial lateral-line system* (SLS) neuromasts, spread all over the body. The geometry of the canal neuromasts (CNs) as well as the number and location of the *superficial lateral-line system* (SLS) neuromasts varies between fish species. Taken from [62].

range below 10 Hz [51–53]. Even in the flow field of a flying fly [10, 54], mainly produced by the motion of the wings, high frequencies are damped rapidly with the distance to the fly.

1.1.1 The lateral-line system of fish

The actual flow sensor of the LLS, the neuromasts, consist of a jelly-like cupola surrounding hair bundles. Through the action of drag on the cupola the hair bundles are deflected and mechanically gate the conductivity of the non-spiking sensory neurons. Details on the transduction mechanism from hair bundle deflection to a change of the membrane voltage of the sensory neuron of vertebrate hair cells can be found in [55–57]. A review of the neuronal processing of the SLS and the CLS in [58].

The neuromasts are distributed more or less regularly all over the surface of the fish body, with an increased density on the head. Or, they are placed in a canal, a fluid filled tube under the skin connected to the surface through a fairly regular arrangement of openings, see fig. 2.1. The geometry and the distribution of the superficial neuromasts (SNs) varies greatly among fish species [1, 59]. Large variations are also found for the CLS. Some fish do not even have a CLS. Others have a highly branched CLS covering almost the complete fish body, but only a few SNs. Differences exist in the diameter and the length of the pores, and the arrangement of the pores [60]. Always one neuromast seems to be placed between two openings as sketched in fig. 2.1. The morphological differences in the FSSs of fish correlate with the habitat and the fluid-flow conditions [61]. Fish living in running or perturbed water seem to have more canal pores than fish living in still water. Conversely, fish in still water seem to possess more SNs than fish inhabiting perturbed water. All fish have at least a few (50) SNs, some have thousands, see [1] and the articles cited therein.

The segments of the canal between the openings have a high length to radius

ratio $L >> r_0$, which is why the viscous incompressible flow through an infinitely long tube is applicable. This geometric condition seems to be fulfilled quite well for all CLSs. Small errors are introduced at the openings of the pores due to an overestimation of the viscous effects. The flow inside the pore is almost translationally invariant along the midline, the x axis, of the pore. Besides the well known stationary parabolic Hagen-Poiseuille flow

$$v_x(r) = -\frac{\Delta p}{4L\mu}(r_0^2 - r^2) \tag{1.1}$$

with pressure difference Δp over the circular tube of length L, tube radius r_0 and dynamic viscosity of the fluid μ, transient solutions also exist. The oscillating flow [63, ch. 5.5.1] with pressure difference amplitude Δp through a circular tube is solved by

$$u_x(r,t) = -\frac{\Delta p}{\rho L\omega}\Re\left\{\frac{\mathrm{J}_0^*\left(-(1-\mathrm{i})\mathfrak{r}\right)}{\mathrm{J}_0^*\left(-(1-\mathrm{i})\mathfrak{r}_0\right)}\mathrm{e}^{(-\mathrm{i}\omega t)}\right\} \tag{1.2}$$

with the Bessel function of zeroth order J_0, frequency ω, $\mathfrak{r} = r/\delta$, $\mathfrak{r}_0 = r_0/\delta$, Stokes' boundary layer thickness $\delta = \sqrt{2\nu/\omega}$ and kinematic viscosity ν, and the complex conjugate is denoted by an asterisk. The flow in a circular tube impulsively started by a pressure difference [63, ch. 5.5.1, p. 343] is given by

$$u_x(r,t) = -\frac{\Delta p}{4L\mu}\left[r_0^2 - r^2 - 8r_0^2\sum_{n=1}^{\infty}\frac{1}{\alpha_n^3}\frac{\mathrm{J}_0(\alpha_n r/r_0)}{\mathrm{J}_1(\alpha_n)}e^{-\alpha_n^2\frac{\nu t}{r_0^2}}\right] \tag{1.3}$$

with the Bessel function of first order J_1 and α_n the real positive zeros of J_0. The first few α_n are $[2.40, 5.52, 8.65, 11.80, 14.93, \ldots]$. The oscillatory Poiseuille flow (1.2) can be approximated by the stationary Poiseuille flow whenever the Womersley number

$$\mathrm{Wo} = r_0\sqrt{\frac{\omega}{\nu}} \tag{1.4}$$

is small. The impulsively started Poiseuille flow (1.3) is approximated well by (1.1) if

$$t \gtrsim \frac{r_0^2}{\nu}\,. \tag{1.5}$$

The kinematic viscosity of water at 20° C is about $1\cdot 10^{-6}\,\mathrm{m}^2/\mathrm{s}$, a typical radius of a canal about 0.25 mm. The distance between two pores is in the range of several millimetres. If the frequency of the external pressure difference applied to the canal is smaller than 10 Hz, it is safe to assume that (1.1) holds. Plots of the flow profile in a tube dependent on $\nu t/r_0^2$ are given in [63, fig. 5.5.1].

The properties of the canal neuromast have been studied with the help of models. The results are briefly reviewed with the focus on frequencies below 10 Hz, which is expected to be relevant for the perception of stationary and moving solid objects, see sec. 2.11. The cupola of the neuromast inside the canal or on the surface of the fish is quite often described [57] as one half of a sphere in viscous flow. Stoke's drag force on a sphere in an oscillating external spatially homogeneous flow is given by

$$f_S = -6\pi r_S\mu A\omega\left[\left(1+\frac{r_S}{\delta}\right)\cos(\omega t) - \frac{r_S}{\delta}\left(1+\frac{2r_S}{9\delta}\right)\sin(\omega t)\right] \tag{1.6}$$

with sphere radius r_S, the amplitude of fluid motion A, frequency ω, Stokes' boundary layer thickness $\delta = \sqrt{2\nu/\omega}$, and the dynamic viscosity $\mu = \nu\varrho$. The force approaches the quasi-stationary value

$$f_S = -6\pi r_S \mu A\omega \cos(\omega t), \tag{1.7}$$

if $\omega \ll 2\nu/r_S^2$. The embedded hairs provide some stiffness to the cupola. Together with the mass, with some additional damping through the mechanotransduction apparatus, with half of the drag on a sphere (1.7) for the fluid-mechanical force on the cupola as driving force, and with an added mass of the displaced fluid due to the acceleration of the cupola, a linear second-order differential equation in time for the deflection of the cupola is obtained [57]. The resonance frequency of the model for typical cupola parameters is about 100 Hz. A frequency-response curve for the deflection of the cupola inside a canal in response to an external pressure difference applied to the openings is obtained by multiplication of the transfer function of the canal, computed from an oscillating Hagen-Poiseuille flow, with the transfer function of the cupola deflection model. Some quantitative errors are probably introduced by neglecting the interaction of the cupola with the wall of the canal, since the cupola covers a significant part of the cross section of the canal. The result is a relatively flat frequency response curve up to 100 Hz to an applied pressure difference. The deflection of the cupola follows the pressure without phase lag up to 10 Hz. Since the CN covers a large part of the cross section of the canal, modelling the drag force on a CN with the drag on one half of a sphere in a uniform Stokes flow introduces some quantitative error.

A similar analysis trying to capture the tapering of the canal through the presence of the cupola was given by [64]. It is argued that the drag on the cupola is maximal, if the cupola radius is more than half of the canal radius.

In summary, the fluid velocity inside the canal and the deflection of the cupola follow the externally applied pressure difference instantaneously without phase lag up to 10 Hz. Typical flow velocities inside the canal are small, the deflection of the cupola is in the range of nanometres. A numerical study of the viscous flow through a canal driven by an oscillating pressure difference was given in [65, 66], confirming that the drag force on the cupola in a quasi-stationary flow follows the applied pressure more or less instantaneously up to 10 Hz.

The size of the cupola of the SNs seems to be significantly smaller than that of CNs (several 100 μm). However, an enormous span of geometrical values for SNs are reported. For example, for zebrafish larvae [18], SNs with a width of 4.2-25.1 μm and heights of 8.7 - 79.1 μm are measured. The blind cave fish, *Astyanax hubbsi*, possesses SNs of a typical height of 80 μm and a width of 50 μm, although some SNs on the head reach a height of 300 μm [67]. The SNs of sighted *Astyanax mexicanus* reach only half the size of the ones of its blind relative. Furthermore, the SNs of *Astyanax mexicanus* are much stiffer than those of zebrafish larvae [68] due to an increased number of hair bundles. In [69] a mechanical model of the SN in the boundary layer of the fish is presented. It is used to estimate the properties of the SN in response to the flow field outside the boundary layer, especially in response to an oscillating sphere, which is usually used to stimulate the LLS. In a modified version [70] for the zebrafish SNs, the model predicts a relatively constant sensitivity up to only a few Herz. This frequency could be

significantly higher for the SNs of the blind Mexican cave fish due to an increased number of hair bundles in the cupola. It is reported from afferent recordings that SNs of the goldfish measure the local flow velocity up to 150 Hz [71].

The model is also used to estimate the threshold sensitivity of the neuromasts. From the gating energies of the mechanotransduction, the Brownian motion of the hair bundles, and the number of hair bundles in the cupola, a minimal resolvable cupola displacement is estimated. A zebrafish SN with 20 hair bundles has an estimated resolution threshold of 1.5 mm/s. Due to the increased number of hair cells and the existence of the canal [70], CNs seem to be much more sensitive than SNs to the same absolute velocity applied. However, large variations are expected in dependence of the number of hair bundles, the size of the cupola, or the length and diameter of a canal pore.

The conclusions relevant for the further course of this work are that most SNs as well as CNs probably measure the instantaneous local flow velocity (free stream or inside the canal) at least up to a frequency of 10 Hz. The flow velocity in a canal seems to follow immediately the pressure difference applied at the pore openings up to 10 Hz.

The exact transfer from the hydrodynamic stimulus to the excitation of the sensor [57, 69, 72–75], the resulting neuronal signals [76–78], and their processing is still under investigation [58, 79–83]. Ricci et al. [84] succeeded in developing an intracellular recording technique from a zebrafish neuromast. The channels and currents identified (A-type inactivating outward K^+ current, weak inward $Ca_2{}^+$ current for vesicle release) are, as expected, similar to many other vertebrate hair cells.

1.1.2 The Mauthner cells of fish

Fish possess two specialized neurons, the Mauthner cells, one on each of its sides, which are involved in eliciting the ultra fast escape reflex upon acoustic, tactile, or visual stimuli [85], called C-start. What makes the Mauthner cell interesting for this work is the fact that besides the input from the vestibular system [86], also LLS afferents directly project onto the Mauthner cells [87, 88]. The Mauthner cells obviously integrate raw data of several sensory modalities within an extraordinary short span of time [89] of less than 20 ms. The typical spike firing rate of the LLS afferents of zebra fish is in the range of 30-50 Hz. Although the firing rate of the afferents can reach more than 200 Hz during stimulation, the typical stimuli to be resolved to perceive an approaching object are rather small, see sec. 2.1. The Mauthner cells are thus able to make a decision on a time scale smaller than the typical interspike interval of the input. Mirjany et al. [89] report having investigated the contribution of the LLS to the decision made by the Mauthner cells of goldfish. The stimulation was presented with a system of loudspeakers in push-pull configuration at opposite sides of a circular aquarium of diameter 75 cm driven by amplified "single sinusoidal waves of 200 Hz produced by a digital waveform generator". The stimulus, called an "auditory stimulus" was simultaneously recorded with a hydrophone. It is impossible to judge from the description of the experiment, whether the stimulus presented to the fish, although obviously eliciting a C-start, could have stimulated the LLS of the goldfish at all. It would be interesting to see, if and how fish make use of the connection between the LLS and the Mauthner cell, and how selective the decisions are.

Figure 1.2: Mediterranean field cricket (*Gryllus bimaculatus*) with the flow-sensory system (*cerci*), covered with filiform hairs, protruding from the abdomen.

1.1.3 The cricket cercal system

Crickets possess a rather highly developed flow-sensory system, the *cercal* system. It consists of two long thin cones, the *cerci*, protruding from the abdomen, and covered with hundreds to thousands of long thin hairs. These hairs, called *filiform* hairs, couple viscously to the motion of the surrounding air. Each hair is innervated by one receptor neuron, mechanically coupled to the motion of the hair [7, 90]. The cuticular structure at the hair base supports the motion of the hair in a preferred direction. The mechanical parameters of filiform hairs can be found in [91, 92]. Rough estimates on the sensitivity threshold of cricket filiform hairs are published in [93]. The receptor neurons directly project onto the so called "giant interneurons" [94] in the terminal abdominal ganglion. The processing and analysis of the flow sensor readings is believed to take place in the terminal abdominal ganglion. It was shown [95, 96], that an escape response can be triggered solely by the flow field of an approaching predator.

1.2 Kinematics of rigid bodies

The next three chapters of this work deal with the generation and perception of flow fields of moving objects or flow fields altered by the presence of stationary objects. Chapter 5 is partly devoted to the dynamics and control of an underwater robot. Throughout this work, all objects, stationary or moving, will be approximated as rigid bodies. The reason is that in 3 dimensions (3D) the position of a rigid body in space is described by just 6 variables, its location and its orientation. In contrast, for a flexible body the motion of each point of the body has to be specified. Furthermore, a volume or a surface integral over a rigid body can be readily evaluated in the respective body-fixed frame.

A rigid body $\mathcal{B}$, equipped with a FSS and an inertia based acceleration measurement system, is supposed to move through the fluid domain $\mathcal{D}$ in an arbitrary fashion, meaning that it is allowed to accelerate in any of the 6 degrees of freedom. Other objects, moving or stationary, will show up from time to time.

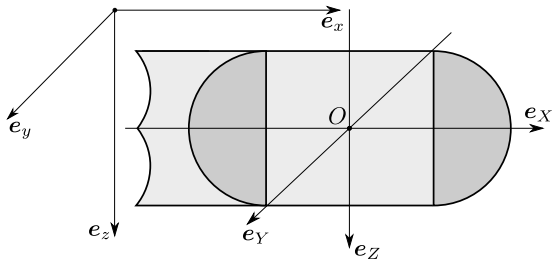

Figure 1.3: Frame of reference $\{\boldsymbol{e}_x, \boldsymbol{e}_y, \boldsymbol{e}_z\}$ and body-fixed system $\{\boldsymbol{e}_X, \boldsymbol{e}_Y, \boldsymbol{e}_Z\}$ with origin O at the geometric centre of the hull.

The task of $\mathcal{B}$ is to extract relevant cues from available sensor readings from the FSS and the inertia measurement system. All quantities measured and all action performed by the $\mathcal{B}$ are with respect to the coordinate system of the $\mathcal{B}$, the *body-fixed system* (BFS). However, for self-localisation, path planning and navigation, the $\mathcal{B}$ also requires its own velocity and position, and the position and velocity of surrounding objects in a global frame, the *frame of reference* (FOR). It provides an inertial system with the fluid at rest, if it were not disturbed by the motion of the $\mathcal{B}$ and further objects. It will be necessary to consider the relations of the relevant dynamic quantities between an accelerated frame of reference such as a BFS and a global and inertial frame of reference FOR. In the following section both frames, the relevant kinematic and dynamic quantities, and their transformations are exemplarily introduced for *Snookie*. The definition of the FOR and BFS is one to one transferable to any other moving object. Usually the depth of a submerged object is chosen as positive z axis with the origin placed on the undisturbed water surface. Objects moving in air usually measure their height above ground in positive z direction. These conventions do not affect the kinematics or dynamics.

1.2.1 Frames of reference

A suitable coordinate system for the description of the environment of *Snookie* is the FOR $\{\boldsymbol{e}_x, \boldsymbol{e}_y, \boldsymbol{e}_z\}$, which is fixed in space. It is an orthonormal inertial system. Stationary objects like the walls of a basin, which enter the fluid mechanics as boundary conditions, are fixed in space and therefore independent of time. The coordinate system is defined in such a way that the directions $\boldsymbol{e}_x$ and $\boldsymbol{e}_y$ are in the plane of the undisturbed water surface and $\boldsymbol{e}_z$ points downwards into the fluid in positive direction.

The second coordinate system is the *BFS*, see fig. 1.3. It is prescribed by $\mathcal{B}$, a rigid body, carrying out arbitrary motion relative to the laboratory system. The system is orthonormal. It is defined by the basis vectors $\{\boldsymbol{e}_X, \boldsymbol{e}_Y, \boldsymbol{e}_Z\}$. The orientation of the basis vector $\boldsymbol{e}_X$ of the BFS shall coincide with the longitudinal axis of *Snookie* pointing to the bow, the $\boldsymbol{e}_Y$ direction points to the starboard side, and $\boldsymbol{e}_Z$ is given by the cross product $\boldsymbol{e}_X \times \boldsymbol{e}_Y$. The natural choice for the position of the origin O of the BFS, expressed in coordinates of the FOR by the vector $\boldsymbol{o}$, is the *centre of mass* of a *rigid body*, since no coupling between rotational and translational degrees of freedom in the equations of motion (1.12) occurs in this system, meaning that resultant forces only affect the translational

momentum and resultant torques only the angular momentum. Whether such a point exists in the presence of hydrodynamic forces acting on the surface of $\mathcal{B}$ is a matter of discussion in sec. 5.1.2. For now, the real position of the centre of mass of $\mathcal{B}$ is unknown. A good choice for O is in the centre of volume of the hull of $\mathcal{B}$. All quantities measured by devices on-board of *Snookie* are provided in the BFS. The position in space of a rigid body is fully described by the location and orientation of the BFS relative to the FOR. In order to clearly distinguish between a quantity expressed in the FOR and the same quantity in the BFS, lower symbols are used for coordinate vectors and matrices in the FOR $\{\boldsymbol{e}_x, \boldsymbol{e}_y, \boldsymbol{e}_z\}$ and capital symbols in the BFS $\{\boldsymbol{e}_X, \boldsymbol{e}_Y, \boldsymbol{e}_Z\}$.

The BFS may be rotated against the laboratory system, which is described by a modified set $\boldsymbol{\phi} = (\phi, \theta, \psi)$ of implicit Euler angles (Tait–Bryan angles). If the orientation of the body and the body-fixed basis vectors were initially parallel to the ones of the FOR, the following procedure describes the rotation of the body at a given instance of time: rotate around $\boldsymbol{e}_z$ about the yaw angle ψ onto $\{\boldsymbol{e}'_x, \boldsymbol{e}'_y, \boldsymbol{e}_z\}$ with $-\pi < \psi \leq \pi$; next, perform a rotation around $\boldsymbol{e}'_y$ about the pitch angle θ onto $\{\boldsymbol{e}_X, \boldsymbol{e}'_y, \boldsymbol{e}'_z\}$ with $-\frac{\pi}{2} \leq \theta \leq \frac{\pi}{2}$; and finally rotate around $\boldsymbol{e}_X$ about the roll angle ϕ onto $\{\boldsymbol{e}_X, \boldsymbol{e}_Y, \boldsymbol{e}_Z\}$ with $-\pi < \phi \leq \pi$. Then, the rotation $\mathcal{R}$ of a vector from the FOR to the BFS is given by

$$\begin{aligned}\mathcal{R} &= \begin{pmatrix} 1 & 0 & 0 \\ 0 & \cos\phi & \sin\phi \\ 0 & -\sin\phi & \cos\phi \end{pmatrix} \begin{pmatrix} \cos\theta & 0 & -\sin\theta \\ 0 & 1 & 0 \\ \sin\theta & 0 & \cos\theta \end{pmatrix} \begin{pmatrix} \cos\psi & \sin\psi & 0 \\ -\sin\psi & \cos\psi & 0 \\ 0 & 0 & 1 \end{pmatrix} \\ &= \begin{pmatrix} \cos\theta\cos\psi & \cos\theta\sin\psi & -\sin\theta \\ \sin\phi\sin\theta\cos\psi - \cos\phi\sin\psi & \sin\phi\sin\theta\sin\psi + \cos\phi\cos\psi & \sin\phi\cos\theta \\ \cos\phi\sin\theta\cos\psi + \sin\phi\sin\psi & \cos\phi\sin\theta\sin\psi - \sin\phi\cos\psi & \cos\phi\cos\theta \end{pmatrix},\end{aligned} \tag{1.8}$$

and its inverse by $\mathcal{R}^{-1} = \mathcal{R}^{\mathrm{T}}$. The definition of the Euler angles depends on the order in which the transformation is carried out and finite rotations are therefore not commutative. The angular velocities in BFS coordinates are computed from the Euler angles [97] by

$$\boldsymbol{\Omega} = \mathcal{W}(\boldsymbol{\phi})\,\dot{\boldsymbol{\phi}} = \begin{pmatrix} 1 & 0 & -\sin\theta \\ 1 & \cos\phi & \sin\phi\cos\theta \\ 0 & -\sin\phi & \cos\phi\cos\theta \end{pmatrix} \begin{pmatrix} \dot{\phi} \\ \dot{\theta} \\ \dot{\psi} \end{pmatrix}. \tag{1.9a}$$

Its inverse is

$$\dot{\boldsymbol{\phi}} = \mathcal{W}^{-1}(\boldsymbol{\phi})\,\boldsymbol{\Omega} = \begin{pmatrix} 1 & \sin\phi\tan\theta & \cos\phi\tan\theta \\ 1 & \cos\phi & -\sin\phi \\ 0 & \sin\phi/\cos\theta & \cos\phi/\cos\theta \end{pmatrix} \begin{pmatrix} \Omega_X \\ \Omega_Y \\ \Omega_Z \end{pmatrix}. \tag{1.9b}$$

The total time derivative of a vector-valued quantity in an accelerated system expressed in BFS coordinates is given by

$$\frac{\mathfrak{D}}{\mathfrak{D}t} = \frac{\mathrm{d}}{\mathrm{d}t} + \boldsymbol{\Omega}\times\,. \tag{1.10}$$

The symbol $\boldsymbol{\Omega}\times$ denotes the totally anti-symmetric matrix representation

$$\boldsymbol{c}\times = \begin{pmatrix} 0 & -c_3 & c_2 \\ c_3 & 0 & -c_1 \\ -c_2 & c_1 & 0 \end{pmatrix} \tag{1.11}$$

of the cross product $\boldsymbol{c}\times$. The additional term $\boldsymbol{\Omega}\times$ stems from the time derivative of the basis vectors of the accelerated BFS.

1.2.2 Rigid-body motion

As will be seen in sec. 4.3, the fluid-mechanical forces on a rigid body due to acceleration in an ideal fluid can be formulated in the framework of rigid body dynamics. Before the forces exerted on the robot by the fluid are treated in depth in ch. 4 and ch. 5, the inertial forces of the rigid body due to its body mass in the BFS shall be briefly introduced.

The velocity $\boldsymbol{u}$ of the origin O of the BFS expressed in coordinates of the BFS is denoted by $\boldsymbol{U}$, the angular velocity $\boldsymbol{\omega}$ of the BFS about O by $\boldsymbol{\Omega}$, the acceleration $\dot{\boldsymbol{u}}$ of O by $\boldsymbol{A}$, the angular acceleration by $\dot{\boldsymbol{\omega}}$ and $\mathcal{A}$, the moments of inertia $\boldsymbol{i}$ of the rigid body computed about its centre of mass by I, and the position of the centre of body mass relative to O by $\boldsymbol{\rho}_M$. The mapping between the two systems is given by $\boldsymbol{o}$, $\boldsymbol{\phi} = (\phi, \theta, \psi)^{\mathrm{T}}$, (1.8), and (1.9).

Instead of formulating the inertial force $\boldsymbol{F}^I$ and inertial torque $\boldsymbol{T}^I$ as a sum or integral over the inertial forces acting on each particle, especially in case of changing masses, it is easier to take the total time derivative of the momentum $\boldsymbol{M} = m\,(\boldsymbol{V} + \boldsymbol{\Omega} \times \boldsymbol{\rho}_M)$ and the angular momentum $\boldsymbol{L} = I\boldsymbol{\Omega} + m\,\boldsymbol{\rho}_M \times (\boldsymbol{\omega} \times \boldsymbol{\rho}_M)$, where m is the body mass and I is the moment of inertia computed about the centre of mass $\boldsymbol{\rho}_M$ relative to O, which results in

$$\begin{pmatrix} \boldsymbol{F}^I \\ \boldsymbol{T}^I \end{pmatrix} = \begin{pmatrix} m\mathbb{1} & -m\boldsymbol{\rho}_M\times \\ m\boldsymbol{\rho}_M\times & I - m\,\boldsymbol{\rho}_M\times\,\boldsymbol{\rho}_M\times \end{pmatrix} \begin{pmatrix} \boldsymbol{A} \\ \mathcal{A} \end{pmatrix} + \begin{pmatrix} \boldsymbol{\Omega}\times m\boldsymbol{V} \\ \boldsymbol{\Omega} \times (I - m\,\boldsymbol{\rho}_M\times\,\boldsymbol{\rho}_M\times)\,\boldsymbol{\Omega} \end{pmatrix}. \tag{1.12}$$

Any other location for the choice of the origin of the BFS than the centre of mass couples translational and angular motion. Equation (1.12) incorporates Steiner's theorem [98] – also called parallel axis theorem – through the transformation of the moments of inertia $I - m\,\boldsymbol{\rho}_M \times \boldsymbol{\rho}_M\times$. With shifted centre of mass, an external force resultant not only changes the velocity of the BFS, but also induces a change in the angular velocity. The coupling between rotation and translation also occurs for an external torque resultant.

The equations of motion (1.12) describing the change of momentum and angular momentum may be further unified to a single equation in a very compact notation, which will be extended in ch. 5.1.2 to incorporate fluid-mechanical forces acting on $\mathcal{B}$. With the definition of the 6×6 mass matrix

$$\Lambda = \begin{pmatrix} m\mathbb{1} & -m\,\boldsymbol{\rho}_M\times \\ m\,\boldsymbol{\rho}_M\times & I - m\,\boldsymbol{\rho}_M\times\,\boldsymbol{\rho}_M\times \end{pmatrix}, \tag{1.13}$$

the definition of the anti-symmetric 6×6 matrix

$$\boldsymbol{\varpi}\times = \begin{pmatrix} \boldsymbol{\Omega}\times & 0 \\ 0 & \boldsymbol{\Omega}\times \end{pmatrix}, \tag{1.14}$$

where $\boldsymbol{\Omega}\times$ denotes the anti-symmetric 3×3 matrix representation (1.11) of the cross product, the the definition of the generalised 6-dimensional (6D) velocity vector $\mathfrak{U} = (\boldsymbol{U}, \boldsymbol{\Omega})$ and the generalised 6D force vector $\mathfrak{F} = (\boldsymbol{F}^I, \boldsymbol{T}^I)$, the equations of rigid body motion without external forces yield

$$\mathfrak{F}^I = \frac{\mathfrak{D}\,(\Lambda\mathfrak{U})}{\mathfrak{D}t} = \frac{\mathrm{d}\boldsymbol{\Lambda}\mathfrak{U}}{\mathrm{d}t} + \boldsymbol{\varpi} \times (\Lambda\mathfrak{U}) = 0\,. \tag{1.15}$$

Chapter 2

Potential Flow

As mentioned in ch. 1, this work focuses on the motion and perception of rigid bodies in an *ideal incompressible irrotational fluid*, also termed *incompressible potential flow*. The restriction to this limiting case of fluid motion is essentially due to the assumptions required to arrive at statements on the motion of the fluid within a certain domain $\mathcal{D}$ in dependence of the fluid motion on the boundaries, see sec. 2.2. In a real fluid, potential flow is found, e.g. around a moving fish, or by proper design around the LLS of a vehicle [99, 100]. The vorticity produced at the surface of the moving body is convected to the rear with the incident flow. This is expressed by a high Reynolds number in front of the moving observer, resulting in an inviscid and irrotational flow well described by a single valued velocity potential Φ [45, 101].

2.1 Potential flow

The fluid motion is fully described by a single valued velocity potential [101, ch. 3, § 35]

$$\Delta\Phi = 0 \tag{2.1}$$

for the velocity field

$$\boldsymbol{v} = \nabla\Phi\,, \tag{2.2}$$

derived from the Euler equations

$$\frac{\partial}{\partial t}\boldsymbol{v} + (\boldsymbol{v}\cdot\boldsymbol{\nabla})\,\boldsymbol{v} = -\frac{\nabla p}{\varrho} \tag{2.3}$$

on a simply-connected domain $\mathcal{D}$ assuming an *irrotational* fluid flow

$$\boldsymbol{\nabla}\times\boldsymbol{v} = 0\,. \tag{2.4}$$

In addition, the fluid is *incompressible*, if

$$\boldsymbol{\nabla}\cdot\boldsymbol{v} = 0\,. \tag{2.5}$$

A domain $\mathcal{D}$ is said to be simply-connected, if any loop inside $\mathcal{D}$ is reducible. A loop is reducible, if it can be shrunk to a point without crossing the boundaries of $\mathcal{B}$. Any multiply connected domain [101, ch. 3, § 47-51] can be converted

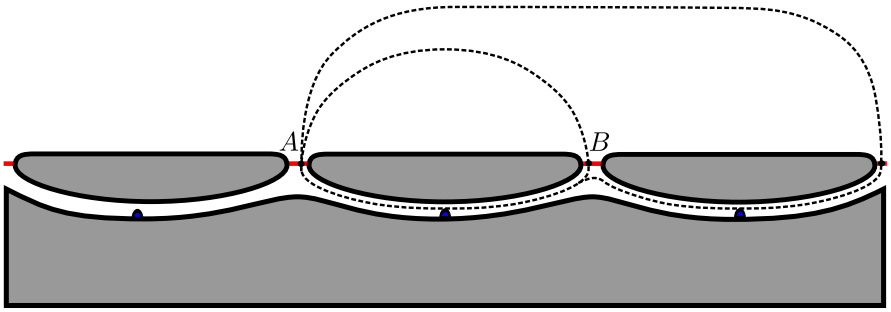

Figure 2.1: Schematic of a lateral line canal. The points A and B denote canal openings, the dotted lines represent irreducible loops, the blue dots canal neuromasts (CNs).

to a simply connected domain by introducing artificial boundaries, so that any irreducible loop is split up. A domain $\mathcal{D}$ is said to be n-ply connected, if $(n-1)$ artificial boundaries $\mathcal{X}_i$ are necessary to render $\mathcal{D}$ simply connected. This is equivalent to the existence of $n-1$ irreconcilable irreducible loops, meaning that they cannot be converted into each other by continuous deformation. Stokes' theorem guarantees that the circulation

$$\oint_{\mathcal{L}} \boldsymbol{v}\,\mathrm{d}\boldsymbol{l} = \iint_{\mathcal{S}} \boldsymbol{\nabla}\times\boldsymbol{v}\,\mathrm{d}\mathcal{S} \tag{2.6}$$

along a closed loop $\mathcal{L}$ enclosing the surface $\mathcal{S}$ in a simply connected domain vanishes, which is necessary to ensure a single valued potential Φ. In a n-ply connected domain with non-vanishing flux through an aperture, e.g. produced by a line vortex placed outside the domain $\mathcal{D}$, the line integral over an oriented irreducible loop

$$m\kappa = \oint_{\mathcal{L}} \boldsymbol{v}\,\mathrm{d}\boldsymbol{l} \tag{2.7}$$

does not vanish, but depends on the number of turns m of the loop and the circulation κ of a single turn. For the combination of n irreducible paths, the circulation of each path times the number of turns is added up,

$$\Gamma = \sum_{i=1}^{n} m_i\kappa_i\,. \tag{2.8}$$

The potential Φ is thus determined only up to Γ with arbitrary m_i, as long as the path of integration over the velocity is not specified. The potential difference between the points A and B in fig. 2.1 is given by

$$\Phi_{AB} = \Gamma + \Phi_{BA}\,. \tag{2.9}$$

It can be seen from (2.9) by putting the points A and B on adjacent sides of $\mathcal{X}_i$ that the potential experiences a jump of $\pm\kappa_i$ depending on the orientation of the circulation and the direction in which $\mathcal{X}_i$ is crossed. The potential is uniquely determined if the circulation in any irreducible loop is specified in addition to the boundary conditions of the multiply connected domain. The potential becomes single valued by means of introducing artificial boundaries $\mathcal{X}_i$. In addition, the circulation must be specified for every $\mathcal{X}_i$. The fluid velocity is always single-valued, but closed streamlines may exist in multiply connected source-free domains that do not end or start on boundaries. If in addition to the boundary conditions on $\partial\mathcal{D}$ the velocity is specified also on the artificial boundaries $\mathcal{X}_i$, the fluid velocity is fully determined on a multiply connected domain $\mathcal{D}$.

Throughout this work, physical boundaries of $\partial\mathcal{D}$ are given by the surfaces of moving rigid objects. Following the naming convention of sec. 1.2.1, capital symbols denote quantities with respect to the BFS. No fluid can cross the surface $\partial\mathcal{B}$ of an impermeable body $\mathcal{B}$. In case $\mathcal{B}$ is *rigid*, the boundary condition is simply given by the normal velocity of the boundary, see sec. 1.2.2. The velocity of a point P at position $\boldsymbol{p}$ on the surface $\partial\mathcal{B}$ of $\mathcal{B}$ defined with respect to the origin of the FOR is given by the translational and rotational velocity $\boldsymbol{u}^{\mathcal{B}}$ and $\boldsymbol{\omega}^{\mathcal{B}}$ of $\mathcal{B}$,

$$\boldsymbol{V}^{\mathcal{B}}(\boldsymbol{p}) = \boldsymbol{u}^{\mathcal{B}} + \boldsymbol{\omega}^{\mathcal{B}} \times \left(\boldsymbol{p} - \boldsymbol{o}^{\mathcal{B}}\right) . \tag{2.10}$$

The boundary condition for the fluid on $\partial\mathcal{B}$, the *no-penetration boundary condition*, is in the FOR given by

$$v^{\perp}(\boldsymbol{p}(t), t) = \frac{\partial\Phi(\boldsymbol{p}(t), t)}{\partial n(\boldsymbol{p}(t))} = \left[\boldsymbol{u}^{\mathcal{B}}(t) + \boldsymbol{\omega}^{\mathcal{B}}(t) \times \left(\boldsymbol{p}(t) - \boldsymbol{o}^{\mathcal{B}}(t)\right)\right] \cdot \boldsymbol{n}(\boldsymbol{p}(t)) \tag{2.11}$$

at any point $\boldsymbol{p}$ on the surface $\partial\mathcal{B}$ of the rigid body. The surface point $\boldsymbol{p}$ and the normal $\boldsymbol{n}$ are functions of time, since $\mathcal{B}$ moves. The surface normal $\boldsymbol{n}$ is supposed to point outward $\mathcal{D}$. The surface normal $\boldsymbol{n}'$ outward of a body and inward to the fluid is denoted with a prime. The time course of Φ is solely given by the right hand side of (2.11). The potential Φ is a linear function of the velocity of the boundaries.

Throughout this work, the FOR is chosen such that the velocity potential and the velocity vanish at infinity, or alternatively the boundaries enclosing $\mathcal{D}$ are at rest. Objects moving through $\mathcal{D}$ are totally immersed in $\mathcal{D}$.

2.2 Helmholtz's decomposition theorem

At first glance, incompressible potential flow, i.e. the motion of an incompressible inviscid irrotational fluid, appears to be a rather strong limitation leading to a small class of special cases of flows occurring in real fluids. The following short discussion of a generalised version of Helmholtz's theorem shows that there are good reasons to impose these limitations in order to be able to easily arrive at relations between the motion of the boundaries and the motion of the fluid on a simply connected domain $\mathcal{D}$. *Helmholtz's decomposition theorem* [102] states that any sufficiently smooth vector field $\boldsymbol{v}$ defined on $\mathcal{D}$ decaying faster than $1/r$ or being bounded in three dimensions can be decomposed into the sum of an irrotational (curl-free) vector field $\nabla\Phi$ and a solenoidal (divergence-free) vector field $\boldsymbol{\nabla}\times\boldsymbol{A}$,

$$\boldsymbol{v} = \nabla\Phi + \boldsymbol{\nabla}\times\boldsymbol{A}\,, \tag{2.12a}$$

where

$$\Phi(\boldsymbol{r}) = -\frac{1}{4\pi}\iiint_{\mathcal{D}} \frac{\boldsymbol{\nabla}'\cdot\boldsymbol{v}(\boldsymbol{r}')}{|\boldsymbol{r}-\boldsymbol{r}'|}\,\mathrm{d}\mathcal{V}' + \frac{1}{4\pi}\oiint_{\partial\mathcal{D}} \boldsymbol{n}\cdot\frac{\boldsymbol{v}\,(\boldsymbol{r}')}{|\boldsymbol{r}-\boldsymbol{r}'|}\,\mathrm{d}\mathcal{S}' \tag{2.12b}$$

and

$$\boldsymbol{A}(\boldsymbol{r}) = \frac{1}{4\pi}\iiint_{\mathcal{D}} \frac{\boldsymbol{\nabla}'\times\boldsymbol{v}(\boldsymbol{r}')}{|\boldsymbol{r}-\boldsymbol{r}'|}\,\mathrm{d}\mathcal{V}' - \frac{1}{4\pi}\oiint_{\partial\mathcal{D}} \boldsymbol{n}\times\frac{\boldsymbol{v}\,(\boldsymbol{r}')}{|\boldsymbol{r}-\boldsymbol{r}'|}\,\mathrm{d}\mathcal{S}' \tag{2.12c}$$

with surface normal $\boldsymbol{n}$ outward $\mathcal{D}$. If $\mathcal{D}$ extends to infinity, the respective contributions of the surface integrals in (2.12) vanish. A quick look at (2.12) reveals that $\boldsymbol{v}(\boldsymbol{r})$ is solely determined by the boundary conditions $\boldsymbol{v}\cdot\boldsymbol{n}|_{\partial\mathcal{D}}$ and $\boldsymbol{n}\times\boldsymbol{v}|_{\partial\mathcal{D}}$, if $\boldsymbol{\nabla}\times\boldsymbol{v}=0$ and $\boldsymbol{\nabla}\cdot\boldsymbol{v}=0$, meaning that $\mathcal{D}$ is irrotational and free of sources. These are exactly the conditions required for incompressible potential flow. Then, the flow field is governed by the velocities of the flow field on the boundaries of $\mathcal{D}$

$$\boldsymbol{v}(\boldsymbol{r}) = \frac{1}{4\pi}\nabla\oiint_{\partial\mathcal{D}} \boldsymbol{n}\cdot\frac{\boldsymbol{v}\,(\boldsymbol{y})}{|\boldsymbol{x}-\boldsymbol{y}|}\,\mathrm{d}\mathcal{S} - \frac{1}{4\pi}\boldsymbol{\nabla}\times\oiint_{\partial\mathcal{D}} \boldsymbol{n}\times\frac{\boldsymbol{v}\,(\boldsymbol{y})}{|\boldsymbol{x}-\boldsymbol{y}|}\,\mathrm{d}\mathcal{S}\,. \tag{2.13}$$

If one wants to acquire information about the boundaries of the fluid by analysing the fluid motion, or vice versa, it is necessary that the dynamics of the fluid is actually governed by the properties of the boundaries. The conditions $\boldsymbol{\nabla}\cdot\boldsymbol{v}$ and $\boldsymbol{\nabla}\times\boldsymbol{v}$ are sufficient conditions to allow fluid flow perception by measurement of the velocity or any other quantity related to it on the boundaries.

2.3 Potential flow in accelerated frames

To develop a theory for the processing of flow sensory data on-board of moving objects, no matter if fish, cricket, or an underwater robot, and to formulate the dynamics of objects in a fluid, it is convenient to express the equations governing potential flow in translationally and rotationally accelerated frames of reference. It turns out that this can be done quite easily.

An inertial FOR shall be given by its basis vectors $\{\boldsymbol{e}_x, \boldsymbol{e}_y, \boldsymbol{e}_z\}$, and an accelerated BFS by $\{\boldsymbol{e}_X(t), \boldsymbol{e}_Y(t), \boldsymbol{e}_Z(t)\}$. The transformation of a vector valued quantity from FOR coordinates to the BFS coordinates was given in sec. 1.2.1. The dynamics of the fluid in a bounded or unbounded simply-connected fluid domain $\mathcal{D}$ in a FOR is governed by $\Delta_x\Phi(\boldsymbol{x},t)=0$ (2.1). The potential in the BFS is identified by its argument $\Phi(\boldsymbol{X},t)$ to avoid the introduction of additional symbols. The Laplacian determining the potential of the flow field is form-invariant under orthogonal coordinate transformations and thus under transformations in an arbitrarily accelerated frame of reference, since

$$\Delta_x\Phi(\boldsymbol{x},t) = \boldsymbol{\nabla}_x\cdot\nabla_x\Phi(\boldsymbol{x},t) = \left(\nabla_X\mathcal{R}^{\mathrm{T}}\right)\cdot\left(\mathcal{R}\nabla_X\right)\Phi(\boldsymbol{X},t) = \\ \boldsymbol{\nabla}_X\cdot\nabla_X\Phi(\boldsymbol{X},t) = \Delta_X\Phi(\boldsymbol{X},t)\,.$$

This result simply follows from the fact that no time derivative appears in (2.1). The time dependence of the motion of the fluid enters Φ solely via the time dependence of the boundary conditions.

To take full advantage of a BFS one would also like to express the velocity with respect to the BFS of a moving body, since $\boldsymbol{V} \cdot \boldsymbol{N} = 0$ in the BFS. This will turn out to be quite useful, since surface integrals containing the normal velocity as a factor will vanish on $\mathcal{B}$. It shall be reminded that upper case symbols are used for quantities in the BFS, lower case symbols for quantities in the FOR. In the FOR the boundary condition (2.11) for the fluid velocity defined with respect to the FOR at a point $\boldsymbol{p}$ on a moving rigid body $\mathcal{B}$ is

$$\boldsymbol{v}^{\perp}(\boldsymbol{p}(t), t) = \frac{\partial \Phi(\boldsymbol{p}(t), t)}{\partial n(\boldsymbol{p}(t))} = \left\{ \boldsymbol{u}^{\mathcal{B}}(t) + \boldsymbol{\omega}^{\mathcal{B}}(t) \times \left[\boldsymbol{p}(t) - \boldsymbol{o}^{\mathcal{B}}(t) \right] \right\} \cdot \boldsymbol{n}(\boldsymbol{p}(t)) \,.$$

As already mentioned, the boundary condition for the same point $\boldsymbol{P} = \mathcal{R}(\boldsymbol{\phi})\left(\boldsymbol{p}(t) - \boldsymbol{o}^{\mathcal{B}}(t)\right)$ on $\partial\mathcal{B}$ in the BFS, where the flow velocity is defined with respect to the origin $O^{\mathcal{B}}$ of $\mathcal{B}$, is given by

$$\boldsymbol{V}^{\perp}(\boldsymbol{P}, t) = \frac{\partial \Phi(\boldsymbol{P}, t)}{\partial N(\boldsymbol{P})} = 0 \,.$$

The flow field $\boldsymbol{v}(\boldsymbol{x}, t)$ relating to the origin of the FOR in coordinates of a BFS $\mathcal{B}$ defined with respect to the origin $O^{\mathcal{B}}(t)$ of $\mathcal{B}$ becomes

$$\boldsymbol{V}(\boldsymbol{X}, t) = \mathcal{R}(\boldsymbol{\phi}(t)) \left\{ \boldsymbol{v}(\boldsymbol{x}, t) - \left[\boldsymbol{u}^{\mathcal{B}}(t) + \boldsymbol{\omega}^{\mathcal{B}}(t) \times \left(\boldsymbol{x} - \boldsymbol{o}^{\mathcal{B}}(t) \right) \right] \right\}$$

with the transformation matrix $\mathcal{R}(\boldsymbol{\phi})$ and the vector of Euler angles $\boldsymbol{\phi}(t)$ as defined in sec. 1.2.1. A flow field $\boldsymbol{V}(\boldsymbol{X}, t)$ is throughout this work defined with respect to a BFS and expressed in coordinates of the BFS. Whenever it is necessary to specify the systems to which the flow velocity relates to, it is indicated by the respective superscript, e.g. $\boldsymbol{V}^{\mathcal{B}}(\boldsymbol{X}, t)$. Lower case symbols are used for flow fields $\boldsymbol{v}(\boldsymbol{x}, t)$ defined with respect to and expressed in coordinates of the FOR, recalling that the FOR is chosen such that the fluid domain $\mathcal{D}$ is either bounded by stationary walls, or the potential and the velocity vanish at infinity, see sec. 2.1. It shall be reminded that this convention does not apply to the velocity of a rigid body. Contrary to the velocity $\boldsymbol{V}^{\mathcal{B}}(\boldsymbol{X}, t)$ of the flow field, the translational and rotational velocities $\boldsymbol{U}^{\mathcal{B}}$ and $\boldsymbol{\Omega}^{\mathcal{B}}$ of $\mathcal{B}$ are defined with respect to the origin of the FOR and expressed in coordinates of $\mathcal{B}$. To obtain the potential corresponding to the velocity field defined with respect to $\mathcal{B}$, just some slight modification are required to match the transformed boundary conditions. A correction Φ^{C} for the velocity potential resulting from a line integral

$$\begin{aligned}
\Phi^{\mathcal{B}}(\boldsymbol{X}, t) &= \Phi^{\mathcal{F}}(\boldsymbol{x}, t) - \int_{\boldsymbol{0}}^{\boldsymbol{x}} \left[\boldsymbol{u}^{\mathcal{B}}(t) + \boldsymbol{\omega}^{\mathcal{B}}(t) \times \left(\boldsymbol{x}' - \boldsymbol{o}^{\mathcal{B}}(t) \right) \right] \cdot \mathrm{d}\boldsymbol{l}(\boldsymbol{x}') \\
&= \Phi^{\mathcal{F}}(\boldsymbol{X}, t) - \boldsymbol{u}^{\mathcal{B}}(t) \cdot \int_{\boldsymbol{0}}^{\boldsymbol{x}} \mathrm{d}\boldsymbol{l}(\boldsymbol{x}') - \boldsymbol{\omega}^{\mathcal{B}}(t) \cdot \int_{\boldsymbol{0}}^{\boldsymbol{x}} \left(\boldsymbol{x}' - \boldsymbol{o}^{\mathcal{B}}(t) \right) \times \mathrm{d}\boldsymbol{l}(\boldsymbol{x}') \\
&= \Phi^{\mathcal{F}}(\boldsymbol{X}, t) - \Phi^{\mathrm{C}}(\boldsymbol{X}, t)
\end{aligned}$$

between, e.g., the origin of the FOR at $\boldsymbol{0}$ and the field point $\boldsymbol{x}$ or $\boldsymbol{X}$ must be introduced, whereby the properties of the scalar triple product have been used. To distinguish the velocity potentials of the flow fields defined with respect to the FOR or the BFS the superscripts $\mathcal{F}$ and $\mathcal{B}$ are used were necessary. The shape of the curve of integration $\mathcal{C}$ does not matter further, since Φ is a conservative potential. The curve integral starts at the origin $\boldsymbol{0}$ of the FOR and ends at

$\boldsymbol{X}$. Even the choice of the start point of $\mathcal{C}$ is irrelevant for the flow field, since changing these points will just add a function of time $C(t)$, which does not affect $\boldsymbol{V} = \nabla\Phi$. However, $C(t)$ matters for the computation of the pressure of transient flows, see sec. 2.9. The adapted potential fulfils $\Delta\Phi^{\mathcal{B}} = 0$ and delivers correct boundary values $\Phi^{\mathcal{B}}/\partial N|_{\partial\mathcal{B}}$.

2.4 Green's identities

As discussed in sec. 2.2, the motion of an incompressible ideal irrotational fluid in a source-free simply connected domain is governed by the boundary conditions and a boundary representation of the flow field in terms of a given velocity on the boundaries. An equivalent boundary representation for the flow potential is given by Green's third theorem, presented in this section.

Let the open domain $\mathcal{D} \subseteq \mathbb{R}^3$ have a piecewise smooth boundary $\partial\mathcal{D}$. For a continuously differentiable vector field $\boldsymbol{v}$ defined on $\mathcal{D}$ and on a neighbourhood of $\partial\mathcal{D}$ outside $\mathcal{D}$, the divergence theorem

$$\iiint_{\mathcal{D}} (\nabla\cdot\boldsymbol{v})\,\mathrm{d}V = \oiint_{\partial\mathcal{D}} (\boldsymbol{v}\cdot\boldsymbol{n})\,\mathrm{d}\mathcal{S} \tag{2.14}$$

with the outward normal $\boldsymbol{n}$ on $\partial\mathcal{D}$ relates the generation or destruction of the quantity $\boldsymbol{v}$ inside $\mathcal{D}$ with the flux of $\boldsymbol{v}$ through the surface $\partial\mathcal{D}$. Application of (2.14) to the product $\Psi\nabla\Phi$ of an once continuously differentiable function Φ and a twice continuously differentiable function Φ, both defined on $\mathcal{D}$, leads to Green's first identity,

$$\iiint_{\mathcal{D}} (\Psi\Delta\Phi + \nabla\Phi\cdot\nabla\Psi)\,\mathrm{d}V = \oiint_{\partial\mathcal{D}} \Psi\,(\nabla\Phi\cdot\boldsymbol{n})\,\mathrm{d}\mathcal{S}\,. \tag{2.15}$$

Green's second identity

$$\iiint_{\mathcal{D}} (\Psi\Delta\Phi - \Phi\Delta\Psi)\,\mathrm{d}V = \oiint_{\mathcal{S}} \left(\Psi\frac{\partial\Phi}{\partial n} - \Phi\frac{\partial\Psi}{\partial n}\right)\mathrm{d}\mathcal{S} \tag{2.16}$$

is obtained by substitution of $\Psi\nabla\Phi - \Phi\nabla\Psi$ into (2.14), where Φ and Ψ are both twice continuously differentiable functions on $\mathcal{D}$. The potential Φ is supposed to be a solution of $\Delta\Phi = 0$, and G_F is the fundamental solution

$$G_F(\boldsymbol{x},\boldsymbol{y}) = -\frac{1}{4\pi\,|\boldsymbol{x}-\boldsymbol{y}|}\,, \tag{2.17}$$

i.e. the *free-space Green's function* of the Laplace operator defined by

$$\Delta G_F(\boldsymbol{x},\boldsymbol{y}) = \delta(\boldsymbol{x}-\boldsymbol{y})\,. \tag{2.18}$$

The open domain $\mathcal{D}$ shall either be bounded by $\partial\mathcal{D}$, or Φ shall vanish at infinity. Inserting (2.17) into Green's second identity (2.16) delivers a singular integral in the case of a field point $\boldsymbol{x}$ located inside $\mathcal{D}$. This can be circumvented by excluding $\boldsymbol{x}$ from $\mathcal{D}$ and introducing a spherical boundary with radius ε around $\boldsymbol{x}$. The surface integral can then be computed in the limit $\varepsilon \to 0$. This leads to the boundary representation of potential flow [101, § 57-58]

$$\Phi(\boldsymbol{x}) = -\oiint_{\partial\mathcal{D}} G_F(\boldsymbol{x},\boldsymbol{y})\frac{\partial\Phi(\boldsymbol{y})}{\partial n}\mathrm{d}\mathcal{S} + \oiint_{\partial\mathcal{D}} \Phi(\boldsymbol{y})\frac{\partial G_F(\boldsymbol{x},\boldsymbol{y})}{\partial n}\mathrm{d}\mathcal{S} \quad \text{if } \boldsymbol{x}\in\mathcal{D}\,. \tag{2.19}$$

The first integral in (2.19) describes the contribution of monopoles distributed on $\partial\mathcal{D}$ with monopole surface density $\partial\Phi/\partial n$, the second integral the contribution of dipoles with density Φ. The potential Φ vanishes, if the field point $\boldsymbol{x}$ is located outside $\mathcal{D}$,

$$0 = -\oiint_{\partial\mathcal{D}} G_F(\boldsymbol{x},\boldsymbol{y})\frac{\partial\Phi(\boldsymbol{y})}{\partial n}\mathrm{d}\mathcal{S} + \oiint_{\partial\mathcal{D}} \Phi(\boldsymbol{y})\frac{\partial G_F(\boldsymbol{x},\boldsymbol{y})}{\partial n}\mathrm{d}\mathcal{S} \quad \text{if } \boldsymbol{x}\notin\mathcal{D}\,, \tag{2.20}$$

since $\Delta\Phi = 0$ and $\Delta G = 0$ when substituted in (2.16). It shall be noted that $\partial\mathcal{D}$ does not necessarily have to consist of substantial boundaries. The surface $\partial\mathcal{D}$ may enclose any arbitrary simply connected fluid domain $\mathcal{D}$. Parts of $\partial\mathcal{D}$ may also extend to infinity with the consequence that, as long as Φ decreases as fast as or faster than $1/r$, these parts do not contribute to Φ up to an irrelevant constant C. In case $\Delta\Phi \neq 0$, meaning that $\mathcal{D}$ contains sources,

$$\Phi(\boldsymbol{x}) = -\oiint_{\partial\mathcal{D}} G_F\frac{\partial\Phi}{\partial n}\mathrm{d}\mathcal{S} + \oiint_{\partial\mathcal{D}} \Phi\frac{\partial G_F}{\partial n}\mathrm{d}\mathcal{S} + \iiint_{\mathcal{D}} G_F\,\Delta_y\Phi\,\mathrm{d}\mathcal{V} \tag{2.21}$$

for $\boldsymbol{x}\in\mathcal{D}$, whereby the arguments of $G_F(\boldsymbol{x},\boldsymbol{y})$ and $\Phi(\boldsymbol{y})$ have been dropped for brevity.

2.5 Boundary value problems of potential flow

The surface densities driving a given flow field with potential Φ on $\mathcal{D}$ are not unique, as the following discussion shows. For example, it is possible to choose either a monopole or a dipole density such that the other source distribution vanishes.

2.5.1 Monopole and dipole distributions on the boundaries

The open fluid domain $\mathcal{D}$ is supposed to be a subset of a larger domain, e.g. $\mathcal{D}\subset\mathbb{R}^3$. The domains $\mathcal{D}$ and $\mathbb{R}^3\backslash\{\mathcal{D}\cup\partial\mathcal{D}\}$ share the same boundary $\partial\mathcal{D}$. Let Φ' be a potential on $\mathbb{R}^3\backslash\{\mathcal{D}\cup\partial\mathcal{D}\}$,

$$\Phi'(\boldsymbol{x}) = -\oiint_{\partial\mathcal{D}} G_F(\boldsymbol{x},\boldsymbol{y})\frac{\partial\Phi'(\boldsymbol{y})}{\partial n'}\mathrm{d}\mathcal{S} + \oiint_{\partial\mathcal{D}} \Phi'(\boldsymbol{y})\frac{\partial G_F(\boldsymbol{x},\boldsymbol{y})}{\partial n'}\mathrm{d}\mathcal{S} \tag{2.22}$$

for $\boldsymbol{x}\in\mathbb{R}^3\backslash\overline{\mathcal{D}}$, represented by its values on the surface $\partial\mathcal{D}$. The potential Φ' and its derivatives $\nabla\Phi'$ vanish at infinity, thus no further boundaries than $\partial\mathcal{D}$ contribute to Φ' on $\mathbb{R}^3$. The surface normal $\boldsymbol{n'}$ on $\partial\mathcal{D}$ inward $\mathcal{D}$ and outward $\mathbb{R}^3\backslash\overline{\mathcal{D}}$ is the negative of the outward surface normal $\boldsymbol{n} = -\boldsymbol{n'}$ of $\mathcal{D}$. Addition of (2.22) and (2.19) delivers

$$\Phi(\boldsymbol{x}) = -\oiint_{\partial\mathcal{D}} G_F\left(\frac{\partial\Phi}{\partial n} + \frac{\partial\Phi'}{\partial n'}\right)\mathrm{d}\mathcal{S} + \oiint_{\partial\mathcal{D}} (\Phi-\Phi')\,\frac{\partial G_F}{\partial n}\mathrm{d}\mathcal{S}$$

for $\boldsymbol{x}\in\mathcal{D}$, whereby the arguments of the potential as well as the arguments of the Green's function have been dropped for brevity. No constraints except sufficient smoothness (continuously differentiable) are imposed on Φ' and $\frac{\partial\Phi'}{\partial n}$ on $\partial\mathcal{D}$. The potential Φ' equals zero on $\mathcal{D}$, and does not affect the potential Φ

on $\mathcal{D}$. Therefore, $\partial\Phi(\boldsymbol{y})/\partial n = -\partial\Phi'(\boldsymbol{y})/\partial n'$ on $\partial\mathcal{D}$ is a valid choice, and the potential

$$\Phi(\boldsymbol{x}) = \oiint_{\mathcal{S}} \left(\Phi(\boldsymbol{y}) - \Phi'(\boldsymbol{y})\right) \frac{\partial G_F(\boldsymbol{x},\boldsymbol{y})}{\partial n} \mathrm{d}\mathcal{S} \tag{2.23}$$

is then represented by a distribution of dipole sources $(\Phi(\boldsymbol{y}) - \Phi'(\boldsymbol{y}))$ only. Analogously, choosing $\Phi(\boldsymbol{y}) = \Phi'(\boldsymbol{y})$ on $\partial\mathcal{D}$ yields the potential

$$\Phi(\boldsymbol{x}) = -\oiint_{\mathcal{S}} G_F(\boldsymbol{x},\boldsymbol{y}) \left(\frac{\partial\Phi(\boldsymbol{y})}{\partial n} + \frac{\partial\Phi'(\boldsymbol{y})}{\partial n'}\right) \mathrm{d}\mathcal{S} \tag{2.24}$$

represented by a distribution of monopole sources $\partial\Phi(\boldsymbol{y})/\partial n + \partial\Phi'(\boldsymbol{y})/\partial n'$ only. Given a valid potential fulfilling the boundary conditions, the source densities $\partial\Phi/\partial n|_{\partial\mathcal{D}}$ and $\Phi|_{\partial\mathcal{D}}$ in (2.19) are identified as the flow velocity $v^{\perp}$ normal to $\partial\mathcal{D}$ and the value of the potential Φ on the boundary. Specifying Dirichlet and Neumann boundary conditions on the whole boundary overdetermines the problem. It is possible to choose $\partial\Phi/\partial n|_{\partial\mathcal{D}}$ and $\Phi|_{\partial\mathcal{D}}$ so that no valid solution for the specified boundary conditions exists. This redundancy is removed in (2.24) and (2.23) by the adapted source densities $\partial\Phi(\boldsymbol{y})/\partial n + \partial\Phi'(\boldsymbol{y})/\partial n'$ and $\Phi(\boldsymbol{y}) - \Phi'(\boldsymbol{y})$, which, however, cannot be easily related to the velocities of the flow field on the boundaries. The boundary representations (2.24) and (2.23) are nevertheless highly useful as they allow the easy computation of potential flow given the motion of the boundaries, i.e. the solution of the forward problem; see sec. 2.8.

2.5.2 Dirichlet problem for the Laplacian

The redundancy in (2.19) may also be removed by replacing the free-space Green's function G_F by a Green's function G_D, which fulfils specified boundary conditions on $\partial\mathcal{D}$. The solution of the Dirichlet problem

$$\Delta\Phi = 0 \quad \text{for} \quad \boldsymbol{x} \in \mathcal{D} \quad \text{and} \quad \Phi(x \in \partial\mathcal{D}) = 0 \tag{2.25}$$

can be formally written with the help of a Green's function

$$G_D(\boldsymbol{x},\boldsymbol{y}) = G_F(\boldsymbol{x},\boldsymbol{y}) + H_D(\boldsymbol{x},\boldsymbol{y})\,,$$

which requires the construction [103, p.24 ff.] of a corrector function $H(\boldsymbol{x},\boldsymbol{y})$ fulfilling

$$\Delta_y H_D(\boldsymbol{x},\boldsymbol{y}) = 0 \quad \text{for} \quad \boldsymbol{y} \in \mathcal{D}$$

and the boundary condition $G_D(\boldsymbol{x},\boldsymbol{y}) = 0$ by

$$H_D(\boldsymbol{x},\boldsymbol{y}) = -G_F(\boldsymbol{x},\boldsymbol{y}) \quad \text{for} \quad \boldsymbol{y} \in \partial\mathcal{D} \tag{2.26}$$

on all boundaries for a given field point $\boldsymbol{x} \in \mathcal{D}$. By substitution of (2.26) into (2.19) the boundary representation of the Dirichlet problem

$$\Phi(\boldsymbol{x}) = \oiint_{\partial\mathcal{D}} \Phi(\boldsymbol{y}) \frac{\partial G_D(\boldsymbol{x},\boldsymbol{y})}{\partial n(\boldsymbol{y})} \mathrm{d}\mathcal{S} \quad \text{for} \quad \boldsymbol{x} \in \partial\mathcal{D} \tag{2.27}$$

is obtained. The problem is now to determine the correct Green's function $G_D(\boldsymbol{x},\boldsymbol{y})$.

2.5.3 Neumann problem for the Laplacian

In the same manner, one wishes to be able to write the solution of the Neumann problem

$$\Delta\Phi = 0 \quad \text{for} \quad \boldsymbol{x} \in \mathcal{D} \quad \text{and} \quad \frac{\partial\Phi}{\partial n} = v^{\perp} \quad \text{for} \quad \boldsymbol{x} \in \partial\mathcal{D} \tag{2.28}$$

in terms of a Green's function

$$G_N(\boldsymbol{x},\boldsymbol{y}) = G_F(\boldsymbol{x},\boldsymbol{y}) + H_N(\boldsymbol{x},\boldsymbol{y})$$

and the normal velocities $v^{\perp}$ on the boundaries with the corrector function $H_N(\boldsymbol{x},\boldsymbol{y})$ fulfilling

$$\Delta_y H_N(\boldsymbol{x},\boldsymbol{y}) = 0 \quad \text{for} \quad \boldsymbol{y} \in \mathcal{D}\,. \tag{2.29}$$

The naive choice for the boundary condition $\partial G_N(\boldsymbol{x},\boldsymbol{y})/\partial n(\boldsymbol{y})|_{\boldsymbol{x}\in\mathcal{D},\boldsymbol{y}\in\partial\mathcal{D}} = 0$

$$\frac{\partial H_N(\boldsymbol{x},\boldsymbol{y})}{\partial n(\boldsymbol{y})} = -\frac{\partial G_F(\boldsymbol{x},\boldsymbol{y})}{\partial n(\boldsymbol{y})} \quad \text{for} \quad \boldsymbol{y} \in \partial\mathcal{D}$$

on all boundaries, however, violates the divergence theorem, since its application on a domain $\boldsymbol{x} \in \mathcal{D}$ with closed boundary $\partial\mathcal{D}$ yields

$$\oiint_{\partial\mathcal{D}} \frac{\partial G_N(\boldsymbol{x},\boldsymbol{y})}{\partial n(\boldsymbol{y})}\,\mathrm{d}\mathcal{S}(\boldsymbol{y}) = \iiint_{\mathcal{D}} \Delta_y G_N(\boldsymbol{y},\boldsymbol{y})\;\mathrm{d}\mathcal{V}(\boldsymbol{y}) = 1\,.$$

The simplest choice [104, ch. 1.10] is

$$\frac{\partial H_N(\boldsymbol{x},\boldsymbol{y})}{\partial n(\boldsymbol{y})} = -\frac{\partial G_F(\boldsymbol{x},\boldsymbol{y})}{\partial n(\boldsymbol{y})} + \frac{1}{|\partial\mathcal{D}|} \quad \text{for} \quad \boldsymbol{y} \in \partial\mathcal{D}\,, \tag{2.30}$$

whereby $|\partial\mathcal{D}|$ denotes the surface area of $\mathcal{D}$. The representation of the potential on $\mathcal{D}$ in terms of its normal derivative on $\partial\mathcal{D}$ is thus given by

$$\Phi(\boldsymbol{x}) = \Phi_0 - \oiint_{\partial\mathcal{D}} \frac{\partial\Phi(\boldsymbol{y})}{\partial n} G_N(\boldsymbol{x},\boldsymbol{y})\,\mathrm{d}\mathcal{S}(\boldsymbol{y}) + \iiint_{\mathcal{D}} \Delta_y\Phi\,(\boldsymbol{y})\,G_N\,(\boldsymbol{x},\boldsymbol{y})\;\mathrm{d}\mathcal{V}(\boldsymbol{y}) \tag{2.31}$$

with

$$\Phi_0 = \oiint_{\partial\mathcal{D}} \Phi(\boldsymbol{y})\,\mathrm{d}\mathcal{S}(\boldsymbol{y})\;,$$

where the volume integral in (2.31) accounts for possibly occurring sources in $\mathcal{D}$. The surface averaged potential automatically provides a correct choice for the additive constant of the potential which is undetermined by the Neumann boundary conditions.

2.5.4 Kelvin's extension to Green's third identity for multiply connected domains

In section sec. 2.1 it was argued that $(n-1)$ circulations κ_i along $(n-1)$ irreducible loops with m_i turns must be specified on a n-ply connected domain to

guarantee an single valued potential on $\mathcal{D}$. Kelvin's extension [101, § 58] complements Green's second identity by surface integrals over the artificial boundaries $\mathcal{X}_i$ necessary to split up $\mathcal{D}$ in a simply connected domain

$$\Phi(\boldsymbol{x}) = -\oiint_{\partial\mathcal{D}} G_F \frac{\partial\Phi}{\partial n}\mathrm{d}\mathcal{S} + \oiint_{\partial\mathcal{D}} \Phi(\boldsymbol{y})\frac{\partial G_F}{\partial n} + \sum_{i=1}^{n-1}\kappa_i \oiint_{\mathcal{X}_i} \frac{\partial G_F}{\partial n}\mathrm{d}\mathcal{S} \tag{2.32}$$

for a field point $\boldsymbol{x}$ in $\mathcal{D}$. Equation (2.32) can be derived directly by application of (2.19) to the boundaries of the domain $\mathcal{D}$ rendered simply connected by the artificial boundaries $\mathcal{X}_i$. The normal component of the velocity must be continuous on both sides of $\mathcal{X}_i$ and thus the surface integrals over $G_F\partial\Phi/\partial n$ on both sides of $\mathcal{X}_i$ cancel due to opposite signs of the surface normal. The potential Φ experiences a jump κ_i when crossing $\mathcal{X}_i$. Only the contributions $\kappa_i\,\partial G_F/\partial n$ remain.

2.6 Decomposition of the velocity potential of rigid bodies

Again, a domain $\mathcal{D}$ filled with an ideal incompressible and irrotational fluid partially or fully bounded by $\partial\mathcal{D}$ is considered. The domain $\mathcal{D}$ may extend to infinity, and if it does so, the potential Φ and the derivative $\nabla\Phi$ are supposed to vanish at infinity. The boundary $\partial\mathcal{D}$ consists of the disjoint smooth surfaces $\partial\mathcal{D} = \bigcup_{\mathcal{I}}\partial\mathcal{I}$ of a set of rigid objects $\mathcal{I}$, each of them moving in an arbitrary fashion. In case $\mathcal{D}$ is fully enclosed by a solid boundary, the FOR is chosen such that this part of the boundary is fixed in the FOR. Otherwise, the velocity and the potential are supposed to vanish at infinity in the FOR. The boundary of a rigid object is said to be stationary if the velocity of the object equals zero in the FOR. The no-penetration boundary condition holds on all moving and stationary solid boundaries $\partial\mathcal{D}$. For the sake of simplicity, the symbol $\mathcal{I}$ is used at the same time for an element of the set of rigid bodies, the whole set, and also as an index to iterate over all elements of the set.

The linearity of the Laplacian can be exploited to split the potential up into the contributions of each moving rigid body. The normal component of the velocity of the fluid at a point $\boldsymbol{y}^{\mathcal{I}}$ on the boundary $\mathcal{I}$ of one of the rigid bodies is given by the no-penetration boundary condition (2.11)

$$\left.\frac{\partial\Phi}{\partial n}\right|_{\partial\mathcal{I}} = \left[\boldsymbol{u}^{\mathcal{I}} + \boldsymbol{\omega}^{\mathcal{I}} \times \left(\boldsymbol{y}^{\mathcal{I}} - \boldsymbol{q}^{\mathcal{I}}\right)\right]\cdot\boldsymbol{n}^{\mathcal{I}} = \boldsymbol{u}^{\mathcal{I}}\cdot\boldsymbol{n}^{\mathcal{I}} + \boldsymbol{\omega}^{\mathcal{I}}\cdot\left[\left(\boldsymbol{y}^{\mathcal{I}} - \boldsymbol{q}^{\mathcal{I}}\right)\times\boldsymbol{n}^{\mathcal{I}}\right],$$

with $\boldsymbol{q}^{\mathcal{I}}$ the position of the BFS of $\mathcal{I}$, whereby the commutativity of the scalar triple product was used for the last conversion. The solution of the potential problem (2.31) given the normal velocities on the boundaries can be split up into

$$\begin{aligned}\Phi(\boldsymbol{x},t) = \Phi_0(t) &- \sum_{\mathcal{I}} \boldsymbol{u}^{\mathcal{I}}(t)\cdot\oiint_{\partial\mathcal{I}(t)} G_N(\boldsymbol{x},\boldsymbol{y})\boldsymbol{n}(\boldsymbol{y})\mathrm{d}\mathcal{S}(\boldsymbol{y}) \\ &- \sum_{\mathcal{I}} \boldsymbol{\omega}^{\mathcal{I}}(t)\cdot\oiint_{\partial\mathcal{I}(t)} G_N(\boldsymbol{x},\boldsymbol{y})\left[\left(\boldsymbol{y}^{\mathcal{I}} - \boldsymbol{q}^{\mathcal{I}}\right)\times\boldsymbol{n}(\boldsymbol{y})\right]\mathrm{d}\mathcal{S}(\boldsymbol{y}).\end{aligned}$$

The Green's function G_N for the Neumann problem with corrector function H_N is chosen such that (2.30) holds for a fixed but arbitrary $\boldsymbol{x} \in \mathcal{D}$ at the given instant of time. The surfaces of integration $\partial\mathcal{I}(t)$ are time-dependent, since the bodies $\mathcal{I}$ are allowed to move. The boundaries $\partial\mathcal{I}$ are fixed in the BFSs of the respective body $\mathcal{I}$. The source points $\boldsymbol{Y}^{\mathcal{I}} = \boldsymbol{y}(t)^{\mathcal{I}} - \boldsymbol{q}^{\mathcal{I}}(t)$ and the surface normal $\boldsymbol{N}^{\mathcal{I}}$ defined with respect to the BFS are then independent of time, and the surface integrals can be evaluated

$$\begin{aligned}\Phi(\boldsymbol{x},t) = \Phi_0(t) - \sum_{\mathcal{I}} \boldsymbol{u}^{\mathcal{I}} \cdot \mathcal{R}^{\mathrm{T}} \oiint_{\partial\mathcal{I}} G_N(\boldsymbol{x}, \boldsymbol{Y} + \mathcal{R}\boldsymbol{q}^{\mathcal{I}})\, \boldsymbol{N}\, \mathrm{d}\mathcal{S}(\boldsymbol{Y}) \\ + \boldsymbol{\omega}^{\mathcal{I}}(t) \cdot \mathcal{R}^{\mathrm{T}} \oiint_{\partial\mathcal{I}} G_N(\boldsymbol{x}, \boldsymbol{Y} + \mathcal{R}\boldsymbol{q}^{\mathcal{I}})\, (\boldsymbol{Y} \times \boldsymbol{N}(\boldsymbol{Y}))\, \mathrm{d}\mathcal{S}(\boldsymbol{Y})\end{aligned}$$

with the rotation matrix $\mathcal{R}^{\mathrm{T}}$ from BFS to FOR coordinates as defined in sec. 1.2.1. The arguments of $\mathcal{R} = \mathcal{R}(\boldsymbol{\phi}^{\mathcal{I}}(t))$ and $\boldsymbol{q}^{\mathcal{I}} = \boldsymbol{q}^{\mathcal{I}}(t)$ have been dropped for brevity. The time-dependent $\Phi_0(t)$ has no effect on the fluid motion. Thus, $\Phi_0(t) = 0$ is a valid choice. The result is the decomposition

$$\Phi(\boldsymbol{x},t) = \sum_{\mathcal{I}} \sum_{i=1}^{6} \mathfrak{u}_i^{\mathcal{I}}(t) \varphi_i^{\mathcal{I}}(\boldsymbol{x},t) \tag{2.33a}$$

with the property

$$\frac{\partial\Phi}{\partial\mathfrak{u}_i^{\mathcal{I}}} = \varphi_i^{\mathcal{I}}\,, \tag{2.33b}$$

and using the 6D vector notion introduced in sec. 1.2.2. Furthermore, the $6D$ surface normal

$$\mathfrak{n} = (\boldsymbol{n}, \boldsymbol{y} \times \boldsymbol{n})^{\mathrm{T}}\,,$$

allows to write the boundary conditions of the potentials $\varphi_i^{\mathcal{I}}$

$$\begin{aligned}\left.\frac{\partial\varphi_i^{\mathcal{I}}(\boldsymbol{x},t)}{\partial n}\right|_{\boldsymbol{x}\in\partial\mathcal{I}} &= n_i \qquad \text{for} \qquad i \in \{1,2,3\} \qquad \text{and} \\ \left.\frac{\partial\varphi_i^{\mathcal{I}}(\boldsymbol{x},t)}{\partial n}\right|_{\boldsymbol{x}\in\partial\mathcal{I}} &= (\boldsymbol{x}\times\boldsymbol{n})_{k-3} \qquad \text{for} \qquad i \in \{4,5,6\}\,,\end{aligned}$$

which fulfil $\Delta\varphi_i^{\mathcal{I}} = 0$ in 6D vector notation

$$\left.\frac{\partial\varphi_i^{\mathcal{I}}(\boldsymbol{x},t)}{\partial n}\right|_{\boldsymbol{x}\in\partial\mathcal{I}} = \mathfrak{n}_i \qquad \text{and} \qquad \left.\frac{\partial\varphi_i^{\mathcal{I}}(\boldsymbol{x},t)}{\partial n}\right|_{\boldsymbol{x}\in\mathcal{J}\neq\mathcal{I}} = 0 \tag{2.33c}$$

for any point $\boldsymbol{x}$ located on any surface $\mathcal{J}$ other than $\mathcal{I}$. The decomposition (2.33a) is remarkable in a number of aspects. The harmonic functions $\varphi_i(\boldsymbol{x}, \boldsymbol{q}^{\mathcal{I}}(t))$ do not depend on the velocity of the boundaries, but on the current shape and position of the boundaries.

If only one body $\mathcal{B}$ exists in an otherwise unbounded fluid domain at rest, the potential is of the form $\Phi(\boldsymbol{x},t) = \boldsymbol{\varphi}(\boldsymbol{x} - \boldsymbol{o}^{\mathcal{B}}) \cdot (\boldsymbol{V}(t), \boldsymbol{\Omega}(t))^{\mathrm{T}}$ with $\boldsymbol{o}^{\mathcal{B}}$ the origin of the BFS of $\mathcal{B}$ and $\boldsymbol{\varphi} = (\ldots, \varphi_i, \ldots)^{\mathrm{T}}$. The potential is stationary in the BFS of the moving body, if $\boldsymbol{V}$ and $\boldsymbol{\Omega}$ are constant in time, and no other boundaries are moving relative to $\mathcal{B}$.

On the other hand, the potential Φ is not necessarily stationary, if $\boldsymbol{\Omega}$ and $\boldsymbol{V}$ are constant. The potential Φ can also vary in time due to changes of the φ_i resulting from the relative motion of other boundaries.

2.7 The hydrodynamic image

The term *hydrodynamic image* was introduced in [20] in the context of the LLS of fish, to express the fact that the water flow velocity on the surface of a body is altered by the presence of other objects. The restriction to water is somewhat artificial. The term *fluid-dynamical image* could be considered to be a more suitable generalisation actually meaning the same, but is emphasising that the physics of inviscid incompressible fluids are independent of the medium, e.g. for air and water, apart from the density.

The definition of the term hydrodynamic image lacks a definition of the term *object*. The term *hydrodynamic object* is often implicitly defined through its contribution to the hydrodynamic image [47, 105], which is a somehow recursive alternating definition of hydrodynamic image and hydrodynamic object. In the framework of potential flow (2.21), a *fluid-dynamical object* can be defined as an *isolated continuous distribution of mono- or dipoles*. A single point source is incorporated in the definition, since it can always be represented by a corresponding distribution of mono- or dipoles on a surface enclosing the point source. An artificial boundary enclosing a fluid domain carrying a distribution of mono- or dipole sources generating the potential is not covered by the definition of a fluid-dynamical object, since it is not isolated. The question, whether a distribution of sources representing an object or the potential created by it is unique, and if it is possible to uniquely conclude to the presence and distribution of mono- or dipoles driving the flow field from the hydrodynamic image is addressed in ch. 3. An answer to this question is implicitly given in the last sentences, in sec. 2.5, and in sec. 2.8: any closed boundary, physical or artificially drawn, can be used to find a mono- or dipole source distribution generating the observed flow field.

In more mathematical terms, the hydrodynamic image of the potential relates the potential on the observer $\mathcal{B}$ to the potential on the rest of the boundary $\partial\mathcal{D}$ of the domain $\mathcal{D}$, whereby $\partial\mathcal{B} \subset \partial\mathcal{D}$.

The potential on the domain $\mathcal{D}$ is represented by the surface integral (2.19)

$$\Phi(\boldsymbol{x}) = \oiint_{\partial\mathcal{D}} \rho(\boldsymbol{y}) G_F(\boldsymbol{x},\boldsymbol{y}) \,\mathrm{d}\mathcal{S} - \oiint_{\partial\mathcal{D}} \sigma(\boldsymbol{y}) \frac{\partial G_F(\boldsymbol{x},\boldsymbol{y})}{\partial n(\boldsymbol{y})} \,\mathrm{d}\mathcal{S} \quad \text{for } \boldsymbol{x} \in \mathcal{D} \tag{2.34}$$

over a monopole distribution ρ and a dipole distribution σ on $\partial\mathcal{D}$, identified in the case of potential flow as the Cauchy data $\partial\Phi/\partial n$ and Φ on $\partial\mathcal{D}$.

As $\boldsymbol{x}$ approaches the boundary, the integral kernels obviously become singular. Which value is to be assigned to Φ when $\boldsymbol{x} \in \partial\mathcal{D}$? The integral kernels $\mathcal{K} \in \{G_F, \partial G_F/\partial n\}$ in the improper integrals of (2.34) are weakly singular kernels in the sense

$$|\mathcal{K}(\boldsymbol{x},\boldsymbol{y})| \leq c\,|\boldsymbol{x}-\boldsymbol{y}|^{-d}$$

with the two constants c and $d < N-1$ and the number of dimensions N. (2.34) is thus locally integrable except in the point $\boldsymbol{x} = \boldsymbol{y}$, [106, ch. 1.2]. It is convenient to define the integral operators V and K,

$$V\rho(\boldsymbol{x} \in \partial\mathcal{D}) = \oiint_{\boldsymbol{y}\in\partial\mathcal{D}\setminus\boldsymbol{x}} G_F(\boldsymbol{x},\boldsymbol{y})\rho(\boldsymbol{y}) \,\mathrm{d}\mathcal{S}(\boldsymbol{y})\,,$$

$$K\sigma(\boldsymbol{x} \in \partial\mathcal{D}) = \oiint_{\boldsymbol{y}\in\partial\mathcal{D}\setminus\boldsymbol{x}} \frac{\partial G_F(\boldsymbol{x},\boldsymbol{y})}{\partial n(\boldsymbol{y})}\sigma(\boldsymbol{y}) \,\mathrm{d}\mathcal{S}(\boldsymbol{y})\,.$$

The normal derivative $\partial\Phi/\partial n$ on $\partial\mathcal{D}$ becomes

$$\frac{\partial\Phi(\boldsymbol{x})}{\partial n(\boldsymbol{x})} = \frac{\partial}{\partial n(\boldsymbol{x})} \oiint_{\partial\mathcal{D}} \rho(\boldsymbol{y}) G_F(\boldsymbol{x},\boldsymbol{y})\,\mathrm{d}\mathcal{S} - \frac{\partial}{\partial n(\boldsymbol{x})} \oiint_{\partial\mathcal{D}} \sigma(\boldsymbol{y}) \frac{\partial G_F(\boldsymbol{x},\boldsymbol{y})}{\partial n(\boldsymbol{y})}\,\mathrm{d}\mathcal{S}\,,$$

whereby the first integral is weakly singular, and the integral operator

$$K'\rho(\boldsymbol{x}\in\partial\mathcal{D}) = \oiint_{\boldsymbol{y}\in\partial\mathcal{D}\setminus\boldsymbol{x}} \frac{\partial G_F(\boldsymbol{x},\boldsymbol{y})}{\partial n(\boldsymbol{x})} \rho(\boldsymbol{y})\,\mathrm{d}\mathcal{S}(\boldsymbol{y})$$

is obtained. The second integral is hypersingular, and can be expressed in 3D by the integral operator

$$D\sigma(\boldsymbol{x}) = -\left(\boldsymbol{n}(\boldsymbol{x})\times\nabla_x\right)\cdot \oiint_{\boldsymbol{y}\in S\setminus\boldsymbol{x}} G_F(\boldsymbol{x},\boldsymbol{y})\left(\boldsymbol{n}(\boldsymbol{y})\times\nabla_y\sigma(\boldsymbol{y})\right)\mathrm{d}\mathcal{S}(y) \tag{2.35}$$

after some cumbersome computations [106, ch. 1.2] in terms of the tangential derivative $\boldsymbol{n}(\boldsymbol{y})\times\nabla_y\sigma(\boldsymbol{y})$. Formulated by the just defined integral operators, the Cauchy data on $\partial\mathcal{D}$ are related through the Calderón projector

$$\begin{pmatrix}\upsilon\\ \sigma\end{pmatrix} = \begin{pmatrix}\frac{1}{2}\mathbb{1} - K & V\\ D & \frac{1}{2}\mathbb{1} + K'\end{pmatrix}\begin{pmatrix}\upsilon\\ \sigma\end{pmatrix} \tag{2.36}$$

with identity $\mathbb{1}$. These overdetermined relations between the Cauchy data may be used to recover incomplete boundary values, e.g. to express the fluid-mechanical image $\Phi(\boldsymbol{x}\in\partial\mathcal{B})$ on $\mathcal{B}$ through the Cauchy data given on the rest of the boundary. This results in Fredholm integral equations of the first and second kind that relate the Neumann $\partial\Phi/\partial n$ and Dirichlet Φ data on the boundary. Or conversely, if the location of the boundaries is known, (2.36) can be used to compute the values of Φ and the normal derivative $\partial\Phi/\partial n(\boldsymbol{x})$ on the remaining part of the boundary from the measured fluid-mechanical image. However, the solution of the resulting boundary integral equations is not trivial and numerically tricky. A short overview on the methods used to complete Cauchy data is given in [107].

2.8 Boundary element method

In ch. 3, numerical solutions of potential flow are computed as input to a LLS in order to demonstrate 2-dimensional (2D) versions of flow field reconstruction methods, see e.g. fig. 3.5. The numerical method used is closely related to the boundary representations of potential flow discussed in the previous section 2.5.1.

The setting is given by solid objects moving through an inviscid incompressible irrotational fluid, which is otherwise at rest. Neumann boundary conditions are imposed on all boundaries. The potential on $\mathcal{D}$ can be represented according to (2.24) by a continuous distribution $\rho(\boldsymbol{y})$ of monopoles

$$\Phi(\boldsymbol{x}) = -\oint_{\partial\mathcal{D}} G_F(\boldsymbol{x},\boldsymbol{y})\,\rho(\boldsymbol{y})\,\mathrm{d}\mathcal{S}(\boldsymbol{y}) \tag{2.37}$$

on the whole boundary $\partial\mathcal{D}$, whereby

$$G_F(\boldsymbol{x},\boldsymbol{y}) = \frac{1}{2\pi}\ln\left(|\boldsymbol{x}-\boldsymbol{y}|\right)$$

is the two dimensional fundamental solution for the Laplace operator.

The basic idea of the boundary-element method (BEM) is to determine the source density $\rho(\boldsymbol{y})$ on the boundaries such that the resulting potential (2.37) satisfies all boundary conditions. In general, it will not be possible to find an explicit solution for ρ. Thus, the problem must be solved numerically, [108].

For this purpose the boundary $\partial\mathcal{D}$ shall be discretised into N line segments $L_1, L_2, \ldots, L_N$ of equal length l. The density ρ is taken to be constant over each line segment. Hence, the monopole source density on the boundary is given by the vector $\boldsymbol{\rho}$ with N elements, whereby the element ρ_i specifies the monopole source density on the line segment L_i. The substitution of this discretisation into (2.37) yields

$$\Phi(\boldsymbol{x}) = -\sum_{i=1}^{N} \rho_i \int_{L_i} G_F(\boldsymbol{x}, \boldsymbol{y}) \,\mathrm{d}l(\boldsymbol{y})\,. \tag{2.38}$$

The monopole source densities $\boldsymbol{\rho}$ are determined by the minimum of the squared difference

$$E = \oint_{\partial\mathcal{D}} \left(\frac{\partial \Phi}{\partial \boldsymbol{n}'}(\boldsymbol{y}) - v^{\perp} \right)^2 \mathrm{d}l(\boldsymbol{y}) \tag{2.39}$$

between the prescribed boundary conditions (2.11) and the normal fluid velocity $\partial\Phi/\partial n'$ obtained from (2.38), where $\boldsymbol{n}'$ is the surface normal pointing inward the fluid and $v^{\perp} = v^{\perp}(\boldsymbol{y})$ is the velocity of motion of the respective surface element at $\boldsymbol{y}$ normal to the boundary along $\boldsymbol{n}'$.

With $\partial\mathcal{D}$ discretised in line segments, the error in the boundary condition (2.39) turns into a sum over all line segments. To be precise, the error E over a line segment is approximated by its value at the centre point $\boldsymbol{p}_i$ of the respective line segment L_i, which means that $v^{\perp}$ and $\partial\Phi/\partial\boldsymbol{n}'$ are evaluated at $\boldsymbol{p}_i$. By virtue of the boundary discretisation (2.38) and

$$F(\boldsymbol{x}, \boldsymbol{y}) = \nabla_x G_F(\boldsymbol{x}, \boldsymbol{y}) \cdot \boldsymbol{n}'(\boldsymbol{y}) = -\frac{(\boldsymbol{x} - \boldsymbol{y}) \cdot \boldsymbol{n}'(\boldsymbol{y})}{2\pi(\boldsymbol{x} - \boldsymbol{y})^2} \tag{2.40}$$

the error (2.39) thus becomes

$$E = \sum_{i=1}^{N} l \left(-\sum_{j=1}^{N} \rho_j \int_{L_j} F(\boldsymbol{p}_i, \boldsymbol{y}) \,\mathrm{d}l(\boldsymbol{y}) - v_i^{\perp} \right)^2 \tag{2.41}$$

with $v_i^{\perp} = v^{\perp}(\boldsymbol{p}_i)$ and $\boldsymbol{v}^{\perp}$ the vector of all $v_i^{\perp}$ of length N. The simple source densities $\boldsymbol{\rho}$ are thus determined by the solution of

$$\mathcal{L}\boldsymbol{\rho} = \boldsymbol{v}^{\perp}\,, \tag{2.42}$$

where

$$\mathcal{L}_{ij} = -\int_{L_j} F(\boldsymbol{p}_i, \boldsymbol{y}) \,\mathrm{d}l(\boldsymbol{y}) \tag{2.43}$$

is the contribution of the flow field generated by a line element L_j to the normal velocity $v_i^{\perp}$ at the centre point p_i of the line element L_i. It shall be noted that the potential and the flow field are linear in all source strengths ρ_i, and thus, E is convex in all ρ_i. The equation system (2.42) will not have an exact

solution, since the boundary value problem is approximated by a discretised boundary . Thus, E has exactly one minimum, and it is numerically easy to find this minimum even for a high number of ρ_i, or alternatively to determine the pseudo-inverse of $\mathcal{L}$. The potential obtained from substituting the ρ_i into (2.38) fulfils the boundary conditions on $\partial\mathcal{D}$ in the least-squares sense.

Furthermore, to avoid numerically costly computations due to the singularities occurring in $F(\boldsymbol{x}, \boldsymbol{y})$ (2.40) if $\boldsymbol{x} = \boldsymbol{y}$ on the diagonal of $\mathcal{L}$, a second surface $\mathcal{C}$ is introduced lying exterior to $\mathcal{D}$ at close distance to the actual boundary $\partial\mathcal{D}$, which carries the source distribution $\boldsymbol{\rho}$. A speed-up in the computation of $\mathcal{L}$ and the flow field is accomplished by analytical solution [109] of the line integral (2.43), and the respective geometric transformations to apply this expression to any line segment [109]. The method described is one of the simplest implementations of a BEM. More efficient, elaborate, and versatile version of BEMs can be found in the already mentioned book of Liu [108].

2.9 Pressure

So far, only the flow potential and the flow field of an ideal incompressible irrotational fluid have been considered. The second quantity that is related to the dynamics of the incompressible Newtonian fluid is the pressure. All other quantities such as temperature, energy, or density are decoupled from the equations of motion of the incompressible Newtonian fluid governed by the incompressible Navier-Stokes equations [45, ch. 10].

The first part of the following discussion of the pressure is carried out for an incompressible Newtonian fluid, which does not affect the applicability of the obtained statements to potential flow. In incompressible flow the pressure p is an explicit function of the flow field, which can be seen simply from reordering the incompressible Navier-Stokes equations

$$\nabla p = -\rho \left[\frac{\partial \boldsymbol{v}}{\partial t} + (\boldsymbol{v} \cdot \boldsymbol{\nabla})\, \boldsymbol{v} \right] + \mu \Delta \boldsymbol{v} \,. \tag{2.44}$$

The following redefinition of the pressure

$$p(\boldsymbol{x}, t) = \tilde{p}(\boldsymbol{x}, t) - \varrho \boldsymbol{g} \cdot \boldsymbol{x}$$

is implicitly used throughout this work, which is the actual pressure $\tilde{p}$ corrected by the static pressure $\varrho \boldsymbol{g} \cdot \boldsymbol{x}$. The static pressure has no effect on the dynamics of the incompressible fluid or on the motion of a rigid body. Application of the divergence to (2.44) with (2.5) yields the so called pressure Poisson equation

$$\Delta p = -\varrho \boldsymbol{\nabla} \cdot \left[(\boldsymbol{v} \cdot \boldsymbol{\nabla})\, \boldsymbol{v} \right] \,,$$

which can be solved in three dimensions using the fundamental solution of the Laplacian (2.17)

$$\hat{p}(\boldsymbol{x}, t) = \varrho \iiint_{\mathcal{D}} \frac{\nabla_y \cdot \left[(\boldsymbol{v} \cdot \boldsymbol{\nabla}_y)\, \boldsymbol{v} \right]}{4\pi \left| \boldsymbol{x} - \boldsymbol{y} \right|} \, \mathrm{d}\mathcal{D} \tag{2.45}$$

up to an additive harmonic function $p = p' + \hat{p}$ fulfilling

$$\Delta p'(\boldsymbol{x}, t) = 0 \,. \tag{2.46}$$

The arguments $\boldsymbol{v} = \boldsymbol{v}(\boldsymbol{y}, t)$ have been dropped for brevity. The harmonic part of the pressure $p(\boldsymbol{x}, t)$ is determined by suitable boundary conditions. But, what are appropriate boundary conditions for the pressure? This question shall be put aside for the moment, and picked up again after expressing (2.45) in terms of the flow velocity on the boundaries of an ideal incompressible and irrotational fluid domain. Using the vector calculus identity

$$\boldsymbol{\nabla} \cdot (\Psi \boldsymbol{A}) = \Psi \boldsymbol{\nabla} \cdot \boldsymbol{A} + \nabla\Psi \cdot \boldsymbol{A}$$

with scalar valued differentiable Ψ and vector valued differentiable $\boldsymbol{A}$, (2.45) can be rewritten by virtue of the divergence theorem (2.14) as

$$\hat{p}(\boldsymbol{x}, t) = \frac{\varrho}{4\pi} \oiint_{\partial\mathcal{D}} \frac{(\boldsymbol{v} \cdot \boldsymbol{\nabla}_y)\, \boldsymbol{v}}{|\boldsymbol{x} - \boldsymbol{y}|} \cdot \boldsymbol{n} \, \mathrm{d}\mathcal{S} - \frac{\varrho}{4\pi} \iiint_{\mathcal{D}} (\boldsymbol{v} \cdot \boldsymbol{\nabla}_y)\, \boldsymbol{v} \cdot \nabla_{\boldsymbol{y}} \frac{1}{|\boldsymbol{x} - \boldsymbol{y}|} \, \mathrm{d}\mathcal{D} \,. \quad (2.47)$$

Further assuming $\boldsymbol{\nabla} \times \boldsymbol{v} = 0$ and $\boldsymbol{\nabla} \cdot \boldsymbol{v}$, i.e. an ideal irrotational incompressible fluid, and applying the vector calculus identity

$$\nabla(\boldsymbol{u} \cdot \boldsymbol{v}) = \boldsymbol{u} \times (\boldsymbol{\nabla} \times \boldsymbol{v}) + \boldsymbol{v} \times (\boldsymbol{\nabla} \times \boldsymbol{u}) + (\boldsymbol{u} \cdot \boldsymbol{\nabla})\, \boldsymbol{v} + (\boldsymbol{v} \cdot \boldsymbol{\nabla})\, \boldsymbol{u}$$

and Green's first identity (2.15), the volume integral in (2.47) becomes

$$\begin{aligned} -\frac{\varrho}{4\pi} \iiint_{\mathcal{D}} (\boldsymbol{v} \cdot \boldsymbol{\nabla}_y)\, \boldsymbol{v} \cdot \nabla_{\boldsymbol{y}} \frac{1}{|\boldsymbol{x} - \boldsymbol{y}|} \, \mathrm{d}\mathcal{D} &= -\frac{\varrho}{8\pi} \iiint_{\mathcal{D}} \nabla_{\boldsymbol{y}} |\boldsymbol{v}|^2 \nabla_{\boldsymbol{y}} \frac{1}{|\boldsymbol{x} - \boldsymbol{y}|} \\ &= -\frac{1}{8\pi} \oiint_{\partial\mathcal{D}} |\boldsymbol{v}|^2 \nabla_y \frac{1}{|\boldsymbol{x} + \boldsymbol{y}|} \cdot \boldsymbol{n} \, \mathrm{d}\mathcal{S} + \frac{\varrho}{8\pi} \iiint_{\mathcal{D}} |\boldsymbol{v}|^2 \Delta_y \frac{1}{|\boldsymbol{x} - \boldsymbol{y}|} \, \mathrm{d}\mathcal{D} \,, \end{aligned}$$

which leads to the pressure boundary integral

$$\hat{p}(\boldsymbol{x}, t) = -\frac{\varrho}{4\pi} \oiint_{\partial\mathcal{D}} \left[\frac{(\boldsymbol{v} \cdot \boldsymbol{\nabla}_y)\, \boldsymbol{v}}{|\boldsymbol{x} - \boldsymbol{y}|} + \frac{1}{2} |\boldsymbol{v}|^2 \nabla_{\boldsymbol{y}} \frac{1}{|\boldsymbol{x} - \boldsymbol{y}|} \right] \cdot \boldsymbol{n} \, \mathrm{d}\mathcal{S} + \frac{\varrho}{2} |\boldsymbol{v}(\boldsymbol{x}, t)|^2 \,. \quad (2.48)$$

Now, the question of appropriate boundary conditions for the pressure on $\partial\mathcal{D}$ shall be picked up briefly. Utilising the same construction as is was used to justify Green's representation formula (2.19), the pressure on the boundary is given by

$$\hat{p}(\boldsymbol{x} \in \partial\mathcal{D}, t) = \lim_{z \in \mathcal{D} \to x \in \partial\mathcal{D}} \hat{p}(\boldsymbol{z}, t) \,.$$

However, to obtain a boundary condition for the pressure, the limit

$$\nabla_x \hat{p}(\boldsymbol{x} \in \partial\mathcal{D}, t) = \lim_{z \in \mathcal{D} \to x \in \partial\mathcal{D}} \nabla_z \hat{p}(\boldsymbol{z}, t)$$

for the gradient of the pressure appearing in (2.3) or (2.44) must be computed, which involves a hypersingular integral kernel. A proper discussion and derivation of suitable boundary conditions for p can be found in [63, ch. 13.3.3] and the articles cited therein, showing that for the more general case of a Newtonian incompressible fluid, it is sufficient to demand

$$\boldsymbol{n} \cdot \nabla p = -\varrho \left[\frac{\partial \boldsymbol{v}}{\partial t} + (\boldsymbol{v} \cdot \boldsymbol{\nabla})\, \boldsymbol{v} \right] \cdot \boldsymbol{n} + \mu \Delta \boldsymbol{v} \cdot \boldsymbol{n} \quad (2.49)$$

on $\partial\mathcal{D}$, which can be easily adapted to the inviscid case by setting $\mu = 0$. Alternatively, the pressure on the boundary can be specified. Both conditions

determine the homogeneous part p'. An additive constant in the pressure does not affect the incompressible fluid.

At this point several statements can be already made about the usefulness of measuring the pressure on the surface of a body, without further discussing in detail how to recover the pressure from measurements of the flow velocity, or the possibility of removing the dependence of the pressure upon the location of unknown boundaries and its value on them. First, equation (2.45) or (2.48) suggest that in general the pressure on $\mathcal{D}$ and thus the information about the boundaries carried by the pressure can *not* be determined from pressure measurements on $\partial\mathcal{D}$ without the knowledge of $\boldsymbol{v}$ at the boundary for potential flow or everywhere for viscid incompressible flow. It is possible to relate the pressure with the motion of the boundaries, but the pressure also contains the velocity of the flow field at the field point $\boldsymbol{x}$ of interest. In summary, without making further assumptions, it is *not* possible to treat the forward problem of the pressure without knowledge of the velocity field, and, conversely, it is *not* possible to reconstruct the pressure field or any information transmitted through the pressure without knowledge of the velocity field, or without making further assumptions.

It follows from (2.46), (2.48) and (2.49) that in principle it should also be possible to reconstruct the pressure field from the velocity measured on the boundaries of an ideal incompressible irrotational fluid. Then, the next question is how to interpret the reconstructed pressure field with respect to the boundaries driving the flow field. Contrary to the pressure, it will be shown in ch. 3 that it is possible to reconstruct the velocity field on a domain with ideal incompressible irrotational fluid from measurements of the tangential velocity and no-penetration boundary condition on a subset of the boundary of the domain, independent of the knowledge of further boundaries. Nevertheless, as discussed in the next section, the measurement of the pressure can contribute to the perception of objects, or might be used to determine the hydrodynamic forces acting on a body.

In an ideal incompressible fluid the pressure $p(\boldsymbol{x},t)$ can be calculated from the flow field $\boldsymbol{v}(\boldsymbol{x},t) = \nabla\Phi(\boldsymbol{x},t)$ up to an arbitrary function of time $C(t)$ by Bernoulli's equation

$$p = -\varrho\left(\frac{\partial\Phi}{\partial t} + \frac{1}{2}\nabla\Phi\cdot\nabla\Phi - C(t)\right), \tag{2.50}$$

which is valid along a streamline or everywhere in an irrotational fluid domain, whereby $\partial_t\Phi$ is the local time derivative of the velocity potential in Eulerian coordinates, i.e. the change of Φ in time at a fixed position in space.

The function $C(t)$ in (2.50) has no effect on the dynamics of the incompressible fluid, since the pressure acts on the fluid by its gradient (2.3). It also has no effect on closed rigid boundaries, since $C(t)$ drops out of the force

$$\boldsymbol{f}^{\mathcal{B}}(t) = \oiint_{\partial\mathcal{B}} p\,\boldsymbol{n}\,\mathrm{d}\mathcal{S} = -\varrho\oiint_{\partial\mathcal{B}}\left(\frac{\partial\Phi}{\partial t} + \frac{1}{2}\nabla\Phi\cdot\nabla\Phi\right)\boldsymbol{n}\,\mathrm{d}\mathcal{S} \tag{2.51a}$$

and torque

$$\boldsymbol{t}^{\mathcal{B}}(t) = \oiint_{\partial\mathcal{B}} p\,(\boldsymbol{x}\times\boldsymbol{n})\,\mathrm{d}\mathcal{S} = -\varrho\oiint_{\partial\mathcal{B}}\left(\frac{\partial\Phi}{\partial t} + \frac{1}{2}\nabla\Phi\cdot\nabla\Phi\right)(\boldsymbol{x}\times\boldsymbol{n})\,\mathrm{d}\mathcal{S} \tag{2.51b}$$

on a body $\mathcal{B}$ given by the surface integral over the pressure on the surface $\partial\mathcal{B}$ with surface normal $\boldsymbol{n}$ outward of the fluid.

2.10 Some rough estimates on flow sensing

The next chapter of this thesis deals with the question of how to reconstruct information about the environment from measurements of the flow velocity of an ideal incompressible irrotational fluid on the boundary of an object. In the previous sections it was shown that the potential flow on a domain is uniquely determined by the normal velocity on the boundaries. Furthermore, the knowledge of the pressure on the boundaries is not sufficient to determine the fluid motion. The purpose of this section is to obtain some rough estimates for the quantities of interest, and the characteristic scales involved in the motion and perception of potential flow caused by the motion of solid objects. The second question addressed is the possible contribution of pressure to the perception of moving objects. The characteristic scales of the forward problem, i.e. the flow field generated by the environment, already provides essential insights in the nature of flow sensing.

2.10.1 Detection of a moving sphere by velocity sensing

The simplest flow field generated by a moving object is that of a sphere S with radius b_S in an undisturbed unbounded fluid otherwise at rest. The centre of the sphere is located at $\boldsymbol{x}^S(t)$ at time t. The sphere S is supposed to move with velocity $\boldsymbol{u}^S(t)$ and acceleration $\mathrm{d}\boldsymbol{u}^S(t)/\mathrm{d}t = \boldsymbol{a}^S(t)$. The velocity potential of the moving sphere at the field point $\boldsymbol{x}$ at time t is given by

$$\Phi_S(\boldsymbol{x},t) = -\frac{(\boldsymbol{x}-\boldsymbol{x}^S(t))\cdot\boldsymbol{d}^S(t)}{4\pi\left|\boldsymbol{x}-\boldsymbol{x}^S(t)\right|^3} = -\frac{b_S^3\,\boldsymbol{r}\cdot\boldsymbol{u}^S}{2r^3} \tag{2.52}$$

with the dipole moment

$$\boldsymbol{d}^S(t) = \left(\frac{4}{3}\pi b_S^3 + \frac{2}{3}\pi b_S^3\right)\boldsymbol{u}^S \tag{2.53}$$

consisting of the volume of the sphere, the additionally displaced fluid volume, see sec. 4.3, and the velocity $\boldsymbol{u}^S$ of the sphere. The velocity $\boldsymbol{v}(\boldsymbol{x},t) = \nabla\phi(\boldsymbol{x},t)$ of the fluid due to the motion of S with $\boldsymbol{r} = \boldsymbol{x}-\boldsymbol{x}^S(t)$ and $r = |\boldsymbol{x}-\boldsymbol{x}^S(t)|$ derived from (2.52) becomes

$$\boldsymbol{v}^S(\boldsymbol{x},t) = -\frac{b_S^3\boldsymbol{u}^S}{2r^3} + \frac{3b_S^3\left(\boldsymbol{r}\cdot\boldsymbol{u}^S\right)\boldsymbol{r}}{2r^5}\,. \tag{2.54}$$

A quick look at (2.54) reveals that the flow velocity $v_S = \left|\boldsymbol{v}^S\right|$ scales with $\propto b_S^3$, $\propto u_S$, and $\propto 1/r^3$ with distance r to the sphere, whereby $u_S = |\boldsymbol{u}^S|$. To mention some numbers, the velocity in the flow field drops to about 1/8 from its maximum value on the surface of the moving sphere at a distance $2b_S$ to the centre of the sphere, and to about a factor 1/27 at a distance of $3b_S$. If one wants to draw any conclusion about the moving sphere from measurements of the velocity field, this measurements must thus be made within a distance of few sphere radii. Velocity sensing in an incompressible irrotational fluid is

limited to a relatively close range of very few object diameters around a flow sensory system.

As an example, a transparent velocity-sensing system $\mathcal{B}$ in the sense that it does not disturb the flow field of the sphere is considered. It shall be placed at r in the direction of motion of S on a line through the centre of S, which is moving with velocity u_S towards r. In this example, (2.54) becomes

$$v_S(r,t) = \frac{b_S^3 u_S}{r^3}\,.$$

Due to the short range of the flow field of S, $\mathcal{B}$ would like to detect the sphere as soon as possible to initiate an evasive motion to, e.g. avoid a collision. Thus, the critical quantity to optimise for $\mathcal{B}$ is the time t_e available for an escape upon the detection of S until the collision occurs at $r = b_S$. The sphere S is detected when the flow field of S at the transparent flow sensory system $\mathcal{B}$ crosses the sensory threshold v_t of $\mathcal{B}$. The threshold v_t expresses the fact that from some time on when S has reached a distance to $\mathcal{B}$ smaller than r_S, the signal of S is strong enough, so that the sensory system $\mathcal{B}$ obtains sufficient certainty to make a decision. The sensing distance r_s is given by the solution of

$$v_t = \frac{b_S u_S}{r_s^3} \tag{2.55}$$

with the velocity u_S at the point in time when (2.55) is fulfilled. The escape time t_e for $\mathcal{B}$ in case S moving at constant speed u_S is

$$t_e^v|_{u_S=\text{const.}} = \sqrt[3]{\frac{b_S^3}{v_t u_S^2}}\,. \tag{2.56}$$

It is remarkable that it is more effective to reduce the time necessary for a reaction than to increase the sensitivity of the flow sensing system in order to increase the chance to escape.

Maximal speeds of fish are in the range of 1.6 m/s for herring, and up to 27m/s for sword fish[1]. Typical speeds seem to be much smaller [110], depending of course on the size of the fish. A rough estimate for the size of fish is 10 cm/s for the radius, 1 m/s for the typical speed of $\mathcal{B}$, and 10 m/s for the maximum speed of S. The flow velocity sensing system $\mathcal{B}$ is supposed to measure the flow velocity with a precision of $v_t = 1$ cm/s, which corresponds to a relative precision of approximately 1% of the typical speed expected due to its own motion. One of the fastest known reactions upon the sensation of strike of a predator is the C-start of fish, an escape reflex, with a latency of less than 20 ms [85, 89]. To be useful for escape, a flow sensory system must provide an escape time t_e of at least 20 ms upon the detection of the predator. The predator with a radius 10 cm is supposed to move at a maximum speed of 10 m/s towards $\mathcal{B}$. The corresponding escape time $t_e = 100$ ms resulting from (2.56) should provide $\mathcal{B}$ with enough time to react.

Similar values are obtained for animals equipped with flow sensory systems for air, e.g. crickets. The typical radius of an animal or the head of an animal hunting for insects is of the order of 1 cm. The typical speed of insects is about 10 cm/s, resulting in a sensory threshold of $v_t = 1$ mm/s for a flow velocity

[1] see e.g. `http://www.nmri.go.jp/eng/khirata/fish/general/speed/speede.htm`

sensing system with 1% accuracy. The fastest running speed known for insects is 1.5 m/s for cockroaches (*Periplaneta Americana*) [111]. Digger wasps hunting for crickets run at 50 cm/s [95]. For the head of lizards catching a grasshopper velocities of 10 m/s [112] are reported. The chance of the cricket to escape from the strike of a lizard, if the cricket hasn't already detected the lizard, before the lizard aims for the cricket, is almost zero [113]. The escape time for an object of radius 1 cm moving steadily at 1 m/s with $v_t = 1\,\mathrm{mm/s}$ is $t_e = 0.1\,\mathrm{s}$.

A common strategy of hunting in the animal kingdom is to ambush or to slowly and unnoticeably sneak up the prey to reduce the distance, and then accelerate as fast as possible. The fastest known acceleration of a water-dwelling animal is $250\,\mathrm{m/s^2}$ observed for pike during a strike. Trout accelerate with up to $100\mathrm{m/s^2}$ [114]. The time to capture for S starting from rest at the distance r_0 with constant acceleration is given by $t_c = \sqrt{2r_0/a_S}$. The escape time in case S constantly accelerates with a_S is determined by the solution of

$$r_s = r_0 - \frac{1}{2}a_S(t_c - t_e)^2\,, \tag{2.57}$$

and r_s by (2.55). The resulting algebraic equation of sixth order determines the escape time t_e. No simple analytic solution of this equation is obtainable. Numerical solution of (2.57) with the parameters $b_S = 0.1\,\mathrm{m}$, $r_0 = 2b_S$, and $a_S = 250\,\mathrm{m/s^2}$ delivers an escape time of about $t_e = 39.5\,\mathrm{ms}$ and time to capture of $t_c = 40\,\mathrm{ms}$. From a distance of $r_0 = 1\,\mathrm{m}$ with all other parameters unchanged, the escape time is about $t_e = 60\,\mathrm{ms}$ and the time to capture about $t_c = 90\,\mathrm{ms}$. The larger the distance r_0, the bigger is the difference between t_c and t_e.

The examples considered suggest that fish equipped with an ultra-fast escape system like the Mauthner cells always succeed to escape. Three essential aspects are missing in this considerations so far. First, it was assumed that any signal stronger than the sensory threshold must be attributed to a predator. The actual task of an escape system, however, is to reliably filter out uncritical events. Second, the considerations were carried out without any background motion in an ideal irrotational fluid at rest. And third, all predatory fish are more or less suction feeders [115], meaning that the actual flow field generated by the predator is a superposition of the flow field of the motion of its body and the flow field of the suction while opening the mouth. Both contributions effectively counteract each other, resulting in a flow field of reduced strength.

2.10.2 Detection of a moving sphere by pressure sensing

By inspection of (2.50) one would assume that the acceleration term in $\partial_t\Phi$ decaying with $1/r^2$ and the squared velocity of motion u_S^2 of a dipole provide a strong and outreaching pressure signal in cases of strongly accelerating or fast moving objects. As before, the example of a moving sphere perceived by a transparent sensory system, now measuring the pressure, is considered. The change of the potential $\partial_t\Phi_S$ at a fixed position $\boldsymbol{x}$ consists of a change of the dipole $\partial\Phi_S/\partial\boldsymbol{d}^S \cdot \mathrm{d}\boldsymbol{d}^S/\mathrm{d}t$ caused by the acceleration $\boldsymbol{a}_S$ of the sphere and a geometric contribution $\partial\Phi_S/\partial\boldsymbol{x}_S(t) \cdot \mathrm{d}\boldsymbol{x}_S(t)/\mathrm{d}t$ due to the motion of the sphere relative to $\boldsymbol{x}$,

$$p_e(\boldsymbol{x},t) = -\varrho\frac{\partial}{\partial t}\Phi(\boldsymbol{x},t) = \frac{\varrho\, b_S^3\, \boldsymbol{r}\cdot\boldsymbol{a}^S}{2\,r^3} - \frac{\varrho\, b_S^3\, \left|\boldsymbol{u}^S\right|^2}{2\,r^3} + \frac{3\varrho\, b_S^3\, \left(\boldsymbol{r}\cdot\boldsymbol{u}^S\right)^2}{2\,r^5}\,. \tag{2.58}$$

This contribution p_e to the total pressure is called *external pressure*, since it results from a change of the boundary conditions, namely the motion of the sphere. The external pressure may further be split up in the already mentioned spatially inhomogeneous contribution of the acceleration of the boundaries, the first term in (2.58), here denoted as *acceleration pressure* $p_a(x,t)$, and the spatially inhomogeneous acceleration of the fluid caused by geometrical changes of the fluid domain denoted as *geometric pressure* $p_g(x,t)$, and given by the second and third term in (2.58). The *dynamic pressure* $p_d(x,t) = -1/2\varrho\,(\nabla\phi(x,t)\cdot\nabla\phi(x,t))$ of a moving dipole is given by the local kinetic energy density

$$p_d(\boldsymbol{x},t) = -\frac{\varrho\, b_S^6 \left|\boldsymbol{u}^S\right|^2}{8r^6} - \frac{3\varrho\, b_S^6 \left(\boldsymbol{u}^S\cdot\boldsymbol{r}\right)^2}{8r^8}\,. \tag{2.59}$$

The pressure $p = p_e + p_d$ consists of a linear combination of terms proportional to the acceleration $\propto b_S^3 a_S/r^2$ and to $\propto b_S^3 u_S^2/r^3$ resulting from the external pressure p_e, and terms proportional to $\propto b_S^6 u_S^2/r^6$ resulting from the dynamic pressure p_d. The acceleration a_S and the velocity u_S denote the absolute values of $a_S = |\boldsymbol{a}^S|$ and $u_S = |\boldsymbol{u}^S|$. For most points in the fluid domain $r > b_S$ holds for not too elongated convex bodies, thus $b_S/r < 1$.

Whether the pressure at a certain field point $\boldsymbol{x}$ is governed by the acceleration a_S or by the velocity u_S of S depends on the dimensionless ratio $\mathrm{A} = r a_S/u_S^2$, the ratio of acceleration and geometric pressure. A good criterion for the usefulness of pressure sensing compared to flow velocity sensing is obtained by introducing the dimensionless ratio P of the absolute values of external and dynamic pressure. The dynamic pressure is just a constant times the square of the flow velocity. Thus, a small disturbance in the flow velocity on $\mathcal{B}$ due to the motion of S will result in an even smaller disturbance in the pressure. If the dynamic pressure exceeds the external pressure, pressure sensing is compared to flow velocity sensing not useful at all. A criterion can be constructed by

$$\mathrm{B} = \frac{p_e/p_t}{v/v_t} \tag{2.60}$$

applied to a sphere moving straight towards the transparent pressure sensing system, as in the examples before. The external pressure simplifies to

$$p_e(x,t) = \frac{\varrho\, b_S^3\, a_S}{2\, r^2} + \frac{\varrho\, b_S^3\, u_S^2}{r^3}\,,$$

the dynamic pressure to

$$p_d(x,t) = -\frac{\varrho\, b_S^6 u_S^2}{2r^6}\,.$$

Then, P becomes

$$\mathrm{P} = \frac{2\partial_t\Phi}{\nabla\Phi\cdot\nabla\Phi} = \frac{r^4 a_S}{b_S^3 u_S^2} + \frac{2r^3}{b_S^3}\,,$$

and criterion (2.60)

$$\mathrm{B} = \frac{v_t}{p_t}\left(\frac{\varrho\, a_S r}{2u_S} + \varrho u_S\right)\,. \tag{2.61}$$

In dependence of the sensory thresholds v_t and p_t, pressure sensing will exceed flow velocity sensing, $\mathrm{B} > 1$, as assumed at larger distances and high accelerations, $\mathrm{A} >> 1$, or high velocities. But the relative changes of the absolute values

of the pressure that have to be resolved are typically very small. The examples in the following demonstrate that pressure sensing is superior to velocity sensing only in some extreme cases.

The two terms in the external pressure of the example can be investigated independently by choosing $\mathrm{A} = \infty$, which occurs e.g. immediately at the start of the motion of S from rest, or by $\mathrm{A} = 0$ during the motion of S with constant velocity. The pressure field will vary on a characteristic scale $p_c = \varrho a_S b_S/2$ or $p_c = \varrho u_S^2$ given by its maximal value on the surface of S in the two extreme cases $\mathrm{A} = \infty$ and $\mathrm{A} = 0$.

The properties of a pressure sensing system shall be compared with the properties of flow velocity sensing previously discussed in sec. 2.10.1. To be able to initiate an evasive reaction from the accelerating pike starting from rest at $t_0 = 0$ from a distance of $2\,b_S$ with $\mathrm{P} = \infty$ and $\mathrm{A} = \infty$, $\mathcal{B}$ must identify S from a signal of 3 kPa in an ambient pressure on the scale of one or several hundred kPa, which corresponds to a relative precision of about 3%. The gain in t_e, however, is less than half a millisecond, compared to the flow sensory system. Pressure sensing should pay off at larger distances since P increases with r. At a distance of $r_0 = 1\,\mathrm{m}$, the pike produces a pressure at the position of $\mathcal{B}$ of 125 Pa at the start from rest, which requires the pressure sensing system to detect a signal 1000 times smaller than the ambient pressure for an gain in t_e of 30 ms compared to the escape time of the flow sensory system with relative precision of 1% of its speed of motion of 1 m/s. After 30 ms, which corresponds to the detection time of the flow sensory system, the pressure, which is now composed of dynamic pressure and both terms of the external pressure, amounts to about 230 Pa.

It shall be reminded that these are values obtained by assuming an incompressible fluid and thus upper bounds. The real pressure disturbance induced by the high acceleration of an object in a compressible fluid is expected to be smaller and flattened in time. A solution of the motion of a sphere in a compressible fluid can be found in [116].

It is interesting to consider the pressure difference measurable over the virtual pressure sensing system of $\mathcal{B}$. The pressure difference would provide $\mathcal{B}$ with directional information. It would eliminate the need to measure a small disturbance of the absolute pressure governed mostly by the ambient pressure. The pike starting from a distance of 1 m from rest produces a pressure difference between the front and back side of $\mathcal{B}$ of 50 Pa. Multiplied with the area of the cross section of $\mathcal{B}$, the force exerted on $\mathcal{B}$ is about 1.5 N, resulting in an acceleration of about $0.35\,\mathrm{m/s^2}$, which fish might be able to detect [117].

2.10.3 Length scales of velocity and pressure

The characteristic length scale x_c^v of the fluid velocity for the example of the moving sphere S discussed in the previous subsections at a distance r to the centre of S is given by $x_c^v(r,t) = |\boldsymbol{v}(\boldsymbol{x},t)|/|\nabla\boldsymbol{v}(\boldsymbol{x},t)| = r/3$. In other words, significant changes of the flow velocity around a point at distance r to the sphere occur on a length scale $x_c^v = r/3$.

The characteristic length scales for the acceleration pressure is $x_c^a = r/2$, $x_c^g = r/3$ for the geometric pressure, and $x_c^d = r/6$ for the dynamic pressure.

2.10.4 Time scales of velocity and pressure

In the examples discussed so far, the precision of the sensory systems was chosen to be a fraction of the ambient signal. One may inject that most sensory systems, no matter whether they are artificial or biological, are tuned to detect and measure relative changes of a physical quantity. The principle is based on the assumption that changes of the background occur on other time scales than the signal to be detected. For flow sensing this assumption is, however, not generally applicable.

The *characteristic time scale* $t_c^v(\boldsymbol{r}, t)$ of the observed velocity at $\boldsymbol{r}$ can be constructed by $|\boldsymbol{v}(\boldsymbol{r}, t)|/|\mathrm{d}/\mathrm{d}t\ \boldsymbol{v}(\boldsymbol{r}, t)|$, resulting in

$$t_c^v = \frac{u_S r}{a_S r + 3u_S^2}\,. \tag{2.62}$$

The time scale of the flow velocity generated on $\mathcal{B}$ by a moving object increases with the distance to the moving object. To obtain short transients in the signals measured by $\mathcal{B}$, either a strong acceleration of the fluid by S is required, S must be close to $\mathcal{B}$, or S has to move very fast.

Essentially the same properties are found for the characteristic time scales of the pressure. The characteristic time scale for the acceleration pressure is given by

$$t_c^a = \frac{2a_S r}{\dot{a}_S r + 2a_S u_S}\,, \tag{2.63}$$

whereby a dot denotes the total time derivative. The characteristic time scale for the geometric pressure becomes

$$t_c^g(r, t) = \frac{u_S r}{2a_S r + 3u_S^2}\,, \tag{2.64}$$

and the characteristic time scale for the dynamic pressure

$$t_c^d(r, t) = \frac{u_S r}{2a_S r + 6u_S^2}\,. \tag{2.65}$$

To obtain a fast transient in the pressure at some distance to S, a strong change of the acceleration such as produced by a starting pike from rest, a strong acceleration, a high velocity, or a short distance is required.

Slowly varying pressure signals can be overlaid by a variety of sources. In the presence of a free surface, the surface elevation of deep water waves induces pressure changes, which are exponentially damped with the depth. For example, an elevation of the water surface of about 1 mm introduces a pressure change of 10 Pa close to it. The same happens when there is a change of depth of $\mathcal{B}$ of 1 mm. Considering the unstable configuration of the pectoral fins of fish in front of the centre of hydrodynamic forces, Munk's moment about the pitch axis, see sec. 5.1.2, and the permanent necessity to control the pitch via the pectoral fins, depth and pitch changes occur, which lead to pressure fluctuations with the time scale of the control of the motion.

Some land-dwelling insects accelerate even faster than pikes. The froghopper bug (*Prosapia bicincta*) accelerates with 400 g over a distance of 2 mm when jumping. Froghopper bugs are, however, not able to produce a significant pressure signal at all. Due to the small density of air $\varrho_A \approx 1.4\,\mathrm{kg/m^3}$, the pressure to be resolved at an ambient pressure of about 100 kPa is about a factor of 700 smaller than the pressure in water.

2.10.5 Conclusion

In summary, the pressure signal of fast accelerating objects in water provides an advantage in the escape time at larger distances. Short transients are measured in the pressure signal of strongly accelerated bodies, which could be extracted with high precision through a separation of the time scales of the background and the signal. At larger distances the gradients of the pressure field along the sensory system of $\mathcal{B}$ decrease with increasing characteristic length and thus become small. It might be difficult to resolve the precise course of the pressure over $\mathcal{B}$. It is thus probably impossible to extract more than just the presence and maybe the direction of an object, in cases where pressure sensing promises and advantage over sensing the flow field. Both features are in principle also provided by a point measurement of p and the acceleration of $\mathcal{B}$ resulting from a pressure difference over $\mathcal{B}$ induced by $\mathcal{P}$.

Fish possess a inertia measurement organ, the vestibular system, also called the otolithic organ, providing information about translational and angular acceleration [118]. It seems that the behaviour of dace (*Leuciscus leuciscus*) can be influenced by acceleration [117] larger than $15\,\mathrm{cm/s^2}$, which approximately matches the acceleration of $\mathcal{B}$ in the example of the starting pike.

It is also known that fish communicate by quasi-periodic pressure disturbances at frequencies in the range from infrasound ($< 20\,\mathrm{Hz}$) up to ultra sound ($> 20\,\mathrm{kHz}$) [9] caused by a muscular contraction of the swimbladder, the resonant vibration of bones [118], or less sophisticated methods [119, 120]. The Weberian apparatus attached to the swimbladder of some teleost fish mechanically couples the swimbladder with the vestibular system. The Weberian apparatus is said to transfer the volume change of the swimbladder to the mechanoreceptive otoliths. Other fish lack a direct connection between the swimbladder on the vestibular system indicating that only the acceleration is perceived.

Likewise sound, the signal produced by the accelerating pike would lead to a contraction of the swimbladder. It is known that the Mauthner cells, see sec. 1.1.2, receive input from the vestibular system. It appears plausible that pressure sensing contributes to the perception of accelerating objects. It is, however, extremely hard to conclude to the presence of slowly moving objects from measurements of the acceleration or the pressure, as sec. 2.12 will show.

The acceleration as well as the pressure are not independent from a velocity measurement. If the velocity measured is flawed by some reason, so that it is not possible to extract any reasonable information, the same holds true for the pressure and the acceleration, since they are coupled through the fluid motion. Pressure or acceleration do not provide an independent modality.

The investigation of the characteristic quantities of flow sensing in the previous subsection revealed that there is no advantage of measuring the pressure compared to measuring the velocity of the fluid motion caused by the moderately accelerated motion of a sphere at moderate speeds.

The discussion of the pressure in sec. 2.9 showed that the flow field on the whole domain is defined by its values on the boundaries. It is, however, impossible to reconstruct the pressure on $\mathcal{D}$ from the pressure on the boundaries without knowledge of the fluid velocity. Gaining full information of the flow field and the boundaries driving the flow field from measurements on a subset of the boundary, e.g. on the surface of $\mathcal{B}$, is only possible by measurement of the velocity. Except for some extreme cases, no disadvantages are expected by

disregarding the pressure for typical tasks an autonomous robot is set to solve by flow sensing such as the detection of objects and the reconstruction of their shape.

If the perception of an object by a flow sensory system is possible, the distance of that object to the flow sensory is in the same order of magnitude as the size of the flow sensory system. Furthermore, the flow velocity varies significantly over the flow sensory system. The time scale of the variation of the flow velocity at a specific sensor is also small. Thus, the signal of single flow sensors should provide a deterministic and precise measurement of the local fluid velocity at any instant of time. In general, it is not feasible to combine the signal of several sensors to improve the signal to noise ratio, e.g. by averaging over nearby sensors. This simply excludes certain types of flow fields from the analysis. Through the action of filtering over nearby sensors, objects producing a steep gradient on $\mathcal{B}$ can not be distinguished from objects producing a flatter gradient. Integrating the signal of one sensor in time makes it impossible to analyse the signal in the available time, or to capture relevant changes in the flow field. An object with radius b_S moving with velocity u_S within the range of a flow sensory system induces a flow velocity of typically $v_c = b_S^3 u_S / r^3$, with a typical characteristic length of $x_c = r/3$ and a characteristic time in case of small acceleration, $a_S r \ll 3u_S^2$, of $t_c = r/3u_S$. Thus, the fluid-mechanical image of the moving object perceived by a flow sensory system of similar size varies significantly over the flow sensory system. Depending on the speed u_S of the moving object, the fluid-mechanical image varies on relatively short time scales. As an example, the flow-velocity signal of a digger wasp with 2 cm in size running towards a cricket, see sec. 2.10.1, with a speed of 80 cm/s from a distance of 10 cm changes significantly on a time scale of less than 40 ms, see fig. 2.2.

2.11 Some analytic potential flows

In this section some analytic potential flows around moving and stationary bodies of simple geometric shape are presented. Idealized analytic test cases are constructed, which will be used later in this work for the demonstration and assessment of flow sensory data processing methods, see ch. 3.

2.11.1 Dipole approximation

The line of argumentation of this section to arrive at basic conclusions on flow sensing is based on the flow field produced by a dipole representing a moving object. In general the potential flow around a moving body can be represented [47] by a multipole expansion. The first non-vanishing term in this expansion with the smallest negative exponent of the distance is the dipole term. The monopole vanishes for any body of constant volume. An explicit expression of the dipole moment of a rigid body $\mathcal{B}$ of arbitrary shape [63, p. 530] is given by

$$\boldsymbol{d}^{\mathcal{B}} = V^{\mathcal{B}} \boldsymbol{u}^{\mathcal{B}} - \oiint_{\partial\mathcal{B}} \Phi \boldsymbol{n}' \, \mathrm{d}\mathcal{S} + \oiint_{\partial\mathcal{B}} \left(\boldsymbol{x} - \boldsymbol{x}^{\mathcal{B}}\right) \left\{ \left[\left(\boldsymbol{x} - \boldsymbol{x}^{\mathcal{B}}\right) \times \boldsymbol{n}' \right] \cdot \boldsymbol{\omega}^{\mathcal{B}} \right\} \mathrm{d}\mathcal{S} \quad (2.66)$$

with outward surface normal $\boldsymbol{n}'$ on $\partial\mathcal{B}$, volume $V^{\mathcal{B}}$ of $\mathcal{B}$, translational speed $\boldsymbol{u}^{\mathcal{B}}$, angular speed $\boldsymbol{\omega}^{\mathcal{B}}$, and geometric centre $\boldsymbol{x}^{\mathcal{B}}$. The flow field obtained from the

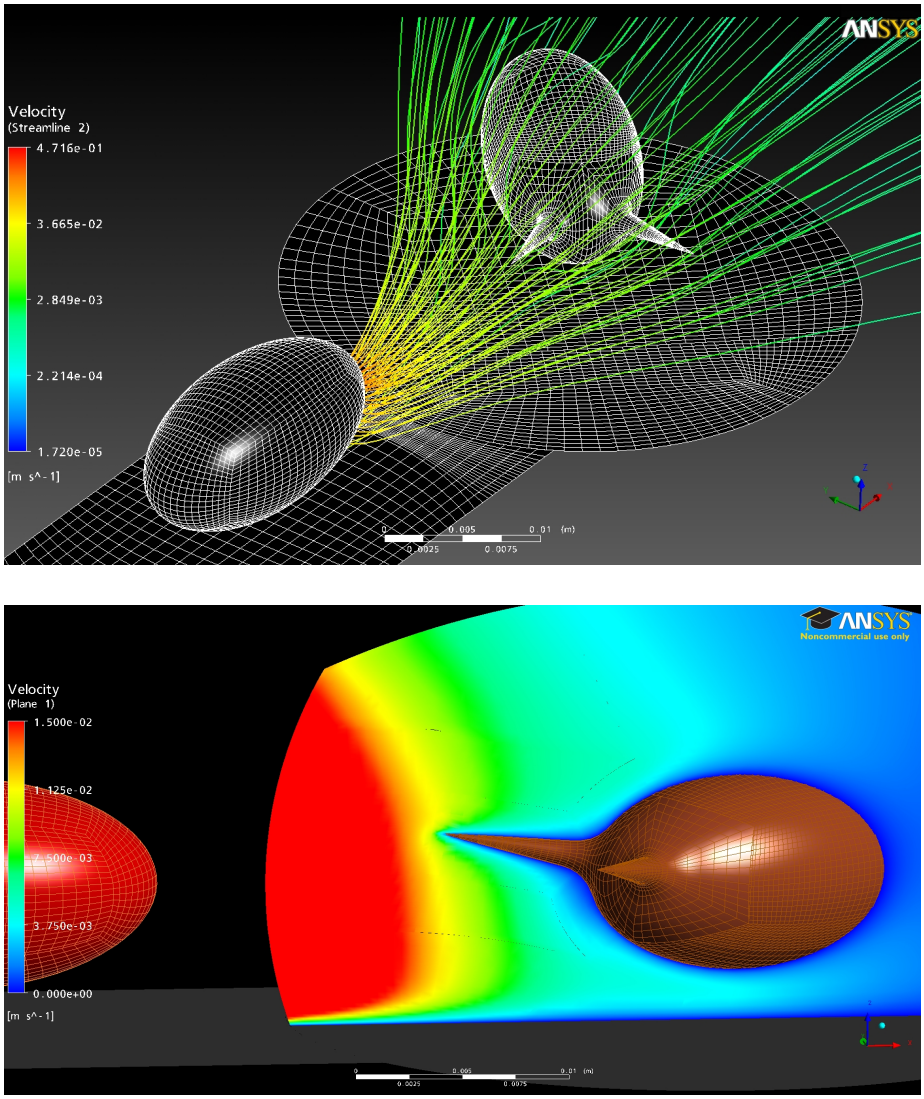

Figure 2.2: The flow field generated by an approaching predator around the cercal system of a cricket. The fluid simulation includes viscous effects in the boundary layer on the cricket.

dipole moment $\boldsymbol{d}^{\mathcal{B}}$ is usually denoted as *far field* of $\mathcal{B}$, since higher multipoles hardly contribute to the flow field at larger distances due to their faster decay. To give a rough estimate, the flow field of bodies with similar spatial extent in any direction is governed by the dipole moment if field points at a distance larger than the object size are considered. Considering the time required for perception, decision making and reaction, the measurements of a flow sensory system will be dominated by the dipole moment of an approaching body.

2.11.2 Monopole and dipole close to wall

So far the potential (2.52), velocity (2.54), and pressure, (2.58) and (2.59), of a moving dipole in an unbounded domain were discussed. The dipole can be identified with a moving sphere with radius b_S, since the no-penetration boundary condition (2.11) is fulfilled at $r = b_S$. However, the solution loses its validity as soon as other boundaries are present.

The image charge method is commonly used in electrodynamics to construct the solution, for an example, of an electric potential problem in the presence of a conducting flat wall or a sphere. This construction makes use of the reflection principle [121, ch. IV § 2.3]:

> "If a function is harmonic in a domain and continuous up to the boundary, and if it vanishes on a spherical or plane part of the boundary, then it can be continued (analytically) by reflection as a harmonic function across that part of the boundary."

Obviously the flow potential Φ is not constant on a boundary with no-penetration boundary condition in any non-trivial case, since otherwise the tangential flow velocity would vanish. Fortunately, the image charge method can be adapted to construct solutions for potential flow. The examples given in this and the following subsections are a monopole and a dipole close to a wall and close to a sphere S with no-penetration boundary condition on the sphere.

The point monopole

$$\Phi_M(\boldsymbol{x}, t) = -\frac{m(t)}{4\pi \left|\boldsymbol{x} - \boldsymbol{x}_M(t)\right|} \tag{2.67}$$

with monopole moment $m(t)$ can be identified with a radially symmetric inlet/outlet or an inflating/shrinking sphere $m(t) = 4\pi b_S^2(t) v^{\perp}(t)$ with normal velocity $v^{\perp}(t)$ on the boundary of the sphere. The flow field of a monopole source in an unbounded fluid otherwise at rest is given by

$$\boldsymbol{v}_M(\boldsymbol{x}, t) = \frac{m(t)\left(\boldsymbol{x} - \boldsymbol{x}_M(t)\right)}{4\pi \left|\boldsymbol{x} - \boldsymbol{x}_M(t)\right|^3}\,.$$

Recalling (2.52), the potential of a dipole with dipole strength $\boldsymbol{d}_D = 2\pi b_D^3 \boldsymbol{u}_D(t)$, source point $\boldsymbol{x}_D(t)$, and translational velocity $\boldsymbol{u}_D(t)$, evaluated at the field point $\boldsymbol{x}$, is described by

$$\Phi_D(\boldsymbol{x}, t) = -\frac{b_D^3 (\boldsymbol{x} - \boldsymbol{x}_D(t)) \cdot \boldsymbol{u}_D(t)}{2\left|\boldsymbol{x} - \boldsymbol{x}_D(t)\right|^3}\,.$$

The solution for the potential of a monopole or a dipole close to a wall $\mathcal{W}$ with no-penetration boundary condition can be constructed by introducing an image

monopole $\breve{m} = m$ or an image dipole $\breve{\boldsymbol{d}} = (d_x, d_y, -d_z)^{\mathrm{T}}$ at the image-source point $\breve{\boldsymbol{x}}_S = (x_S, y_S, -z_S)^{\mathrm{T}}$. The corresponding potentials are $\breve{\Phi}_M$ and $\breve{\Phi}_D$. The no-penetration boundary condition on $\mathcal{W}$ is fulfilled for an arbitrary arrangement of dipoles and monopoles complemented by the respective image charges. This simple construction is possible, since there are no boundary conditions to be fulfilled on the point sources. When the monopole or the dipole in the presence of the wall or the sphere are identified with an inflating / shrinking or moving sphere, the solution is not exact any more. The additional no-penetration boundary condition on the surface of the sphere represented by the monopole or dipole source is violated by the image sources introduced by the wall or the sphere. The error in the boundary condition on the sphere can be corrected by an additional source inside the sphere, see sec. 2.11.4, which in turn needs to be compensated by the corresponding image source mirrored on the wall, in order to fulfil the boundary conditions on the wall, and so forth [122, ch. 16-31]. The result is an infinite but converging series of decreasing contributions to the potential. The speed of convergence of this series depends on the distance between sphere and wall [123]. For a distance from the centre of the sphere to the wall larger than two sphere radii good approximations are already obtained using just the dipole inside the sphere and one mirror charge.

2.11.3 Monopole and dipole close to a sphere

The solution of a monopole or a dipole close to a sphere S with radius b_S requires much more efforts than the case of a flat wall, leading to a distribution of sources on a line between the centre of the sphere and the dipole inside the sphere. By means of Weiss' sphere theorem [63, ch. 7.5.15]

$$\Phi_d(\boldsymbol{x}, t) = \frac{b_S}{r}\Phi_0(\breve{\boldsymbol{x}}(b_S), t) - \frac{2}{b_S r}\int_0^{b_S} \Phi_0(\breve{\boldsymbol{x}}(\eta), t)\,\eta\,\mathrm{d}\eta\,, \tag{2.68}$$

it is possible to construct the disturbance potential Φ_d around a stationary sphere S with radius b_S located at $\boldsymbol{x}_S$ from the undisturbed external potential Φ_0, the potential that would arise if the sphere S was absent. The external potential Φ_0 must not have singularities inside S. Each field point $\boldsymbol{x}$ has an inverse point $\breve{\boldsymbol{x}}(\eta)$ mirrored on the surface of a sphere with radius η concentric with S,

$$\breve{\boldsymbol{x}}(\eta) = \boldsymbol{x}_S + \frac{\eta^2}{r^2}(\boldsymbol{x} - \boldsymbol{x}_S)\ ,$$

where $r = |\boldsymbol{x} - \boldsymbol{x}_S|$. Instead of having one mirror source placed at the corresponding inverse point inside the sphere, as in case of a conducting sphere close to an electric point charge, a source distribution inside the sphere on a line connecting the source and the centre of the sphere is required to fulfil the no-penetration boundary condition on the sphere. With Weiss' sphere theorem (2.68), the disturbance potential introduced by S in the vicinity of a monopole source is given by

$$\Phi_{dM} = -\frac{m(t) b_S}{4\pi r_M \breve{r}_M} + \frac{m(t)}{2\pi b_S r_M}\int_0^{b_S} \frac{\eta}{\breve{r}_M(\eta)}\,\mathrm{d}\eta \tag{2.69}$$

with $r_M = |\boldsymbol{x}_M - \boldsymbol{x}_S|$ the distance between the monopole and the centre of S, and $\breve{r}_M(a) = |\boldsymbol{x}_M - \breve{\boldsymbol{x}}_M(a)|$.

Without loss of generality one may choose the sphere S to be located at $\boldsymbol{x}_S = (0,0,0)$. The disturbance potential according to (2.68) introduced by S in the presence of a dipole at $\boldsymbol{x}_D$ with dipole strength (2.53) $\boldsymbol{d}_D = 2\pi b_D^3 \boldsymbol{u}_D$ becomes

$$\Phi_{dD}(\boldsymbol{x},t) = -\frac{b_S b_D^3 \left(\frac{b_S^2}{r^2}\boldsymbol{x} - \boldsymbol{x}_D\right)\cdot \boldsymbol{u}_D}{2r\left|\frac{b_S^2}{r^2}\boldsymbol{x} - \boldsymbol{x}_D\right|^3} + \frac{b_D^3 \boldsymbol{u}_D}{b_S r}\cdot \int_0^{b_S} \frac{\left(\frac{\eta^2}{r^2}\boldsymbol{x} - \boldsymbol{x}_D\right)\eta}{\left|\frac{\eta^2}{r^2}\boldsymbol{x} - \boldsymbol{x}_D\right|^3}\,\mathrm{d}\eta\,.$$

The integral can be solved explicitly yielding

$$\begin{aligned}\Phi_{dD}(\boldsymbol{x},t) = &-\frac{b_S b_D^3 \left(\frac{b_S^2}{r^2}\boldsymbol{x} - \boldsymbol{x}_D\right)\cdot \boldsymbol{u}_D}{2r\left|\frac{b_S^2}{r^2}\boldsymbol{x} - \boldsymbol{x}_D\right|^3} + \frac{b_D^3 r\left[r_D^2\boldsymbol{x} - (\boldsymbol{x}\cdot\boldsymbol{x}_D)\,\boldsymbol{x}_D\right]\cdot\boldsymbol{u}_D}{2b_S r_D\left[r^2 r_D^2 - (\boldsymbol{x}\cdot\boldsymbol{x}_D)^2\right]}\\ &- \frac{b_D^3\left[r^2 r_D^2\boldsymbol{x} - r^2(\boldsymbol{x}\cdot\boldsymbol{x}_D)\,\boldsymbol{x}_D + r^2 b_S^2\boldsymbol{x}_D - b_S^2(\boldsymbol{x}\cdot\boldsymbol{x}_D)\,\boldsymbol{x}\right]\cdot\boldsymbol{u}_D}{\sqrt{b_S^4 - 2b_S^2\boldsymbol{x}\cdot\boldsymbol{x}_D + r_D^2 r^2}\left[r^2 r_D^2 - (\boldsymbol{x}\cdot\boldsymbol{x}_D)^2\right]}\,,\end{aligned} \tag{2.70}$$

where $r_D = |\boldsymbol{x}_D - \boldsymbol{x}_S|$ the distance between the point dipole and the centre of S. The potential of the dipole close to the sphere is in total given by

$$\Phi_{DS}(\boldsymbol{x},t) = \Phi_D(\boldsymbol{x},t) + \Phi_{dD}(\boldsymbol{x},t)\,. \tag{2.71}$$

The velocity $\boldsymbol{v}(\boldsymbol{x},t) = \nabla\Phi(\boldsymbol{x},t)$ and the pressure $p(x,t) = -\varrho(\partial_t\Phi + 1/2\nabla\Phi\cdot\nabla\Phi)$ are quite cumbersome to compute by hand. An analytic expression for the velocity and the pressure field can be computed by any computer algebra program such as Sage[2]. An example for the potential, the velocity, and the pressure of a dipole moving towards a stationary sphere is depicted in fig. 2.3.

2.11.4 Wall close to a sphere

The potential of a dipole close to a sphere composed of (2.52) and (2.70) can be directly used to construct an approximative solution of the flow field of a sphere S close to a solid wall $\mathcal{W}$ with exactly fulfilled no-penetration boundary conditions on the sphere and approximately fulfilled no-penetration boundary condition on the wall.

The BFS located in the centre of S is chosen as the frame of reference. In a FOR with fixed wall, the sphere is supposed to move with velocity $\boldsymbol{u}_S$ towards $\mathcal{W}$ with the wall surface being perpendicular to $\boldsymbol{e}_x$ and located at x_W. For simplicity, the basis vectors and the origins of both systems, the FOR $\{\boldsymbol{e}_x, \boldsymbol{e}_y, \boldsymbol{e}_z\}$ and the BFS $\{\boldsymbol{e}_X, \boldsymbol{e}_Y, \boldsymbol{e}_Z\}$, shall coincide. In the BFS of the sphere all object velocities and the flow field refer to the origin of the BFS. In this system the wall moves relative to the sphere with velocity $-\boldsymbol{U}^S$, whereby only the component along $\boldsymbol{e}_X$ matters, since the no-penetration boundary condition imposed on the flat wall is invariant in y and z direction. This construction is possible, independent of the state of motion of S or $\mathcal{W}$, due to the invariance of the governing equations under transformation in an accelerated system, see sec. 2.3.

[2] `http://www.sagemath.org/`

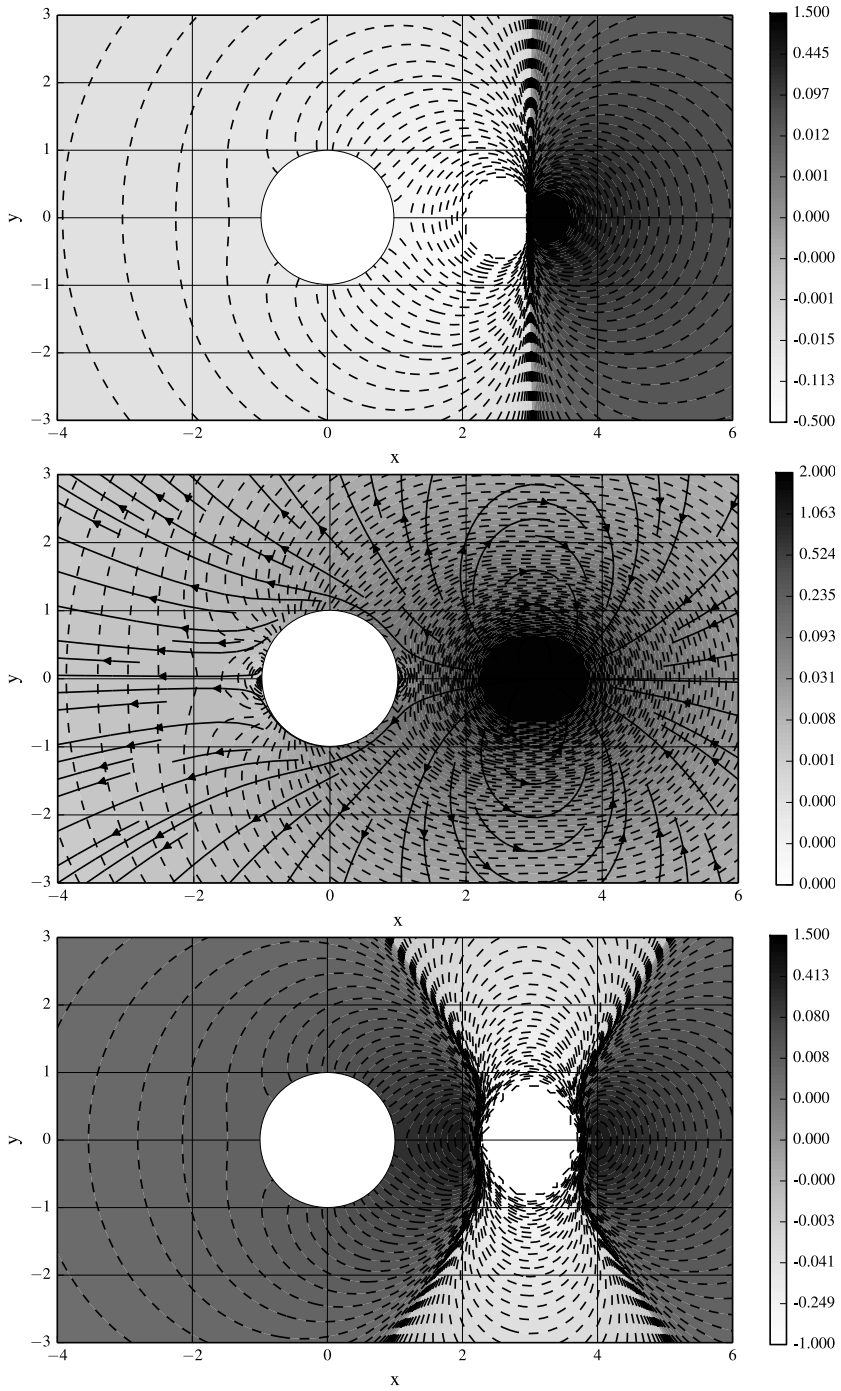

Figure 2.3: Flow potential (*top*) with equi-potential surfaces, flow velocity (middle) with equi-velocity surfaces and streamlines, and normalised pressure (*bottom*) with isobaric surfaces of a dipole with dipole moment $\boldsymbol{d} = (-2\pi, 0, 0)^{\mathrm{T}}$ moving at constant velocity $u_x = -1$ towards a sphere of radius 1 with no-penetration boundary condition on its surface. All quantities are defined with respect to the origin of the BFS located in the centre of the sphere.

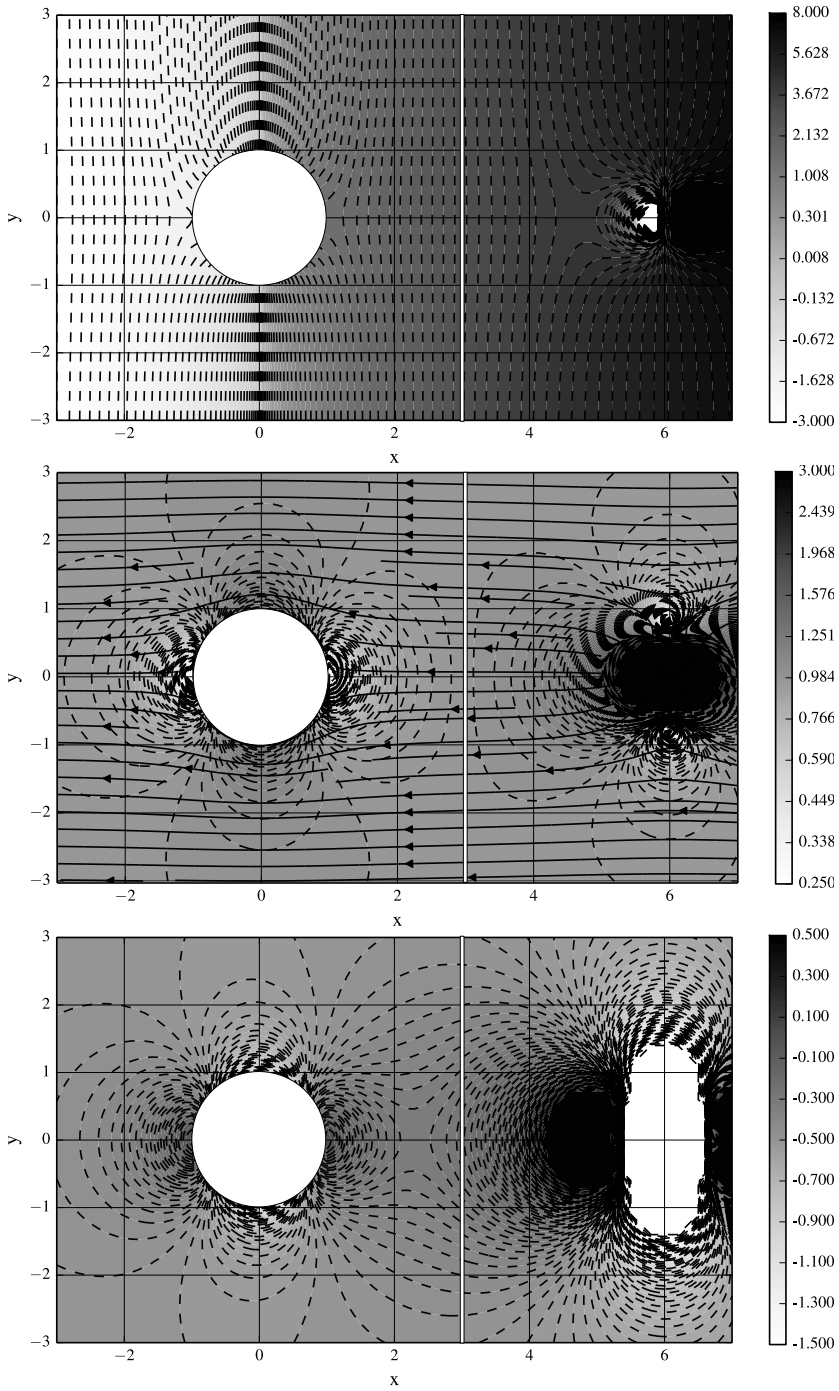

Figure 2.4: Flow potential (*top*) with equi-potential surface, flow velocity (*middle*) with equi-velocity surfaces and streamlines, and pressure (*bottom*) with isobaric surfaces in the BFS of a sphere of radius 1 with no-penetration boundary condition on its surface close to a wall at distance 3. The potential of the image source on the opposite side of the wall is constructed by means of Weiss' sphere theorem to fulfil the no-penetration boundary condition on the sphere.

At infinite distance the wall produces an uniform flow past the sphere. The potential including the disturbance of the sphere [63, p. 547] is given by

$$\Phi_{WS}(\boldsymbol{X},t) = -(1+\frac{b_S^3}{R^3})\,\boldsymbol{U}^S\cdot\boldsymbol{X}$$

with $R=|\boldsymbol{X}|$. This results in the velocity field

$$\boldsymbol{V}^{WS} = -\boldsymbol{U}^S - \frac{b_S^3}{2R^3}\left[\boldsymbol{U}^S - \frac{3}{R^2}\left(\boldsymbol{U}^S\cdot\boldsymbol{X}\right)\boldsymbol{X}\right].$$

In sec. 2.11.2 an image dipole was introduced to fulfil the boundary condition on the wall in the presence of a dipole. If the potential of the image dipole in the mirror-source method is supplemented by the respective disturbance potential Φ_{DS} (2.71) of a dipole close to the sphere, the no-penetration boundary condition on S is exactly maintained. The no-penetration boundary condition on $\mathcal{W}$ is only approximated. In the BFS of S, with all velocities referring to the origin of the BFS, and the wall moving towards S with $-\boldsymbol{U}^S$, the mirror dipole strength located at $\boldsymbol{X}^I=(2x_{\mathcal{W}},0,0)^{\mathrm{T}}$ is given by $\boldsymbol{D}^I = 2\pi a^3(-2U_X^S,U_Y^S,U_Z^S)^{\mathrm{T}}$. The velocity potential in the BFS of the sphere is thus given by

$$\Phi(\boldsymbol{X},t) = \Phi_{WS}(\boldsymbol{X},t) + \Phi_{DS}(\boldsymbol{X},t)\,. \tag{2.72}$$

An example of the potential, the velocity, and the pressure for a sphere close to a wall is depicted in fig. 2.4.

To summarise the essential properties of this approximation, it shall be mentioned again that the no-penetration boundary condition on S is exactly fulfilled. The no-penetration boundary condition on $\partial\mathcal{W}$ is fulfilled only approximately. The additional sources inside S introduced by Weiss' sphere theorem lack an appropriate counteracting source, i.e. an image, on the opposite side of the wall. The quality of the approximation deteriorates with decreasing distance between S and $\mathcal{W}$. The opposite situation is obtained with the image source method described in sec. 2.11.2. The boundary condition on the wall is precisely fulfilled, but the sphere moving towards the wall represented by the dipole suffers a net influx through its boundary, effectively reducing the velocity of the flow field between the wall and the sphere. Which one of the approximations of the motion of a sphere close to a wall is to be preferred depends on the application. If one is interested in physical quantities related to the flow field on the surface of S, the error introduced by disturbed boundary conditions on the wall is smaller than the error due to unfulfilled boundary conditions on S, noting that the error decreases with increasing distance between sphere and wall.

A further generalisation of the problem of a dipole and a wall close to a sphere as used in ch. 3 can be easily obtained by virtue of the linearity of the problem. Starting with the sphere close to a wall, the potential of a dipole close to the sphere and its image source mirrored on the wall can be simply added, maintaining the no-penetration boundary condition on the sphere and approximatively the no-penetration boundary condition on the wall.

2.12 Forces of fluid-mechanical interaction

Astonishingly simple expressions [63, ch. 7.3.2] for the force and torque on a body close to stationary point sources of constant strength at a constant distance

are found. The force and torque on a body $\mathcal{B}$ close to a stationary monopole located at $\boldsymbol{x}_M$ is given by

$$\begin{aligned} \boldsymbol{f}^{\mathcal{B}} &= \varrho m \boldsymbol{v}_d^{\mathcal{B}}(\boldsymbol{x}^M) - \varrho V_{\mathcal{B}} \boldsymbol{g} \\ \boldsymbol{t}^{\mathcal{B}} &= \varrho m \left(\boldsymbol{x}^M - \boldsymbol{x}^P\right) \times \boldsymbol{v}_d^{\mathcal{B}}(\boldsymbol{x}^M) - \varrho V_{\mathcal{B}} \left(\boldsymbol{x}^{\mathcal{B}} - \boldsymbol{x}^P\right) \times \boldsymbol{g} \end{aligned} \tag{2.73}$$

with buoyancy force $-\varrho V_{\mathcal{B}} \boldsymbol{g}$, which is compensated in case of a buoyancy neutral body by the gravitational force, the volume $V_{\mathcal{B}}$ of $\mathcal{B}$, the monopole moment m, the disturbance field $\boldsymbol{v}_d^{\mathcal{B}}(\boldsymbol{x}^M)$ of the body $\mathcal{B}$ at the position of the monopole, $\boldsymbol{x}^P$ the pivot point of $\mathcal{B}$, and the geometric centre $\boldsymbol{x}^{\mathcal{B}}$ of $\mathcal{B}$. As in sec. 2.11.2, the disturbance field is defined as the contribution $\boldsymbol{v}_d^{\mathcal{B}}$ of $\mathcal{B}$ to the external flow field introduced to fulfil the no-penetration boundary condition on the surface of the body $\mathcal{B}$. The force and torque on $\mathcal{B}$ in the vicinity of a stationary dipole are

$$\begin{aligned} \boldsymbol{f}^{\mathcal{B}} &= \varrho\, \boldsymbol{d} \cdot \nabla \boldsymbol{v}^{\mathcal{B}}(\boldsymbol{x}^D) - \varrho V_{\mathcal{B}} \boldsymbol{g} \\ \boldsymbol{t}^{\mathcal{B}} &= \varrho\, \boldsymbol{d} \times \boldsymbol{v}^{\mathcal{B}}(\boldsymbol{x}^D) - \varrho V_{\mathcal{B}} \left(\boldsymbol{x}^{\mathcal{B}} - \boldsymbol{x}^P\right) \times \boldsymbol{g}\,. \end{aligned} \tag{2.74}$$

By linear superposition of the respective forces (2.73) and (2.74) of mono- and dipoles, the force and torque exerted on $\mathcal{B}$ by an arbitrary stationary source distribution can be obtained. Equations (2.73) and (2.74) are derived from the surface integral over the pressure (2.51) on $\mathcal{B}$ with $\partial_t \Phi = 0$. To obtain the force on $\mathcal{B}$ close to a transient monopole with time-dependent monopole strength $m(t)$ and location $\boldsymbol{x}_M(t)$, or close to a transient dipole with $\boldsymbol{d}(t)$ and $\boldsymbol{x}_D(t)$, it is necessary to add the expressions

$$-\varrho \oiint_{\mathcal{B}} \frac{\partial \Phi(\boldsymbol{x}, t)}{\partial t} \boldsymbol{n}\, \mathrm{d}\mathcal{S} \qquad \text{and} \qquad -\varrho \oiint_{\mathcal{B}} \frac{\partial \Phi(\boldsymbol{x}, t)}{\partial t} \left(\boldsymbol{x} \times \boldsymbol{n}\right) \mathrm{d}\mathcal{S} \tag{2.75}$$

which considerably complicate the simple stationary expressions.

2.12.1 Numerical treatment of fluid-mechanical interaction

To obtain values for the pressure generated by a dipole and a wall close to a sphere with no-penetration boundary condition fulfilled on the surface of the sphere, an analytic expression was computed for the pressure from the potentials (2.70) and (2.72) with a computer algebra program (Sage). The functions were exported as C-code and used by means of SciPy Weave[3] as the kernel function for a numerical integration over the surface of a sphere with SciPy's standard double quadrature method with default (10^{-6}) absolute and relative error bounds. The result for the force on a sphere with radius $b_S = 1\,\mathrm{m}$ located at $(0, 0, 0)$ moving along the x axis with velocity $1\,\mathrm{m/s}$ perpendicular towards a wall at $x_{\mathcal{W}} = 3\,\mathrm{m}$, see fig. 2.4, is $-43.5\,\mathrm{N}$, which is really small compared to the mass of $4190\,\mathrm{kg}$ of the buoyancy neutral sphere in water. The result for the force on a stationary sphere of radius $b_S = 1\,\mathrm{m}$ in the presence of a dipole with $b_D = 1\,\mathrm{m}$ moving at a constant speed of $1\,\mathrm{m/s}$ towards the sphere at a distance of $3\,\mathrm{m}$, see fig. 2.3, is approximately $-109\,\mathrm{N}$. Scaling arguments allow to estimate the force on objects of different size and speed.

[3] `http://scipy.org/`

2.12.2 Analytical treatment of fluid-mechanical interaction

As mentioned in sec. 2.11.2, a lower bound of the kinetic energy of the fluid around a sphere S approaching a flat wall $\mathcal{W}$ can be obtained by approximating the potential or the flow field with a dipole of suitable strength placed in the centre of the sphere and the respective image dipole mirrored on the wall. The kinetic energy stored in the motion of an ideal incompressible and irrotational fluid [122, ch. 16, sec. 31] around a sphere moving perpendicular to $\mathcal{W}$ with velocity v_S at distance h is given by

$$\mathcal{T}_F = \frac{1}{6}\pi b_S^3 \varrho \left(1 + \frac{3}{8}\frac{b_S^3}{h^3}\right) v_S^2 \,.$$

The kinetic energy of the buoyancy neutral sphere is given by $\mathcal{T}_S = \frac{2}{3}\pi b_S^3 \varrho\, v_S^2$. In total, the kinetic energy becomes

$$\mathcal{T} = \pi b_s^3 \varrho \left(\frac{5}{6} + \frac{b_s^3}{16h^3}\right) v_S^2 = \text{const.}\,.$$

In the absence of external forces the kinetic energy of the ideal fluid remains constant during the motion of the sphere. Without anticipating ch. 4, the total mass consisting of the mass of the sphere and the mass of the displaced fluid depends on the distance of the sphere to the wall. Thus, with decreasing h the added mass increases, which in turn must be compensated by a reduction of v_S, and thus causes an acceleration a_S. An ordinary differential equation is obtained for the acceleration of the buoyancy neutral sphere moving perpendicular towards a stationary wall,

$$\left(\frac{5}{3} + \frac{b_s^3}{8h^3}\right) a_S = -\frac{3b_s^3}{16h^4} v_S^2 \,,$$

in dependence of the velocity v_S^2 of the sphere and the distance h to the wall. A sphere with radius $b_S = 12.5\,\text{cm}$ (the snout of *Snookie*) moving perpendicular to a flat wall with a velocity of $10\,\text{cm/s}$ velocity at a distance of $2b_S$ experiences an acceleration of $< 10^{-3}\text{m/s}^2$, which is rather small.

Similar results are obtained for a sphere moving at constant speed parallel to a flat wall. The kinetic energy of the potential flow [122, ch. 16, sec. 31] and the sphere is given by

$$\mathcal{T} = \pi b_s^3 \varrho \left(\frac{5}{6} + \frac{b_s^3}{32h^3}\right) v_S^2 = \text{const.}\,, \tag{2.76}$$

and a force perpendicular to the direction of motion of the sphere towards the wall exists,

$$f_\perp = \frac{3}{32}\frac{\pi \varrho\, b_s^6}{h^4} v_S^2 \,, \tag{2.77}$$

which is also quite small. At short distances, at which the interaction with the wall becomes important, other fluid-dynamical effects related to the viscosity of the fluid may significantly contribute to the hydrodynamic interaction with the wall [124].

2.13 Conclusion

The properties of the measurement of the pressure and the fluid velocity of a moving sphere in an unbounded undisturbed fluid by a transparent sensory system, although artificial at first glance, are worth to consider, as they allow an easy assessment of the essential scaling properties. The hydrodynamic dipole moment (2.66) represents the main effect of a body on the motion of the fluid quite well at distances larger than one object radius. The monopole moment vanishes as long as no sources or sinks are present, which produce or annihilate fluid. The flow field of a dipole is thus the first non-vanishing contribution in a multipole expansion of the flow field of a moving body [21, p. 24 ff.].

Pressure sensing has been considered as an alternative to the measurement of the flow field, [125, 126]. Bouffanais et al. [105] proposed a method to reconstruct the 2D pressure field of the stationary flow potential around one body from the measurements of the pressure on its surface. The pressure is successively approximated by substituting the leading terms of a Laurent series for the complex velocity potential in the stationary Bernoulli equation. This allows to discuss the dependence of the pressure on the distance and the shape of the moving object, and provides an estimate of the position and orientation of the object independent of its shape. There is a catch: the potential is stationary, if nothing moves relative to the object. Except for the case of strongly accelerating or fast moving objects, no advantage of pressure sensing compared to flow velocity sensing was found, see sec. 2.10.5. In an incompressible fluid the pressure is an explicit function of the flow velocity, see sec. 2.9, but not vice-versa. Thus, pressure sensing cannot provide full or universal information about the fluid and the enclosing unknown boundaries. The analysis in sec. 2.9 and sec. 2.10.2 shows that pressure sensing must be combined with flow velocity sensing to be universally applicable without further assumptions.

Recently pressure sensing has been considered as a means to stabilize the control of underwater vehicles [127, 128]. If one is interested in the fluid-mechanical forces acting upon a body, the advantage of directly measuring the pressure is evident from a quick look at (2.51).

The method of choice for an *artificial lateral-line system* (ALL) to be universally applicable is thus to measure the tangential velocity to make use of the information provided by the flow field. In ch. 3 it will be shown that knowledge of the tangential velocity on a subset of a boundary with no-penetration boundary condition is sufficient to determine the velocity field on a source-free potential flow domain.

The conclusion relevant for the dynamics of an object moving in potential flow in the presence of further boundaries is that the equations of motion of the object moving in unbounded potential flow will be excellent approximations, as long as the distance to other boundaries is larger than one object radius, see sec. 2.12.

Chapter 3

Flow Field Reconstruction

In ch. 2 some important results for the design of an artificial lateral line system and the closely related problem of extracting information from the sensory data were obtained through simple examples and from basic considerations of the underlying equations of motion of the fluid.

First, the flow field of an ideal irrotational incompressible fluid in a simply connected domain $\mathcal{D}$, also called potential flow, is solely governed by the velocity of motion of its boundaries, see sec. 2.2. This work confines itself to continuously differentiable boundaries, which allow an easy computation of the limit of the singular integrals appearing, whenever the gradient of the 3D Green's function in (2.19) is evaluated at a point on a boundary, although relatively simple generalisations to Lipschitz continuous boundaries are possible. The potential Φ and the flow field $\boldsymbol{v} = \nabla\Phi$ are uniquely determined by the specification of $\nabla\Phi \cdot \boldsymbol{n}$ or Φ on $\partial\mathcal{D}$. However, $\nabla\Phi \cdot \boldsymbol{n}$ or Φ can also be specified on any smooth simply connected manifold $\partial\mathcal{E}$ enclosing the domain of interest $\mathcal{E} \subset \mathcal{D}$, resulting in the same potential and flow field on $\mathcal{E}$.

Second, it is possible to reconstruct the pressure from the velocity field, see sec. 2.9. The reversal of this statement is, however, in general wrong. The simplest and most universal FSS for a rigid body $\mathcal{B}$ with boundary $\partial\mathcal{B}$, trying to gather information from physical quantities transmitted through fluid motion consists of flow velocity sensors distributed over the surface of $\mathcal{B}$. A measurement of the pressure can expediently contribute to perception of strongly accelerating or fast moving objects. Assuming comparable resolution, pressure sensing is not expected to be advantageous in any other case of object perception.

Third, the range of view of that FSS will be limited to at most a few object sizes, depending on the shape and velocity of motion of $\mathcal{B}$ and the rest of the boundaries, denoted in the following as the environment.

Fourth, $\mathcal{B}$ may move in an arbitrary fashion as long as the conditions for potential flow are preserved around its FSS, since the governing equations of fluid motion are invariant under transformations in an accelerated frame of reference, see sec. 2.3.

Finally, a simply connected domain $\mathcal{D}$ in 3D as opposed to 2D does not necessarily mean that $\mathcal{D}$ may not include holes, see sec. 2.5.4. And thus, incompressible and irrotational flow on the 3D domain $\mathcal{D}$ does not mean that no sources or vortices exist, which are driving the flow field. An oblique arrangement of sources may be placed in the closed holes outside $\mathcal{D}$, e.g. a closed line of point

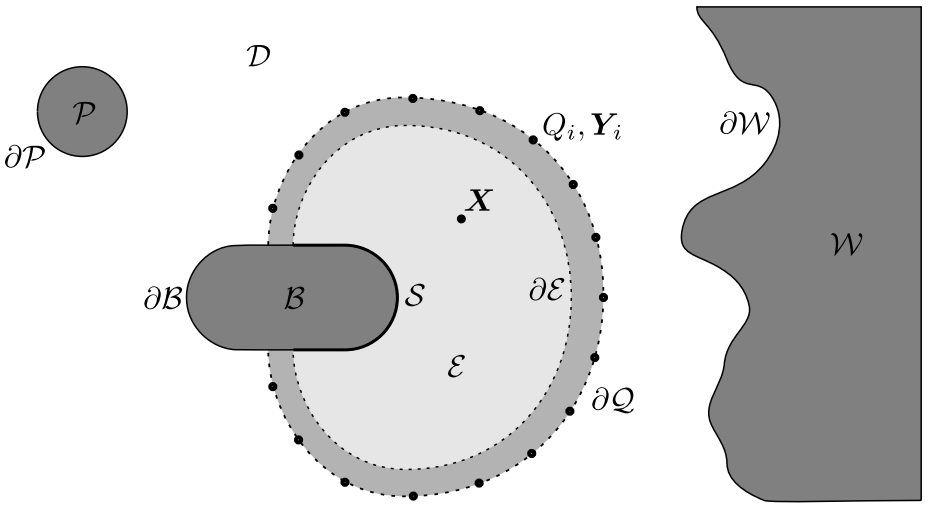

Figure 3.1: A body $\mathcal{B}$ with surface $\partial\mathcal{B}$ equipped with a flow-sensory system (FSS) on $\mathcal{S}$, surrounded by a domain of interest $\mathcal{E}$ bounded by $\partial\mathcal{E}$, point sources Q_i on $\partial\mathcal{Q}$, fluid domain $\mathcal{D}$, field point $\boldsymbol{x}$, wall $\mathcal{W}$, and a moving body $\partial\mathcal{P}$.

vortices [101, ch. VII, §150], producing a ring vortex. The resulting flow field on $\mathcal{D}$ is an ideal irrotational vortex. The outer regions of real vortices, which are flattened after some time by the action of viscosity, are well represented by ideal irrotational vortices, e.g. the Oseen vortex [63, ch. 3.13.1]. The basis of this statement is the fact that any flow potential and the corresponding pressure computed via the Bernoulli equation solve the Navier-Stokes equation incorporating viscous forces, but not the no-slip boundary conditions [63, ch.7.1]. As long as the outer regions of a vortex are not dominated by viscous interaction with a no-slip boundary condition, irrotational potential-flow is an acceptable approximation of vortex structures. But, the irrotational ring vortex can also be produced by a distribution of dipoles on a surface enclosed by the closed vortex line. Thus, the alternative representation by dipoles could also be interpreted as the normal velocity on a surface with no-penetration condition. This directly leads to the question of how to interpret potential flow, discussed in sec. 3.3. At some distance to the vortex line, the vortex can further be approximated simply by a point vortex [3].

Studies focused on the Mexican cave fish usually only consider the forward problem, modelling the stimulus that occurs from the hydrodynamic interference with objects on the fish's body [41–44, 129, 130]. To utilise data gathered from the sensors of *Snookie* and to obtain information about the environment the inverse problem has to be solved. Attempts to reconstruct the environment from the hydrodynamic image so far are limited to special cases with strong assumptions or prior knowledge about the environment.

The previously mentioned estimation of multipole moments of a 3D moving body requires exactly one body moving though an unbounded inviscid incompressible fluid initially at rest. The flow velocities are measured by a transparent – or more accurately, virtual – FSS, which may not disturb the flow field of the moving body by its presence. Position and multipole moments up to order

three are estimated simultaneously by means of a maximum-likelihood estimator given the flow velocities measured by the virtual lateral-line system. The generalisation to further incorporate an estimate of the velocity of the moving object is straightforward. The moving object may move in an arbitrary fashion.

Quite often, the shape of one object – usually a sphere – moving relative to the FSS is assumed to be known. The position of the dipole can then be extracted easily from its hydrodynamic image [74, 75, 131–133]. The theory presented in this chapter allows to reconstruct arbitrary potential flow. First, the 2D reconstruction from simple geometries like a plate, a circle, and an airfoil is presented. Then, a 3D reconstruction method from arbitrarily shaped smooth object is presented, which is applied to a sphere. The CLS is incorporated. Methods for the interpretation of the reconstructed flow fields are presented.

Before starting with the flow reconstruction theory, basic results obtained by Hadamard at the beginning of the 19th century are summarised that relate the existence, uniqueness and posedness of the flow potential on $\mathcal{D}$ with the knowledge of Φ and $\partial\Phi/\partial n$ on $\mathcal{S}$, the FSS of $\mathcal{B}$. Then, explicit formulas and regularisation techniques for the 3D reconstruction of the potential and the flow field given boundary data on $\mathcal{S}$ for an arbitrarily shaped smooth body $\mathcal{B}$ are derived, and 2D special cases are presented, followed by a discussion of wall and vortex extraction methods.

The underlying assumption is that within a simply connected domain $\mathcal{D}$ partially bounded by the surface of the FSS $\mathcal{S} \subset \partial\mathcal{D}$, the real incompressible viscous flow shall be closely approximated by the potential flow Φ produced by an arbitrary distribution of sources outside $\mathcal{D}$.

To summarise, the statement of the problem of flow field reconstruction is: Given the tangential velocity $\boldsymbol{V}^{\parallel}$ on a subset $\mathcal{S}$ of the surface $\partial\mathcal{B}$ of a moving rigid body $\mathcal{B}$ totally immersed in an incompressible potential flow in the domain $\mathcal{D}$ and the no-penetration boundary condition $\boldsymbol{V}^{\perp} = 0$ on $\partial\mathcal{B}$, what can be said about the flow field $\boldsymbol{V}$ on $\mathcal{D}$ and the boundaries $\partial\mathcal{D}\backslash\partial\mathcal{B}$ of the environment?

3.1 The nature of the problem

For the aforementioned conditions the flow field around the sensory system $\mathcal{S}$ of the moving body is well described by a velocity potential $\boldsymbol{v}(\boldsymbol{x}, t) = \nabla\Phi(\boldsymbol{x}, t)$ that suffices the Laplace equation

$$\Delta\Phi = 0 \tag{3.1}$$

on the fluid domain $\mathcal{D}$ with respect to a FOR. The domain is bounded by the surface of the moving body $\partial\mathcal{B}$ and eventually by other moving bodies $\mathcal{P}$ with boundaries $\partial\mathcal{P}$ or stationary solid walls $\mathcal{W}$ with surfaces $\partial\mathcal{W}$. $\mathcal{B}$ with boundary $\partial\mathcal{B}$ is equipped with a FSS on $\mathcal{S} \subset \partial\mathcal{B}$ and moves through the fluid with arbitrary, but known, translational $\boldsymbol{U}^{\mathcal{B}}$ and rotational $\boldsymbol{\Omega}^{\mathcal{B}}$ velocity. The shape of $\mathcal{B}$ shall also be known. The conventions of sec. 1.2.1 are used to distinguish between quantities in the FOR and in the BFS. The velocity $\boldsymbol{V}$ of the flow field refers to the origin of the BFS of $\mathcal{B}$, the velocity $\boldsymbol{\mathfrak{U}}^{\mathcal{B}} = (\boldsymbol{U}^{\mathcal{B}}, \boldsymbol{\Omega}^{\mathcal{B}})^{\mathrm{T}}$ of the BFS to the origin of the FOR, in which $\mathcal{W}$ is stationary. On $\mathcal{B}$ the no-penetration boundary condition $\boldsymbol{V}^{\perp} = 0$ holds. The sensory system $\mathcal{S}$ measures the tangential flow velocity $\boldsymbol{V}^{\parallel} = \boldsymbol{N} \times (\boldsymbol{N} \times \nabla\Phi)$ at discrete points on $\mathcal{S}$ with a certain precision

and some finite error. The essential properties of the hydrodynamic image can be discussed with the help of a simple 2D example.

3.1.1 Potential flow between a curved wall and a flat observer

The 2D potential flow between a flat observer (plate) with surface $\mathcal{S}$ at $y = 0$ and an arbitrary shaped wall $\mathcal{W}$, see fig. 3.2a, both fixed in a FOR, allows direct insight into the properties of the hydrodynamic image and its inversion. A segment of the contoured wall $\mathcal{W}$ shall be described by $y = d + w(x)\,,\ x \in [0, L]$ using the wall function $w(x)$ with $w(0) = w(L) = 0$ and the distance $d > 0$ between $\mathcal{W}$ and $\mathcal{S}$. The conduit is flat everywhere else. Fluid enters and leaves the area $\mathcal{D}$ at $x = 0$ and $x = L$ through cross sections of equal size with

$$\begin{aligned} &v_x(0, y) = v_x(L, y) = v_0, \\ &v_y(0, y) = v_y(L, y) = 0 \quad \text{for } y \in [0, d]\,. \end{aligned} \tag{3.2}$$

The no-penetration conditions $v_y(x, 0) = 0$ and $\boldsymbol{n} \cdot \boldsymbol{v}(x, d + w(x)) = 0$ with surface normal $\boldsymbol{n}$ hold on $\mathcal{S}$ and $\mathcal{W}$. The flow potential $\Phi(x, y)$ fulfilling these boundary conditions is

$$\Phi(x, y) = 2 \sum_{\alpha=1}^{\infty} A_\alpha \cosh\Big(\frac{\pi}{L}\alpha y\Big) \cos\Big(\frac{\pi}{L}\alpha x\Big) + v_0 x \tag{3.3}$$

with spatial frequency α. The free-slip and no-penetration boundary conditions on $\mathcal{W}$ imply that the stream function

$$\Psi(x, y) = -2 \sum_{\alpha=1}^{\infty} A_\alpha \sinh\Big(\frac{\pi}{L}\alpha y\Big) \sin\Big(\frac{\pi}{L}\alpha x\Big) + v_0 y \tag{3.4}$$

must be constant along the wall surface $\Psi(x, d + w(x)) = \Psi(0, d)$. The stream function is determined only up to a constant, since $v_x = \partial\Psi/\partial x$ and $v_y = -\partial\Psi/\partial y$, thus $\Psi(y = 0) = 0$ is a valid choice. This determines A_α for every α. For computational purposes the harmonic series (3.3) is truncated at $\alpha = N$ and the wall $w(x)$ is discretised by D nodes $(x_i,\ w_i := w(x_i)),\ i = 1, 2, \ldots, D$. This yields the linear system

$$\mathcal{H}\boldsymbol{A} = -v_0 \boldsymbol{w}$$

with the matrix $\mathcal{H} \in \mathbb{R}^{D \times N}$ defined by

$$\mathcal{H}_{i\alpha} := -2 \sinh\left(\frac{\pi\alpha(d + w_i)}{L}\right) \sin\Big(\frac{\pi\alpha x_i}{L}\Big)\,.$$

The best solution (in the least-squares sense) for the coefficients $\boldsymbol{A}$ is given by

$$\boldsymbol{A} = -v_0 \mathcal{H}^+ \boldsymbol{w}\,,$$

where $\mathcal{H}^+$ is the Moore-Penrose pseudoinverse of $\mathcal{H}$.

In order to distinguish the influence of shape and distance, the approximation

$$\sinh(\pi\alpha(d + w_i)/L) \approx \exp(\pi\alpha(d + w_i)/L)/2$$

is applied, which is valid for $\pi\alpha d/L \gg 1$, to factorize $\mathcal{H}$ into

$$\mathcal{H} \approx \tilde{\mathcal{H}}\mathrm{diag}_\alpha[\exp(\pi\alpha d/L)] \ ,$$

where $\tilde{\mathcal{H}}$ is given by

$$\tilde{\mathcal{H}}_{i\alpha} = -\exp(\pi/L\alpha w_i)\sin(\pi/L\alpha x_i) \ ,$$

which solely depends on the shape of the wall $w(x)$. Thus, the dependence of the coefficients A_α on the distance d between the wall and $\mathcal{S}$ is

$$\boldsymbol{A} \approx -v_0\,\mathrm{diag}_\alpha[\exp(-\pi\alpha d/L)]\,\tilde{\mathcal{H}}^+\boldsymbol{w}\,.$$

For $\pi\alpha y/L \gg 1$ the spatial frequency components of the hydrodynamic image $v_x(x,0)$ are dampened exponentially with increasing distance d and increasing spatial frequency α/L. This resembles the results of Sichert et al. [47], which state that higher multipole moments hardly contribute to the hydrodynamic image of objects at a distance larger than the size of the object.

The solution of the flow field over the infinite flat wall is directly applicable to a flat observer of finite size and suitable geometry moving with velocity U_0 parallel to the wall as long as the boundary conditions for $\boldsymbol{v}$ at the entrance and exit of the investigated domain are sufficiently well satisfied (fig. 3.2b).

3.1.2 Existence and uniqueness of the inversion

Given $\boldsymbol{V}^\parallel$ measured on $\mathcal{S}$, what can be said about the flow field $\boldsymbol{V}$ on $\mathcal{D}$ and the presence and shape of further objects $\mathcal{W}$ and $\mathcal{P}$?

For the moment, an idealised FSS shall be assumed in the sense that $\boldsymbol{V}^\parallel$ is known precisely at every point on $\mathcal{S}$ meaning that it is a continuous function on $\mathcal{S}$, and that valid boundary conditions are granted. Starting from some fixed reference point P_0 on $\mathcal{S}$ the tangential velocity $\boldsymbol{V}^\parallel$ may be integrated to obtain the potential $\Phi|_\mathcal{S}$ on $\mathcal{S}$ up to an irrelevant time-dependent function Φ_0 which disappears when computing $\boldsymbol{V} = \nabla\Phi$. Then, together with the Neumann boundary condition $\boldsymbol{V}^\perp = 0$ in the BFS given by the no-penetration condition on $\mathcal{S}$, Cauchy boundary conditions

$$\Phi|_\mathcal{S} \qquad \text{and} \qquad \left.\frac{\partial\Phi}{\partial N}\right|_\mathcal{S} = 0 \tag{3.5}$$

are obtained on $\mathcal{S}$. As opposed to sec. 2.5.3 and sec. 2.5.2, where Φ or $\nabla\Phi$ on $\mathcal{D}$ is uniquely defined by specifying either Φ or $\partial\Phi/\partial n$ on the whole boundary $\partial\mathcal{D}$, now Φ and $\partial\Phi/\partial N$ are simultaneously specified on the subset $\mathcal{S}$ of the boundary, and the existence and location of the rest of the boundary $\partial\mathcal{D}\backslash\partial\mathcal{B}$ is unknown.

The Cauchy-Kowalevski theorem guarantees the existence and uniqueness of the solution of the Cauchy problem in some neighbourhood of $\mathcal{S}$. The solution of the potential problem (3.1) is a harmonic and analytic function on $\mathcal{D}$. Therefore, the analytic continuation of the potential to the whole fluid domain on $\mathcal{D}$ [121, p. 505 ff.] and even beyond is possible. Given the exact knowledge of the potential and the normal derivative of the potential on $\mathcal{S}$, the reconstruction of the potential on $\mathcal{D}$ exists and is unique. But, similar to many other inverse

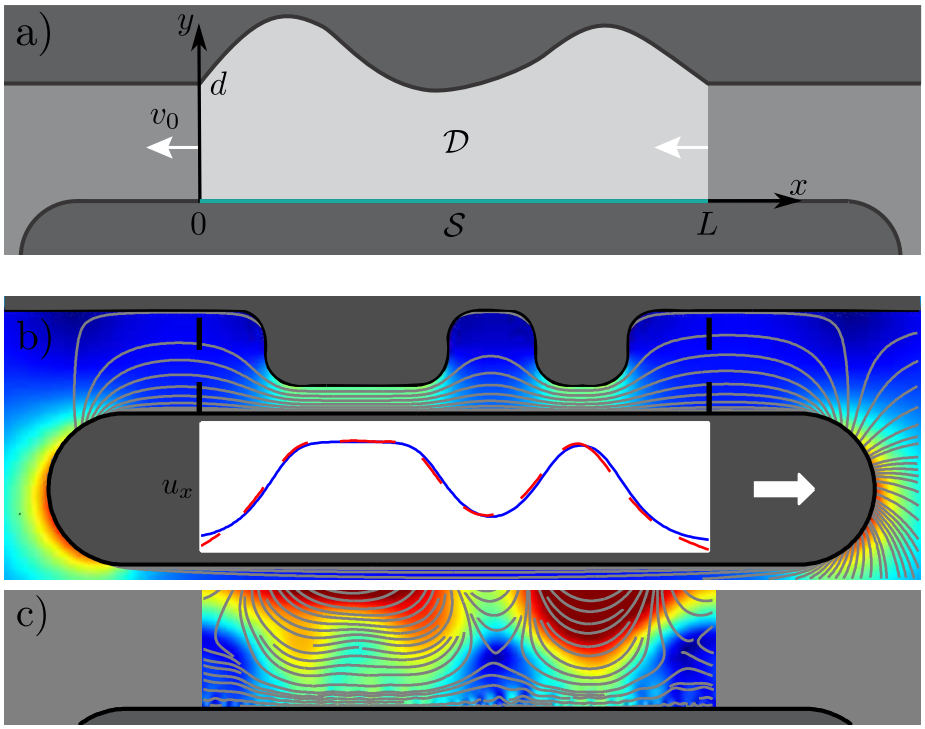

Figure 3.2: a) A conduit formed by a stationary wall and a flat plate with flow-sensory system (FSS) $\mathcal{S}$ and flow velocity v_0 at the inlet and outlet of $\mathcal{D}$. b) The velocity field in the conduit as obtained by means of a boundary-element method (BEM) simulation, see sec. 2.8, with the plate moving parallel to the wall. Inlet in the plate: Comparison of the flow velocity on the surface $\mathcal{S}$ of the plate $\mathcal{S}$ from 1000 equally spaced sensors as predicted by the model (3.3) (dashed red) and obtained by means of the BEM simulation (solid blue) with moving plate. c) Reconstruction of the velocity field between plate and wall from the velocities on $\mathcal{S}$ as shown in the inlet of fig. b) using the regularisation factor $\gamma = 0.004$. White Gaussian noise ($\sigma^2 = 4 \cdot 10^{-4}$, SNR ≈ 21) has been superimposed on the velocities on $\mathcal{S}$ for the reconstruction.

problems, the problem is ill-posed in the sense that any small error in determining the boundary values on $\mathcal{S}$ is amplified exponentially with the distance to $\mathcal{S}$ and therefore needs regularisation; see [134] or sec. 3.2.1 for an example.

Given a finite number of sensors (or a discretised boundary), in the presence of noise, it is even unlikely to obtain consistent boundary values so that an inverse exists. And if it exists, it is always possible to find an additional potential with zero velocity at the measurement points, which destroys uniqueness. Applied to the inversion of measured (or computed) boundary values, properly chosen regularisation also restricts possible solutions so that existence and uniqueness are preserved [134].

3.1.3 The source and the domain problem

So far, the existence, the uniqueness and the stability of the flow potential and the flow field given the measurement $\boldsymbol{V}^{\parallel}$ on $\mathcal{S}$ were discussed. One might assume that fish, crickets, or any FSS carrying animal is more interested in the sources and the boundaries of objects driving the fluid motion than the fluid motion itself. Since the 1960s a plethora of inverse source [134] or domain problems have been studied such as inverse gravimetry where one wishes to find the density distribution inside a domain from measurement of the gravitational force on its boundary. Under certain assumptions the inhomogeneity of the Laplacian, i.e. the source term and in this case the density, can be reconstructed.

In inverse domain problems one seeks to find the shape of the domain, i.e. the location of the boundaries from measurement of the boundary conditions on a subset of the boundary. An example of a domain problem is given by electrical impedance tomography with known conductivities, see e.g. [135], where one wishes to determine the shape of domains with a certain conductivities within a body by the application and measurement of the electric field on the surface of the body.

However, the knowledge of the velocity of the fluid on a subset of the boundary is not sufficient to solve the source or the domain problem of potential flow. The example of the sphere close to a wall (2.11.2) demonstrates that an infinite series of dipoles inside the centre of the sphere and a continuous distribution of dipoles on the wall, as well as an infinite series of dipoles in the centre of the sphere and in the image sphere on the adjacent side of the wall solve the boundary conditions on the wall and the sphere. The inverse source problem is thus not unique. Regularisation, which restricts the space of admissible solutions, does not help either, since both possible source distributions are highly relevant to the sphere. The sphere certainly wants to distinguish between both cases, since the reaction due to the appearance of the wall would certainly be different from the reaction to another object moving towards the sphere. Another example was already given by the ring vortex in the introduction of this chapter.

Contrary to inverse gravimetry or to electrical impedance tomography the no-penetration boundary condition for the flow potential over a solid surface only specifies one component of the flow field, the normal component. Since no negative mass exists, the gravitational force always points towards the centre of total mass. The normal component of the electric field is discontinuous on the boundary between domains of different conductivity, whereby the jump is given by the quotient of the conductivities. Its tangential component is continuous.

In contrast, any solenoidal and irrotational flow field with correct normal component on the boundaries is a valid solution of potential flow. Accordingly, since no restrictions are imposed on the tangential velocity component, any stream surface of the flow field might be a boundary with a no-penetration condition. It is thus impossible to solve the domain as well as the source problem of potential flow.

The flow field, as shown in the previous section, is uniquely defined by its values on parts of the boundary. So, the measurements of the tangential flow velocity on $\mathcal{S}$ are reasonably used for a reconstruction of the flow field in some domain chosen around $\mathcal{S}$. The size of the chosen domain will in general depend on the precision of the measurement of $\boldsymbol{V}^{\parallel}$, the shape of $\mathcal{S}$, the precision of the reconstruction required, and the regularisation. The existence, shape and motion of other objects must then be inferred from analysis of the flow field with suitable heuristic or additional information such as its evolution in time, see sec. 3.3.

There is plenty of literature on the Cauchy problem of the Laplacian, and it receives ongoing interest due to its importance in many applications such as image inpainting [136], corrosion detection [137], and many other fields. A brief overview of methods to numerically solve the Cauchy problem can be found in [107]. Most methods found in the literature are dedicated to a specific task. This is partly due to the fact that the knowledge of the resolution of the sensors, the geometry of the sensory system, and the characteristics of the noise are the basis for a reasonable assessment, which is missing for biological as well as technical FSSs. Usually additive Gaussian white noise such as in fig. 3.2 and fig. 3.4 is used to demonstrate the dependence of a method upon measurement errors. The largest contribution to what is usually referred to as noise, does not stem from the measurement electronics itself, termed sensor noise, but is introduced by deviations from potential flow, see sec. 5.2.3, caused by initial disturbances and vorticity in the fluid, by the action of viscosity in the vicinity to boundaries, or separation of the flow from boundaries. This disturbance simply cannot be treated as identically independently distributed (IID) Gaussian white noise, since fluid dynamics will propagate the disturbance to some extend depending on the geometry of the sensory system to all other sensors. At present, no experience and experiments with FSSs in real fluid is available that allow such an assessment.

The second big issue of a transfer of specific methods is that the quality of a solution depends on a well chosen and tuned regularisation, which is effectively a restriction of the solutions allowed to occur. This in turn implies that given some prior knowledge, one is interested in certain types of solutions, which are specific to a certain task.

Suitable methods for the present state of flow sensing have to be simple, easy implementable and universally applicable, which on the one hand offer easy access and insight to the essential properties of flow-field reconstruction. On the other hand, such a method should allow to analyse and interpret data provided from prototypes of FSSs, see sec. 5.2. In the following section, methods suitable for the application to FSSs are presented. A comparison of these methods with the biological role model is expected to provide further hints and insights for the development of FSSs.

As just described, the quality of a reconstruction depends on several factors, namely the deviation from potential flow around the FSS, the sensitivity of the flow sensors, the geometry of the FSS, and prior knowledge about possibly

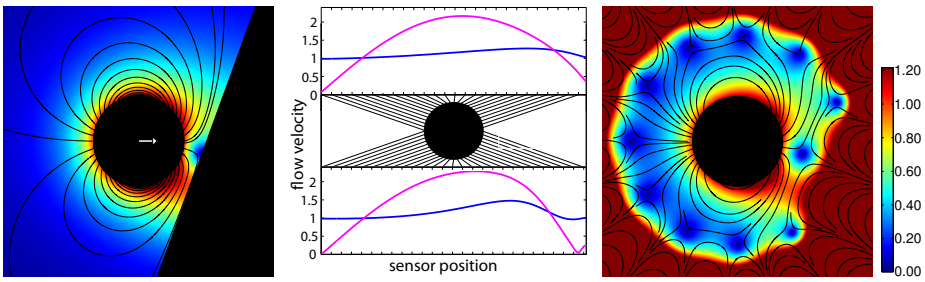

Figure 3.3: Reconstruction of the flow field around a circle. The flow velocity is colour coded in units of the speed of the sphere, lengths are scaled by the size of the sphere. *Left*: A circular disk with 1000 sensors equally distributed on its surface moves towards a wall at a 20° angle. The flow field, computed by means of a boundary-element method (BEM) simulation, see sec. 2.8, is plotted with respect to the FOR. *Middle*: The tangential velocities on the surface of the circle are used to determine the coefficients A_α. The measured flow velocities are shown in the *body-fixed system* (BFS) (pink line) and the *frame of reference* (FOR) (blue line). The middle part illustrates the mapping of the measured velocity from Cartesian coordinates to the surface of the circle. *Right*: The wall can be deduced from the parallel streamlines in the reconstructed flow field in front of the circle.

occurring solutions. But as the rest of this section will show, the quality also depends on the requirements and restrictions on the solution such as demanded precision, the range of view, the time and computational power available to compute a solution, and the consequences of a possible failure of a method. These questions need to be addressed in the view of a specific application. The following discussion of flow reconstruction methods deliberately ignores these questions.

3.2 Flow-field reconstruction

In sec. 3.1.2 it was shown that given consistent Cauchy data on $\mathcal{S}$ a solution exists and is unique. The purpose of this section is to introduce simple methods to express the flow field on a source-free domain of interest $\mathcal{E}$ surrounding $\mathcal{S}$ as a function of the measured tangential velocities $\boldsymbol{V}^{\parallel}$ on $\mathcal{S}$.

3.2.1 Matching a homogeneous solution

The flow potential on $\mathcal{E}$ can be expressed by explicit representations of the homogeneous solution around a 3D or 2D body $\mathcal{B}$, e.g. in terms of a Fourier series or a multipole series. The coefficients of such a series can be matched to the measured surface velocities, and the resulting series can be evaluated at any point in $\mathcal{E}$. If the surface of $\mathcal{B}$ can be described by a coordinate line or a coordinate surface of a coordinate system in which the solution of the Laplacian factorises, one may hope to find a good approximation of the flow field through the first few elements of the corresponding series. Here, the 2D inverse problem of determining the flow field on a rectangular domain from measurement of the

tangential velocity on one side of the domain and the reconstruction from a circle are described.

In sec. 3.1.1, the solution of the forward problem of the potential over a flat plate was given. Dropping constraint (3.2) and replacing the Fourier series by a Fourier transform, the potential (3.3) becomes

$$\Phi(x,y) = \int_{-\infty}^{\infty} \hat{C}(\alpha)\, \cosh(2\pi\alpha y)\, \mathrm{e}^{2\pi \mathrm{i}\alpha x}\, \mathrm{d}\alpha\,, \tag{3.6}$$

with $\mathrm{i} = \sqrt{-1}$, and the flow field $\boldsymbol{v}$ with redefinition of $\hat{C}(\alpha) := 2\pi\alpha\hat{C}(\alpha)$

$$\boldsymbol{v}(x,y) = \int_{-\infty}^{\infty} \hat{C}(\alpha)\, \mathrm{e}^{2\pi \mathrm{i} x\alpha} \big(\mathrm{i}\cosh(2\pi y\alpha),\, \sinh(2\pi y\alpha)\big)^{\mathrm{T}}\, \mathrm{d}\alpha\,. \tag{3.7}$$

In order to obtain a *reconstruction* of the flow field on a rectangular domain, the coefficients $\hat{C}(\alpha)$ have to be determined by inverse Fourier transform

$$\hat{C}(\alpha) = \frac{1}{2\pi} \int v_x(x,0) \mathrm{e}^{-2\pi \mathrm{i}\alpha x} \mathrm{d}\alpha$$

from the measured velocities $v^{\parallel} = v_x(x,0)$ on $\mathcal{S}$. Since (3.6) and (3.7) do not converge for arbitrary $\hat{C}(\alpha)$ the reconstruction can only approximate the true potential flow by setting $\hat{C}(\alpha) = 0$ for $|\alpha| > \alpha_{\max}$ to obtain convergence. Small errors in $\hat{C}(\alpha)$ are amplified exponentially with frequency α and distance y. Omitting frequency components above a certain $\alpha_{\max}$ (*frequency regularisation*) helps to globally stabilize the flow field $\boldsymbol{\mathfrak{v}}$ reconstructed through determination of $\hat{C}(\alpha)$ to some extent.

A second example is the flow field reconstruction from a circle. The origin of the polar coordinate system (R, Θ) shall be placed in the centre of the circular FSS with radius R_0. The surface of a moving circle is a streamline and the flow velocity component normal to the circle is zero in a BFS of the circle. Then, the Laplace equation (3.1) on a region of interest $\mathcal{E}$ around the circle is solved in polar coordinates $(R, \Theta)^{\mathrm{T}}$ with

$$(X, Y)^{\mathrm{T}} = (R\cos\Theta, R\sin\Theta)^{\mathrm{T}}$$

by the Ansatz

$$\Phi(R,\Theta) = \sum_{\alpha=-\infty}^{\infty} \left(A_\alpha \frac{R^\alpha}{R_0^{\alpha-1}} + B_\alpha \frac{R^{-\alpha}}{R_0^{-\alpha-1}} \right) \mathrm{e}^{\mathrm{i}\alpha\Theta} \tag{3.8}$$

with complex A_α and B_α, and furthermore $A_{-\alpha} = A_\alpha^*$ and $B_{-\alpha} = B_\alpha^*$. In the BFS the no-penetration condition (3.5) on the surface of the circle requires $A_\alpha = B_\alpha$, and the radial $\mathfrak{V}_R$ and angular $\mathfrak{V}_\Theta$ velocities of the reconstructed flow field on $\mathcal{E}$ are given by

$$\mathfrak{V}_R(R,\Theta) = \frac{\partial\Phi}{\partial R} = \sum_{\alpha=-\infty}^{\infty} A_\alpha\, \alpha \left[\left(\frac{R}{R_0}\right)^{\alpha-1} - \left(\frac{R}{R_0}\right)^{-\alpha-1} \right] \mathrm{e}^{\mathrm{i}\alpha\Theta}\,, \tag{3.9a}$$

$$\mathfrak{V}_\Theta(R,\Theta) = \frac{1}{R}\frac{\partial\Phi}{\partial\Theta} = \mathrm{i} \sum_{\alpha=-\infty}^{\infty} A_\alpha\, \alpha \left[\left(\frac{R}{R_0}\right)^{\alpha-1} + \left(\frac{R}{R_0}\right)^{-\alpha-1} \right] \mathrm{e}^{\mathrm{i}\alpha\Theta}\,. \tag{3.9b}$$

The complex coefficients A_α have to be determined from the measured tangential velocities

$$V^{\parallel}(R_0, \Theta) = 2\mathrm{i} \sum_{\alpha} \alpha A_\alpha \mathrm{e}^{\mathrm{i}\,\alpha\,\Theta}$$

on the surface of the circle by the Fourier transform,

$$A_\alpha = \frac{1}{4\pi\mathrm{i}\alpha} \int_0^{2\pi} V^{\parallel}(R_0, \Theta)\, \mathrm{e}^{-\mathrm{i}\alpha\Theta}\, \mathrm{d}\Theta\,,$$

or in case of a finite number of flow sensors, by a Fourier series. As for the plate, disregarding terms with higher frequencies in the computation of (3.9) automatically provides *frequency regularisation*. How strong the reconstruction $\mathfrak{V} = (\mathfrak{V}_R, \mathfrak{V}_\Theta)^{\mathrm{T}}$ is affected by an error in the estimation of the coefficients A_α depends largely on the spatial frequency α. The reconstruction is unstable for any non-trivial flow field $\alpha > 1$ due to the positive exponents of $(R/R_0)^{\alpha-1}$ amplifying any error with the distance to the circle. Omitting higher frequencies improves the stability due to the smaller amplification of errors. Given an acceptable error in the reconstruction, one has to find a trade off between range of view and the level of detail. Figure 3.3 shows the flow field around a circle moving towards a wall at an angle of 20°. The flow-field reconstruction is extensible to other 2D geometries by the application of conformal mapping – see sec. 3.2.3.

An investigation of the number of terms in the series and thus, the number of sensors necessary to perform obstacle detection and wall extraction from the reconstructed flow field measured on a circle in 2D potential flow using the method, can be found in [138, 139]. Given a desired range of view of one circle radius, the first five terms of the series already deliver sufficient detail to detect and extract wall shapes with sufficient resolution to carry out tasks like self-localisation and map formation of the environment. The procedure is transferable to, e.g. a 3D sphere using a multipole expansion.

The representation of the solution as an infinite sum of terms diverging with distance makes it impossible to control the error at larger distances, and leads to physically implausible solutions.

3.2.2 Regularised statistical inversion

The drawbacks of the method of estimating a finite number of coefficients of the series solution of the Laplacian inspired a Bayesian approach described in this section. Quite often inverse problems are regularised by minimizing

$$\|\mathcal{A}\boldsymbol{x} - \boldsymbol{b}\|^2 + \|\Gamma\boldsymbol{x}\|^2 \tag{3.10}$$

including a Tikhonov regularising functional with Tikhonov matrix Γ, frequently chosen as $\Gamma = \gamma\mathbb{1}$. Here, one wishes to identify $\boldsymbol{x}$, e.g. with the flow field on the boundaries of the domain of interest $\partial\mathcal{E}$, $\boldsymbol{b}$ with the tangential velocities measured on $\mathcal{S}$, and $\mathcal{A}$ with an operator that relates the flow field on the boundaries $\partial\mathcal{E}$ with the velocities measured on $\mathcal{S}$, e.g. by taking the limit of (2.13) similar to (2.36) as $\boldsymbol{x}$ approaches the boundary. The regularizing functional is interpreted as the kinetic energy of the flow field on the boundary. Having determined the regularised velocity on the boundary, the flow field on $\mathcal{E}$ is given by (2.13). Following such an approach, it is impossible to obtain an explicit solution of the

flow field as a function of the measured velocities, since $\mathcal{A}$ effectively represents singular boundary integrals similar to those in (2.36).

In addition, the quality of the reconstruction and eventually the range of view could be further improved, if it were possible to formulate the reconstruction by including a distance dependent regularisation such that the rapid increase of the error of the reconstruction with distance to the FSS is limited. This goal shall be pursued by a discussion of the previous examples with a slightly different method.

The velocities $\boldsymbol{v}(x, y)$ occurring on $\mathcal{E}$ over the flat plate of sec. 3.2.1 carrying the FSS $\mathcal{S}$ are assumed to be normally IID a priori with $\mathcal{V}_x(x, y)$, $\mathcal{V}_y(x, y) \sim \mathcal{N}(0, \sigma_r^2)$. For the moment, the question, as to whether this is a valid and reasonable choice for the velocities, shall be deferred.

Let $\mathcal{H}_{y_0}[v_x^{y_0}]$ be a functional that calculates the velocities $v_x^0 := v_x(x, 0)$ on $\mathcal{S}$ resulting from a given velocity $v_x^{y_0}(x) := v_x(x, y_0)$ at a fixed, but oblique, coordinate line y_0. A comparison with (3.7) shows that the Fourier transform of $\mathcal{H}_{y_0}$ is given by

$$\hat{\mathcal{H}}_{y_0}[v_x^{y_0}](\alpha) = \hat{v}_x^{y_0}(\alpha)/\cosh(2\pi\alpha y)\,. \tag{3.11}$$

The measurement $v^{\parallel}$ of $v_x^{y_0}$ mapped on $\mathcal{S}$ through (3.11) introduces additional noise, which is assumed to be also normally IID with zero mean and variance σ^2. Interpreted as random variables, the measured velocities $v^{\parallel}(x)$ are therefore conditionally normally distributed by

$$v^{\parallel}(x) \,|\, \mathcal{V}_x^{y_0} \sim \mathcal{N}(H_{y_0}[\mathcal{V}_x^{y_0}](x), \sigma^2)\,.$$

The log likelihood

$$L := \log P(v^{\parallel} | \mathcal{V}_x^{y_0})$$

of $v^{\parallel}$ on $\mathcal{S}$ assuming $\mathcal{V}_x^{y_0}$ after application of Parseval's theorem and (3.11) is up to a constant given by

$$L = -\frac{1}{2\sigma^2}\int_{-\infty}^{\infty} \left|\hat{v}^{\parallel}(\alpha) - \hat{\mathcal{V}}_x^{y_0}(\alpha)/\cosh(2\pi y_0\alpha)\right|^2 \mathrm{d}\alpha\,,$$

whereby $\hat{v}^{\parallel}$ and $\hat{\mathcal{V}}_x^{y_0}$ denote the Fourier transformations of $v^{\parallel}$ and $\mathcal{V}_x^{y_0}$. Analogously, the log prior $Q = \log(P(\mathcal{V}_x^{y_0}))$ is

$$Q(\mathcal{V}_x^{y_0}) = -\frac{1}{2\sigma_r^2}\int_{-\infty}^{\infty} \left|\hat{\mathcal{V}}_x^{y_0}(\alpha)\right|^2 \mathrm{d}\alpha\,.$$

Bayes' theorem allows to compute the a-posteriori logarithmic probability

$$\log P(\mathcal{V}_x^{y_0} \,|\, v^{\parallel}) = \frac{1}{2}\int_{-\infty}^{\infty} \left[\frac{1}{\sigma^2}\left|\hat{v}^{\parallel}(\alpha) - \frac{\hat{\mathcal{V}}_x^{y_0}(\alpha)}{\cosh(2\pi y_0\alpha)}\right|^2 + \frac{1}{\sigma_r^2}\left|\hat{\mathcal{V}}_x^{y_0}(\alpha)\right|^2\right] \mathrm{d}\alpha\,. \tag{3.12}$$

The maximum-a-posteriori estimator $\hat{\mathfrak{v}}_x^{y_0}$ for each Fourier component of v_x at $y = y_0$ is given by the maximum of the integrand in (3.12),

$$\hat{\mathfrak{v}}_x^{y_0}(\alpha) = \frac{\hat{v}^{\parallel}(\alpha)}{1/\cosh(2\pi y_0\alpha) + \gamma\cosh(2\pi y_0\alpha)}\,, \tag{3.13a}$$

with $\gamma = \sigma^2/\sigma_r^2$, and after an analogous derivation for $\mathfrak{v}_y$,

$$\hat{\mathfrak{v}}_y^{y_0}(\alpha) = -\mathrm{i}\frac{\hat{v}^{\parallel}(\alpha)}{1/\sinh(2\pi y_0\alpha) + \gamma\sinh(2\pi y_0\alpha)}\,, \tag{3.13b}$$

see fig. 3.2c. Higher velocities have been a priori chosen to be less likely than smaller velocities. Solving for the flow field with the highest probability effectively realises an energy regularisation in the Tikhonov sense.

Turning back to the question of whether normally distributed flow velocities as prior are a valid flow field. Therefore, the flow model allows non-harmonic solutions to occur, which approximate a valid physical solution. The trade-off between reconstruction accuracy and regularisation is tuned by the *regularisation factor* γ which is adjusted according to the expected measurement noise. For $\gamma = 0$ the reconstruction may diverge. However, if it exists, the reconstructed velocity field $\mathfrak{v}$ is a valid potential flow in the sense that it satisfies the Laplace equation. For $\gamma > 0$ the second terms in the denominators of (3.13) ensure convergence and, since the influence of the regularisation increases with αy_0, higher frequencies are more suppressed with increasing distance.

The same line of argumentation used to arrive at (3.13) for a flat FSS can be used to obtain the flow field by a regularised inversion from $V^{\parallel}$ on a circle with radius R_0. As before, a BFS is used with the origin placed in the centre of the sphere. The homogeneous solution of $\Delta\Phi = 0$ fulfilling the boundary condition $V^{\perp}(R_0, \Theta) = 0$ on $\mathcal{S}$ was given in (3.8), and the velocities in (3.9). Again, a functional can be constructed that maps a Fourier component of the flow field on a fixed but oblique coordinate line $R = R_1$ of the polar coordinate system onto the surface $R = R_0$ of the circle. The angular component of the reconstructed velocity $\mathfrak{V}_\Theta^{R_1}$ field at R_1 is then obtained by minimization of

$$\log P\Big(\mathcal{V}_\Theta^{R_1}\,\Big|V^{\parallel}\Big) = \sum_{\alpha=-\infty}^{\infty}\left(\left|\hat{V}^{\parallel} - \frac{2\hat{\mathcal{V}}_\Theta^{R_1}}{\mathcal{R}^{\alpha-1}+\mathcal{R}^{-\alpha-1}}\right|^2 + \gamma\,|\hat{\mathcal{V}}_\Theta^{R_1}|^2\right)$$

with respect to $\mathcal{V}_\Theta^{R_1}$ and the substitution $\mathcal{R} = R_1/R_0$.

Following the derivation of (3.13), the Fourier components of the radial $\hat{\mathfrak{V}}_R^{\mathcal{R}}(n)$ and the angular $\hat{\mathfrak{V}}_\Theta^{\mathcal{R}}$ regularised reconstructed velocity field at $\mathcal{R}$ given $V^{\parallel}$ measured on $\mathcal{S}$ are given by

$$\hat{\mathfrak{V}}_R^{\mathcal{R}}(\alpha) = \mathrm{i}\frac{2\mathcal{R}^{\alpha+1}\left(1-\mathcal{R}^{2\alpha}\right)}{\gamma+\gamma\mathcal{R}^{4\alpha}-2\mathcal{R}^{2\alpha}\left(\gamma-2\mathcal{R}^2\right)}\hat{V}^{\parallel}(\alpha)\,,$$
$$\hat{\mathfrak{V}}_\Theta^{\mathcal{R}}(\alpha) = \frac{2\mathcal{R}^{\alpha+1}\left(1+\mathcal{R}^{2\alpha}\right)}{\gamma+\gamma\mathcal{R}^{4\alpha}+2\mathcal{R}^{2\alpha}\left(\gamma+2\mathcal{R}^2\right)}\hat{V}^{\parallel}(\alpha)\,,$$

where γ is the regularisation factor. An example for the reconstruction of the velocity field using this method is shown in Fig. 3.4. Conformal mapping then allows the transfer to further 2D shapes.

3.2.3 Flow field reconstruction from a fish-like shape

The method proposed in (3.2.2) for the regularised flow field reconstruction from a circle can be adapted by conformal mapping to, e.g. a fish like shape,

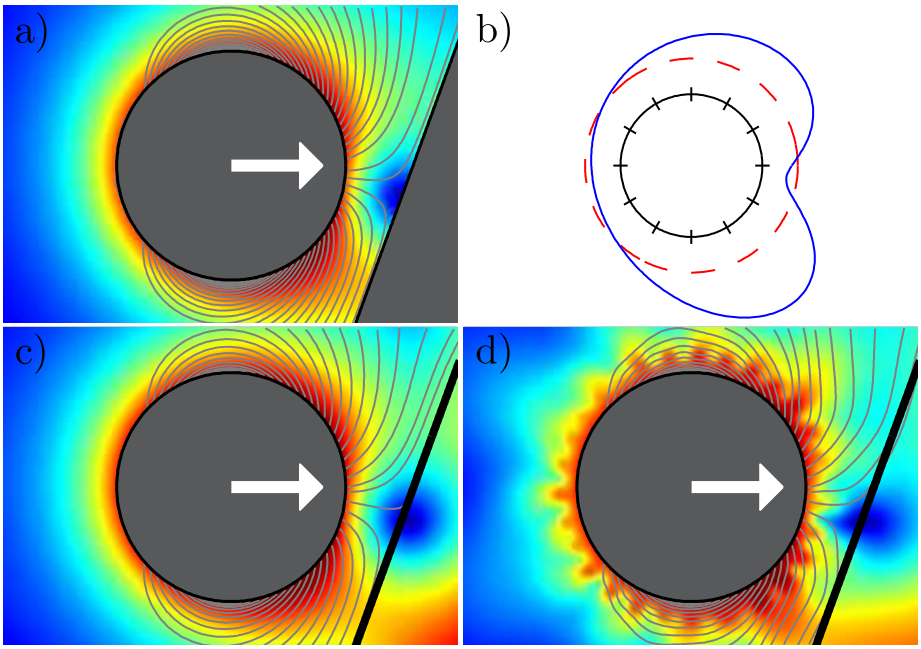

Figure 3.4: A circular disk moving towards a wall at an angle of 20°. a) The actual velocity field is obtained by means of a boundary-element method (BEM) simulation, see sec. 2.8. b) Radial plot of the velocities on the surface of the circular disk with (blue line) and without (dashed red line) the presence of the wall. c) Reconstruction of the velocity field with 1000 sensors equally distributed on the circle using a regularisation factor of $\gamma = 0.002$. d) Gaussian white noise ($\sigma^2 = 0.0016$, SNR ≈ 25) was superimposed on the velocities used for reconstruction with $\gamma = 0.004$.

often described by a Joukowski airfoil. Two BFSs will be used. The first system is a polar system (r, θ) placed in the centre of a circle $\mathcal{S}_C$ with radius r_0, no-penetration boundary condition $v_\perp = \partial\Phi/\partial n = 0$, and surface normal $\boldsymbol{n}$. The second system, (R, Θ), is placed in a fish like shape $\mathcal{S}_F$, an airfoil, which is obtained from (r, θ) by Joukowski transformation (3.15). An exception is made from the convention used throughout the rest of the work in which lower-case symbols are used for quantities in FOR coordinates and upper case symbols for quantities in BFS coordinates. In this section, lower case symbols are used for quantities in the circle frame, and upper case symbols for quantities in the fish frame. A Fourier component with angular frequency α of the regularised flow field reconstructed from a circle, see sec. 3.2.2, written in quantities of the redefined circle system is

$$\hat{\mathfrak{v}}_\theta(\mathfrak{r}, \alpha) = \frac{2\mathfrak{r}^{n+1}\left(1+\mathfrak{r}^{2n}\right)}{\gamma + \gamma\mathfrak{r}^{4n} + 2\mathfrak{r}^{2n}\left(\gamma + 2\mathfrak{r}^2\right)}\hat{v}^{\parallel}(\alpha)\,, \tag{3.14a}$$

$$\hat{\mathfrak{v}}_r(\mathfrak{r}, \alpha) = \mathrm{i}\frac{2\mathfrak{r}^{n+1}\left(1-\mathfrak{r}^{2n}\right)}{\gamma + \gamma\mathfrak{r}^{4n} - 2\mathfrak{r}^{2n}\left(\gamma - 2\mathfrak{r}^2\right)}\hat{v}^{\parallel}(\alpha)\,, \tag{3.14b}$$

with the Fourier component $\hat{v}^{\parallel}(\alpha)$ calculated from the measured tangential velocity $v^{\parallel}$ on $\mathcal{S}_C$, $\mathfrak{r} = r/r_0$, and the regularisation factor $\gamma = \sigma^2/\sigma_r^2$. The standard deviation of possibly occurring velocities components in the flow field is σ, and the standard deviation of noise of the flow velocity measurement σ_r.

A circle with radius r_0 centred at the origin of a complex plane $z = x + \mathrm{i}y$ is transformed into an airfoil by the Joukowski transformation [140],

$$Z(z) = a + z + \frac{c^2}{a+z}\,, \tag{3.15}$$

with $Z = X + \mathrm{i}Y$. Its inverse is denoted by Z^{-1}. The parameters $r_0 = 1.26$, $a = 0.16$, and $c = 1.26$, were chosen to closely approximate the form of the blind Mexican cave fish [41]. Accordingly, the velocity field $\boldsymbol{v}(x, y)$ around the circle and the velocity field $\boldsymbol{V}(X, Y)$ around the airfoil [63, ch. 7.11.5, p.596] are related by

$$\frac{\mathrm{d}Z}{\mathrm{d}z} = \frac{v_x(x,y) - \mathrm{i}\,v_y(x,y)}{V_X(X,Y) - \mathrm{i}\,V_Y(X,Y)}\,. \tag{3.16}$$

The procedure of reconstructing the flow field from the airfoil now consists of the following steps: first, transform the measured velocities $V^{\parallel}$ to the circle; second, compute the Fourier transform of $v^{\parallel}$; third, perform the reconstruction from the circle for each frequency; fourth, compose the Fourier components of the reconstruction; and finally, transform the reconstructed velocity field $\mathfrak{v}$ around the circle back into the system of the airfoil to obtain $\mathfrak{V}$. An example for the reconstruction is shown in fig. 3.5. A boundary element method as described in sec. 2.8 was used to calculate the potential flow given the boundary condition and the tangential velocities $V^{\parallel}$ on the airfoil. An application of the Joukowski transform to obtain the reconstruction from a fish-like shape based on the frequency regularised matching of the homogeneous solution in polar coordinates as described in sec. 3.2.1 can be found in [141].

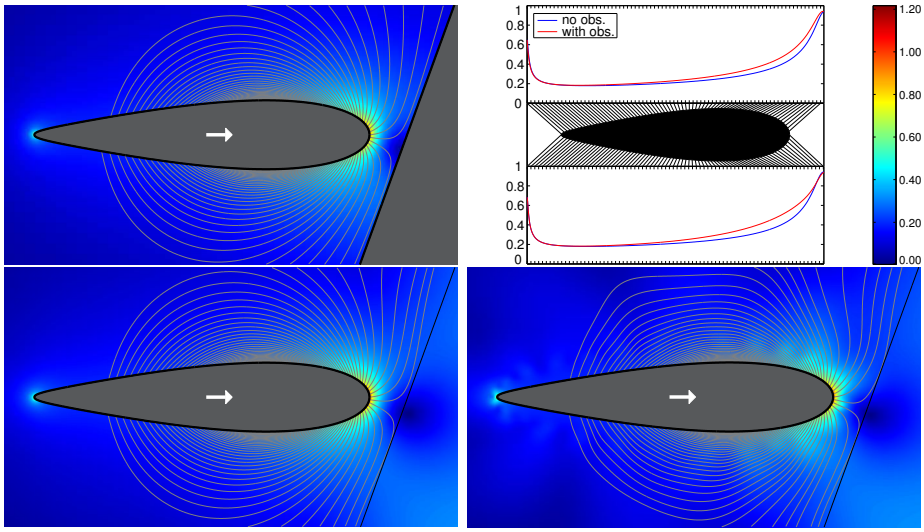

Figure 3.5: A fish gliding towards a wall at an angle of 20°. *Top left*: The actual potential flow is obtained by means of a boundary-element method (BEM) simulation, see sec. 2.8, with colour coded velocity normed by the velocity of the fish in a frame of reference with the wall fixed. *Top right*: Velocities on the surface of the fish (*red line*) due to the presence of the wall and for comparison without wall (*blue line*). *Bottom left*: Reconstruction of the velocity field from the velocities on the surface of the fish measured by 1000 sensors using a regularisation factor of $\gamma = 0.004$. The wall is indicated by the *black line*. *Bottom right*: Reconstruction with Gaussian white noise ($\sigma_r^2 = 3.24 \cdot 10^{-4}$, SNR ≈ 18) superimposed on the measured velocities.

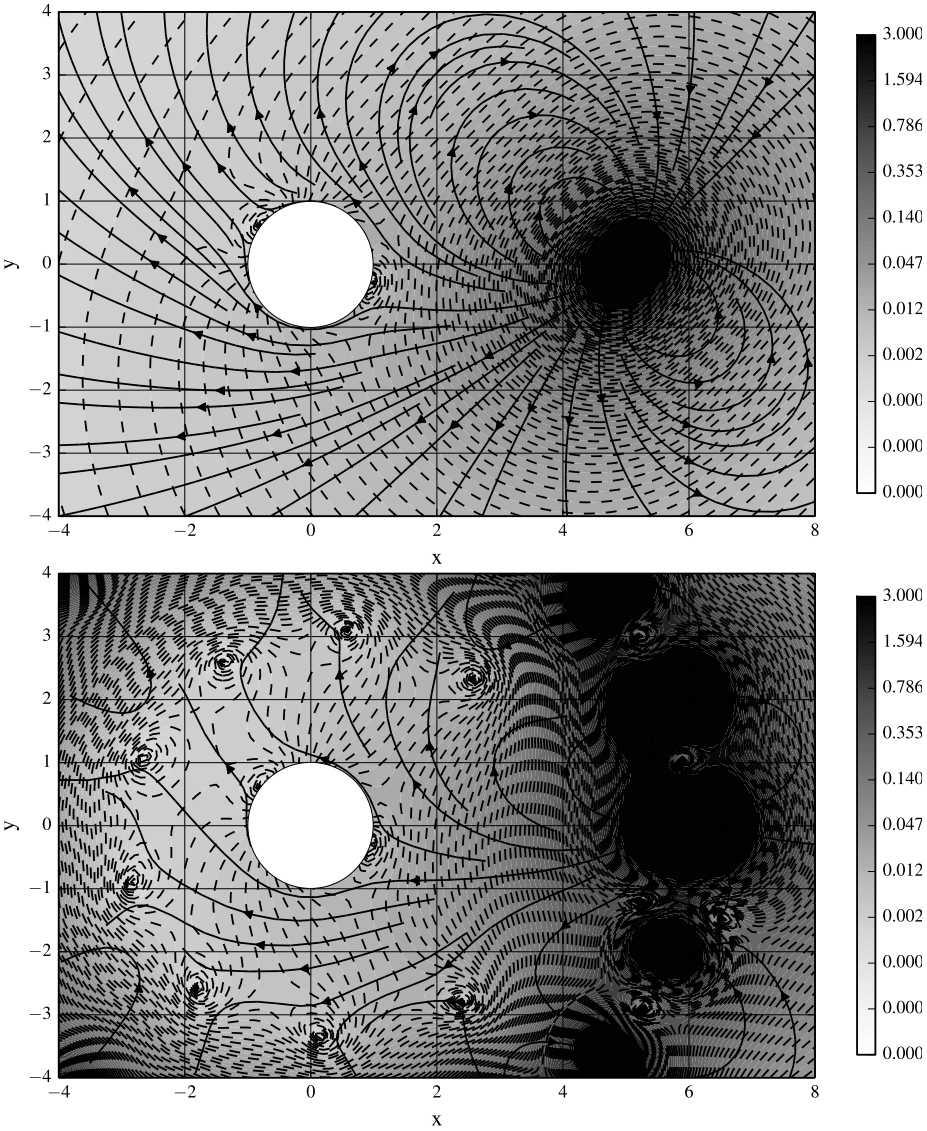

Figure 3.6: Flow field (top) with equi-velocity surfaces and streamlines of a dipole located at $(3, 0, 0)$ with radius 1 and velocity $(-1, -1, 0)$ close to a sphere with radius 1 at $(0, 0, 0)$ with no-penetration boundary condition on its surface. The 3D flow field reconstruction (bottom) is carried out with the source-term regularisation method with 20 dipoles directing towards the sphere equally spaced on a circle with radius 6 in the equatorial x-y plane of the sphere. The dipole strengths of the artificial sources driving the flow field is matched to the measurements of the tangential velocity of 256 equally spaced flow sensors on the surface of the sphere. The velocity of the flow field is defined with respect to the BFS of the sphere.

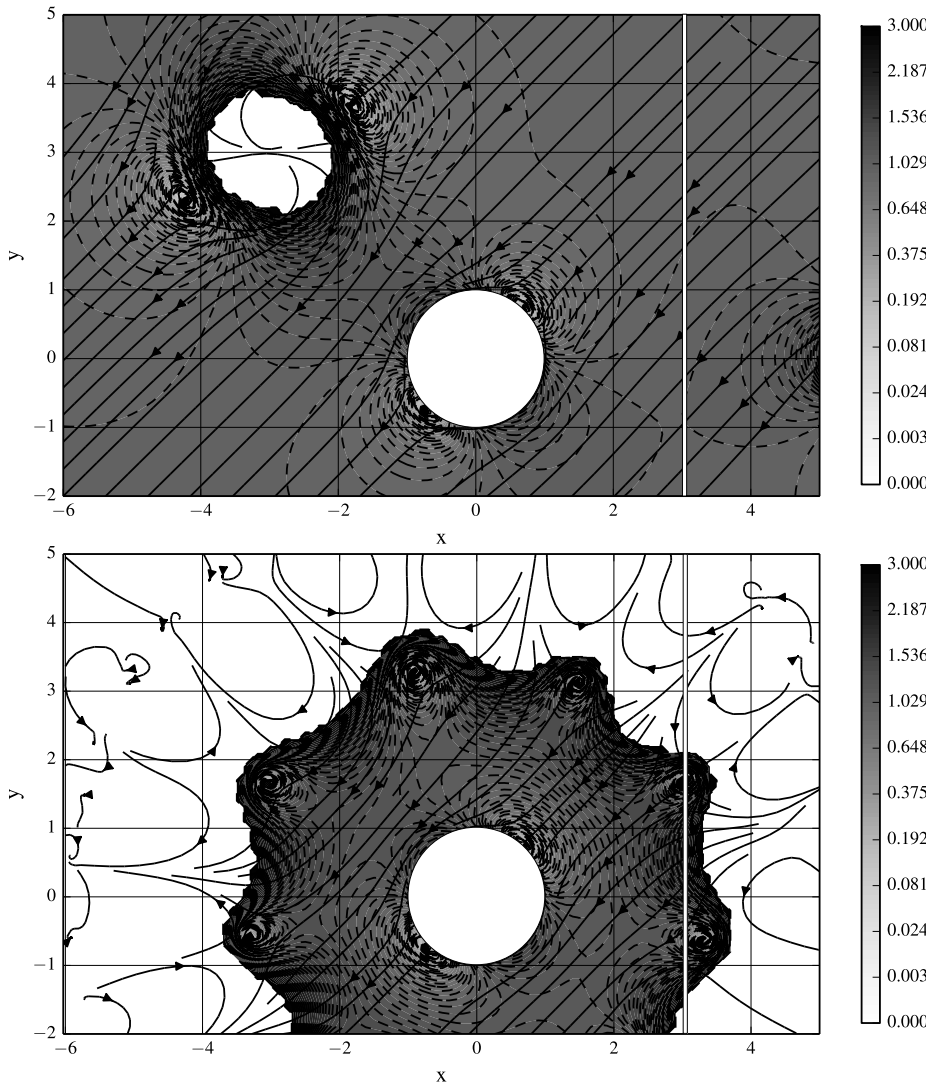

Figure 3.7: Flow field (top) with equi-velocity surfaces and streamlines of a dipole located at $(-3, 3, 0)$ with radius 1 and velocity $(3, 0, 0)$ close to a sphere with radius 1 at $(0, 0, 0)$ with no-penetration boundary condition on its surface moving with velocity $(1, 1, 0)$ towards a flat wall at $x = 3$. The 3D flow field reconstruction is carried out with the source-term regularisation method, with 40 dipoles directing towards the sphere equally spaced on a circle with radius 6 in the equatorial y-y plane of the sphere. The dipole strengths of the artificial sources driving the flow field are matched to the measurements of the tangential velocity of 256 equally spaced flow sensors on the surface of the sphere. The velocity of the flow field is defined with respect to the BFS of the sphere.

3.2.4 Source-term regularised flow-field reconstruction

The goal of the previous sections was to find expressions for the flow velocity at a point in the 2D fluid domain $\mathcal{D}$ as an explicit function of the tangential velocity measured on the FSS. In a way, the idea behind the method proposed in this section is the opposite. The Neumann representation (2.31) of the potential in terms of the normal velocities states that it is possible to express the potential and the flow field by its normal derivative on the boundary on a domain of interest $\mathcal{E}$ enclosed by the FSS $\mathcal{S}$ and the remaining boundary $\partial\mathcal{E}$. The normal velocity $\boldsymbol{V}^{\perp} = 0$ on $\mathcal{S}$ vanishes by choice of a BFS prescribed in the rigid body $\mathcal{B}$ carrying the FSS. In the sense of (2.31), the normal velocities on $\partial\mathcal{E}$ are the sources driving the flow field on $\mathcal{E}$. The simplest approximation for a source distribution driving the flow field is a finite number m of point-monopole sources at fixed positions $\boldsymbol{Y}_i$ with $i = 1 \dots m$. The sources are however not placed on $\partial\mathcal{E}$, but on a second surface $\partial\mathcal{Q}$ outside $\mathcal{E}$, see fig. 3.1. The additional artificial boundary $\partial\mathcal{Q}$ is introduced since the reconstructed flow field close to a source point $\boldsymbol{Y}_i$ will be dominated by the singularity of that source point. A single source will, in general, not be a suitable approximation of the flow field, and thus the error is expected to be large. By putting the source distribution outside the domain of interest $\mathcal{E}$ on $\partial\mathcal{Q}$ at some distance to $\partial\mathcal{E}$, the flow field at a point $\boldsymbol{X}$ inside $\mathcal{E}$ can be influenced by several sources, which promises a much better approximation. At the end of the section a possibility how to avoid the peculiarities involved in a distribution of discrete sources is outlined. The strengths Q_i of the sources have to be determined by the tangential velocities $\boldsymbol{V}_j^{\parallel}$ with $j = 1 \dots n$ on $\mathcal{S}$, measured by a finite number n of sensors located at at $\boldsymbol{X}_j$.

The sensory system $\mathcal{S}$ is part of the boundary of the rigid body $\mathcal{B}$ with the no-penetration boundary condition on its surface. The domain of interest $\mathcal{E}$ is chosen to be fixed with respect to $\mathcal{B}$, and thus moving with $\mathcal{B}$ as well as the point sources Q_i at $\boldsymbol{Y}_i$. Thereby, the geometry of the sources and $\mathcal{E}$ is fixed. $\mathcal{B}$ assumes that the fluid domain $\mathcal{D}'$, differently from $\mathcal{D}$, extends to infinity. According to (2.31), the potential of the point sources located in $\mathcal{D}'$ on $\mathcal{E}$, approximating the normal velocity component on $\partial\mathcal{Q}$ is given by

$$\Phi(\boldsymbol{X}, t) = \sum_{i=1}^{m} Q_i(t) G_N(\boldsymbol{X}, \boldsymbol{Y}_i) \; . \tag{3.17}$$

The actual task is to find the corrector function H_N for $G_N = G_F + H_N$ fulfilling $\Delta_Y H_N(\boldsymbol{X}, \boldsymbol{Y})$ and the boundary condition

$$\frac{\partial H_N(\boldsymbol{X}, \boldsymbol{Y})}{\partial n(\boldsymbol{Y})} = -\frac{\partial G_F(\boldsymbol{X}, \boldsymbol{Y})}{\partial n(\boldsymbol{Y})} \quad \text{for} \quad \boldsymbol{Y} \in \partial\mathcal{B} \, , \tag{3.18}$$

which guarantees that the no-penetration condition on $\mathcal{B}$ is fulfilled. The term $1/|\partial\mathcal{D}'|$ in (2.31) vanishes, since the surface area of $\mathcal{D}'$, which extends to infinity is infinitely large. H_N is harmonic on $\mathcal{E}$ by virtue of Green's representation formula (2.19)

$$H_N(\boldsymbol{X}, \boldsymbol{Y}) = -\oiint_{\partial\mathcal{E}} G_F(\boldsymbol{Y}, \boldsymbol{Z}) \frac{\partial H_N(\boldsymbol{X}, \boldsymbol{Z})}{\partial N(Z)} \, \mathrm{d}\mathcal{S} + \oiint_{\partial\mathcal{E}} H_N(\boldsymbol{X}, \boldsymbol{Z}) \frac{\partial G_F(\boldsymbol{Y}, \boldsymbol{Z})}{\partial N(Z)} \, \mathrm{d}\mathcal{S} \tag{3.19}$$

for $Y \in \mathcal{D}'$. After taking the limit $\boldsymbol{Y} \to \partial\mathcal{B}$ a weakly singular boundary integral [106, ch. 1.4.2] is obtained, similar to the first component of Calderon's projector (2.36). Using (3.18) the result is a Fredholm integral equation of the second kind

$$\frac{1}{2}H_N(\boldsymbol{X},\boldsymbol{Y}) = \oiint_{\partial\mathcal{E}\setminus\boldsymbol{Y}} H_N(\boldsymbol{X},\boldsymbol{Z})\frac{\partial G_F(\boldsymbol{Y},\boldsymbol{Z})}{\partial N(Z)}\,\mathrm{d}\mathcal{S} + \oiint_{\partial\mathcal{E}\setminus\boldsymbol{Y}} G_F(\boldsymbol{Y},\boldsymbol{Z})\frac{\partial G_F(\boldsymbol{X},\boldsymbol{Z})}{\partial N(Z)}\,\mathrm{d}\mathcal{S}\,, \quad (3.20)$$

which possesses an unique solution for $H_N(\boldsymbol{X},\boldsymbol{Y})$. Analytic expressions for G_N are available in only a few cases, such as the monopole close to a sphere, (2.67) and (2.69), with no-penetration condition on its surface obtained by virtue of Weiss' sphere theorem (2.68). Taking the gradient of (3.17)

$$\boldsymbol{V}_j = \sum_{i=1}^{m} Q_i\ \nabla_X G_N\left(\boldsymbol{X},\boldsymbol{Y}_i\right)|_{\boldsymbol{X}=\boldsymbol{X}_j} \quad (3.21)$$

to obtain the flow velocity at the sensor S_j will in general not reproduce the measured velocities exactly, since the finite number of sources Q_i is not able to capture any detail of the flow field and the measured value will be superimposed by measurement noise. The system of linear equations connecting the measured velocities $\boldsymbol{V}_j^{\parallel}$ and the source strengths

$$V_{jl}^{\parallel} = \mathcal{M}_{jil} Q_i \quad (3.22)$$

with the $j \times i \times 3$ matrix

$$\mathcal{M}_{jil} = \partial_l^X G_N\left(\boldsymbol{X},\boldsymbol{Y}_i\right)_{\boldsymbol{X}=\boldsymbol{X}_j}\,,$$

where l denotes the spatial component of the velocity vector $\boldsymbol{V}_j^{\parallel}$ of sensor j, will not have an exact solution. The pseudo-inverse $\mathcal{M}^+$ of $\mathcal{M}$ delivers the best approximation for $Q_i = \mathcal{M}_{ijl}^{+} V_{jl}^{\parallel}$ in the least squares sense.

It shall be noted that $\mathcal{M}^+$ is determined solely by the geometry of $\mathcal{B}$, the position of the sensors $\boldsymbol{X}_j$ on $\partial\mathcal{B}$, and the location $\boldsymbol{Y}_i$ of sources driving the flow field on $\mathcal{E}$. Since $\boldsymbol{Y}_i$ as well as the shape of $\mathcal{B}$ are chosen to be constant in time, $\mathcal{M}^+$ has to be computed only once and is known for all times. The actual regularisation happens through the choice of the number and the location of the source points. The reconstruction produces only flow fields that can be represented by the chosen source distribution.

The reconstructed velocity $\mathfrak{V}$ at a point $\boldsymbol{X} \in \mathcal{E}$ is nothing more but a weighted sum over the measured tangential velocities

$$\mathfrak{V}_k(\boldsymbol{X},t) = \sum_i \partial_k^X G_N\left(\boldsymbol{X},\boldsymbol{Y}_i\right)\mathcal{M}_{ijl}^{+} V_{jl}^{\parallel}(t)\,. \quad (3.23)$$

To arrive at (3.23) it was assumed that $\mathcal{D}'$ extends to infinity and is free of further boundaries and sources other than Q_i, which is clearly not the case for $\mathcal{D}$. $\mathcal{B}$ wishes to gather knowledge about the flow field on $\mathcal{E}$, which is a subset of $\mathcal{E} \subset \mathcal{D}$ as well as $\mathcal{E} \subset \mathcal{D}'$. As discussed in sec. 3.1.3, the source problem is not uniquely solvable. For $\mathcal{B}$ there is no difference between a flow field driven

by additional boundaries or sources on $\mathcal{D}$ and the flow field of the artificial sources Q_i in $\mathcal{D}'$, as long as the same measured tangential velocities $\boldsymbol{V}_j^{\parallel}$ on $\mathcal{S}$ are obtained, provided the sources Q_i at suitably chosen source points $\boldsymbol{Y}_i$ are capable to closely approximate the $\boldsymbol{V}_j^{\parallel}$.

Figures 3.6 and 3.7 show examples for the method of the source-term regularised flow-reconstruction in 3D. Instead of monopole sources, which represent the generation and extinction of fluid, which is not expected to happen in incompressible flow without inlets or outlets, dipole sources are used, since their strength can be adapted independently while preserving the fluid volume. The potential of a dipole source $\boldsymbol{Q}_i^D$ is constructed from the potential of two monopole sources at infinitely small distance by

$$\Phi_i^D = -\iiint \boldsymbol{Q}_i^D \cdot \nabla_Y G_N(\boldsymbol{X}, \boldsymbol{Y}) \delta(\boldsymbol{Y} - \boldsymbol{Y}_i^D)\, \mathrm{d}\mathcal{V}\,,$$

see e.g. [21, ch. 2.7]. The orientation of the dipoles is supposed to be normal to $\partial\mathcal{Q}$, as required by (2.19), the normal component of the dipole i is denoted by Q_i^D. The potential of a single dipole source Q_i^D is given by

$$\Phi_i^D = -Q_i^D \left.\frac{\partial G_N(\boldsymbol{X}, \boldsymbol{Y})}{\partial N(\boldsymbol{Y})}\right|_{\boldsymbol{Y}=\boldsymbol{Y}_i^D}\,. \tag{3.24}$$

The same considerations used to arrive at the explicit representation of the flow field (3.23) given the $\boldsymbol{V}_j^{\parallel}$ on $\mathcal{S}$ can be carried out with (3.24) replacing the monopole potential.

Improvements of the method, especially in vicinity of the source points $\mathcal{Q}_i$, can be achieved by using techniques described in sec. 2.8. Instead of approximating the flow field by a small discrete number of point sources, the boundary $\partial\mathcal{Q}$ could be discretised, e.g. in triangles with constant source strength on each triangle. To capture the influence of one triangle $\mathcal{T}_i$ on a field point $\boldsymbol{X}$, the Green's function of a point source must then be replaced by the surface integral of G_N over $\boldsymbol{Y} \in \mathcal{T}_i$. This surface integral over a triangle with constant source strength can be in principal also carried out analytically in 3D [142, 143]. With modified $\mathcal{M}$, the problem to be solved (3.22) remains the same.

3.3 Object extraction

Having reconstructed the flow field around $\mathcal{B}$, the question arises how to extract other objects altering the flow field. Potential theory, [101], states that on a source-free domain streamlines start and end on boundaries, streamlines do not intersect, a streamline might be a wall, and the extrema of the potential occur on boundaries. A similar statement regarding the extrema of the absolute value of the flow field can be made, [63, ch. 2.4, p. 137]. In the absence of singularities the absolute value of the flow velocity has its maximum on the boundaries.

It is convenient to transform the reconstructed flow field in the FOR with the fluid $\mathcal{D}$ or the boundary enclosing $\mathcal{D}$ at rest at infinity, which requires the knowledge of the translational $\boldsymbol{u}^{\mathcal{B}}$ and rotational speed $\boldsymbol{\omega}^{\mathcal{B}}$ of $\mathcal{S}$. A straightforward heuristic approach to extract the walls of a stationary environment is: first, search for local zeros of the velocity in the reconstructed flow field in the inertial frame; then compute a set of streamlines starting in the neighbourhood

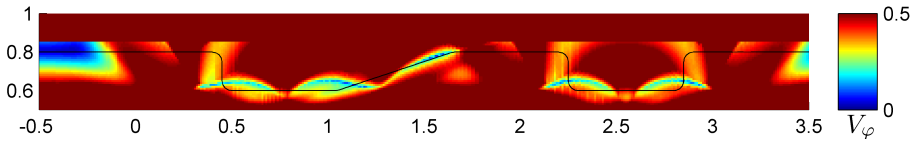

Figure 3.8: Directional variances of the reconstructed velocity field over time computed as a circular FSS with radius 0.5 moves on the x-axis along a stationary solid wall. The wall is indicated by the black line. The directional variance is minimal along the wall.

of the stagnation points; finally remove all streamlines from the set that start or end on $\partial\mathcal{B}$. The method presented here is based on the fact that the boundary of a solid object is a streamline and no flow through the boundary may exist under all possible motions occurring within the fluid. The remaining streamlines deliver estimates for the contours of stationary objects. A solid boundary separates the flow field and its analytic continuation due to the no-penetration boundary condition in an admissible fluid domain and a wall domain, see fig. 3.4. Therefore, the area filled with streamlines starting on the surface of $\mathcal{B}$ represents the fluid. After the elimination of the streamlines starting on $\mathcal{B}$ the remaining streamlines in the range of view of the sensory system represent walls.

In case the environment is moving, this heuristic will avoid collisions since it delivers at least an admissible area within the fluid. The correct interpretation of the flow field of moving bodies requires the analysis of the temporal evolution of the streamlines or streamsurfaces. A criterion for the detection of a moving rigid boundary is that the surface of a rigid body and thus the streamsurface on the body maintains its shape during motion. The flow field is always tangential to the surface of a solid object. This fact can also be exploited quite easily for a method to extract stationary objects. Consider a point $\boldsymbol{r}$ somewhere in the fluid at some time close to the FSS of $\mathcal{B}$. As $\mathcal{B}$ moves relative to $\boldsymbol{r}$, the flow at $\boldsymbol{r}$ will change in speed and direction. For a point $\boldsymbol{r'}$ located on a solid boundary, less degrees of freedom are possible since the flow direction is limited to its tangential component on the surface independent of the position of $\mathcal{B}$. Thus, the variance of the directions of the flow field is expected to be minimal on boundaries. A strategy is to find regions of minimal variance of direction in the reconstructed flow field over time. With the knowledge of its current velocity and acceleration, $\mathcal{B}$ can record the reconstructed directions of motions in the flow field at sample points on $\mathcal{D}$ in the FOR at each instant of time in a global map. Since the accuracy of the reconstruction rapidly decreases with the distance to $\mathcal{S}$, an additional distance dependent weighting ($\sim 1/r$) of the calculated direction is used, and the variance for each point in space is computed over time from the weighted sum of directions. The weighted variances of the reconstructed angular velocities around a circular $\mathcal{B}$ moving parallel to a stationary wall can be seen in fig. 3.8. As expected, the variance is minimal on the boundary of the wall.

The considerations just presented lead back to the question raised in the introduction of this chapter: How is it then possible to distinguish the flow field of a vortex structure from the flow field of a moving solid object? The shape of a solid object, rigid or not, will be hardly influenced by the hydrodynamic interaction with $\mathcal{B}$. Vorticity, however, is a physical quantity associated with

the fluid itself, a material quantity, and thus can be convected. When moving relative to $\mathcal{S}$, the vortex structure will be deformed under the influence of $\mathcal{B}$. A streamsurface or streamline with constant shape in time can be attributed to a solid boundary.

3.4 Incorporating a canal

For the moment disregarding the action of viscosity, the existence of a canal, see fig. 2.1, turns the simply connected domain of fluid $\mathcal{D}$ into a multiply connected domain. Without the knowledge of the circulation through each canal, the flow potential is not a single valued function, see sec. 2.1 or [101, ch. 3, §49-51]. Conversely, without a canal, the flow potential is always single valued. However, viscosity will damp any cyclic motion of the fluid through the canal. But, the question remains: Why do fish possess a lateral-line canal at all? The answers given so far are, different filter properties and surprisingly, despite an increased moving mass inside the canal, an increased sensitivity to higher stimulus frequencies [70] compared to SN at least for ruffe.

Assuming quasi-stationary laminar viscous flow through the CLS, which is expected to occur for low frequencies in the exterior flow field, see sec. 1.1.1, the shape of the flow velocity profile inside the canal is independent of the stimulus. With the measurement of the flux or the velocity inside the canal by the CN the pressure difference between two pores Δp is known. In this flow regime, the details of how the flow inside the canal is precisely measured do not matter further. The flow velocity measured at some fixed radial position within the canal is proportional to the total flux of the fluid through the canal, and the flow velocity at some radial position is proportional to the pressure difference between entrance and exit of the canal pore. The opening of the canal pores is small compared to the typical length scales in the flow field. In summary, it is a good approximation to assume that the exterior flow field is not affected by the flow through the canal, and that the precise shape of the flow field in the canal or at the pore openings does not further matter.

As in sec. 3.2.4, the potential on the domain of interest $\mathcal{E}$, which is assumed to be unaffected by the flow through the canal, is generated by m monopole sources placed on $\partial\mathcal{Q}$

$$\Phi(\boldsymbol{X},t) = \sum_{i=1}^{m} Q_i(t) G_N\left(\boldsymbol{X},\boldsymbol{Y}_i\right) .$$

The pressure on $\mathcal{E}$ by virtue of Bernoulli's equation is

$$\frac{p(\boldsymbol{X},t)}{\varrho} = -\sum_{i=1}^{m} \frac{\partial Q_i(t)}{\partial t} G_N(\boldsymbol{X},\boldsymbol{Y}_i) - \frac{1}{2}\sum_{i,j=1}^{m} Q_i(t)Q_j(t)\nabla_X G_N(\boldsymbol{X},\boldsymbol{Y}_i)\cdot\nabla_X G_N(\boldsymbol{X},\boldsymbol{Y}_j) .$$

It is convenient to define the symmetric $m\times m$ tensor

$$\mathcal{H}_{ij}(\boldsymbol{X}) = \nabla_X G_N(\boldsymbol{X},\boldsymbol{Y}_i)\cdot\nabla_X G_N(\boldsymbol{X},\boldsymbol{Y}_j) ,$$

the vector

$$\boldsymbol{G}(\boldsymbol{X}) = (\ldots, G_N(\boldsymbol{X}, \boldsymbol{Y}_i), \ldots)^{\mathrm{T}}$$

of length m, and the source strength vector

$$\boldsymbol{Q} = (\ldots, Q_i(t), \ldots)^{\mathrm{T}} ,$$

also of length m. Using these substitutions, the pressure becomes

$$\frac{p(\boldsymbol{X}, t)}{\varrho} = -\frac{\partial \boldsymbol{Q}(t)}{\partial t} \cdot \boldsymbol{G}(\boldsymbol{X}) - \frac{1}{2}\boldsymbol{G}(\boldsymbol{X})^T \mathcal{H}(\boldsymbol{X})\boldsymbol{G}(\boldsymbol{X}) .$$

The pressure difference $\Delta^{op}p(t) = p(\boldsymbol{X}^o, t) - p(\boldsymbol{X}^p, t)$ between two adjacent pore openings $\boldsymbol{X}^o$ and $\boldsymbol{X}^p$ with $o, p = 0 \ldots l$ and the number of pore openings l with $l - 1$ CNs delivers a non-linear ordinary differential system of equations

$$\frac{\Delta^{op}p(t)}{\varrho} = -\frac{\partial \boldsymbol{Q}^{\mathrm{T}}(t)}{\partial t} \cdot \Delta^{op}\boldsymbol{G} - \frac{1}{2}\boldsymbol{Q}^{\mathrm{T}}(t)\Delta^{op}\mathcal{H}\boldsymbol{Q}(t) \tag{3.25}$$

for the temporal evolution of the source strengths $\boldsymbol{Q}(t)$, with the definitions

$$\Delta^{op}\mathcal{H} = \mathcal{H}(\boldsymbol{X}^o) - \mathcal{H}(\boldsymbol{X}^p)$$

and

$$\Delta^{op}\boldsymbol{G} = \boldsymbol{G}(\boldsymbol{X}^o) - \boldsymbol{G}(\boldsymbol{X}^p) .$$

It is in principle possible to solve (3.25), and then to compute the flow field on $\mathcal{E}$ analogously to sec. 3.2.4. The initial values for $\boldsymbol{Q}(t)$ must be obtained from additional measurement, e.g. from the SLS. Due to the integration over $\Delta^{op}p(t)$ measured with finite precision and biased by the properties of the canal, the solution $\boldsymbol{Q}(t)$ will suffer an increasing error over time. A large improvement of the flow field reconstructed from the SLS incorporating the CLS thus cannot be expected. An obvious advantage of (3.25) is that it delivers an explicit expression for the change of the source strengths at the given instant of time. It could serve to highlight fast and urgent changes in the ambient flow field. Then, it will be probably necessary to remove the assumption of quasi-stationary flow through the canal.

3.5 Conclusion

To the knowledge of the authors not much has been published yet on inverse problems in fluid-mechanics [144–146]. The nature of the the fluid-mechanical image and it inversion was presented. It was argued that information on the boundaries in the environment must be extracted from the reconstructed flow field, since neither the source nor the domain problem are reasonably solvable. Regularised reconstruction methods for 2D and 3D were presented and the CLS was incorporated.

The results obtained in this chapter can be summarised in view of an application to an artificial lateral line system as follows. The measurement of the tangential velocity at discrete points on a body allows to reconstruct the flow field on some domain of interest in the vicinity of the FSS. The reconstruction is ill-posed and not unique for a finite number of sensors and thus needs regularisation. The number of sensors required for an ALL capable of perceiving a

stationary environment with suitable resolution is about 20 in 2D. Each sensor must instantaneously deliver a reliable representation of the flow velocity at its position. This is imposed by the gradients in the flow field over the FSS, the small range of view, and hence the short time available for a reaction. Then spatial resolution of the reconstruction deteriorates with the range of view. Boundaries and vortices can be identified by the temporal evolution of the reconstructed streamsurfaces or streamlines. The CLS promises advantages in the perception of rapidly changing or fast moving environments.

Chapter 4

Forces in Potential Flow

The obvious reason to consider the hydrodynamic forces acting on a body $\mathcal{B}$ moving in an ideal incompressible fluid is to account for this forces in the control of the movement of $\mathcal{B}$. The presence of other objects, the release of wakes, free surfaces, instabilities in the flow field over $\mathcal{B}$, and so forth, may cause inhomogeneities in the flow around $\mathcal{B}$ leading to additional forces on it. These forces could be detected and estimated by measuring the pressure on $\mathcal{B}$ or other quantities related to it.

A less obvious motivation to examine fluid-dynamical forces on a body is the information provided by the forces about the immediate environment. By means of the simple example of a sphere close to a wall in sec. 2.12, it was demonstrated that the hydrodynamic interaction in incompressible inviscid irrotational flow is only important in the very close vicinity to other objects, say within less than one object radius. But, it strongly increases with further decreasing distance. Considering the short range and typical speed of the object, there is only a very limited span of time available for perception, evaluation, decision making, and to change the state of motion in an appropriate way. The measurement of the fluid flow velocity with the exception of highly accelerated flow provides in principle a larger range of view than the resulting fluid-mechanical forces or the acceleration, see sec. 2.10.2. The question arises, whether it is feasible for $\mathcal{B}$, equipped with a FSS, to use one of the flow reconstruction methods developed in ch. 3 as a basis for urgent and immediate behavioural decisions, which have to be taken facing an event such as the appearance of objects in the range of a FSS.

Starting from the fluid-mechanical force on a rigid body $\mathcal{B}$, a heuristic is developed in the course of this chapter that relates the tangential velocities on the surface of $\mathcal{B}$ with the existence of further boundaries.

4.1 Some thoughts on flow sensing heuristic

The flow field reconstruction in combination with wall and wake extraction methods introduced in the previous chapter promises to solve quite complex tasks, such as self-localisation, map formation, and wake tracking [3, 139]. To be useful for collision avoidance or the escape from a predator, the reconstruction method and the wall extraction must be carried out permanently with only a

few milliseconds of latency. It is not impossible to realize such a system. A 2D simulation [139] with potential flow computed by a BEM around a cylindrical FSS and a flow field reconstruction based on the homogeneous solution of the Laplacian in polar coordinates followed by a computation of the streamlines and the extraction of the walls only took about 10 ms on desktop computer hardware of the year 2011. The execution was accelerated by massive parallelisation and execution on a graphics card. The power consumption was about 300 W. The extension of the reconstruction to 3D will further increase the computation time for each time step by more than a factor of three. The power consumption for such a emergency or warning system, which must be running permanently at full power is rather high. Although not completely impossible, such a solutions seems hardly feasible.

Are there possibly simpler solutions with similar effectiveness as suggested by the Mauthner cells of fish, see sec. 1.1.2, which are capable of making decision in a few milliseconds? It is certainly worth thinking about alternative methods, which are faster and more efficient. Such a method should rely on as weak assumptions and restrictions of the environment as possible. It will not be possible to provide full information on the environment, such as the flow-field reconstruction does. Any heuristic must be selective and robust enough to filter the important events with a high reliability of positive detected true events and only a few false positives, as any well working warning device.

Due to the short range of view of a FSS, the situations that have to be resolved cannot be very complex. The space available in the immediate surroundings monitored by a FSS is limited to only a few objects. The objects can be either moving with $\mathcal{B}$ such as during schooling, move away from $\mathcal{B}$, be at rest such as a stationary wall $\mathcal{W}$, or move towards $\mathcal{B}$ such as a predator $\mathcal{P}$. The latter two cases enforce an appropriate reaction.

The essential requirement for an escape or collision avoidance system is to signal immediately the appearance of a moving object $\mathcal{P}$ and its direction of relative motion. Neither the precise shape nor the exact size of an object matters. The estimate of the direction provides the first information to initiate an appropriate evasive movement.

The objective for a flow-sensory warning device is therefore to reliably detect the motion of one object relative to $\mathcal{B}$ from measurable physical quantities onboard of $\mathcal{B}$ mediated by the ideal incompressible irrotational fluid within a few milliseconds in a robust way. The physical quantities available on-board are the tangential velocity of the fluid on the surface of $\mathcal{B}$ and the translational and angular acceleration obtained from inertia measurements systems, see sec. 5.1.1, which in principle can be used to obtain the current velocity of $\mathcal{B}$ (5.12) up to some error, which slowly increases due to drifts in the integration.

Some of the methods discussed in the literature are already ruled out by the objectives. It is obviously true that changes in the velocity distribution on the surface of $\mathcal{B}$ due to the presence of $\mathcal{P}$ will be detected. A change of the measured velocities $\boldsymbol{v}_i$ averaged over all N sensors

$$\langle \boldsymbol{v} \rangle^N (t) = \sum_{i=1}^{N} g_i \boldsymbol{v}_i(\boldsymbol{p}_i, t) \tag{4.1}$$

placed at positions $\boldsymbol{p}_i$ eventually weighted by some g_i, e.g. to correct the influence of the shape of $\mathcal{B}$ on the external flow field, signals a change in the

boundary conditions of the fluid. To be useful at all, additional, more specific, information is required. The possible contribution of (4.1) as any estimate of the direction of a flow field [147–151] to the certainty of a decision is rather small. Unfortunately, such an estimator is not even capable to differentiate between the approach of an object from one direction and the striding away in the opposite direction. The same arguments hold true for the resulting pressure distribution on $\partial\mathcal{B}$ and the acceleration due to the fluid-mechanical force and torque acting on $\mathcal{B}$ with the additional disadvantage of a smaller range, see sec. 2.12. Thus, using the acceleration of $\mathcal{B}$ as a source of information on an imminent collision, provides more or less the same limited information as an averaged weighted velocity (4.1).

To lead over to what follows in this chapter, a simple thought experiment shall be conducted. Imagine a dipole placed somewhere on the positive x axis moving towards $\mathcal{B}$, which is fixed at $x = 0$, see fig. 2.3 . $\mathcal{B}$ would experience a slightly higher velocity in x direction than in $-x$ direction. The conclusion of $\mathcal{B}$ in an otherwise undisturbed fluid at rest using (4.1) would be that something either approaches from $x > 0$ in $-x$ direction or strived away from $x < 0$ in $-x$ direction. If $\mathcal{B}$ measures the pressure, it could realise that the pressure is slightly lager on the side towards $x > 0$ than at the opposite side towards $x < 0$. The flow field on the surface of $\mathcal{B}$ is obviously asymmetric, and for some reason the absolute value of the flow velocity is larger at $x > 0$. $\mathcal{B}$ could interpret this as an object of finite size at $x > 0$ moving towards it. By comparing the pressure with the velocity $\mathcal{B}$ has obtained better information on the direction of one moving object.

The purpose of the second part of this chapter is to formulate this considerations in a more general way. First, a framework for the fluid-mechanical forces on a moving body, used for the dynamical model of Snookie, see sec. 5.1.2, is developed.

4.2 Fluid forces in terms of the pressure

A body $\mathcal{B}$ shall be totally immersed in a fluid domain $\mathcal{D}$. As in the previous chapter, the fluid in $\mathcal{D}$ shall be ideal, irrotational and incompressible. As introduced in sec. 2.1 the surface normal $\boldsymbol{n}$ on $\partial\mathcal{D}$ points out of the fluid volume into a body. The corresponding surface normal on the boundary $\partial\mathcal{I}$ of a body $\mathcal{I}$ pointing out of a body and into the fluid is denoted by $\boldsymbol{n}' = -\boldsymbol{n}$. The force $\boldsymbol{f}_P^{\mathcal{B}}$ and torque $\boldsymbol{t}_P^{\mathcal{B}}$ on $\mathcal{B}$ exerted by the pressure acting normal onto the surface $\partial\mathcal{B}$ are given by

$$\boldsymbol{f}_P^{\mathcal{B}} = \varrho \oiint_{\partial\mathcal{B}} p\,\boldsymbol{n}\,\mathrm{d}\mathcal{S} \qquad \text{and} \qquad \boldsymbol{t}_P^{\mathcal{B}} = \varrho \oiint_{\partial\mathcal{B}} p\,(\boldsymbol{y}\times\boldsymbol{n})\,\mathrm{d}\mathcal{S}\,,$$

or in $6D$ vector notation

$$\mathfrak{f}_P^{\mathcal{B}} = \varrho \oiint_{\partial\mathcal{B}} p\,\mathfrak{n}\,\mathrm{d}\mathcal{S}\,,$$

see sec. 1.2.2. By virtue of Bernoulli's equation with potential flow on $\mathcal{D}$

$$\mathfrak{f}_P^{\mathcal{B}} = -\varrho \oiint_{\partial\mathcal{B}} \left(\frac{\partial\Phi}{\partial t} + \frac{1}{2}\nabla\Phi\cdot\nabla\Phi\right)\mathfrak{n}\,\mathrm{d}\mathcal{S}\,. \tag{4.2}$$

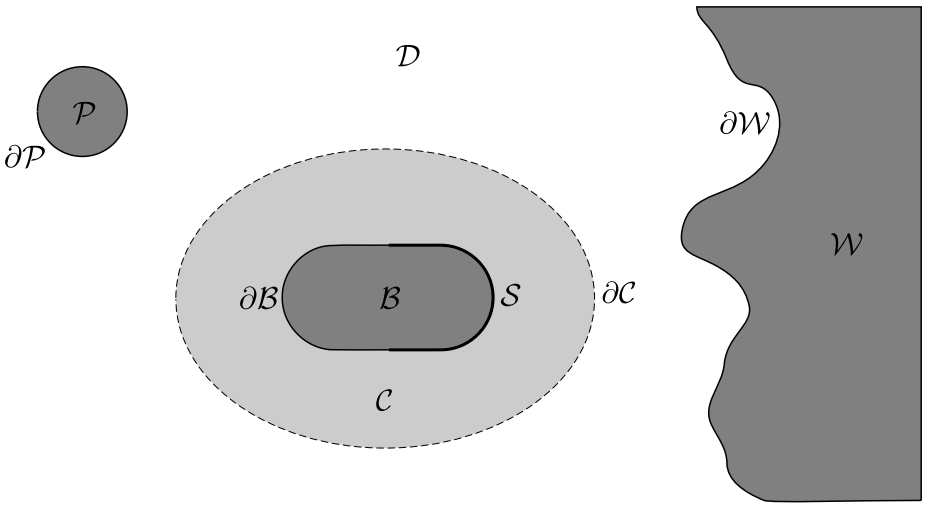

Figure 4.1: Two moving bodies $\mathcal{B}$ and $\mathcal{P}$ totally immersed in an ideal incompressible irrotational fluid in the presence of a solid wall $\mathcal{W}$. An artificial stationary control surface $\partial\mathcal{C}$ is drawn around $\mathcal{B}$ enclosing the control volume $\mathcal{C}$.

The pressure integrals over $\mathcal{B}$ deliver another possible explanation for the existence of the CLS. By a suitable distribution of pores over the surface of a fish it would be possible to sample the pressure differences and to obtain an estimate of the hydrodynamic force acting on the fish by integration over the surface including the fluid-mechanical interaction with the environment. A time-dependent constant in the pressure is not covered by the sampling of the pressure differences, but will drop out of the surface integration over any closed surface. The plausibility of this proposition not only depends on the concrete design of the CLS and the number of pores, but also on the accuracy required and the concrete method [108] used, to carry out the surface integration.

The following considerations will be carried out mostly in the FOR, since this will allow to easily incorporate arbitrary shaped stationary walls. The integral identities

$$\iiint_{\mathcal{D}} \nabla f \,\mathrm{d}\mathcal{D} = \oiint_{\partial\mathcal{D}} f\,\boldsymbol{n}\,\mathrm{d}\mathcal{S} \tag{4.3a}$$

and

$$\iiint_{\mathcal{D}} \boldsymbol{y}\times\nabla f \,\mathrm{d}\mathcal{D} = \oiint_{\partial\mathcal{D}} f\,(\boldsymbol{y}\times\boldsymbol{n})\,\mathrm{d}\mathcal{S} \tag{4.3b}$$

are used to relate ∇f integrated over the domain $\mathcal{D}$ with f integrated over the boundary $\partial\mathcal{D}$. Another important relation between surface and volume integrals is given by Reynolds' transport theorem [152, ch. 3.3]

$$\frac{\mathrm{d}}{\mathrm{d}t}\iiint_{\mathcal{D}(t)} f\,\mathrm{d}\mathcal{V} = \iiint_{\mathcal{D}(t)} \frac{\partial f}{\partial t}\,\mathrm{d}\mathcal{V} + \oiint_{\partial\mathcal{D}(t)} f\,\left(\boldsymbol{u}^B\cdot\boldsymbol{n}\right)\,\mathrm{d}\mathcal{S} \tag{4.4}$$

with $\boldsymbol{u}^B$ the velocity of the boundary $\partial\mathcal{D}(t)$ at the respective point of integration. Application of (4.3) and (4.4) to Φ on the surface $\partial\mathcal{B}$ and to a control

surface $\partial\mathcal{C}$ around $\mathcal{B}$, which is fixed in space, yields the rate of change of momentum

$$\begin{aligned}\varrho\frac{\mathrm{d}}{\mathrm{d}t}\oiint_{\partial\mathcal{C}\cup\partial\mathcal{B}}\Phi\boldsymbol{n}\,\mathrm{d}\mathcal{S} &= \varrho\frac{\mathrm{d}}{\mathrm{d}t}\iiint_{\mathcal{C}}\nabla\Phi\,\mathrm{d}\mathcal{V}\\ &= \varrho\iiint_{\mathcal{C}}\nabla\frac{\partial\Phi}{\partial t}\,\mathrm{d}\mathcal{V}+\varrho\oiint_{\partial\mathcal{C}\cup\partial\mathcal{B}}\nabla\Phi\left(\boldsymbol{u}^{B}\cdot\boldsymbol{n}\right)\,\mathrm{d}\mathcal{S} \qquad (4.5)\\ &= \varrho\oiint_{\partial\mathcal{C}\cup\partial\mathcal{B}}\frac{\partial\Phi}{\partial t}\,\mathrm{d}\mathcal{S}+\varrho\oiint_{\partial\mathcal{B}}\nabla\Phi\frac{\partial\Phi}{\partial n}\,\mathrm{d}\mathcal{S}\end{aligned}$$

on the volume $\mathcal{C}$ enclosed by the control surface $\partial\mathcal{C}$ and by $\partial\mathcal{B}$. For the last step the fact was used that the boundary velocity $\boldsymbol{u}^{B}(\boldsymbol{y},t)$ of the fixed surface $\partial\mathcal{C}$ is zero, and that the normal component of boundary velocity of $\partial\mathcal{B}$ equals $\partial\Phi/\partial n$. The result of (4.5) is unaffected by the choice of $\partial\mathcal{C}$ and thus can be split up into the contributions of each surface. Therefore

$$\varrho\frac{\mathrm{d}}{\mathrm{d}t}\oiint_{\partial\mathcal{B}}\Phi\,\boldsymbol{n}\,\mathrm{d}\mathcal{S}=\varrho\oiint_{\partial\mathcal{B}}\left(\frac{\partial\Phi}{\partial t}\boldsymbol{n}+\nabla\Phi\frac{\partial\Phi}{\partial n}\right)\,\mathrm{d}\mathcal{S}\,. \qquad (4.6)$$

A similar relation can be derived for the rate of change of angular momentum on $\mathcal{C}$ using (4.3) and (4.4),

$$\begin{aligned}\varrho\frac{\mathrm{d}}{\mathrm{d}t}\oiint_{\partial\mathcal{C}\cup\partial\mathcal{B}}\Phi\left(\boldsymbol{y}\times\boldsymbol{n}\right)\,\mathrm{d}\mathcal{S} &= -\varrho\frac{\mathrm{d}}{\mathrm{d}t}\iiint_{\mathcal{C}}\boldsymbol{\nabla}\times\left(\Phi\boldsymbol{y}\right)\,\mathrm{d}\mathcal{V} \qquad (4.7)\\ &= -\varrho\iiint_{\mathcal{C}}\boldsymbol{\nabla}\times\left(\frac{\partial\Phi}{\partial t}\boldsymbol{y}\right)\,\mathrm{d}\mathcal{V}-\varrho\oiint_{\partial\mathcal{C}\cup\partial\mathcal{B}}\boldsymbol{\nabla}\times\left(\frac{\partial\Phi}{\partial t}\boldsymbol{y}\right)\left(\boldsymbol{u}_{B}\cdot\boldsymbol{n}\right)\,\mathrm{d}\mathcal{S}\\ &= \varrho\oiint_{\partial\mathcal{C}\cup\partial\mathcal{B}}\frac{\partial\Phi}{\partial t}\left(\boldsymbol{y}\times\boldsymbol{n}\right)\,\mathrm{d}\mathcal{S}+\varrho\oiint_{\partial\mathcal{B}}\boldsymbol{y}\times\nabla\Phi\frac{\partial\Phi}{\partial n}\mathrm{d}\mathcal{S}\,.\end{aligned}$$

By the same arguments used to arrive at (4.6),

$$\varrho\frac{\mathrm{d}}{\mathrm{d}t}\oiint_{\partial\mathcal{B}}\Phi\left(\boldsymbol{y}\times\boldsymbol{n}\right)\,\mathrm{d}\mathcal{S}=\varrho\oiint_{\partial\mathcal{B}}\boldsymbol{y}\times\left(\frac{\partial\Phi}{\partial t}\boldsymbol{n}+\nabla\Phi\frac{\partial\Phi}{\partial n}\right)\,\mathrm{d}\mathcal{S}\,. \qquad (4.8)$$

With (4.6) and (4.8) the pressure force and torque (4.2) on $\mathcal{B}$ become

$$\begin{aligned}\boldsymbol{f}_{P}^{\mathcal{B}} &= -\varrho\frac{\mathrm{d}}{\mathrm{d}t}\oiint_{\partial\mathcal{B}}\Phi\,\boldsymbol{n}\,\mathrm{d}\mathcal{S}+\varrho\oiint_{\partial\mathcal{B}}\left(\nabla\Phi\frac{\partial\Phi}{\partial n}-\frac{1}{2}\nabla\Phi\cdot\nabla\Phi\,\boldsymbol{n}\right)\,\mathrm{d}\mathcal{S}\,, \qquad (4.9)\\ \boldsymbol{t}_{P}^{\mathcal{B}} &= -\varrho\frac{\mathrm{d}}{\mathrm{d}t}\oiint_{\partial\mathcal{B}}\Phi\left(\boldsymbol{y}\times\boldsymbol{n}\right)\,\mathrm{d}\mathcal{S}+\varrho\oiint_{\partial\mathcal{B}}\boldsymbol{y}\times\left(\nabla\Phi\frac{\partial\Phi}{\partial n}-\frac{1}{2}\nabla\Phi\cdot\nabla\Phi\,\boldsymbol{n}\right)\,\mathrm{d}\mathcal{S}\,.\end{aligned}$$

Furthermore, the relation [152, p. 143]

$$\oiint_{\partial\mathcal{D}}\left[\nabla\Phi\frac{\partial\Phi}{\partial n}-\frac{1}{2}\left(\nabla\Phi\cdot\nabla\Phi\right)\boldsymbol{n}\right]\,\mathrm{d}\mathcal{S}=0 \qquad (4.10)$$

holds, which is proven by application of the integral identity (4.3) and the divergence theorem (2.14) to (4.10),

$$\begin{aligned}&\oiint_{\partial\mathcal{D}}\left[\partial_{j}\Phi n_{j}\,\partial_{i}\Phi-\frac{1}{2}\partial_{j}\Phi\,\partial_{j}\Phi\,n_{i}\right]\,\mathrm{d}\mathcal{S}=\\ &\quad=\iiint_{\mathcal{D}}\left[\partial_{j}\left(\partial_{i}\Phi\,\partial_{j}\Phi\right)-\frac{1}{2}\partial_{i}\left(\partial_{j}\Phi\,\partial_{j}\Phi\right)\right]\,\mathrm{d}\mathcal{V}=\\ &\quad=\iiint_{\mathcal{D}}\left[\partial_{i}\Phi\,\partial_{j}\partial_{j}\Phi+\partial_{i}\partial_{j}\Phi\,\partial_{j}\Phi-\partial_{j}\Phi\,\partial_{i}\partial_{j}\Phi\right]\,\mathrm{d}\mathcal{V}=0\,,\end{aligned}$$

whereby ∂_i denotes the partial derivative $\partial/\partial x_i$ and doubly appearing indices are to be added up. Analogous calculations are used to show

$$\oiint_{\partial\mathcal{D}} \boldsymbol{y} \times \left[\nabla\Phi \frac{\partial\Phi}{\partial n} - \frac{1}{2}\left(\nabla\Phi \cdot \nabla\Phi\right)\boldsymbol{n}\right] \mathrm{d}\mathcal{S} = 0\,. \tag{4.11}$$

Equations (4.2), (4.9), (4.10), and (4.11) will proof their usefulness later in this chapter. They relate fluid forces exerted on a body with the flow field velocities $\nabla\Phi$ on the surface of the body measured by the FSS.

4.3 Fluid forces in terms of added masses

Under certain assumptions, the pressure forces acting on a body can be expressed in terms of additional masses and the acceleration of an object. D'Alambert's paradox states that no fluid-mechanical forces act on a body steadily moving in an ideal irrotational incompressible and otherwise unbounded fluid. However, as it accelerates, the body not only has to accelerate it's own body mass, but also the mass of the displaced fluid, the so called *added masses*. The additional inertia forces of the fluid are mediated through the pressure on the surface of $\mathcal{B}$. Simple equations of motion will be obtained for a body moving in unbounded potential flow. To be able to study the fluid-mechanical forces of potential flow in the presence of further objects, the added masses are treated in a more complex environment consisting of an arbitrarily shaped smooth solid stationary wall $\mathcal{W}$, a moving rigid object of arbitrary smooth shape $\mathcal{P}$, and the moving body $\mathcal{B}$ equipped with a FSS. The fluid domain $\mathcal{D}$ shall be bounded by $\partial\mathcal{D} = \partial\mathcal{B} \cup \partial\mathcal{P} \cup \partial\mathcal{W}$ consisting of the disjoint surfaces $\partial\mathcal{B}$, $\partial\mathcal{P}$, $\partial\mathcal{W}$ of the rigid bodies $\mathcal{B}$, $\mathcal{P}$, $\mathcal{W}$. The convention of ch. 2 that $\mathcal{W}$ is fixed in the FOR is chosen. The flow potential Φ and the flow velocity $\nabla\Phi$ shall vanish at infinity, if $\mathcal{D}$ is not fully bounded by $\partial\mathcal{W}$. The bodies $\mathcal{B}$ and $\mathcal{P}$ are allowed to move in an arbitrary fashion in the presence of $\mathcal{W}$. The motion of $\mathcal{B}$ and $\mathcal{P}$ and the motion of the fluid in $\mathcal{D}$, which is governed by the motion of its boundaries, is fully described by the 6D generalised coordinates $\mathbf{q}^{\mathcal{B}} = (\boldsymbol{q}^{\mathcal{B}}, \boldsymbol{\phi}^{\mathcal{B}})^{\mathrm{T}}$ and $\mathbf{q}^{\mathcal{P}} = (\boldsymbol{q}^{\mathcal{P}}, \boldsymbol{\phi}^{\mathcal{P}})^{\mathrm{T}}$, and the 6D velocities $\boldsymbol{u}^{\mathcal{B}} = (\boldsymbol{u}^{\mathcal{B}}, \boldsymbol{\omega}^{\mathcal{B}})^{\mathrm{T}}$ and $\mathbf{u}^{\mathcal{P}} = (\boldsymbol{q}^{\mathcal{P}}, \boldsymbol{\omega}^{\mathcal{P}})^{\mathrm{T}}$. The generalised coordinates consist of the 3D vectors $\boldsymbol{q}^{\mathcal{B}} = (x^{\mathcal{B}}, y^{\mathcal{B}}, z^{\mathcal{B}})^{\mathrm{T}}$ and $\boldsymbol{q}^{\mathcal{P}} = (x^{\mathcal{P}}, y^{\mathcal{P}}, z^{\mathcal{P}})^{\mathrm{T}}$ denoting the position of the origins of the BFSs of $\mathcal{B}$ and $\mathcal{P}$ in the FOR. The 3D orientation vectors $\boldsymbol{\phi}^{\mathcal{B}} = (\phi^{\mathcal{B}}, \theta^{\mathcal{B}}, \psi^{\mathcal{B}})^{\mathrm{T}}$ and $\boldsymbol{\phi}^{\mathcal{P}} = (\phi^{\mathcal{P}}, \theta^{\mathcal{P}}, \psi^{\mathcal{P}})^{\mathrm{T}}$ define the rotation of the BFSs of $\mathcal{B}$ and $\mathcal{P}$ relative to the FOR according to the definition of the modified Euler angles in sec. 1.2.2. The translational velocity $\boldsymbol{u}$ in the 6D velocity vectors is a generalised velocity in the sense that $\boldsymbol{u} = \mathrm{d}/\mathrm{d}t\, \boldsymbol{q}$. The angular velocity is, however, not. It is a quasi-velocity [98, p. 157], since $\boldsymbol{\omega} = \mathcal{R}^{\mathrm{T}}(\Phi)\mathcal{W}(\boldsymbol{\phi})\mathrm{d}/\mathrm{d}t\, \boldsymbol{\phi}$.

For simplicity, the same symbols $\mathcal{B}$, $\mathcal{P}$ and $\mathcal{W}$ are used for both, the set of points belonging to the respective bodies, and the BFSs prescribed in the bodies. The position and orientation coordinates of $\mathcal{B}$ and $\mathcal{P}$ are functions of time, and so are the generalised coordinates $\mathbf{q}^{\mathcal{B}}$ and $\mathbf{q}^{\mathcal{P}}$ and the velocities $\mathbf{u}^{\mathcal{B}}$ and $\mathbf{u}^{\mathcal{P}}$.

4.3.1 Added masses of rigid body motion

The kinetic energy stored in the flow field $\nabla\Phi$ in $\mathcal{D}$

$$\mathcal{T} = \frac{\varrho}{2} \iiint_{\mathcal{D}(t)} |\nabla\Phi(\boldsymbol{x})|^2 \,\mathrm{d}\mathcal{V}$$

can be expressed by application of Green's first identity (2.15) as an integral over all closed surfaces $\partial\mathcal{D}(t)$ of all boundaries

$$\mathcal{T} = \frac{\varrho}{2} \oiint_{\partial\mathcal{D}(t)} \Phi \frac{\partial\Phi}{\partial n} \, \mathrm{d}\mathcal{S} \,, \tag{4.12}$$

whereby $\mathcal{D}(t)$ may extend to infinity. Recalling sec. 2.6, the flow potential of moving rigid bodies in the presence of a wall $\mathcal{I} \in \{\mathcal{B}, \mathcal{P}, \mathcal{W}\}$ can be decomposed into

$$\Phi(\boldsymbol{x}, t) = \sum_{\mathcal{I}} \sum_{i=1}^{6} \mathfrak{u}_i^{\mathcal{I}}(t) \varphi_i^{\mathcal{I}}(\boldsymbol{x}, t) \tag{4.13}$$

and the boundary conditions to be fulfilled are

$$\left.\frac{\partial\varphi_i^{\mathcal{I}}(\boldsymbol{x}, t)}{\partial n}\right|_{\boldsymbol{x}\in\partial\mathcal{I}} = \mathfrak{n}_i \qquad \text{and} \qquad \left.\frac{\partial\varphi_i^{\mathcal{I}}(\boldsymbol{x}, t)}{\partial n}\right|_{\boldsymbol{x}\in\partial\mathcal{J}\neq\partial\mathcal{I}} = 0 \tag{4.14}$$

with $\partial\mathcal{J}, \partial\mathcal{I} \in \{\partial\mathcal{B} \cup \partial\mathcal{P} \cup \partial\mathcal{W}\}$. Substitution of (4.13) into (4.12) and exploiting (4.14) leads to a sum of surface integrals

$$\mathcal{T} = \frac{\varrho}{2} \sum_{\mathcal{I},\mathcal{J}} \mathfrak{u}_i^{\mathcal{I}}(t) \mathfrak{u}_j^{\mathcal{J}}(t) \oiint_{\partial\mathcal{J}(t)} \varphi_i^{\mathcal{I}}(\boldsymbol{x}, t) \, \frac{\partial\varphi_j^{\mathcal{J}}(\boldsymbol{x}, t)}{\partial n} \, \mathrm{d}\mathcal{S} \tag{4.15}$$

for the kinetic energy of the fluid induced by the motion of the rigid bodies with $\mathcal{I}, \mathcal{J} \in \{\mathcal{B}, \mathcal{P}\}$. The contribution of the wall vanishes since $\partial\Phi/\partial n = 0$ on $\partial\mathcal{W}$.

The surface integrals can be evaluated in the respective BFSs by choosing $\boldsymbol{x}(t) = \boldsymbol{X} + \boldsymbol{p}^{\mathcal{I}}(t)$ for a point on $\partial\mathcal{I}$. The surface of integration $\partial\mathcal{I}$ of the rigid body $\mathcal{I}$ is fixed in time in the BFS. For two bodies $\mathcal{B}$ and $\mathcal{P}$ moving in the presence of a stationary wall $\mathcal{W}$ four 6×6 matrices in the respective BFS coordinates

$$\begin{aligned}
\mathcal{A}_{ij}(t) &= \varrho \oiint_{\partial\mathcal{B}} \varphi_i^{\mathcal{B}}\big(\boldsymbol{X} + \boldsymbol{q}^{\mathcal{B}}(t), t\big) \, \frac{\partial\varphi_j^{\mathcal{B}}\big(\boldsymbol{X} + \boldsymbol{q}^{\mathcal{B}}(t), t\big)}{\partial N(\boldsymbol{X})} \, \mathrm{d}\mathcal{S}(\boldsymbol{X}) \,, \\
\mathcal{B}_{ij}(t) &= \varrho \oiint_{\partial\mathcal{B}} \varphi_i^{\mathcal{P}}\big(\boldsymbol{X} + \boldsymbol{q}^{\mathcal{B}}(t), t\big) \, \frac{\partial\varphi_j^{\mathcal{B}}\big(\boldsymbol{X} + \boldsymbol{q}^{\mathcal{B}}(t), t\big)}{\partial N(\boldsymbol{X})} \, \mathrm{d}\mathcal{S}(\boldsymbol{X}) \,, \\
\mathcal{C}_{ij}(t) &= \varrho \oiint_{\partial\mathcal{P}} \varphi_i^{\mathcal{B}}\big(\boldsymbol{X} + \boldsymbol{q}^{\mathcal{P}}(t), t\big) \, \frac{\partial\varphi_j^{\mathcal{P}}\big(\boldsymbol{X} + \boldsymbol{q}^{\mathcal{P}}(t), t\big)}{\partial N(\boldsymbol{X})} \, \mathrm{d}\mathcal{S}(\boldsymbol{X}) \,, \\
\mathcal{D}_{ij}(t) &= \varrho \oiint_{\partial\mathcal{P}} \varphi_i^{\mathcal{P}}\big(\boldsymbol{X} + \boldsymbol{q}^{\mathcal{P}}(t), t\big) \, \frac{\partial\varphi_j^{\mathcal{P}}\big(\boldsymbol{X} + \boldsymbol{q}^{\mathcal{P}}(t), t\big)}{\partial N(\boldsymbol{X})} \, \mathrm{d}\mathcal{S}(\boldsymbol{X})
\end{aligned} \tag{4.16}$$

are obtained. The transformation back to coordinates of the FOR is given by

$$\begin{aligned}
\mathcal{a}(t) &= \mathcal{R}^{\mathrm{T}}(\boldsymbol{\phi}^{\mathcal{B}}) \mathcal{A}(t) \, \mathcal{R}(\boldsymbol{\phi}^{\mathcal{B}}) \,, \\
\mathcal{b}(t) &= \mathcal{R}^{\mathrm{T}}(\boldsymbol{\phi}^{\mathcal{B}}) \mathcal{B}(t) \, \mathcal{R}(\boldsymbol{\phi}^{\mathcal{B}}) \,, \\
\mathcal{c}(t) &= \mathcal{R}^{\mathrm{T}}(\boldsymbol{\phi}^{\mathcal{P}}) \mathcal{C}(t) \, \mathcal{R}(\boldsymbol{\phi}^{\mathcal{P}}) \,, \\
\mathcal{d}(t) &= \mathcal{R}^{\mathrm{T}}(\boldsymbol{\phi}^{\mathcal{P}}) \mathcal{D}(t) \, \mathcal{R}(\boldsymbol{\phi}^{\mathcal{P}}) \,.
\end{aligned} \tag{4.17}$$

The decomposition of the velocity potential by (4.13) is possible, since the flow potential is a linear function of the velocities of the rigid bodies. The potentials

$\varphi_i^{\mathcal{B}}$ and $\varphi_i^{\mathcal{P}}$ are solely determined by the location and orientation $\mathfrak{q}^{\mathcal{B}}(t)$ and $\mathfrak{q}^{\mathcal{P}}(t)$ of the rigid bodies, which are functions of time. It is therefore legitimate to write $\varphi(\boldsymbol{x}, \mathfrak{q}^{\mathcal{B}}(t), \mathfrak{q}^{\mathcal{P}}(t))$. The same holds true for the added masses, which can be written as $a(\mathfrak{q}^{\mathcal{B}}(t), \mathfrak{q}^{\mathcal{P}}(t))$, $b(\mathfrak{q}^{\mathcal{B}}(t), \mathfrak{q}^{\mathcal{P}}(t))$, $c(\mathfrak{q}^{\mathcal{B}}(t), \mathfrak{q}^{\mathcal{P}}(t))$, and $d(\mathfrak{q}^{\mathcal{B}}(t), \mathfrak{q}^{\mathcal{P}}(t))$. In the formulation of the kinetic energy of the fluid,

$$\mathcal{T} = \frac{1}{2}\left(a_{ij}\mathfrak{u}_i^{\mathcal{B}}\mathfrak{u}_j^{\mathcal{B}} + b_{ij}\mathfrak{u}_i^{\mathcal{P}}\mathfrak{u}_j^{\mathcal{B}} + c_{ij}\mathfrak{u}_i^{\mathcal{B}}\mathfrak{u}_j^{\mathcal{P}} + d_{ij}\mathfrak{u}_i^{\mathcal{P}}\mathfrak{u}_j^{\mathcal{P}}\right), \tag{4.18}$$

these 6×6 matrices fulfil the role of masses, which is why they are called *added masses* [153], or sometimes also *virtual masses*. The arguments of the velocities and the added masses have been dropped for brevity. In addition to the physical mass of a body, additional inertia appear due to the motion of the body in the fluid. As already mentioned, the body displaces a certain amount of fluid, which is related to its size and shape, and eventually also to the size and shape of further boundaries in its surroundings. During acceleration, not only its own body mass, but also the displaced fluid streaming around the body must be accelerated, resulting in additional inertia. Fluid must also be accelerated at motion relative to another boundary, resulting in a change of the added masses. The added masses represent the additional inertia of rigid body motion in an ideal incompressible and irrotational fluid. Application of Green's first identity (2.15) to (4.17) shows that the added-mass matrices $\mathcal{A}$ and $\mathcal{D}$ are symmetric, i.e. $\mathcal{A}_{ij} = \mathcal{A}_{ji}$ and $\mathcal{D}_{ij} = \mathcal{D}_{ji}$. Furthermore, $\mathcal{B}_{ij} = \mathcal{C}_{ij}$ which can be also shown by application of Green's first identity (2.15)

$$\begin{aligned}\mathcal{B}_{ij} = \varrho \oiint_{\partial\mathcal{B}} \varphi_i^{\mathcal{P}} \frac{\partial \varphi_j^{\mathcal{B}}}{\partial n}\,\mathrm{d}\mathcal{S} &= \varrho \iint_{\partial\mathcal{D}} \varphi_i^{\mathcal{P}} \frac{\partial \varphi_j^{\mathcal{B}}}{\partial n}\,\mathrm{d}\mathcal{S} \\ &= \varrho \iiint_{\mathcal{D}} \nabla\varphi_i^{\mathcal{P}} \cdot \nabla\varphi_j^{\mathcal{B}}\,\mathrm{d}V = \mathcal{C}_{ji}\,.\end{aligned}$$

The added mass matrices $\mathcal{B}$ and $\mathcal{C}$ are called the added masses of interaction [154, p. 114 ff.] of $\mathcal{B}$ and $\mathcal{P}$, since they depend on the position and orientation of both moving rigid bodies $\mathcal{B}$ and $\mathcal{P}$.

So far, the formulation of fluid-mechanical interaction in terms of added masses does not provide any advantage over the conventional formulation in terms of a pressure integral, since the potential must be solved at any instant of time, and a surface integral must be computed to obtain the added masses. The presence of purely stationary objects like the wall $\mathcal{W}$ enters the added masses only indirectly via the boundary condition $\partial\varphi_i^{\mathcal{I}}/\partial n|_{\partial\mathcal{W}} = 0$ and directly via the dependence of the added masses on the positions $\mathfrak{q}^{\mathcal{B}}$ and $\mathfrak{q}^{\mathcal{P}}$ of $\mathcal{B}$ and $\mathcal{P}$. The kinetic energy of the fluid for $\mathcal{B}$ moving in presence of a stationary wall $\mathcal{W}$ only is given by

$$\mathcal{T} = \frac{1}{2}\mathfrak{u}_i^{\mathcal{B}}(t)a_{ij}(\mathfrak{q}^{\mathcal{B}}(t))\mathfrak{u}_j^{\mathcal{B}}(t)\,.$$

In the special case of $\mathcal{B}$ moving through an unbounded ideal incompressible irrotational fluid at rest without any further boundaries than $\partial\mathcal{B}$, the added masses of $\mathcal{B}$, now denoted as Λ in the BFS of $\mathcal{B}$, become independent of $\boldsymbol{q}^{\mathcal{B}}$, and are constant in time. The fluid-mechanical forces of free motion in an ideal fluid are fully accounted for by one-time computation of the 6×6 added mass matrix Λ, and the kinetic energy of the fluid is solely determined by the velocity and

the shape of $\mathcal{B}$, which in body-fixed coordinates becomes

$$\mathcal{T} = \frac{1}{2}\mathfrak{U}_i^{\mathcal{B}}(t)\Lambda_{ij}\mathfrak{U}_j^{\mathcal{B}}(t)\,. \tag{4.19}$$

The contribution of the fluid to the dynamics of a body moving in unbounded potential flow is fully described by increased inertia.

4.3.2 Transformation of the added mass matrix

For the sake of simplicity, the added mass matrix Λ of free motion of one body is usually computed with respect to the point of maximum symmetry in body fixed coordinates. It is then often necessary to adapt Λ to a given geometry, e.g. shift the axis of rotation, since other constraints such as the choice of the origin of the BFS force the body to rotate around a different point than that assumed for the computation of the added masses.

The idea behind the derivation of a transformation formula for the added masses is that the kinetic energy of the flow field around the body must be invariant under a change of the coordinate system in which the added masses are computed in. All summands in the expression for the kinetic energy of the fluid are quadratic forms of the velocities of the rigid body. The transformation formulas for the added masses are determined by expressing the kinetic energy of the flow field in a new coordinate system and collect all terms of a certain product $\mathfrak{U}_i\mathfrak{U}_j$. The coefficients represent the added masses in the new system.

In the most general case the new system $\{\boldsymbol{e}_X, \boldsymbol{e}_Y, \boldsymbol{e}_Z\}$ is shifted by the vector $\boldsymbol{\xi}$, translates with velocity $\boldsymbol{u}$ relative to the original system $\{\boldsymbol{e}_x, \boldsymbol{e}_y, \boldsymbol{e}_z\}$, and rotates with the original system about the origin of the original system with angular velocity $\boldsymbol{\omega}$. Due to the analogy to the transformation between a FOR and a BFS, the same notation as in sec. 1.2.2 is used. The added masses shall be known in the system $\{\boldsymbol{e}_x, \boldsymbol{e}_y, \boldsymbol{e}_z\}$, and are supposed to be determined in $\{\boldsymbol{e}_X, \boldsymbol{e}_Y, \boldsymbol{e}_Z\}$. The velocity expressed in coordinates of the new system is given by $\boldsymbol{U} = \mathcal{R}(\boldsymbol{\phi})(\boldsymbol{u} + \boldsymbol{\omega} \times \boldsymbol{\xi})$ with rotation matrix $\mathcal{R}$ as defined in (1.8). Again, 6D vectors are used to express the velocity of the new system in coordinates of the original $\mathfrak{u} = (\boldsymbol{u}, \boldsymbol{\omega})$ and the new $\mathfrak{U} = (\boldsymbol{U}, \boldsymbol{\Omega})$ system. Written component-wise, the transformation of the velocity and angular velocity is given by

$$\mathfrak{u}_{i=1..3} = \sum_{m=1}^{3} \mathfrak{U}_m R_{mi} - \varepsilon_{ijk}\omega_j\xi_k \quad \text{and} \quad \mathfrak{u}_{3+i} = \sum_{m=1}^{3} \mathfrak{U}_{3+m} R_{mi} \text{ for } i = 1, 2, 3 \tag{4.20}$$

with the Levi-Civita symbol ε_{ijk}, and the transformation matrix $R_{mn} = \boldsymbol{e}_m \cdot \boldsymbol{e}_n$, where $m \in \{x, y, z\}$ and $n \in \{X, Y, Z\}$.

Substitution of (4.20) in (4.19) leads to the coordinate transformation rules for added masses [154, p. 5 ff.], consisting of the added inertia for $m, n = 1, 2, 3$,

$$\Lambda_{mn} = \sum_{i=1}^{3}\sum_{j=1}^{3} \lambda_{ij}\mathcal{R}_{mi}\mathcal{R}_{nj}\,, \tag{4.21a}$$

the coupling between translational and angular motion for $m = 1, 2, 3$ and $n = 4, 5, 6$ or $m = 4, 5, 6$ and $n = 1, 2, 3$,

$$\Lambda_{mn} = \sum_{i=1}^{3}\sum_{j=4}^{6} \lambda_{ij}\mathcal{R}_{mi}\mathcal{R}_{nj} + \sum_{i=1}^{3}\sum_{j=1}^{3} \lambda_{ij}\mathcal{R}_{mi}\left(\mathcal{R}_{n,j+2}\xi_{j+1} - \mathcal{R}_{n,j+1}\xi_{j+2}\right)\,, \tag{4.21b}$$

and the added inertia for rotational motion with $m = 4, 5, 6$ and $n = 4, 5, 6$,

$$\begin{aligned}\Lambda_{mn} = &\sum_{i=4}^{6}\sum_{j=4}^{6}\lambda_{ij}\mathcal{R}_{mi}\mathcal{R}_{nj} \; + \\ &\sum_{i=1}^{3}\sum_{j=4}^{6}\lambda_{ij}\mathcal{R}_{mj}\left(\mathcal{R}_{n,i+2}\xi_{i+1} - \mathcal{R}_{n,i+1}\xi_{i+2}\right) \; + \\ &\sum_{i=1}^{3}\sum_{j=4}^{6}\lambda_{ij}\mathcal{R}_{nj}\left(\mathcal{R}_{m,i+2}\xi_{i+1} - \mathcal{R}_{m,i+1}\xi_{i+2}\right) \; + \\ &\sum_{i=1}^{3}\sum_{j=1}^{3}\lambda_{ij}\left(\mathcal{R}_{m,i+2}\xi_{i+1} - \mathcal{R}_{m,i+1}\xi_{i+2}\right)\left(\mathcal{R}_{n,j+2}\xi_{j+1} - \mathcal{R}_{n,j+1}\xi_{j+2}\right) ,\end{aligned} \tag{4.21c}$$

where

$$\mathcal{R}_{ij} = \mathcal{R}_{i,j+3}, \quad \mathcal{R}_{ij} = \mathcal{R}_{i+3,j} \quad \text{and} \quad \xi_i = \xi_{i+3} \, . \tag{4.21d}$$

In case the new coordinate system is just shifted against the original frame by the vector $\boldsymbol{\xi}$, and not rotated, the transformation formulas significantly simplify to the added inertia for $m, n = 1, 2, 3$,

$$\Lambda_{mn} = \lambda_{mn} \, , \tag{4.22a}$$

the coupling between translational and angular motion for $m = 1, 2, 3$ and $n = 4, 5, 6$ or $m = 4, 5, 6$ and $n = 1, 2, 3$,

$$\begin{aligned}
\Lambda_{14} &= \lambda_{14} + \lambda_{12}\xi_3 - \lambda_{13}\xi_2 \, , & \Lambda_{15} &= \lambda_{15} + \lambda_{13}\xi_1 - \lambda_{11}\xi_3 \, , \\
\Lambda_{24} &= \lambda_{24} + \lambda_{22}\xi_3 - \lambda_{23}\xi_2 \, , & \Lambda_{25} &= \lambda_{25} + \lambda_{23}\xi_1 - \lambda_{21}\xi_3 \, , \\
\Lambda_{34} &= \lambda_{34} + \lambda_{32}\xi_3 - \lambda_{33}\xi_2 \, , & \Lambda_{35} &= \lambda_{35} + \lambda_{33}\xi_1 - \lambda_{31}\xi_3 \, , \\
\Lambda_{16} &= \lambda_{16} + \lambda_{11}\xi_2 - \lambda_{12}\xi_1 \, , & \Lambda_{26} &= \lambda_{26} + \lambda_{21}\xi_2 - \lambda_{22}\xi_1 \, , \\
\Lambda_{36} &= \lambda_{36} + \lambda_{31}\xi_2 - \lambda_{32}\xi_1 \, ,
\end{aligned} \tag{4.22b}$$

and the rotational motion $m = 4, 5, 6$ and $n = 4, 5, 6$,

$$\begin{aligned}
\Lambda_{44} &= \lambda_{44} + 2\lambda_{24}\xi_3 - 2\lambda_{34}\xi_2 + \lambda_{22}\xi_3^2 - 2\lambda_{23}\xi_3\xi_2 + \lambda_{33}\xi_2^2 \, , \\
\Lambda_{45} &= \lambda_{45} + \lambda_{43}\xi_1 - \lambda_{41}\xi_3 + \lambda_{25}\xi_3 - \lambda_{35}\xi_2 + \lambda_{23}\xi_1\xi_3 - \lambda_{12}\xi_3^2 - \lambda_{33}\xi_1\xi_2 + \lambda_{13}\xi_2\xi_3 \, , \\
\Lambda_{46} &= \lambda_{46} + \lambda_{14}\xi_2 - \lambda_{24}\xi_1 + \lambda_{26}\xi_3 - \lambda_{36}\xi_2 + \lambda_{12}\xi_2\xi_3 - \lambda_{22}\xi_1\xi_3 - \lambda_{13}\xi_2^2 + \lambda_{23}\xi_1\xi_2 \, , \\
\Lambda_{55} &= \lambda_{55} + 2\lambda_{35}\xi_1 - 2\lambda_{15}\xi_3 + \lambda_{33}\xi_1^2 - 2\lambda_{13}\xi_1\xi_3 + \lambda_{11}\xi_3^2 \, , \\
\Lambda_{56} &= \lambda_{56} + \lambda_{15}\xi_2 - \lambda_{25}\xi_1 + \lambda_{36}\xi_2 - \lambda_{16}\xi_3 + \lambda_{13}\xi_1\xi_2 - \lambda_{23}\xi_1^2 - \lambda_{11}\xi_2\xi_3 + \lambda_{12}\xi_1\xi_3 \, , \\
\Lambda_{66} &= \lambda_{66} + 2\lambda_{16}\xi_2 - 2\lambda_{26}\xi_1 + \lambda_{11}\xi_2^2 - 2\lambda_{12}\xi_1\xi_2 + \lambda_{22}\xi_1^2 \, .
\end{aligned} \tag{4.22c}$$

The transformation of the added masses turns out to be quite simple, if the coordinate transformation consists of just a shift $\boldsymbol{\xi}$, i.e. a shift of the axis of rotation by $-\boldsymbol{\xi}$, and if the added mass matrix to be transformed has diagonal shape. This means that the original mass matrix is computed about the centre of the fluid-mechanical forces acting on the body and the axes of the BFS coincide with the principal axes of the moment of inertia submatrix of the added mass tensor. The transformation directive the becomes

$$\Lambda_{mn} = \lambda_{mn} \qquad \text{for} \qquad m, n \in \{1, 2, 3\} \, , \tag{4.23a}$$

$$\begin{aligned} \Lambda_{15} &= -\lambda_{11}\xi_3\,, & \Lambda_{24} &= \lambda_{22}\xi_3\,, & \Lambda_{34} &= -\lambda_{33}\xi_2\,, \\ \Lambda_{35} &= \lambda_{33}\xi_1\,, & \Lambda_{16} &= \lambda_{11}\xi_2\,, & \Lambda_{26} &= \lambda_{22}\xi_1 \end{aligned} \tag{4.23b}$$

for $m \in \{1,2,3\}$ and $n \in \{4,5,6\}$ or $m \in \{4,5,6\}$ and $n \in \{1,2,3\}$, and

$$\begin{aligned} \Lambda_{44} &= \lambda_{44} + \lambda_{22}\xi_3^2 + \lambda_{33}\xi_2^2\,, & \Lambda_{45} &= -\lambda_{33}\xi_1\xi_2\,, \\ \Lambda_{46} &= -\lambda_{22}\xi_1\xi_3\,, & \Lambda_{55} &= \lambda_{55} + \lambda_{33}\xi_1^2 + \lambda_{11}\xi_3^2\,, \\ \Lambda_{56} &= -\lambda_{11}\xi_2\xi_3\,, & \Lambda_{66} &= \lambda_{66} + \lambda_{11}\xi_2^2 + \lambda_{22}\xi_1^2 \end{aligned} \tag{4.23c}$$

for $m \in \{4,5,6\}$ and $n \in \{4,5,6\}$. Any entry not covered by the symmetry of Λ and thus not listed vanishes. A careful comparison of the transformed added masses with the inertia of a rigid body (1.12) shows that the added masses behave like body masses in every way.

In sec. 5.1.2 the *total inertia* of *Snookie* is composed from the body mass and inertia and the added masses of independent geometrical primitives, resembling the fluid-mechanically active parts of the robot, and using these transformation directives to obtain the added masses.

4.3.3 Lagrangian formulation of the fluid forces in potential flow

It was shown in sec. 4.3.1 that the kinetic energy of the fluid due to the motion of two rigid bodies $\mathcal{B}$ and $\mathcal{P}$ in the presence of a stationary wall $\mathcal{W}$ can be easily expressed in terms of added masses (4.18), and the translational and angular velocities $\mathfrak{u}^{\mathcal{B}}$ and $\mathfrak{u}^{\mathcal{P}}$ of $\mathcal{B}$ and $\mathcal{P}$,

$$\mathcal{T} = \frac{1}{2}\left(a_{ij}\mathfrak{u}_i^{\mathcal{B}}\mathfrak{u}_j^{\mathcal{B}} + b_{ij}\mathfrak{u}_i^{\mathcal{P}}\mathfrak{u}_j^{\mathcal{B}} + c_{ij}\mathfrak{u}_i^{\mathcal{B}}\mathfrak{u}_j^{\mathcal{P}} + d_{ij}\mathfrak{u}_i^{\mathcal{P}}\mathfrak{u}_j^{\mathcal{P}}\right)\,.$$

As already mentioned, the angular velocities $\boldsymbol{\omega}$ are sometimes called *quasi-velocities* [98, p.156], since the respective generalised coordinate cannot be obtained by integration over time such as the translational velocities $\boldsymbol{u} = \mathrm{d}\boldsymbol{q}/\mathrm{d}t$. They are obtained from the respective generalised coordinates $\boldsymbol{\phi}$ by

$$\boldsymbol{\omega} = \mathcal{R}^T(\boldsymbol{\phi})\mathcal{W}(\boldsymbol{\phi})\dot{\boldsymbol{\phi}}\,, \tag{4.24}$$

see (1.9). No external potential for a conservative force on $\mathcal{B}$ and $\mathcal{P}$ exists, since the bodies are supposed to be buoyancy neutral. No dissipative drag forces occur in an ideal incompressible fluid. No vorticity may exist and thus no velocity dependent lifting forces act on a body perpendicular to the incident flow. Under this conditions, the total energy of the fluid is given by the kinetic energy of the fluid, which in turn is a function of the position and the velocity of $\mathcal{B}$ and $\mathcal{P}$. The Euler-Lagrange equations deliver the forces $\mathfrak{f}^{\mathcal{B}}$ and $\mathfrak{f}^{\mathcal{P}}$ exerted by the bodies $\mathcal{B}$ and $\mathcal{P}$ onto the fluid resulting from their acceleration, velocity, and position. Thus, $\mathfrak{f}^{\mathcal{B}} = -\mathfrak{f}_P^{\mathcal{B}}$, see sec. 4.2. But, special care has to be taken to correctly deal with the quasi-velocities $\boldsymbol{\omega}^{\mathcal{B}}$ and $\boldsymbol{\omega}^{\mathcal{P}}$.

A derivation of the Euler-Lagrange equations for quasi-velocities can be found in [98, ch. 4.12]. For the force on the rigid body $\mathcal{B}$ exerted by the fluid the standard Euler-Lagrange equation

$$f_i^{\mathcal{B}} = \frac{\mathrm{d}}{\mathrm{d}t}\frac{\partial\mathcal{T}}{\partial u_i} - \frac{\partial\mathcal{T}}{\partial q_i} \tag{4.25}$$

is obtained. The torque on $\mathcal{B}$ experiences some significant modifications

$$t_i^{\mathcal{B}} = \frac{\mathrm{d}}{\mathrm{d}t}\frac{\partial \mathcal{T}}{\partial \omega_i} + \varepsilon_{ijk}\omega_j \frac{\partial \mathcal{T}}{\partial \omega_k} - \mathcal{W}_{ij}^{-1}\mathcal{R}_{jk}\frac{\partial \mathcal{T}}{\partial \phi_k}, \tag{4.26}$$

with $\mathcal{R}$ and $\mathcal{W}^{-1}$ as defined in sec. 1.2.2. The Euler angles $\boldsymbol{\phi}$ express the rotations about no-orthogonal axes of rotation, whose orientations in turn depend on the Euler angels. The angular velocities appearing in the kinetic energy $\mathcal{T}$ are defined with respect to the orthogonal axis of the BFS, and thus are not generalised velocities. The relation (4.24) between $\boldsymbol{\omega}$ and $\boldsymbol{\phi}$ significantly complicates the equations of motion. In addition, the 6×6 added mass matrices will couple angular and translational motion, see sec. 5.1.2. Furthermore, the added masses of interaction deliver terms in the resulting equations of motions, depending on the generalised coordinates, the velocities and the acceleration of $\mathcal{B}$ and $\mathcal{P}$. Unpleasant and longish expressions are obtained for the force and torque exerted by the rigid bodies. Thus, the discussion of the force and torque exerted by $\mathcal{B}$ and $\mathcal{P}$ on the fluid in terms of added masses is carried out for the force only, and assuming $\boldsymbol{\omega}^{\mathcal{B}} = 0$ and $\boldsymbol{\omega}^{\mathcal{P}} = 0$. The bodies $\mathcal{B}$ and $\mathcal{P}$ are only allowed to translate, but not to rotate. This reduces the degrees of freedom of the problem from 12 dimensions, $\mathbf{q}^{\mathcal{B}}$ and $\mathbf{q}^{\mathcal{P}}$, to the 6 dimensions, $\boldsymbol{q}^{\mathcal{B}}$ and $\boldsymbol{q}^{\mathcal{P}}$, of the translation of $\mathcal{B}$ and $\mathcal{P}$ in $\mathcal{D}$. The notation $u_i \boldsymbol{a}_{ij} u_j$ with the 3D vector $\boldsymbol{u}$ is used to indicate that only the first three indices, $i = 1, 2, 3$ and $j = 1, 2, 3$, of an added masses $\boldsymbol{a}$ shall be included in the sum over i and j, as opposed to $\mathbf{u}_i \boldsymbol{a}_{ij} \mathbf{u}_j$, where $i = 1, \ldots, 6$ and $j = 1, \ldots, 6$.

In the presence of one moving rigid object $\mathcal{P}$ and an arbitrarily shaped solid stationary wall $\mathcal{W}$, the force on $\mathcal{B}$ in terms of added masses (4.18) in coordinates of the FOR, using the symmetry of $\boldsymbol{a}$, becomes

$$\begin{aligned} f_k^{\mathcal{B}} &= \frac{\mathrm{d}}{\mathrm{d}t}\left(u_i^{\mathcal{B}} \boldsymbol{a}_{ik}\right) + \frac{\mathrm{d}}{\mathrm{d}t}\left(u_i^{\mathcal{P}} \boldsymbol{b}_{ik}\right) \\ &\quad - \frac{1}{2}\left(u_i^{\mathcal{B}} u_j^{\mathcal{B}} \frac{\partial \boldsymbol{a}_{ij}}{\partial q_k^{\mathcal{B}}} + u_i^{\mathcal{P}} u_j^{\mathcal{B}} \frac{\partial \boldsymbol{b}_{ij}}{\partial q_k^{\mathcal{B}}} + u_i^{\mathcal{B}} u_j^{\mathcal{P}} \frac{\partial \boldsymbol{c}_{ij}}{\partial q_k^{\mathcal{B}}} + u_i^{\mathcal{P}} u_j^{\mathcal{P}} \frac{\partial \boldsymbol{d}_{ij}}{\partial q_k^{\mathcal{B}}} \right) \\ &= a_i^{\mathcal{B}} \boldsymbol{a}_{ik} + a_i^{\mathcal{P}} \boldsymbol{b}_{ik} + u_i^{\mathcal{B}} u_l^{\mathcal{B}} \frac{\partial \boldsymbol{a}_{ik}}{\partial q_l^{\mathcal{B}}} + u_i^{\mathcal{B}} u_l^{\mathcal{P}} \frac{\partial \boldsymbol{a}_{ik}}{\partial q_l^{\mathcal{P}}} + u_i^{\mathcal{P}} u_l^{\mathcal{B}} \frac{\partial \boldsymbol{b}_{ik}}{\partial q_l^{\mathcal{B}}} + u_i^{\mathcal{P}} u_l^{\mathcal{P}} \frac{\partial \boldsymbol{b}_{ik}}{\partial q_l^{\mathcal{P}}} \\ &\quad - \frac{1}{2}\left(u_i^{\mathcal{B}} u_j^{\mathcal{B}} \frac{\partial \boldsymbol{a}_{ij}}{\partial q_k^{\mathcal{B}}} + u_i^{\mathcal{P}} u_j^{\mathcal{B}} \frac{\partial \boldsymbol{b}_{ij}}{\partial q_k^{\mathcal{B}}} + u_i^{\mathcal{B}} u_j^{\mathcal{P}} \frac{\partial \boldsymbol{c}_{ij}}{\partial q_k^{\mathcal{B}}} + u_i^{\mathcal{P}} u_j^{\mathcal{P}} \frac{\partial \boldsymbol{d}_{ij}}{\partial q_k^{\mathcal{B}}} \right) \end{aligned} \tag{4.27}$$

with $i = 1, 2, 3$, $j = 1, 2, 3$, and $k = 1, 2, 3$. If the environment is stationary, meaning $\mathbf{u}^{\mathcal{P}} = 0$, (4.27) simplifies to

$$\mathfrak{f}_k^{\mathcal{B}} = a_i^{\mathcal{B}} \boldsymbol{a}_{ik} + u_i^{\mathcal{B}} u_l^{\mathcal{B}} \frac{\partial \boldsymbol{a}_{ik}}{\partial q_l^{\mathcal{B}}} - \frac{1}{2} u_i^{\mathcal{B}} u_j^{\mathcal{B}} \frac{\partial \boldsymbol{a}_{ij}}{\partial q_k^{\mathcal{B}}}\,. \tag{4.28}$$

Another easily treatable special case is the force and torque on a moving rigid body $\mathcal{B}$ in an undisturbed unbounded ideal fluid in BFS coordinates

$$\mathfrak{F}^{\mathcal{B}} = \frac{\mathfrak{D}\left(\Lambda \mathfrak{U}^{\mathcal{B}}\right)}{\mathfrak{D}t} = \frac{\mathrm{d}\left(\Lambda \mathfrak{U}^{\mathcal{B}}\right)}{\mathrm{d}t} + \boldsymbol{\varpi} \times \left(\Lambda \mathfrak{U}^{\mathcal{B}}\right)\,, \tag{4.29}$$

which can be derived from (4.19) using (4.25) and (4.26), with Λ being the added mass matrix of $\mathcal{B}$ otherwise denoted as $\mathcal{A}$ to clearly distinguish the case of free motion, $\mathfrak{U} = (\boldsymbol{U}, \boldsymbol{\Omega})^T$, $\boldsymbol{U} = \mathcal{R}\boldsymbol{u}$, and $\boldsymbol{\varpi}$ as defined in sec. 1.2.2.

4.4 Object perception

The fluid forces acting on a boundary $\mathcal{B}$ not only originate from the motion of $\mathcal{B}$, but also from the flow field induced by the environment. One may ask the question, which conclusions can be drawn about the environment by analysing the forces exerted on $\mathcal{B}$. In water, the forces resulting from the fluid-mechanical interaction of bodies are relevant only at a distance, which is usually too small to provide sufficient time for a reaction. The situation is even worse for objects in air due to its small density, see sec. 2.12. By virtue of Bernoulli's equation the fluid-mechanical interaction forces, (4.2) or (4.9), can be partly computed from measurements of the fluid flow velocity on the surface of a body. The fluid flow velocity induced on $\mathcal{B}$ by a moving object promises to be easier measurable than the resulting fluid-mechanical force or torque, except for cases of fast motion or high acceleration in water, see sec. 2.10.

The setting investigated in this section is, like in earlier sections, a body $\mathcal{B}$ equipped with a FSS moving with known velocity $\boldsymbol{u}^{\mathcal{B}}$ relative to a FOR in a fluid domain $\mathcal{D}$ described by potential flow. The domain $\mathcal{D}$ is bounded by $\mathcal{B}$, moving with $\boldsymbol{u}^{\mathcal{B}}$, an arbitrarily shaped wall $\mathcal{W}$, which is stationary in the FOR, and by a second rigid body $\mathcal{P}$ moving with $\boldsymbol{u}^{\mathcal{P}}$. The goal of this section is to relate the forces on a rigid body $\mathcal{B}$ obtained from measurement of the tangential velocity on its surface, its velocity of motion, and the knowledge about its shape, with the relative motion of the environment through the integrals

$$\frac{1}{2}\oiint_{\partial\mathcal{B}} \nabla\Phi\cdot\nabla\Phi\,\mathfrak{n}\,\mathrm{d}\mathcal{S}$$

and

$$\oiint_{\partial\mathcal{B}} \nabla\Phi\frac{\partial\Phi}{\partial n}\,\mathrm{d}\mathcal{S} \qquad \text{or} \qquad \oiint_{\partial\mathcal{B}} (\boldsymbol{y}\times\nabla\Phi)\frac{\partial\Phi}{\partial n}\,\mathrm{d}\mathcal{S}$$

appearing in the fluid-mechanical force and torque (4.9) on $\mathcal{B}$. The means of choice to associate the surface velocity integrals with the motion of the rigid bodies $\mathcal{B}$ and $\mathcal{P}$ are the Euler-Lagrange equations. When applied to the kinetic energy of the fluid expressed in terms of added masses and velocities (4.27) of the rigid bodies $\mathcal{B}$ and $\mathcal{P}$, the force and the torque exerted by $\mathcal{B}$ onto the fluid, see sec. 4.3.3, are obtained. The angular velocities $\boldsymbol{\omega}^{\mathcal{B}}=0$ and $\boldsymbol{\omega}^{\mathcal{P}}=0$ of $\mathcal{B}$ and $\mathcal{P}$ shall vanish to avoid the computation of rather complicated expressions for the force and the torque. The discussion of the torque $\boldsymbol{t}^{\mathcal{B}}$ on $\mathcal{B}$ is disregarded.

4.4.1 Forces applied to the fluid

Given the knowledge of the fluid velocity $\boldsymbol{V}^{\parallel}$ on the surface of $\mathcal{B}$, it is difficult — but in principle not impossible — to recover the precise course of the potential on $\mathcal{B}$ from a line integral on $\partial\mathcal{B}$. However, a proper distribution of the flow sensors to sample the velocity on $\partial\mathcal{B}$ is not only determined by the curvature of $\mathcal{B}$ but also by the a priori unknown fluid-mechanical image of the environment. The potential is determined only up to a time-dependent $\Phi_0(t)$ at some reference point on $\mathcal{B}$, which is cancelled by integration over a closed surface. It is therefore in general not a promising strategy to calculate the contribution

$$\varrho\frac{\mathrm{d}}{\mathrm{d}t}\oiint_{\partial\mathcal{B}(t)} \Phi\,\boldsymbol{n}\,\mathrm{d}\mathcal{S}$$

to the fluid force from the measurements of $\boldsymbol{V}^{\parallel}$ on $\partial\mathcal{B}$. The other two integrals appearing in the fluid force (4.9) on $\mathcal{B}$,

$$\boldsymbol{\mathcal{M}} = \oiint_{\partial\mathcal{B}(t)} \nabla\Phi \frac{\partial\Phi}{\partial n}\,\mathrm{d}\mathcal{S} \quad \text{and} \quad \boldsymbol{\mathcal{N}} = \frac{1}{2}\oiint_{\partial\mathcal{B}(t)} (\nabla\Phi\cdot\nabla\Phi)\,\boldsymbol{n}\,\mathrm{d}\mathcal{S} \tag{4.30}$$

can be computed from the tangential fluid velocity $\boldsymbol{V}^{\parallel}$ measured in BFS coordinates relative to $\mathcal{B}$. The translational velocity $\boldsymbol{u}^{\mathcal{B}}$, and the geometry of $\mathcal{B}$ shall be known. The fluid velocity $\boldsymbol{v} = \nabla\Phi$ at the respective point on $\boldsymbol{y}^{\mathcal{B}}$ on the surface $\partial\mathcal{B}$ of $\mathcal{B}$ relative to the FOR is given by

$$\boldsymbol{v} = \mathcal{R}^{\mathrm{T}}(\boldsymbol{\phi}^{\mathcal{B}})\boldsymbol{V}^{\parallel} + \boldsymbol{u}^{\mathcal{B}}$$

with $\boldsymbol{q}^{\mathcal{B}}$ the location of $\mathcal{B}$ in the FOR. To easily relate $\boldsymbol{\mathcal{M}}$ and $\boldsymbol{\mathcal{N}}$ with the motion of objects in the environment, one wishes to identify $\boldsymbol{\mathcal{M}}$ and $\boldsymbol{\mathcal{N}}$ with the corresponding terms appearing in (4.27).

According to (4.9), the force exerted by $\mathcal{B}$ on $\mathcal{D}$ is given by

$$\boldsymbol{f}^{\mathcal{B}} = \varrho\frac{\mathrm{d}}{\mathrm{d}t}\oiint_{\partial\mathcal{B}(t)} \Phi\,\boldsymbol{n}\,\mathrm{d}\mathcal{S} - \varrho\oiint_{\partial\mathcal{B}} \nabla\Phi\frac{\partial\Phi}{\partial n}\,\mathrm{d}\mathcal{S} + \varrho\oiint_{\partial\mathcal{B}} \frac{1}{2}\nabla\Phi\cdot\nabla\Phi\,\boldsymbol{n}\,\mathrm{d}\mathcal{S}\,. \tag{4.31}$$

The momentum of the fluid on $\mathcal{D}$ is determined by the position and the velocities of the rigid bodies $\mathcal{B}$ and $\mathcal{P}$, thus

$$\frac{\mathrm{d}}{\mathrm{d}t}\oiint_{\mathcal{B}(t)} \Phi\,\boldsymbol{n}\,\mathrm{d}\mathcal{S} = \left(\boldsymbol{a}^{\mathcal{B}}\cdot\frac{\partial}{\partial\boldsymbol{u}^{\mathcal{B}}} + \boldsymbol{a}^{\mathcal{P}}\cdot\frac{\partial}{\partial\boldsymbol{u}^{\mathcal{P}}} + \boldsymbol{u}^{\mathcal{B}}\cdot\frac{\partial}{\partial\boldsymbol{q}^{\mathcal{B}}} + \boldsymbol{u}^{\mathcal{P}}\cdot\frac{\partial}{\partial\boldsymbol{q}^{\mathcal{P}}}\right)\oiint_{\partial\mathcal{D}(t)} \Phi\,\boldsymbol{n}\,\mathrm{d}\mathcal{S}\,.$$

After substitution of (4.13), the surface integral and total time derivative are evaluated,

$$\begin{aligned}\frac{\mathrm{d}}{\mathrm{d}t}\varrho\oiint_{\partial\mathcal{B}(t)} \Phi\,n_k\,\mathrm{d}\mathcal{S} = a_i^{\mathcal{B}}\,\boldsymbol{a}_{ik} + a_i^{\mathcal{P}}\,\boldsymbol{b}_{ik} + \\ u_i^{\mathcal{B}}u_l^{\mathcal{B}}\frac{\partial\boldsymbol{a}_{ik}}{\partial q_l^{\mathcal{B}}} + u_i^{\mathcal{B}}u_l^{\mathcal{P}}\frac{\partial\boldsymbol{a}_{ik}}{\partial q_l^{\mathcal{P}}} + u_i^{\mathcal{P}}u_l^{\mathcal{B}}\frac{\partial\boldsymbol{b}_{ik}}{\partial q_l^{\mathcal{B}}} + u_i^{\mathcal{P}}u_l^{\mathcal{P}}\frac{\partial\boldsymbol{b}_{ik}}{\partial q_l^{\mathcal{P}}}\,,\end{aligned} \tag{4.32}$$

in terms of the added masses, the velocities, and the accelerations of $\mathcal{B}$ and $\mathcal{P}$. By comparison of (4.32) with (4.27)

$$\varrho\,(\boldsymbol{\mathcal{M}} - \boldsymbol{\mathcal{N}}) = \frac{1}{2}\left[u_i^{\mathcal{B}}u_j^{\mathcal{B}}\frac{\partial\boldsymbol{a}_{ij}}{\partial q_k^{\mathcal{B}}} + u_i^{\mathcal{P}}u_j^{\mathcal{B}}\frac{\partial\boldsymbol{b}_{ij}}{\partial q_k^{\mathcal{B}}} + u_i^{\mathcal{B}}u_j^{\mathcal{P}}\frac{\partial\boldsymbol{c}_{ij}}{\partial q_k^{\mathcal{B}}} + u_i^{\mathcal{P}}u_j^{\mathcal{P}}\frac{\partial\boldsymbol{d}_{ij}}{\partial q_k^{\mathcal{B}}}\right] \tag{4.33}$$

is obtained.

4.4.2 Object perception with velocity surface integrals

In special cases, $\boldsymbol{\mathcal{M}}$ and $\boldsymbol{\mathcal{N}}$ readily provide direct knowledge about the environment. Supposing $\mathcal{B}$ is at rest $\boldsymbol{u}^{\mathcal{B}} = 0$. Then obviously $\boldsymbol{\mathcal{M}} = 0$ and $\boldsymbol{\mathcal{N}} = 0$ if $\boldsymbol{u}^{\mathcal{P}} = 0$. The same is true for $\mathcal{B}$ moving through an otherwise undisturbed flow field, or $\mathcal{B}$ placed at fixed position in a homogeneous flow field. The surface integrals $\boldsymbol{\mathcal{M}} = 0$ and $\boldsymbol{\mathcal{N}} = 0$ vanish, since the added masses of $\mathcal{B}$ are independent of the location of $\mathcal{B}$ and the partial derivatives of the added masses with respect to $\boldsymbol{q}^{\mathcal{B}}$ or $\boldsymbol{q}^{\mathcal{P}}$ vanish. The example can be transferred to the motion of $\mathcal{B}$ over a

flat plate at $z = \text{const.}$, or the homogeneous flow over $\mathcal{B}$ on a flat plate. The components parallel to the plate of $\boldsymbol{\mathcal{M}}$ and $\boldsymbol{\mathcal{N}}$ are zero. This situation occurs for an insect with a flow sensory system placed in a stationary environment and exposed to the flow field of loudspeakers [155]. $\mathcal{B}$ could conclude that probably nothing critical happens since $\mathcal{N}_x = \mathcal{N}_y = 0$. Thus, (4.33) is capable of filtering any background motion with large characteristic length scales compared to the size of $\mathcal{B}$. Or conversely, (4.33) is not affected by the motion of $\mathcal{B}$ in a spatially homogeneous fluid.

When $\mathcal{B}$ is moving in a more complex environment consisting of objects stationary in the FOR and $\mathcal{P}$ moving, the interpretation of (4.33) becomes tricky. In this situation, the integrals $\boldsymbol{\mathcal{M}}$ and $\boldsymbol{\mathcal{N}}$ signal the existence of one or more objects. However, the resulting direction cannot be attributed to one object. The presence of a moving object cannot be detected and discerned from the stationary background, unless additional knowledge is provided or assumptions are made.

4.5 Conclusion

In this chapter, the added mass formalism was developed, which will be used in the next section to formulate the dynamical model of the autonomous underwater robot *Snookie*. Furthermore, starting with the fluid-mechanical forces on a rigid body $\mathcal{B}$ in an ideal, incompressible, and irrotational fluid, a method was developed to perceive the presence of another object from the tangential velocity on $\mathcal{B}$. The method ignores any background motion in the fluid with typical length scales larger than the size of the flow sensory system. It just consists of sums over velocities and squared velocities on the surface of $\mathcal{B}$ weighted with the velocity of motion and the surface normal at a sensor to account for the geometry of $\mathcal{B}$. It can be computed easily in a stable fashion at any instant of time over any subset of randomly chosen sensors readings. Due to its property as a sum over the signal of the sensors distributed over the surface of $\mathcal{B}$, sensor noise or local hydrodynamic instabilities on a subset of the sensors can be partly averaged away. It signals the appearance of an object in the range of the FSS and therefore can serve as a collision warning system.

Chapter 5

Snookie

As already mentioned in the introduction to this thesis, *Snookie* is an *autonomous underwater vehicle* (AUV) to be equipped with an ALL. The term *artificial lateral-line system* is commonly used as a synonym for FSS, emphasising that it is tried to mimic the function and capabilities of the LLS of fish. *Snookie* started as a small student project, and triggered several research activities concerning different aspects of how to realize and how to make use of a FSS. Now, the project *Snookie* actually consists of three sub-projects. The first part is to design and build an underwater vehicle that can be equipped with an ALL. The second part is the development of flow sensors and the arrangement of these sensors to an ALL. Chapters 3 and 4.4 already dealt with the third part, the mathematical methods to analyse the flow sensory readings from the ALL.

Transferring the capabilities of the LLS to a robotic system would be beneficial in a number of ways. It would complement existing established sensor technology. For instance, sonar sensors require a minimum distance to an object to be measured, with a blind zone in the immediate environment. In geometrically complex environments and narrow spaces reflections impair the sonar sensor readings. Camera- or laser-based systems depend on visual conditions. The function of a FSS is passive in the sense that it uses information that is present anyway due to the physics of bodies moving in water. There is no need for data exchange to control the motion of a group of vehicles equipped with flow sensory systems.

From the constraints of the hydrodynamic image severe requirements follow for the implementation of an ALL on a moving robot. The lateral-line sensors must be capable of detecting small, often slowly varying [53] changes in the comparably strong flow field caused by the motion of the robot. The information processing must be very fast to enable the robot to react on detected changes in the immediate environment, and the robot must be highly manoeuvrable in order to change its state of motion appropriately within this narrow range.

In the course of this chapter, the hardware of the robot is briefly described, followed by the development of its dynamical model used to control the motion of the robot. Finally, the current state of the development of *Snookie* and the ALL including the calibration of sensors is summarised.

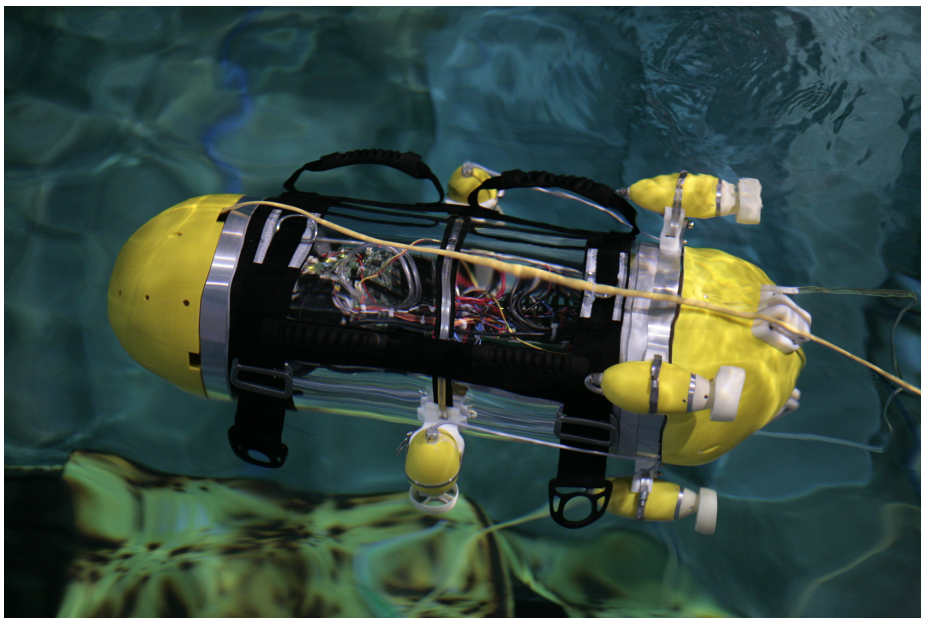

Figure 5.1: *Snookie*, an autonomous underwater vehicle with an artificial lateral-line system.

5.1 The autonomous underwater vehicle *Snookie*

The submarine *Snookie* is an AUV specifically designed as a test bed for an ALL. In this section, the concept of the robot is presented and a brief overview of its structure is given.

Special care has to be taken of the dynamics due the limited range of view of the lateral-line system. The robot must be capable of precise motion in the close vicinity of other objects at a distance of typically the diameter of the snout. Therefore, high manoeuvring capabilities are crucial. It must also be able to react on the sudden appearance of other objects in the range of view. A careful design of the hull, the fins, and the thruster arrangement, driven by an accurate physical model of its dynamics is required, which also serves the tuning of the controllers of motion.

One of the most important design considerations concerns the shape of the robot. Not only must the components of the robot fit inside, but the outline has direct influence on the functionality of the ALL. The expected sensing quality depends on the shape of the robot, which determines the properties of the flow field of the surrounding fluid. A good compromise between ease of realisation, a simple mathematical treatise, and the quality of the hydrodynamic image is a cylindrical shape with hemispheres as caps on both ends.

The sensors of the ALL are intended to be placed in a cross in allocated mountings in the frontal sphere. They extend $2 - 3\,\mathrm{mm}$ above the surface to avoid boundary layer effects introduced by the surface of the hull. The spherical shape of the sensory system allows to perform analytic calculations, see ch. 3.

5.1.1 The robot

The robot consists of a cylindrical watertight main compartment, in which all of the electronics is encapsulated, two half-spheres at the end of the cylinder, and six thrusters. It has a total length of $L = 74\,\text{cm}$ and a diameter of $2R = 25\,\text{cm}$. The overall physical mass is $32.234\,\text{kg}$ including the flooded bow and stern, which can be fine tuned to match the water displacement of the robot for neutral buoyancy.

To achieve high manoeuvrability, a helicopter-like multi-propeller propulsion system is adapted from the AMOUR V robot [156]. The basic layout incorporates four thrusters arranged in a symmetric cross in the stern pointing in forward direction – see fig. 5.2. This allows direct control over the forward/backward movement along the robot's longitudinal axis, the pitch angle and the yaw angle. All four motors work in combination for the acceleration/deceleration. Additionally two vertically mounted thrusters control the depth and the roll angle. Since motors are a source of vibrations and the propellers induce vorticity to produce thrust, the thrusters have to be mounted at the stern, as far away as possible from the flow sensors. Each thruster on the robot is coupled with a motor controller. The controllers receive thrust and direction commands from the low-level controller.

A low-level control unit, based on an autopilot board by Ascending Technologies, is the central hub for the embedded systems and controls the 6D motion. It consists of two 60 MHz ARM7 RISC processors. One of them is freely programmable. The other one combines three micro-electro-mechanical systems (MEMS) gyroscopes, a three-axis acceleration sensor, a three-axis magnetometer, and a pressure sensor to an inertia-force measurement unit and preprocesses the data of these sensors. The command unit can utilize this angular and translational data over a direct on-board link. Decoupling the translational and rotational movements of the robot allows to control each of the five accessible degrees of freedom of the robot with a proportional-integral-derivative (PID) controller. Sidewards motion is not supported by the thruster layout. The structure of the controller is explained in subsection 5.1.3.

The command unit of the high-level control can utilise the angular and translational data from the inertia measurement unit over a direct on-board link (CAN bus). The high-level control is done on a standard PC in a small form factor integrated in the robot. The Robot Operating System (ROS) infrastructure running on the PC allows an easy implementation of typical high level tasks such as to decide on the desired speed and direction, the processing of the sensor data, object recognition and avoidance, data logging, and interfacing to command and control.

A land-based station can be used to monitor the status of the robot and to give new commands. Direct control of the movement of the robot is also possible via either a wiiMote, Joystick or keyboard. The robot can operate tethered via an Ethernet cable for a high bandwidth communication. Alternatively for untethered operation the link between command and control and the robot can be established via an acoustic modem by Tritech. The Micron Data Modem sends and receives with 40 bits per second in simplex mode over a specified range up to 500 m. If considering the working range and the speed of sound in water, the delay between sending and receiving can be up to 337 ms.

The ALL is described in detail in sec. 5.2. The flow sensors are arranged in

two arrays to a cross on the frontal hemisphere with 17 sensors in total. A National Instruments USB data acquisition (DAQ) Card (NI USB-6218) is used for the acquisition and conversion to digital of the analogue sensor readings of the FSS. It provides 32 single-ended channels at 16 Bit resolution with a sensitivity of up to $91.6\mu V$. The sample rate used is $10\,\mathrm{kS/s}$ per channel. Data readings are buffered and polled from the connected high-level control PC over USB 2.0. A custom ROS node logs the raw data and pipes it to the flow-field reconstruction and object detection algorithms.

5.1.2 Model of the dynamics of *Snookie*

As mentioned in the introduction to this section, for a proper design and control of the robot capable of manoeuvring on the basis of flow perception, a careful description and analysis of the dynamics is crucial. Estimating the forces acting on a body in a fluid is a non-trivial problem. The traditional approach to describe the dynamics of bodies moving in fluids is an approximative analytic one. Such an approach delivers good estimates of the relevant forces.

To avoid both, additional contributions due to the wave drag and complications in the calculation of the flow field due to a nonlinear boundary condition at the force-free surface, the robot is assumed to dive sufficiently deep. This condition is met in good approximation at a depth larger than five times the diameter of the robot [157, Sec. 3.8] below an undisturbed water surface. The forces acting on the body are empirically split up into contributions of viscous drag, pressure drag (also called form drag), lift, and increased inertia expressed in terms of *added masses* as a consequence of the acceleration of displaced fluid. The viscous and pressure drag contributions may be considered as corrections due to viscosity of the stationary motion of a body in an ideal fluid, which otherwise would not experience any forces. The lift contribution stems from lifting surfaces with sharp trailing edges, the fins. In general, the drag as well as fluid inertia depend on the current and previous velocity and acceleration [158]. Also effects like Basset forces, and drag and lift forces, arising from the shedding of vortices, which in principle can be accounted for by a semi-analytic model, are ignored throughout this work, to obtain a treatable model.

Forces on the hull

As discussed in sec. 4.3.1, the favourable system to compute the added masses is a body-fixed frame of reference using all available symmetries. For the purpose of computational simplicity the trunk of *Snookie* shall be approximated by a prolate spheroid with long axis $2a_H$ and short axis $2b_H$, whose axis of revolution lies along the X-axis, with a_H being the semi-length of the axis and b_H the radius in the Y-Z plane at $X = 0$. Then, the added masses with respect to the geometric centre of the ellipsoid are given by [152, p. 144 ff.]

$$
\begin{aligned}
m_{H1} := \Lambda^H_{11} &= \frac{4}{3}\pi\varrho\, a_H b_H^2 \frac{\alpha_H}{2-\alpha_H}\,, \qquad m_{H2} := \Lambda^H_{22} = \Lambda^H_{33} = \frac{4}{3}\pi\varrho\, a_H b_H^2 \frac{\beta_H}{2-\beta_H}\,,\\
\iota_H := \Lambda^H_{55} &= \frac{4}{3}\pi\varrho\, a_H b_H^2 \left(a_H^2 + b_H^2\right) \frac{e^4\left(\beta_H - \alpha_H\right)}{\left(2-e^2\right)\left[2e^2 - \left(2-e^2\right)\left(\beta_H - \alpha_H\right)\right]}\,,\\
\Lambda^H_{66} = \Lambda^H_{55}\,, &\qquad \Lambda^H_{44} = 0\,, \qquad \text{and} \qquad \Lambda^H_{ij} = 0 \quad \text{for} \quad i \neq j\,,
\end{aligned}
\tag{5.1a}
$$

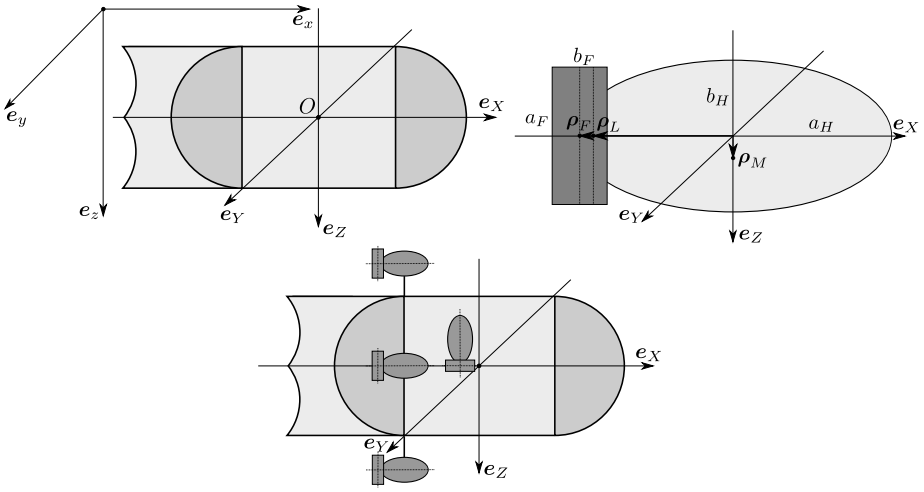

Figure 5.2: *Left*: Frame of reference $\{\boldsymbol{e}_x, \boldsymbol{e}_y, \boldsymbol{e}_z\}$ and body-fixed system $\{\boldsymbol{e}_X, \boldsymbol{e}_Y, \boldsymbol{e}_Z\}$ with origin O at the geometric centre of the hull. *Right*: Geometry of the fluid-mechanically active parts of the robot with equivalent fin and equivalent hull without the thrusters. *Bottom*: Arrangement of the 6 thrusters in the body-fixed system of the robot.

where

$$\alpha_H = \frac{2(1-e^2)}{e^3}\left[\frac{1}{2}\ln\left(\frac{1+e}{1-e}\right) - e\right], \qquad \beta_H = \frac{1}{e^2} - \left(\frac{1-e^2}{2e^3}\right)\ln\left(\frac{1+e}{1-e}\right),$$
$$e^2 = 1 - \left(\frac{b_H}{a_H}\right)^2. \tag{5.1b}$$

The parameters a_H and b_H are chosen so that, first, the volume $V_E = 4/3 a_H b_H^2$ of the prolate spheroid is equal to the volume of the trunk of *Snookie* consisting of the water tight cylinder and the two semi-spheres at the bow and the stern. And second, the surface of the ellipsoid

$$S_E = 2\pi b_H^2 + \frac{2\pi a_H b_H}{\sqrt{1-\frac{b_H^2}{a_H^2}}} \arcsin\left(\sqrt{1-\frac{b_H^2}{a_H^2}}\right)$$

has to be equal to the surface of *Snookie* $S_H = 4\pi R^2 + 2\pi R(L-2R)$. Numerical solution of these two conditions yields $a_H = 41.484\,\mathrm{cm}$ and $b_H = 13.620\,\mathrm{cm}$. The added masses are $m_{H1} = 5.922\,\mathrm{kg}$ and $m_{H2} = 23.573\,\mathrm{kg}$, the added moment of inertia $\iota_H = 1.822\,\mathrm{kg\,m^2}$.

The viscosity induced drag on the surface of the moving body is hard to determine analytically and usually described by empirical drag coefficients [45]. The main drag on *Snookie* stems from the separation of the boundary layer around the hull and the breaking of the symmetry of the flow field, which finally leads to a wake with reduced pressure at the stern. A different drag force is expected

for the forward and sidewards motion of *Snookie*,

$$F_{fd} = -\frac{1}{2}\varrho\, C_{fd} A_H \left|V_X\right| V_Y\,, \quad \boldsymbol{F}_{sd} = -\frac{1}{2}\varrho\, C_{sd} B_H \begin{pmatrix} V_Y \\ V_Z \end{pmatrix} \sqrt{V_Y^2 + V_Z^2}\,, \quad (5.2)$$

where C_{fd} and C_{sd} are the forward and sidewards drag coefficients and $A_H = \pi R^2$ and $A_B = \pi R^2 + 2R\,(L - 2R)$ the respective cross-sections with $L = 74\,\mathrm{cm}$ being the overall length and $R = 12.5\,\mathrm{cm}$ the radius of the robot. The total pressure drag is approximated by a linear composition [152, p. 13 ff.] of forward and sidewards drag. It acts on the geometric centre of the hull, the origin O of the BFS. The drag coefficient is a non-trivial function of the Reynolds number. It varies e.g. for a circular cylinder between $C \approx 20$ at $\mathrm{Re} = 1$ and $C \approx 1.1 \ldots 1.3$ at $\mathrm{Re} = 1000$. In absence of measured data and better assumptions, the forward and sidewards drag coefficients are set to $C_{fd} = C_{sd} = 0.3$. For the Reynolds numbers considered here, this value is a safe estimate of the lower bound of the pressure drag coefficient of a sphere [46, p. 161 ff.]. Overestimation of the pressure drag would lead to underestimated thruster forces required to stop the robot when an obstacle appears. The drag on the robot due to a rotation is neglected, since high angular velocities are not intended to occur. The drag force on the hull $\boldsymbol{D}_H = (F_{fd}, \boldsymbol{F}_{sd})^T$ acts opposite to the direction of motion with the force resultant attacking at the geometric centre of the hull. It does not produce a torque. Thus, the resultant drag force vector of the hull is given by $\mathfrak{F}_H = (\boldsymbol{D}_H, \boldsymbol{0})^T$.

Forces on the fins

The motion of an elongated blunt body like *Snookie* in the direction of its main axes, even if it were perfectly symmetric with respect to the main axis and the fluid were perfectly at rest, is unstable. Any small disturbance in pitch or yaw causes torque about the centre of mass, called Munk's moment [97, p. 39 ff.], throwing the body out of the desired trajectory. The yaw and pitch instability of forward motion is balanced by a vertical and a horizontal fin at the stern of *Snookie*. The fins consist of thin plates of length 20.2 cm and height $b_F = 2R = 25\,\mathrm{cm}$ equal to the diameter of the robot, with a cut-out for the spherical stern. This results in an effective surface of $260\,\mathrm{cm}^2$ per fin with a mean effective length $a_F = 10.4\,\mathrm{cm}$ of a fin. The geometric centre of the rectangular equivalent fin is located $l_h = 39.3\,\mathrm{cm}$ behind the geometric centre of the hull. The vertical and horizontal fin are arranged to form a symmetric cross like shape.

The incident flow to the fins is taken to be spatially homogeneous, and it is assumed that it is not affected by the presence of the hull or the thrusters. The relative velocity between fin and undisturbed fluid is approximated by the velocity $\boldsymbol{V}_F = -\boldsymbol{U} - \boldsymbol{\Omega} \times \boldsymbol{\rho}_F$ of the geometric centre of the fin. Analytic expressions are available for the lift on a 2D cross section of a plate of zero thickness and cord length l in a homogeneous free stream and an angle of attack α [159, p. 66 ff.]. The circulation around a cross section of the fin according to the 2D theory is given by $\Gamma_F = \pi a_F V_F \sin\alpha$, which results in the lift $F_F = \pi\varrho A_F V_F^2 \sin\alpha$ on the fin with fin area $A_F = a_F b_F$. In 3D the lift on a plate of finite length h is overestimated depending on the ratio h/l. Due to the absence of analytic expressions for the full 3D case, the 2D expression is widely used for hydrofoils. The plate also experiences a torque $1/4\pi\varrho A_F^2 \sin\alpha$ per unit length

about the centre of pressure forces at the so called quarter-cord point, located halfway between the leading edge and the centre line of the fin. The quarter-cord point of the fins is located at $\boldsymbol{\rho}_Q = (-36.7, 0, 0)^T$ cm behind the geometrical centre O of the hull on the long axis of the robot. The occurring torques on the fin are balanced by the mounting and do not affect the dynamics.

The Z (Y) component of the incident flow due to the presence of the horizontal (vertical) fin does not significantly contribute to the lift produced by the vertical (horizontal) fin. The incident flow $\boldsymbol{V}_F$ is therefore decomposed into the lift producing components $\boldsymbol{V}_V = \boldsymbol{V}_F - (\boldsymbol{V}_F \cdot \boldsymbol{e}_Z)$ for the vertical and $\boldsymbol{V}_H = \boldsymbol{V}_F - (\boldsymbol{V}_F \cdot \boldsymbol{e}_Y)$ for the horizontal fin. With the angles $\sin\alpha_V = (\boldsymbol{V}_V \cdot \boldsymbol{e}_Y) / \|\boldsymbol{V}_V\|$ and $\sin\alpha_H = (\boldsymbol{V}_H \cdot \boldsymbol{e}_Z) / \|\boldsymbol{V}_H\|$ between the fin and the lift producing components of the incident flow an estimate of the lift on the vertical and horizontal fin, acting on the quarter-cord point $\boldsymbol{\rho}_Q$ is given by

$$\boldsymbol{L}_V = \tilde{A}_F \sin\alpha_V \|\boldsymbol{V}_V\| \begin{pmatrix} -V_{VY} \\ V_{VX} \\ 0 \end{pmatrix} \text{ and } \boldsymbol{L}_H = \tilde{A}_F \sin\alpha_H \|\boldsymbol{V}_H\| \begin{pmatrix} -V_{HZ} \\ 0 \\ V_{HX} \end{pmatrix}$$

with $\tilde{A}_F = -\pi \varrho\, a_F b_F$. These results are applicable within a range of $\alpha = -10^\circ \ldots 10^\circ$ [152, pp 20], provided the plate has a smooth surface. The breakdown of the lift at higher angles of attack due to stall is accounted for by an additional factor of $\Theta(\alpha_0 - \alpha)\,\Theta(\alpha_0 + \alpha)$ for the respective force components with Θ being the Heaviside step function and α_0 the critical angle. The lift forces on the quarter cord-point have the force and torque resultants

$$\boldsymbol{F}_L = \boldsymbol{L}_V + \boldsymbol{L}_H \qquad \text{and} \qquad \boldsymbol{T}_L = (\boldsymbol{L}_V + \boldsymbol{L}_H) \times \boldsymbol{\rho}_Q \tag{5.3}$$

about O, which may be combined for a compact notation to the 6D force vector $\boldsymbol{\mathfrak{F}}_L = (\boldsymbol{F}_L, \boldsymbol{T}_L)^T$. As mentioned previously, the effective lift of hydrofoils or wings of finite length is reduced in 3D contrary to the 2D results due to the flow over the tip of the wing. The lift therefore enters the equations of motion in the dynamical model with an additional safety margin of 1/2 to ensure that the stabilising effects of the fins are not overestimated.

Viscosity induced pressure drag on the fins in X direction is modelled due to the absence of better alternatives by the drag coefficient $C_P = 1.28$ of a flat plate perpendicular to the incident flow $F_P = \frac{1}{2} C_P \varrho\, \hat{A}_F U^2$, corrected by the net frontal area $\hat{A}_F = a_F b_F \sin(\alpha)$ exposed to the incident flow, which is also taken as as a rough estimate for the lift induced drag for $|\alpha| < 10^\circ$.

Correct estimates of the drag on the fins due to sidewards motion or rotations are challenging. Since lift and drag scale with V_F^2, an error in the estimates of these forces does not cause large effects on the dynamics, since the rotational velocity of the robot is supposed to be small. Drag coefficients of similar shapes, e.g. a cube, a cube at an angle of 45°, and a circular cylinder, are in the range of $0.8 \ldots 1.3$ for Reynolds numbers $\mathrm{Re} \approx 1000$. A safe estimate of the lower bound of the drag forces of the fins at sidewards or vertical motion is therefore given by the drag coefficient $C_F \approx 1$ of a cylinder with the net frontal area of the fin A_F with mathematically convenient independence of the roll angle. The drag of the fin acts upon the geometric centre of the fin located at $\boldsymbol{\rho}_F$. The incident flow $\boldsymbol{U}_F$ is decomposed in the X component and the components perpendicular to the fins $V_{FY} = \boldsymbol{e}_Y \cdot \boldsymbol{V}_F$ and $V_{FZ} = \boldsymbol{e}_Z \cdot \boldsymbol{V}_F$, and the drag on the fins is given

by

$$\boldsymbol{D}_F = -\frac{1}{2}\varrho\, C_F A_F \sqrt{V_{FY}^2 + V_{FZ}^2} \begin{pmatrix} 0 \\ V_{FY} \\ V_{FZ} \end{pmatrix} .$$

The resulting force and torque $\mathfrak{F}_F = (\boldsymbol{F}_F, \boldsymbol{T}_F)^T$ on the origin O of the BFS are

$$\boldsymbol{F}_F = F_P\, \boldsymbol{e}_X + \boldsymbol{D}_F \qquad \text{and} \qquad \boldsymbol{T}_F = \boldsymbol{F}_F \times \boldsymbol{\rho}_F \,. \tag{5.4}$$

The fins stabilise the forward motion. Their disadvantage are increased added masses constraining the manoeuvrability. The added masses of the perpendicular arrangement of the vertical and horizontal fin is approximated by the 2D result of a cross-shaped section of two perpendicular plates of zero thickness. Both plates have a length of $a_F = 10.4\,\text{cm}$ and a width of $b_F = 25\,\text{cm}$. The added masses per unit length of the cross-shaped arrangement [152, p. 144 ff.] are given by $\Lambda_{11} = 0$, $\Lambda_{22} = \Lambda_{33} = \pi\varrho\,(l/2)^2$, $\Lambda_{44} = 2/\pi\varrho\,(h/2)^4$, and $\Lambda_{55} = \Lambda_{66} = 1/8\pi\varrho\,(l/2)^4$, which results in the added masses

$$\begin{aligned} m_F &= \Lambda_{22}^F = \Lambda_{33}^F = \pi\varrho\,\frac{a_F b_F^2}{4}\,, \quad \iota_{F1} = \Lambda_{44}^F = \varrho\,\frac{b_F^4 a_F}{8\pi}\,, \\ \iota_{F2} &= \Lambda_{55}^F = \Lambda_{66}^F = \varrho\,\frac{\pi a_F^4 b_F}{128} \end{aligned} \tag{5.5}$$

of the cross shaped fins computed about their common geometric centre. Their numerical values are $m_F = 5.105\,\text{kg}$, $\iota_{F1} = 16.16 \cdot 10^{-3}\,\text{kg m}^2$, and $\iota_{F2} = 0.718 \cdot 10^{-3}\,\text{kg m}^2$.

Vertical motion remains unstable since the motion in $\boldsymbol{e}_Z$-direction cannot be stabilised by fixed fins without affecting motions in $\boldsymbol{e}_X$-direction. During submerging and descending Munk's moment appears due to both, the round shape of the bow and the large angle of an attack at the tip of the fin. Since the vertical speed is usually small, the thrust needed for balancing is also small.

Combination of mass, moment of inertia and added masses

Snookie is buoyancy neutral, meaning that its mass is equal to the equivalent volume of water. But the mass is not distributed homogeneously. Counterweights are mounted below the longitudinal axis so that the robot is balanced about the pitch axis including fins and thrusters, and stable about the roll axis. The symmetry with respect to the vertical plane is preserved. The mass of *Snookie* including balancing weights and the flooded bow and stern is equal to its water displacement, $m = 32.324\,\text{kg}$. The actual centre of mass is shifted below the origin O of the BFS by the vector $\boldsymbol{\rho}_M = (0, 0, \rho_M)$. Integration over the mass distribution carried out by the computer aided design (CAD) program SolidWorks leads to a centre of mass $\boldsymbol{\rho}_M = (0, 0, 1.5)^T$ cm and moments of inertia

$$I_{11} = 0.23\,, \quad I_{22} = 1.68\,, \quad I_{33} = 1.70\,, \quad \text{and} \quad I_{ij} = 0 \quad \text{for} \quad i \neq j$$

in units of kg m^2 computed in body-fixed coordinates about the centre of mass. Accordingly, the axis of rotation must be shifted by $-\boldsymbol{\rho}_M$,

$$\Lambda^M = \begin{pmatrix} m\,\mathbb{1} & -m\,\boldsymbol{\rho}_M\times \\ m\,\boldsymbol{\rho}_M\times & I - m\,\boldsymbol{\rho}_M\times\,\boldsymbol{\rho}_M\times \end{pmatrix} ,$$

which has been already incorporated in the inertia of the rigid body in sec. 1.2.2.

The added mass matrices have been determined with respect to the geometric centre of each shape independently and now have to be transformed and combined according to their location in the BFS relative to O – see sec. 4.3.2. The added mass matrix of the hull (5.1a) is already computed about the origin of the BFS and does not need any further treatment. The coordinate systems of the added mass matrix of the fin (5.5) has to be shifted by $-\boldsymbol{\rho}_F$. The resulting total mass matrix of the robot is given by

$$\Lambda = \Lambda^M + \Lambda^H + \Lambda^F \tag{5.6}$$

with the entries

$$\begin{aligned}
&\Lambda_{11} = m + m_{H1}\,, && \Lambda_{22} = m + m_{H2} + m_F\,,\\
&\Lambda_{33} = \Lambda_{22}\,, && \Lambda_{15} = \Lambda_{51} = -\Lambda_{24} = -\Lambda_{42} = -m\rho_M\,,\\
&\Lambda_{26} = \Lambda_{62} = -\Lambda_{35} = -\Lambda_{53} = -m_F\rho_F\,, && \Lambda_{44} = I_{11} + m\rho_M^2 + \iota_{F1}\,,\\
&\Lambda_{55} = I_{33} + m_F\rho_F^2 + \iota_H + \iota_{F2}\,, && \Lambda_{66} = I_{22} + m\rho_M^2 + m_F\rho_F^2 + \iota_H + \iota_{F2}\,.
\end{aligned}$$

The remaining entries of Λ vanish.

A closer look at the combined added masses reveals that the added mass, depends on the direction of motion. The net frontal area for forward motion is much smaller than the net frontal area for sidewards motion, and accordingly the amount of displaced fluid. The centre of total mass for pure forward motion is for example given by

$$\boldsymbol{s}_F = \left(0, 0, \frac{m\rho_M}{m + m_{H1}}\right)^T,$$

the centre of total mass for pure sidewards or vertical motion by

$$\boldsymbol{s}_V = (s_{VX}, 0, s_{VZ})^T = \left(\frac{m_F\rho_F}{m + m_{H2} + m_F}, 0, \frac{m\rho_M}{m + m_{H2} + m_F}\right)^T.$$

Obviously, the centre of total mass has its own dynamics coupled to the motion of the robot. The position of each mass contribution, i.e. the added masses of the hull, the added mass of the fin, and body mass, is fixed in the BFS. The centre of total mass moves, since the quantities of the added masses – their relative weights in the barycentre – change with the direction of motion. With the origin of the BFS fixed in an arbitrary point on the rigid body, e.g. O, the location of each mass is fixed, and the equations of motion of a rigid body can be used, keeping in mind that the total mass depends on the direction of motion.

Thrusters

The thrusters are neglected in the computation of the added masses, the drag, and the lift. They provide the robot with acceleration in forward/backward and vertical direction, and also angular momentum about pitch, roll, and yaw. The thrusters enter the equations of motions via the force generated by the

propellers. The four horizontal thrusters are placed at

$$\begin{aligned} \boldsymbol{\rho}_{T1} &= \left(l_H, \frac{r_H}{\sqrt{2}}, \frac{r_H}{\sqrt{2}}\right), \quad & \boldsymbol{\rho}_{T2} &= \left(l_H, \frac{r_H}{\sqrt{2}}, -\frac{r_H}{\sqrt{2}}\right), \\ \boldsymbol{\rho}_{T5} &= \left(l_H, -\frac{r_H}{\sqrt{2}}, \frac{r_H}{\sqrt{2}}\right), \quad & \boldsymbol{\rho}_{T6} &= \left(l_H, -\frac{r_H}{\sqrt{2}}, -\frac{r_H}{\sqrt{2}}\right), \end{aligned} \tag{5.7}$$

symmetrically in a plane $l_H = 22.0\,\text{cm}$ behind the geometric centre of the hull parallel to the $\boldsymbol{e}_Y$-$\boldsymbol{e}_Z$ plane in $\boldsymbol{e}_X$ direction at a distance of $r_H = 18.5\,\text{cm}$ to the longitudinal axis of the hull, see fig. 5.2. The two vertical thruster are located at $\boldsymbol{\rho}_{T3} = (s_{VX}, r_V, 0)$ and $\boldsymbol{\rho}_{T4} = (s_{VX}, -r_V, 0)$ symmetrically in a plane parallel to the $\boldsymbol{e}_Y$ – $\boldsymbol{e}_Z$ plane at $\boldsymbol{\rho}_V = (s_{VX} = -6.2, \pm r_V = \pm 19.0, 0)$ cm in $\boldsymbol{e}_Z$ direction. The added masses of the hull and the fins depend of the direction of motion, therefore the total centre of mass also depends on the direction of motion – see sec. 5.1.2. Any other arrangement of the vertical thrusters would effectively cause angular momentum about the Y axis at pure vertical motion.

The thrust, the force in the direction of the axle of a propeller, is generated by the blades moving relative to the surrounding fluid. The essential geometrical parameters influencing the performance of a propeller are its diameter d, the span s, the cord length l, the latter both determining the planform area S of the blade, and the pitch angle α_p. Imagine, the blades were extruded to form a screw. The pitch ratio P is defined as the ratio of the pitch p and the diameter $d = 2s$ of the screw. For simple propellers the blade is twisted from its mounting on the axle to its tip such that a relatively homogeneous flow profile over the propeller is obtained. This is expressed by the notion of the local pitch angle $\arcsin(p/2\pi r)$ at radial position r relative to the axle. The advance ratio

$$J = V/\nu d \tag{5.8}$$

consisting of the relative axial velocity V between thruster and fluid, the number of rotations ν of the propeller per second, and the diameter of the propeller expresses how far the propeller actually moves through the fluid during one rotation.

For a propeller with similar performance desired for forward and backward thrust, blades with symmetrical cross section are used. At an advance ratio $J = P$ the propeller is moving with the incident flow at zero angle of attack. No thrust is produced by a symmetric blade under this condition. In case the advance ratio is smaller than the pitch ratio, the propeller produces forward thrust, and backward thrust in the opposite case.

Since the lift on a blade acts perpendicularly to the local relative flow, the force generated by a blade is composed of the thrust and the torque balanced by the motor. The total thrust and torque are approximated by the sum of the respective quantities over the single blades. Then, the thrust T

$$T = K_T(J)\,\varrho\,\nu^2 d^4 \tag{5.9a}$$

and the torque

$$Q = K_Q(J)\,\varrho\,\nu^2 d^5 \tag{5.9b}$$

of the propeller can be expressed in terms of non-dimensional parameters, the thrust coefficient K_T, and torque coefficient K_Q, both functions of the advance

ratio J, and in terms of d and ν [152, 159]. The efficiency of the propeller is given by the ratio

$$\eta_P = \frac{VT}{2\pi\nu Q} = \frac{J}{2\pi}\frac{K_T}{K_Q}\,.$$

The essential scaling properties of force, torque, and efficiency obtained from the actuator disc essentially remain the same [159, ch. 9], no matter which theory is used to describe the propeller. The thrust and torque coefficients have been measured for various blade shapes, which allows to roughly estimate the properties of a given propeller design. Elaborate methods and big efforts have been devoted [159] to the design of blades to optimise the thrust, maximum speed, and efficiency of propellers because of their great impact on the cost efficiency of the propulsion system of ships, which go far beyond the simple model just described.

Nevertheless, the model is highly useful to control the forces generated by the thrusters to maintain a desired state of motion as the following considerations show. The thrusters are equipped with brushed pulse-width-modulated (PWM) direct current (DC) motors. The question at hand is now how to choose the correct pulse width to generate a certain thrust. As (5.9) shows, given the geometry of a propeller with fixed pitch, the thrust depends on the current revolution number of the propeller and the relative velocity between the thruster and the fluid. The pulse width itself is in general a useless measure. The power delivered to the motor does not directly depend on the pulse width, since the impedance of the thrusters not only depends on the properties of the motor itself, but also on the relative flow velocity and the current speed of revolution. For example, if the advance ratio equals the pitch ratio, which means that the blades are moving with the fluid without exerting any forces, also called "wind milling", the torque is zero independently of the pulse width. If the relative velocity is increased further, the flow over the propeller even drives the motor, now acting as a generator.

In general, additional information about the state of the thruster must therefore be used to control the generated forces. The thrust and torque coefficient are strictly monotonically decreasing functions of J [159]. The voltage delivered to the motor is chosen to be constant. Measuring the current I provided to the thruster, delivers the advance ratio, as the torque coefficient (5.9b) is invertible. Given the advance ratio, the measurement of the revolution number of the motor delivers the relative velocity using (5.8). The advance ratio together with revolution number delivers the current thrust (5.9a). Now the pulse width can be adapted accordingly. But, this requires the knowledge of the current delivered to each motor and the rotation number of each axle. So far, due to missing feedback from the motors of the thrusters, a fairly simple thruster model is used.

The thrust and torque coefficient have their maximum and their smallest slope at zero advance ratio. The focus of the robot is put on slow motion and high acceleration. Accordingly, the thrust coefficients were taken to be constant. It was further assumed that a unique relation between pulse width and thrust force in the regime of $0 \ldots 2\,\mathrm{m/s}$ incident flow velocity exists. This is acceptable for small advance ratios.

Figure 5.3 shows the measured non-linear characteristic line of the thrust force in both directions for a thruster with a three-blade 50 mm diameter propeller. Measurements were carried out with a thruster mounted on a JR3 six-

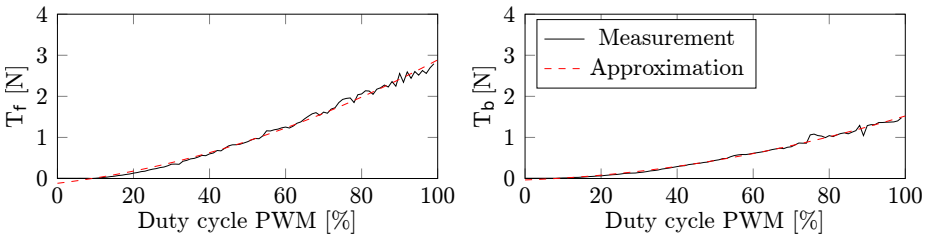

Figure 5.3: *Solid line*: Measured forward (*left*) and reverse (*right*)) thrust. *Dashed line*: 2nd order polynomial approximation.

axis force-torque sensor. It automatically sweeps through the PWM of the motor driver, which results approximately in a current control of the motor for low advance ratios. The resulting characteristic line for forward and backward thrust is fitted with a 2nd-order polynomial function. The forward T_f and backward T_b thrust are given by

$$1T_f = 2 \cdot 10^{-4} x^2 + 1.11 \cdot 10^{-2} x - 1.186 \cdot 10^{-1} \tag{5.10}$$

and

$$T_b = 10^{-4} x^2 + 3.4 \cdot 10^{-3} x - 3.5 \cdot 10^{-2}$$

with $x \in [0, 100]$ for the PWM duty cycle. The resultant external force and torque acting on the total centre of mass given the current thrust T_i of the thrusters $i = 1 \dots 6$ are given by

$$\boldsymbol{F}_T = \sum_{i \in \{1,2,5,6\}} T_i \, \boldsymbol{e}_X - \sum_{i \in \{3,4\}} T_i \, \boldsymbol{e}_Z \tag{5.11}$$

and

$$\boldsymbol{T}_T = \sum_{i \in \{1,2,5,6\}} T_i \boldsymbol{e}_X \times \boldsymbol{\rho}_{Ti} - \sum_{i \in \{3,4\}} T_i \, \boldsymbol{e}_Z \times \boldsymbol{\rho}_{Ti} \, .$$

The respective 6D force vector is denoted by $\mathfrak{F}_T = (\boldsymbol{F}_T, \boldsymbol{T}_T)^{\mathrm{T}}$.

Rigid-body motion with drag, lift and thrust

The inertial forces (4.29) of the rigid body (1.15) complemented by the added masses (5.6) with the origin of the BFS at the geometric centre of hull

$$\frac{\mathfrak{D}\,(\Lambda \mathfrak{U})}{\mathfrak{D}t} = \mathfrak{Q} \tag{5.12}$$

must be balanced by the external forces

$$\mathfrak{Q} = (\mathfrak{F}_L + \mathfrak{F}_F + \mathfrak{F}_H + \mathfrak{F}_T) \, , \tag{5.13}$$

consisting of lift, drag, and thrust, which results in equations similar to the standard equations of submarine motion [152, 160, 161]. It shall be noted that contrary to the convention used in analytical mechanics, where $\mathfrak{Q}$ denotes the forces acting along a generalized coordinate, the first three entries denote the force acting along the respective BFS axes, and the last three components the torques around the axes of the BFS system. These equations can be solved easily by numerical integration in real-time on recent hardware [99]. The transformation of all dynamical quantities to the FOR is given in sec. 1.2.1.

Validity and benefit of the model of the dynamics

Numerous assumptions and simplifications have been made to arrive at equation (5.12). The most important ones shall be briefly reviewed and discussed. The assumptions and approximation were necessary to obtain a treatable model of the dynamics of the robot. The model is far from being perfect since there is no easy solution for the forces exerted on the robot by the surrounding fluid. However, it provides reasonable estimates of the dynamics at low computational efforts.

As briefly discussed in the introduction to sec. 5.1.2, the model is restricted to the motion of the robot in an unbounded inviscid irrotational fluid at rest. No location dependent fluid-mechanical forces like additional pressure forces due to the presence of a wall [154] on the robot exist. The state of motion is fully determined by the translational and rotational velocity. In case additional boundaries were present, the added masses of *Snookie*, if computable at all, had to be adapted by an expression depending on the current position of the robot relative to the surrounding boundaries [154, ch. 4-5]. The effects of a free surface are negligible at sufficiently large distances, typically larger than 5 times the radius of the robot. Significant forces resulting from the interaction with a wall appear at distances smaller than the half of snout radius of *Snookie*, see sec. 2.12.

While the inertia due to the physical mass of the robot are obtained directly from CAD, the estimates of the added masses are composed from the fluid-mechanical inertia of simple shapes resembling the shape of the robot. Each element is treated independently of the others including the thrusters, which means that in the model disturbances of the fluid caused by the elements do not interfere. The conditions for non-viscous estimates of the inertia are strictly only met e.g. at Reynolds numbers up to 10 or 15 or during the early stages of rapid acceleration from rest [152, p. 34 ff.].

Furthermore, it is assumed that the disturbance of the flow field of the robot due to the action of the thrusters is negligible. This assumption is justified for small thrust values and large distances between the thruster and the hull, which is not fulfilled very well for *Snookie*. If one wanted to take the interactions of the thrusters with the hull and the fin into account, one had to deal with added masses depending on the state of all six thrusters in the equations of motions. The added masses could be estimated by 3D BEM simulations or tow car experiments, with the robot attached to a force meter as a function of the six thrust values.

Nevertheless, as soon as additional boundaries like a free surface or a solid wall in close vicinity are present, possibly significant errors are made in the estimation of the added masses as well as in the estimates of forces generated by the thrusters and forces that result from changing added masses. The estimates of the thrust forces required to stop the robot due to the appearance of an obstacle in the range of the ALL, however, remains the same. The added masses are indeed increased in the vicinity of a stationary obstacle. But, without further external forces, the total kinetic energy of the robot and the surrounding fluid remains constant, since the added masses result from the motion of the incompressible, inviscid and irrotational fluid. The robot and the fluid moving with the robot are decelerated to the same extent to which the *added mass* is increased while approaching the stationary object. The power necessary to re-

duce the kinetic energy within a certain distance remains unchanged, no matter if the robot moves close to a wall or in open water. Due to the presence of a wall not only decelerating forces, but also torque might be exerted onto the robot. Therefore, it should be taken care of sufficient thrust reserve. The current strategy to deal with the appearance of an object is to use all available thrusters to decelerate.

Viscosity is accounted for by quasi-stationary semi-empirical drag coefficients. This approximation breaks down at high accelerations. Furthermore, the assumption that viscous drag forces just add linearly to inertial forces and that viscous forces can be decomposed into forward and sidewards forces is only an approximation. The decomposition is correct in the special cases that the vehicle moves forward, sidewards, upward, or downward.

Even if the model of the dynamics of the robot would be perfect, due to the a priori unknown environment of the robot, the motion controller must be flexible enough, react fast enough, and have enough power available to compensate for external effects such as changing boundary conditions like the presence of a wall.

5.1.3 Motor control

The equations of motion (5.12) are the basis to set up a control strategy for the robot. The equations are independent of the position and the orientation of the robot, but couple the velocities of all degrees of freedom. For conventional submarines with a main propeller and steering fins, the equations of motion are usually modelled as decoupled in longitudinal, lateral, and angular motion [161]. For the control of *Snookie* a similar approximation is used. Each degree of freedom is treated independently, since by design the state of motion for basic operation can be reduced to a much lower number of degrees of freedom. The decoupling is achieved simply by restricting the motion, by adding passive stabilising forces due to the lift of the fins, and by shifting the centre of body mass below the centre of buoyancy.

Snookie is supposed to always maintain a horizontal orientation, which means that pitch and roll and the respective angular velocities are small. A change in depth is supposed to happen in pure vertical motion. *Snookie* shall move mainly forward. The yaw angle during forward motion is kept small except for turns in place.

As already mentioned, the centre of mass $\boldsymbol{\rho}_M$ is shifted below the centre of buoyancy. A deflection in roll angle ϕ leads to a restoring force and a slowly damped oscillation about ϕ_0. This oscillation must be damped by a proportional-derivative (PD) controller in ϕ. The lowered centre of mass also leads to a self-stabilisation with a small stability margin about the pitch angle θ. Pitch θ and yaw ψ are stabilised by the fins counteracting Munk's moment – see sec. 5.1.2 – to reduce thrust forces necessary to maintain the orientation with the PD controllers. The angular velocity $\boldsymbol{\omega}$ is implicitly given by the derivative part of the PD controllers for θ and ψ.

At pure forward motion the robot is self-stabilising in the horizontal plane aiding the desired horizontal orientation. The shift of the centre of mass below the geometric centre would lead to a roll motion induced for an acceleration $A_Y \neq 0$ in Y direction and a change in pitch for $A_x \neq 0$, which is counteracted by the fins, as described in sec. 5.1.2. With the robot being kept horizontal, A_Z is decoupled for $\phi \approx 0$ and $\theta \approx 0$, as depth change happens solely through vertical

motion. Depth control is achieved by a proportional–derivative (PD) controller in Z. Finally, forward velocity V_X is controlled by a proportional-integral (PI) controller to counteract a steady-state error.

5.2 The artificial lateral-line system

Research on ALLs, the processing of the sensory data and the transfer to technical systems is not a completely new idea, but faces some inherent challenges, which are still to be solved.

The basic functionality and morphology of the lateral-line system is well known [1, 58, 74]. However, the exact transfer from the hydrodynamic stimulus to the excitation of the sensor [57, 69, 72, 73, 75], the resulting neuronal signals [76–78], and their processing is still under investigation [58, 79–83]. This means that attempts to rebuild the lateral-line system can only lead to an approximation or abstraction of the biological counterpart.

Some groups try to directly mimic the working principle of cricket of fish flow sensors. For air, building biomimetic flow sensors is significantly simpler due to the properties of the medium, especially due to its viscosity and conductivity. Research in biomimetic flow sensing is, e.g. driven by the upcoming interest in insect-like microflight. A review on different technologies in this sector is given by Motamed and Yan [162] highlighting sensor design and experiments. The focus is on the determination of forces acting on the microrobot as a feedback for control. One step further in terms of object/stimulus localisation are projects utilising arrays of biomimetic hair cells (*cilia*) as sensors. Work by Izadi et al. [163] and Dagamseh et al. [164] show the localisation of a dipole source – a vibrating sphere – in air by measuring the deflection of artificial hair sensors. The deflection of the hair induces a capacitive change in the hair base of the sensor, which can be related to the flow velocity. Other artificial cilia are based on the piezoelectric effect, for example with polyvinylidene fluoride fibers (PVDF) [165]. The sensors are either used as surface neuromasts [166–168], or integrated in a canal [60, 169–171]. In principle, both approaches can be used for dipole localisation [169, 172]. An extension of the cilia approach is encapsulating them with a hydrogel cupula [68]. While biomimetic cilia might come close to the biological source of inspiration, the robustness, manufacturing complexity and signal-to-noise ratio are still challenges that prevent the application in an AUV.

A different approach for underwater sensing is to use thermal transport as a means for measuring the flow velocity. Hot-wire anemometers have been used for measuring flow velocities in gases and fluids [173] for a long time, but advances in the miniaturisation make them applicable to ALLs. First trial runs were done by Coombs et al. [174], as a means of "measuring water motions used in stimulating the mechanosensory lateral-line system of a teleost fish". Micromachined arrays of hot-wire elements show the ability of localising dipole sources as good as biomimetic cilia [175–178].

Only recently, there have been some works on the integration of ALLs or comparable sensors on underwater robots. A general overview on the state of underwater robotics is given by Kinsey et al. [179] and Nicholson and Healey [180]. Hsieh et al. [167] describe the implementation of PVDF sensors on a robotic fish, in which the robot is supposed to sense pressure deviations due to the presence of a wall. The modelling of the wall presence is done with an image

charge method that is similar to the method proposed in [99].

5.2.1 Physics of hot thermistor velocimetry

The temperature of the heated element is given by $T = T_\infty + T_\theta$ with T_∞ being the ambient temperature of the fluid and T_θ the over-temperature. The heat dissipation in a fluid from a small element $P \approx (A + Bv^n)\, T_\theta$ is a function of the fluid's relative velocity v, where $n \approx 0.5$ and the constants A and B depend on the geometry and the properties of fluid [173, 181–188]. For a sphere with diameter d [183, 187] the dissipated power can be approximated by

$$P = \left[2 + 0.55 \left(\frac{\nu c_p \rho}{k}\right)^{0.33} \left(\frac{vd}{\nu}\right)^{0.5}\right] 4\pi \left(\frac{d}{2}\right)^2 \frac{k}{d} T_\theta \tag{5.14}$$

with specific heat capacity c_p, heat conductivity k, and kinematic viscosity ν. Constant temperature anemometer sense the velocity of a fluid or gas by measuring the power P necessary to keep a heated element at an over-temperature T_θ.

5.2.2 The artificial lateral-line system of *Snookie*

As summarised in the introduction to this section, several groups have already used different types of sensor concepts to realise an ALL. At present none of these sensors are commercially available yet. Flow sensors available on the market, which would promise acceptable accuracy and stability, can hardly be integrated to an ALL and mounted on a robot. For several reasons, a conservative design decision in favour of hot thermistor velocimetry was made for the ALL of *Snookie*.

There is plenty of theory and experience with a very similar sensor concept, the hot wire. Hot wires were shown to in principle provide the necessary accuracy and temporal resolution [100, 174]. The electronics and the sensors are relatively easy to develop and fabricate. The energy dissipation of the smallest commercially available thermistors allows high integration densities and low energy consumption. A small thermistor can be embedded in solid material providing the robustness necessary for operation on a moving robot.

Thermistors are semiconductors with a non-linear negative dependency of the electrical resistance upon the temperature. In previous versions of the flow sensors, as described in [141], glass-coated thermistors with a diameter of 0.36 mm from the Honeywell 111 series were used as heated elements for the artificial lateral-line sensors of Snookie, see fig. 5.4. The resistance $R_\vartheta \approx 240\,\Omega$ of a thermistor at working temperature $T \approx 80°$ C with an over-temperature T_θ of approximately 60° C is

$$R_\vartheta = R_0 e^{\beta_\vartheta (1/T_0 - 1/T)}\,, \tag{5.15}$$

given the resistance $1400\,\Omega < R_0 < 2.4\,\mathrm{k}\Omega$ at room temperature T_0 and the constant $2000\,°\mathrm{K} < \beta_\vartheta < 5000\,°\mathrm{K}$. To sustain a constant thermistor temperature the supplied electrical power $P = P_{el} = UI = U^2/R_\vartheta$ must equal the dissipated energy, if all energy is converted to heat and no leakage currents, e.g. due to deficient isolation appear. The voltage to keep the thermistor at a constant resistance — and thus at constant temperature — is provided by

specially designed boards, which incorporate a Wheatstone bridge and a two-stage amplifier. A cooling of the sensor due to changed flow conditions leads to an imbalance of the resistances in the branches of the Wheatstone bridge, which in turn leads to a potential difference across the bridge. The potential difference is amplified with an instrumental amplifier (INA103-KU low-noise, low-distortion instrumental amplifier) and filtered in a RLC low-pass filter with a cut-off frequency of $fc = 65\,\mathrm{kHz}$. The filter is employed to prevent spikes and high frequency electromagnetic interference. The signal is recorded by a DAQ card providing a measure for the fluid velocity. The amplified and filtered potential difference is also fed back to a second instrumental amplifier, which acts as a supply for the Wheatstone bridge. Adjusting the voltage over the bridge compensates any resistance (or temperature) deviation of the thermistor. The thermistor is placed at the tip of a bullet shaped casing, see fig. 5.4 and fig. 5.5 that provides the thermistor with mechanical stability, shields the wiring from the water, and allows to easily mount the sensors.

The following rough estimates show that it is entirely legitimate to treat the thermistor adiabatically in the sense that it immediately adapts its temperature and thereby its resistance to changes in the transport of heat, as it has been implicitly assumed in the thermistor model. The voltage necessary to maintain a stable resistance of about $240\,\Omega$ of the thermistor in water at rest is approximately $1.5\,\mathrm{V}$, though the properties of the individual sensors are scattered. This results in a dissipated power of approximately $9\,\mathrm{mW}$. For comparison, the total heat stored in a sphere of the size of the thermistor with over-temperature 60° C made of silicon or glass is only less than a factor of three larger than the heat dissipated per second. Within a temperature range of 60° the thermistor changes its resistance by approximately a factor of five. A change of the heat transport due to changing flow conditions must be therefore immediately compensated by a change in the voltage supplied to the thermistor to hold a constant temperature. The voltage

$$U^2 \approx R_\vartheta (A + Bv^n) T_\theta \tag{5.16}$$

over the sensor is therefore an adiabatic measure for the fluid velocity. The application of the calibration function to obtain the actual fluid velocity is implemented in software.

The properties of the thermistor regarding the time constant, the power consumption, and the sensitivity perfectly meet the requirements of an ALL. The thermistor itself consists of a glass-coated spherical semi-conductor and two thin platinum-iridium wires protruding from the thermistor at opposite sides. However, it turned out to be very difficult to, on the one hand, isolate the thin wires from the water and to mount the thermistor thermally and mechanically stable, and, on the other hand, to maintain good thermal contact to the water. Many tests with different materials to embed the sensors were carried out. After ongoing stability and manufacturing problems, and after a series of tests of alternatives, it was decided to switch to thermistors of the General Electric FP07 series (FP07DA802N). Although specified with a slightly larger time constant of $7\,\mathrm{ms}$, the great advantage of these thermistors is that the glass-coated thermistor sits on top of a thin glass rod, see fig. 5.5, with the wires shielded inside the glass rod for several millimetres. The isolation of the wires by the glass rod solves the mechanical stability, the electrical shielding,

and the problem of high temperature differences leading to mechanical stresses around the thermistor between the on and off state. The essential properties of the new thermistors are as already mentioned an increased specified time constant of 7 ms, a reduced power dissipation of 0.25 mW/C° at 25 C°, leading to a power dissipation of 15 mW/C° at an overtemperature of 60 C°. At this overtemperature an estimated heat energy of approximately 25 mJ is stored in the thermistor. The resistance at a temperature of 25 C° is about $8\,\mathrm{k}\Omega \pm 25\%$ and changes about a factor of 12 over a temperature difference of 60 C°. Not only the electric properties vary greatly between the single thermistors, but also the precise shape of the glass coating and the position of the thermistor on the glass rod, which affects the transport of heat to the fluid. To be useful for flow sensing at all, each sensor needs a careful calibration. The large differences in the resistance compared to the previously used Honeywell thermistors enforced changes in the layout of the Wheatstone bridge of the amplifier boards and the power supply.

This, however, induced severe complications with the INA103-KU amplifiers. Although the amplifiers were able to provide the thermistor with sufficient voltage during operation, the high resistance of the thermistors at switch-on time and the high voltage demanded from the amplifiers lead to uncontrolled and indeterministic behaviour of the amplifiers, also mentioned in their manual, including an inversion of the signal provided to the DAQ and an additional uncontrolled offset. As soon as the thermistors are heated, the behaviour of the amplifiers is perfectly deterministic, except from strong temperature drifts of the amplifiers with a timescale of approximately 5 s, which can be controlled by cooling, see the white fans in fig. 5.6. Together with the requirements for a unnecessarily complicated power supply (3 voltage levels), these were the deciding factors to push the development of new thermistor control boards based on a only recently available instrumentation amplifier by Analog Devices (AD8220). First test runs with a prototype promise to solve the problems mentioned. The development and the fabrication of the boards did not proceed fast enough for being able to present a calibration and tests of the flow field reconstruction and the collision warning methods described in ch. 3 and sec. 4.4 in this work. The calibration of four sensors shown in the next subsection was carried out with an adapted old thermistor control board and the new flow sensors. Due to the uncontrolled behaviour of the amplifiers at switch-on the calibration shown in the next section may be seen as a proof of the sensor concept.

5.2.3 Flow-sensor calibration

The flow sensor calibration was realised with a tow car. A linear motor (Thrust-Tube, motor 2504 from Copley Controls, encoder resolution 10 μm) pulled the sensor through a swimming pool of a diameter of 5 m and a depth of 1.20 m, see fig. 5.6. With constant acceleration from rest all velocities from 0 to 70 cm/s were present in one measurement. The flow sensors were mounted perpendicular to the direction of motion on a flat plate of thickness 3 mm oriented parallel to the direction of motion, with the thermistors pointing downwards into the fluid. The fitting of the sensors, the cables, and the rod connecting the plate with the linear axis were located on the upper side of the plate and thus not disturbing the homogeneous flow over the sensor at the bottom side of the plate. Furthermore, due to the size of the plate, vibrations in the vertical direction of

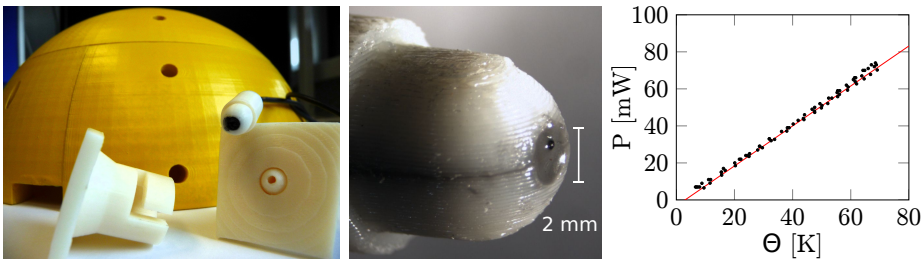

Figure 5.4: *Left*: Hull integration. *Middle*: Close-up view of the artificial lateral-line sensor. *Right:* Power dissipated by a thermistor ($R_0 = 1523\,\Omega$ at $T_0 \approx 293\,\mathrm{K}$, mounted on a PCB board and coated) in water vs. over-temperature T_θ. *Black dots*: Measurement of dissipated power P. *Red line*: Linear fit. The relation between energy dissipation and over-temperature is perfectly linear ($1.8\,\mathrm{mW/K}$) as predicted by theory.

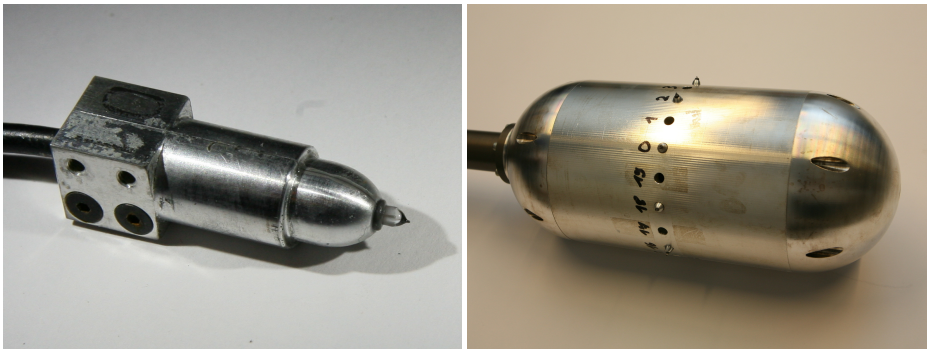

Figure 5.5: *Left*: Artificial lateral-line sensor consisting of a thermistor (GE FP07), the tiny black dot on the glass tip, in an aluminium casing. *Right:* An aluminium body with a diameter of 15 cm and a height of 35 cm with sensor mountings (partly equipped with flow sensors), used as dummy for *Snookie* dragged past, e.g. stationary obstacles, to test the artificial lateral-line system and the flow reconstruction methods.

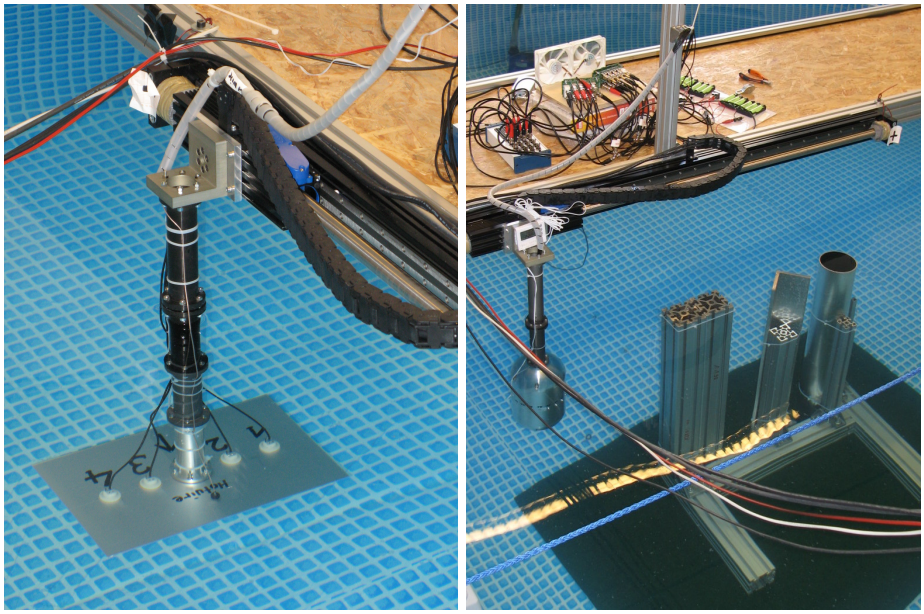

Figure 5.6: *Left*: An aluminium plate dragged by a linear axis used as carrier for the flow-sensor calibration. Four flow sensors mounted in the white plastic holders point downwards into fluid, placed close to the bottom surface of the aluminium plate. Additionally, for comparison, a constant-temperature hot-wire probe by Dantec records the flow field in parallel, protruding approximately 3 cm from the surface of the aluminium plate downwards into the fluid. *Right:* The aluminium body of fig. 5.5, used as dummy for *Snookie*, dragged past stationary obstacles by a linear axis to test the artificial lateral-line and the flow reconstruction.

the bridge spanning the pool and carrying the linear axis and the electronics hardly affected the flow field around the thermistors, since they were placed at the stagnation point of the plate for motion in vertical direction. The flow velocity at the tip of the sensors was thus very accurately approximated by the velocity of the linear axis. The fitting of the sensor through the plate were the same as the fittings in the snout of *Snookie*, see fig. 5.4, and thus the location of the thermistor at the tip of the sensors relative to the surface were the same as if they were mounted on the robot. Consistent initial conditions with the fluid at rest in the pool were obtained simply by waiting for the water to settle in between tests.

The voltage applied to the sensors was sampled with 10 kHz and recorded with a DAQ card. A low pass filter with a smooth transition (3rd order polynomial) from total transmission at 75 Hz to total filtering at 500 Hz was applied to the sensor readings. The processing of the position data provided by the linear axis is discussed further below in this subsection. The voltages of each sensors were sorted on the corresponding velocity, see fig. 5.7. To obtain the calibration function, the calibrations curves were fitted with

$$v = \sqrt[n]{\widetilde{A}U^2 + \widetilde{B}}\,, \tag{5.17}$$

which would be expected by inversion of (5.16), which in turn results from (5.14). Surprisingly, a power law of the suggested form only applies for high fluid velocities, but with different parameters than expected for a sphere (5.14). Throughout all calibrations, independent of the acceleration of the linear axis, a piecewise fit function of the form

$$v(U) = \begin{cases} a + bU^{1/2} + cU^{3/2} + dU^{5/2} & \text{if } U \le U_L \\ aU^5 + bU^4 + cU^3 + dU^2 + eU + f & \text{if } U_L < U < U_H \\ a\,(U-b)^6 & \text{if } U \ge U_H \end{cases} \tag{5.18}$$

with suitably chosen bounds U_L and U_H, separating the low, the middle, and the high velocity regime, excellently describes the velocity as a function of the thermistor voltage. Calibration curves for four sensors, all recorded on the same run, can be seen in fig. 5.7. Larger deviations from the calibration curve can be seen only in the velocity range around 15 cm/s. These variations coincide well with a short decrease of the linear axis velocity at a certain linear axis position and are closely related to the difficulties to control the motion of the calibration holder and therefore the flow velocity at the sensors by control of the linear axis velocity. It seems that induced by the unsteady motion some transition in the flow field over the sensors occurs. The velocity of the linear axis was computed from the derivative of a 3rd order spline least square fitted to the position data provided by the linear axis. The fitting parameters (essentially the number of position data used to compute one segment of the spline) were chosen by inspection in a series of test runs such that the variance of the calibration curve became minimal. The reason for this procedure was that no precise independent direct observation of the relative flow velocity between the thermistor and the fluid at the thermistor tip is possible. The precise control of the velocity of the linear axis is difficult for several reasons. A resolution of the position of 10 μm is sufficient for most positioning tasks, but it is not sufficient to obtain a good estimate of the current velocity at a rate of 1000 Hz

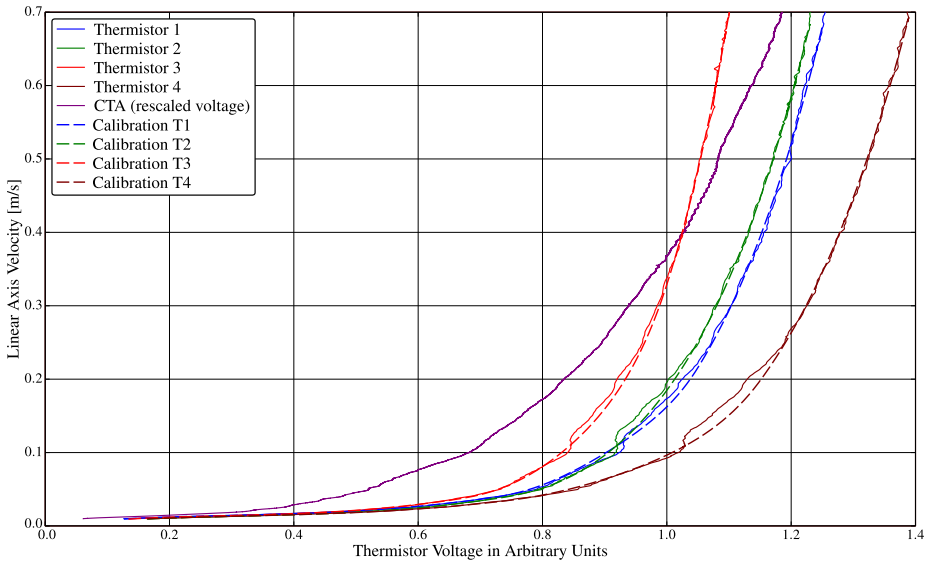

Figure 5.7: Calibration curves of four sensors obtained from a calibration run as depicted in fig. 5.6. The linear axis velocity closely approximates the local fluid flow velocity by design of the calibration holding. For comparison a constant-temperature hot-wire velocimeter by Dantec was simultaneously recorded.

required by the linear-axis controller. Second, the control of a constant velocity is complicated by the fact that position dependent forces such as a changing friction are usually not foreseen in the control of a linear axes. And finally, the probe holder does not immediately follow the linear motor due to its inertia and due to finite tolerances. In summary, it is impossible to improve the calibration of the linear axis by filtering, except for the high frequency noise introduced by the activity of the controller. Nevertheless, the calibration curves perfectly match the sensor readings, except for the velocity range between 15 cm/s and 30 cm/s. The resolution of the sensors will sufficient to demonstrate the fluid flow reconstruction developed in ch. 3 in a suitable designed experiment, see fig. 5.6.

5.3 Conclusion

In this chapter, the design and the hardware of the robot were briefly described. The control of the motion of the robot is based on a linearisation of the dynamical model. The model accurately reflects the dynamics of the robot as long as the robot does not approach other objects closer than approximately half of its snout radius. The largest improvement of the dynamics of the robot can be achieved by stronger thrusters with an improved model based thrust control. This requires a thruster model based on the voltage and current provided to a motor, the rotation number of the propeller axle, and eventually the speed of the fluid relative to the thruster. The model based thruster control could be verified during operation, if the force generated by each thruster was monitored by direct measurement. The force measurement could also be used to account

for hydrodynamic interactions of the thrusters with the hull of the robot and the environment.

The progress in the development of the flow sensors and the improvements of the experimental situation is evident by a comparison with the results obtained with the previous sensor generation [141]. The major contributions to an improved experimental situation are the large swimming pool placed on a solid foundation and the fluid-mechanical design of the calibration holder. The stability and endurance of the new thermistors allowed to systematically identify and remove sources of distortions on the recorded sensors readings, particularly the thermal drifts of the amplifiers and the power supply. A prototype of the currently developed new thermistor control board showed an even better electronic noise level. The stability problems occurring due to the operation of the new thermistors on the adapted old thermistor control boards seem to be solved. A discussion of the noise introduced by the electronics can be found in [138]. It is negligible compared to deviations in the flow field from the expected fluid flow velocity at the tip of the sensor, e.g. introduced by passing a region of vorticity present in the otherwise quiescent fluid during of a calibration run. Accordingly, the largest improvements of the calibration can be achieved by a better control of the movement of the linear axis, e.g. by incorporating acceleration sensors on the linear axis and the calibration mounting.

Chapter 6

Summary

In this work the knowledge about the flow-sensory systems of fish and crickets has been used as source of inspiration for the development of an ALL. The ALL is supposed to be mounted on an autonomous underwater vehicle called *Snookie*. To be able to utilize the perception of the environment through a flow-sensory system on a moving robot, severe requirements due to its limited range of view follow for the dynamics of the robot. A dynamical model of the robot, see ch. 5, including added masses, drag, lift generated from the fins, and the thrusters, has been developed. The model incorporates the dependence of the total mass, composed of the physical mass and the added masses, and the dependence of the centre of the total mass on the direction of motion. These effects are usually neglected for streamlined underwater vehicles moving mainly straight ahead. The model captures the essential effects of the dynamics of *Snookie* in all degrees of freedom and can serve as the basis to extend the currently used simple motion controller to motion in further degrees of freedom.

The added mass formalism introduced for the dynamics of the robot, see sec. 4.3, inspired a heuristics for the detection of objects appearing in the range of the FSS. This heuristic, see sec. 4.4, requires little computational effort, and is able to filter background fluid motion on length scales larger than the size of the FSS. Due to its efficiency and speed, it will be implemented as a ROS node in parallel to the flow-field reconstruction, acting as collision warning system.

The biological source of inspiration [15, 29, 189, 190] of *Snookie* is known to solve quite complex tasks on the basis of fluid-flow perception, e.g. map formation of the environment and self-localisation. The flow-field reconstruction methods described in ch. 3 can serve as the basis for such high level tasks. To the knowledge of the author, no theory for an inversion of the hydrodynamic image or on inverse problems in fluid-mechanics exists so far. The flow-field reconstruction introduced in ch. 3 is the indispensable basis to take advantage of flow sensing for high level tasks. It allows to extract the location, size and shape of solid objects from the reconstructed flow field, and it is in principle capable of discerning them from vortex structures. Using the simple frequency-regularised version of a 2D flow reconstruction from a circle, is was shown in simulations, that similar capabilities can be implemented on *Snookie*. *Snookie* is equipped with an inertia sensor system, see sec. 5.1.1, enabling the robot to estimate the current acceleration and by integration the current speed and relative position. Based on its own position, *Snookie* can use the extracted shape of stationary solid objects

to build up a map of the boundaries of the fluid. One challenge is that the quality of a map generated during motion depends on the accuracy of the position estimate, which is subject to drift. To counteract this drift, usually external references such as GPS are used, which is unavailable underwater. A method without external signals is called simultaneous localisation and mapping (SLAM) [191]. It builds a map of the environment on the fly, which can then be used for matches to verify the position. Although the reconstruction of the environment around the robot is due to its mathematical nature restricted to a close range, the matching of the reconstructed wall against the existing continuously refined map allows to compensate for the drifts of the inertial sensory system [138, 139].

To be widely applicable and useful under variable environmental conditions, several problems had to be solved in the development of an ALL. First, the reconstruction due to the nature of the problem is very sensitive against small errors in the flow velocity measurement. This requires a precise and carefully calibrated set of flow sensors. Furthermore, the sensors must be robust and stable enough to be mounted on a moving robot. The energy consumption of the sensors and the disturbances introduced into the fluid by the sensors must be small enough, so that they can be reasonably integrated to an ALL. The sensors and the electronics developed for the ALL of Snookie, see sec. 5.2, meet this requirement.

Potential flow is assumed for the flow-field reconstruction as well as for the object detection heuristics, see sec. 2.2. In real fluids, potential flow around the FSS can be expected during motion in an otherwise quiescent fluid. At present, no theory is available to estimate the errors introduced by deviations from potential flow, or how to deal with the complete break down of potential flow.

The next step in the development of the ALL is the experimental demonstration of a successful reconstruction of a stationary environment from a moving object under ideal potential flow conditions, see fig. 5.6.

Acronyms

2D	2-dimensional
3D	3 dimensions
6D	6-dimensional
ALL	*artificial lateral-line system*
AUV	*autonomous underwater vehicle*
BEM	boundary-element method
BFS	*body-fixed system*
CAD	computer aided design
CAN	controller area network
CLS	*canal lateral-line system*
CN	canal neuromast
DAQ	data acquisition
DC	direct current
FSS	flow-sensory system
GPS	Global Positioning System
IID	identically independently distributed
FOR	*frame of reference*
LLS	*lateral-line system*
MEMS	micro-electro-mechanical systems
PC	Personal Computer
PD	proportional-derivative
PI	proportional-integral
PID	proportional-integral-derivative
PVDF	polyvinylidene fluoride fibers
PWM	pulse-width modulation
RLC	resistance-inductance-capacitance
ROS	Robot Operating System
SLAM	simultaneous localisation and mapping
SLS	*superficial lateral-line system*
SN	superficial neuromast
SNR	signal-to-noise ratio

Bibliography

[1] H. Bleckmann and R. Zelick. Lateral line system of fish. *Integrative Zoology*, 4(1):13–25, 2009.

[2] R. Winklbauer. Development of the lateral line system in Xenopus. *Progress in neurobiology*, 32(3):181–206, January 1989.

[3] J.-M. Franosch, H. Hagedorn, J. Goulet, J. Engelmann, and J. L. van Hemmen. Wake tracking and the detection of vortex rings by the canal lateral line of fish. *Physical Review Letters*, 103(7), 2009.

[4] B. U. Budelmann and H. Bleckmann. A lateral line analogue in cephalopods: water waves generate microphonic potentials in the epidermal head lines ofSepia andLolliguncula. *Journal of Comparative Physiology A*, 164(1):1–5, 1988.

[5] S. Komak, J. G. Boal, L. Dickel, and B. U. Budelmann. Behavioural responses of juvenile cuttlefish (Sepia officinalis) to local water movements. *Marine and Freshwater Behaviour and Physiology*, 38(2):117–125, June 2005.

[6] J. Lancaster and B. J. Downes. *Aquatic Entomology*. Oxford University Press, 2013.

[7] W. Gnatzy and K. Schmidt. Die Feinstruktur der Sinneshaare auf den Cerci von Gryllus bimaculatus Deg. (Saltatoria, Gryllidae). *Zeitschrift für Zellforschung und mikroskopische Anatomie*, 122(2):190–209, June 1971.

[8] F. G. Barth. How to catch the wind: spider hairs specialized for sensing the movement of air. *Die Naturwissenschaften*, 87(2):51–8, February 2000.

[9] A. N. Popper, R. R. Fay, C. Platt, and O. Sand. Sound Detection Mechanisms and Capabilities of Teleost Fishes. In S. P. Collin and N. J. Marshall, editors, *Sensory Processing in Aquatic Environments*, chapter 1, pages 3–38. Springer New York, 2003.

[10] F. G. Barth. The Slightest Whiff of Air: Airflow Sensing in Arthropods. In H. Bleckmann, J. Mogdans, and S. L. Coombs, editors, *Flow Sensing in Air and Water*, chapter 7, pages 169–196. Springer Berlin Heidelberg, 2014.

[11] O. Dangles, N. Ory, T. Steinmann, J.-P. Christides, and J. Casas. Spider's attack versus cricket's escape: velocity modes determine success. *Animal Behaviour*, 72(3):603–610, September 2006.

[12] C. von Campenhausen, I. Riess, and R. Weissert. Detection of stationary objects by the blind cave fish *Anoptichthys jordani* (*Characidae*). *Journal of Comparative Physiology A*, 143:369–374, 1981.

[13] R. Weissert and C. von Campenhausen. Discrimination between stationary objects by the blind cave fish *Anoptichthys jordani* (*Characidae*). *Journal of Comparative Physiology A*, 143(3):375–381, 1981.

[14] T. Teyke. Learning and remembering the environment in the blind cave fishAnoptichthys jordani. *Journal of Comparative Physiology A*, 164(5): 655–662, 1989.

[15] T. Burt de Perera. Spatial parameters encoded in the spatial map of the blind Mexican cave fish, *Astyanax fasciatus*. *Animal Behaviour*, 68(2): 291–295, 2004.

[16] S. Dijkgraaf. Untersuchungen über die Funktion der Seitenorgane an Fischen. *Zeitschrift für Vergleichende Physiologie*, 20(1-2):162–214, 1933.

[17] S. Dijkgraaf. The functioning and significance of the lateral-line organs. *Biological Reviews*, 38(1):51–105, 1963.

[18] W. J. Van Trump and M. J. McHenry. The morphology and mechanical sensitivity of lateral line receptors in zebrafish larvae (*Danio rerio*). *The Journal of Experimental Biology*, 211(13):2105–15, 2008.

[19] J. Mogdans and H. Bleckmann. Coping with flow: behavior, neurophysiology and modeling of the fish lateral line system. *Biological Cybernetics*, 106(11-12):627–42, 2012.

[20] E.-S. Hassan. Hydrodynamic Imaging of the Surroundings by the Lateral Line of the Blind Cave Fish Anoptichthys jordani. In S. Coombs, P. Görner, and H. Münz, editors, *The Mechanosensory Lateral Line*, pages 217–227. Springer New York, 1989.

[21] M. S. Howe. *Hydrodynamics and Sound*. Cambridge University Press, 2006.

[22] S. Coombs. Nearfield detection of dipole sources by the goldfish (*Carassius auratus*) and the mottled sculpin (*Cottus bairdi*). *The Journal of Experimental Biology*, 190(1):109–129, 1994.

[23] S. Coombs and R. A. Conley. Dipole source localization by mottled sculpin I. approach strategies. *Journal of Comparative Physiology A*, 180(4):387–399, 1997.

[24] R. A. Conley and S. Coombs. Dipole source localization by mottled sculpin III. orientation after site-specific, unilateral denervation of the lateral line system. *Journal of Comparative Physiology A*, 183(3):335–344, 1998.

[25] S. Coombs, C. B. Braun, and B. Donovan. The orienting response of Lake Michigan mottled sculpin is mediated by canal neuromasts. *The Journal of Experimental Biology*, 204(2):337–348, 2001.

[26] S. Coombs and P. Patton. Lateral line stimulation patterns and prey orienting behavior in the Lake Michigan mottled sculpin (*Cottus bairdi*). *Journal of Comparative Physiology A*, 195(3):279–97, 2009.

[27] D. Vogel and H. Bleckmann. Behavioral discrimination of water motions caused by moving objects. *Journal of Comparative Physiology A*, 186(12): 1107–1117, 2001.

[28] B. L. Partridge and T. J. Pitcher. The sensory basis of fish schools: Relative roles of lateral line and vision. *Journal of Comparative Physiology A*, 135(4):315–325, 1980.

[29] T. Teyke. Collision with and avoidance of obstacles by blind cave fish *Anoptichthys jordani* (*Characidae*). *Journal of Comparative Physiology A*, 157(6):837–843, 1985.

[30] E. S. Hassan. On the discrimination of spatial intervals by the blind cave fish (*Anoptichthys jordani*). *Journal of Comparative Physiology A*, 159 (5):701–710, 1986.

[31] S. P. Windsor, D. Tan, and J. C. Montgomery. Swimming kinematics and hydrodynamic imaging in the blind Mexican cave fish (*Astyanax fasciatus*). *Journal of Experimental Biology*, 211(18):2950–2959, 2008.

[32] W. Hanke, C. Brucker, and H. Bleckmann. The ageing of the low-frequency water disturbances caused by swimming goldfish and its possible relevance to prey detection. *The Journal of Experimental Biology*, 203(7): 1193–1200, 2000.

[33] W. Hanke. The hydrodynamic trails of *Lepomis gibbosus* (*Centrarchidae*), *Colomesus psittacus* (*Tetraodontidae*) and *Thysochromis ansorgii* (*Cichlidae*) investigated with scanning particle image velocimetry. *Journal of Experimental Biology*, 207(9):1585–1596, 2004.

[34] K. Pohlmann, F. W. Grasso, and T. Breithaupt. Tracking wakes: the nocturnal predatory strategy of piscivorous catfish. *Proceedings of the National Academy of Sciences of the United States of America*, 98(13): 7371–4, 2001.

[35] K. Pohlmann, J. Atema, and T. Breithaupt. The importance of the lateral line in nocturnal predation of piscivorous catfish. *The Journal of Experimental Biology*, 207(17):2971–8, 2004.

[36] G. Dehnhardt, B. Mauck, W. Hanke, and H. Bleckmann. Hydrodynamic trail-following in harbor seals (*Phoca vitulina*). *Science (New York, N.Y.)*, 293(5527):102–4, 2001.

[37] S. Wieskotten, B. Mauck, L. Miersch, G. Dehnhardt, and W. Hanke. Hydrodynamic discrimination of wakes caused by objects of different size or shape in a harbour seal (*Phoca vitulina*). *The Journal of Experimental Biology*, 214(11):1922–30, 2011.

[38] O. Akanyeti, R. Venturelli, F. Visentin, L. Chambers, W. M. Megill, and P. Fiorini. What information do Kármán streets offer to flow sensing? *Bioinspiration & Biomimetics*, 6(3):036001, 2011.

[39] R. A. Handelsman and J. B. Keller. Axially symmetric potential flow around a slender body. *Journal of Fluid Mechanics*, 28(01):131–147, 1967.

[40] J. Geer. Uniform asymptotic solutions for potential flow about a slender body of revolution. *Journal of Fluid Mechanics*, 67(04):817–827, 1975.

[41] E.-S. Hassan. Mathematical analysis of the stimulus for the lateral line organ. *Biological Cybernetics*, 52(1):23–36, 1985.

[42] E.-S. Hassan. Mathematical description of the stimuli to the lateral line system of fish derived from a three-dimensional flow field analysis I. The cases of moving in open water and of gliding towards a plane surface. *Biological Cybernetics*, 66(5):453–461, 1992.

[43] E.-S. Hassan. Mathematical description of the stimuli to the lateral line system of fish derived from a three-dimensional flow field analysis II. The case of gliding alongside or above a plane surface. *Biological Cybernetics*, 66(5):443–452, 1992.

[44] E.-S. Hassan. Mathematical description of the stimuli to the lateral line system of fish, derived from a three-dimensional flow field analysis III. The case of an oscillating sphere near the fish. *Biological Cybernetics*, 69 (5-6):525–538, 1993.

[45] R. Panton. *Incompressible flow*. J. Wiley, New York, 3rd ed. edition, 2005.

[46] H. Oertel and K. Mayes, editors. *Prandtl's Essentials of Fluid Mechanics*. Applied Mathematical Sciences. Springer, 2nd edition, 2004.

[47] A. Sichert, R. Bamler, and J. L. van Hemmen. Hydrodynamic object recognition: When multipoles count. *Physical Review Letters*, 102(5), 2009.

[48] J. M. Camhi and W. Tom. The escape behavior of the cockroachPeriplaneta americana. *Journal of Comparative Physiology ? A*, 128(3):193–201, 1978.

[49] H. GRAS and M. HORNER. Wind-Evoked Escape Running of the cricket Gryllus Bimaculatus: I. Behavioural Analysis. *J. Exp. Biol.*, 171(1):189–214, October 1992.

[50] E. Tauber and J. Camhi. The wind-evoked escape behavior of the cricket Gryllus bimaculatus: integration of behavioral elements. *J Exp Biol*, 198: 1895–1907, 1995.

[51] W. Gnatzy and G. Kämper. Digger wasp against crickets. II. An airborne signal produced by a running predator. *Journal of Comparative Physiology A: Neuroethology, Sensory, Neural, and Behavioral Physiology*, 167(4): 551–556, September 1990.

[52] J. Casas, T. Steinmann, and O. Dangles. The Aerodynamic Signature of Running Spiders. *PLoS ONE*, 3(5):2116—-, 2008.

[53] H. Bleckmann, T. Breithaupt, R. Blickhan, and J. Tautz. The time course and frequency content of hydrodynamic events caused by moving fish, frogs, and *Crustaceans*. *Journal of Comparative Physiology A*, 168(6), 1991.

[54] F. G. Barth and A. Holler. Dynamics of arthropod filiform hairs. V. The response of spider trichobothria to natural stimuli. *Philosophical Transactions of the Royal Society B: Biological Sciences*, 354(1380):183–192, January 1999.

[55] A. J. Hudspeth, Y. Choe, A. D. Mehta, and P. Martin. Putting ion channels to work: mechanoelectrical transduction, adaptation, and amplification by hair cells. *Proc. Natl. Acad. Sci. U. S. A.*, 97(22):11765–11772, 2000.

[56] S. M. van Netten and C. J. Kros. Gating energies and forces of the mammalian hair cell transducer channel and related hair bundle mechanics. *Proceedings. Biological sciences / The Royal Society*, 267(1455):1915–23, September 2000.

[57] S. M. van Netten. Hydrodynamic detection by cupulae in a lateral line canal: functional relations between physics and physiology. *Biological Cybernetics*, 94(1):67–85, 2006.

[58] H. Bleckmann. Peripheral and central processing of lateral line information. *Journal of Comparative Physiology A*, 194(2):145–158, 2008.

[59] J. Webb. Lateral Line Morphology and Development and Implications for the Ontogeny of Flow Sensing in Fishes. In H. Bleckmann, J. Mogdans, and S. L. Coombs, editors, *Flow Sensing in Air and Water*, chapter 10, pages 247–270. Springer Berlin Heidelberg, 2014.

[60] A. Klein, H. Münz, and H. Bleckmann. The functional significance of lateral line canal morphology on the trunk of the marine teleost *Xiphister atropurpureus* (*Stichaeidae*). *Journal of comparative physiology A*, 199(9): 735–49, 2013.

[61] H. Bleckmann. Role of the Lateral Line in Fish Behaviour. In T. Pitcher, editor, *The Behaviour of Teleost Fishes*, pages 177–202. Springer US, 1986.

[62] C. Schemmel. Vergleichende Untersuchungen an den Hautsinnesorganen ober- und unterirdisch lebender Astyanax-Formen. *Zeitschrift für Morphologie der Tiere*, 61(2):255–316, 1967.

[63] C. Pozrikidis. *Introduction to Theoretical and Computational Fluid Dynamics*. Oxford University Press, 2 edition, 9 2011.

[64] J. A. C. Humphrey. Drag force acting on a neuromast in the fish lateral line trunk canal. II. Analytical modelling of parameter dependencies. *Journal of the Royal Society, Interface / the Royal Society*, 6(36):641–53, July 2009.

[65] C. Barbier and J. A. C. Humphrey. Numerical calculation of the flow in the fish lateral line canal: Applications to predators tracking prey. In *Fluids Engineering*, number 47705, pages 283–292. ASME, 2006.

[66] C. Barbier and J. A. C. Humphrey. Drag force acting on a neuromast in the fish lateral line trunk canal. I. Numerical modelling of external-internal flow coupling. *Journal of the Royal Society, Interface / the Royal Society*, 6(36):627–40, July 2009.

[67] T. Teyke. Morphological differences in neuromasts of the blind cave fish Astyanax hubbsi and the sighted river fish Astyanax mexicanus. *Brain, behavior and evolution*, 35(1):23–30, January 1990.

[68] S. Peleshanko, M. D. Julian, M. Ornatska, M. E. McConney, M. C. LeMieux, N. Chen, C. Tucker, Y. Yang, C. Liu, J. A. C. Humphrey, and V. V. Tsukruk. Hydrogel-encapsulated microfabricated haircells mimicking fish cupula neuromast. *Advanced Materials*, 19(19):2903–2909, 2007.

[69] M. J. McHenry, J. A. Strother, and S. M. van Netten. Mechanical filtering by the boundary layer and fluid-structure interaction in the superficial neuromast of the fish lateral line system. *Journal of Comparative Physiology A*, 194(9):795–810, 2008.

[70] S. van Netten and M. McHenry. The Biophysics of the Fish Lateral Line. In S. Coombs, H. Bleckmann, R. R. Fay, and A. N. Popper, editors, *The Lateral Line System*, volume 48 of *Springer Handbook of Auditory Research*, chapter 14, pages 99–119. Springer New York, 2014.

[71] J. Goulet, J. L. van Hemmen, S. N. Jung, B. P. Chagnaud, B. Scholze, and J. Engelmann. Temporal precision and reliability in the velocity regime of a hair-cell sensory system: the mechanosensory lateral line of goldfish, Carassius auratus. *Journal of neurophysiology*, 107(10):2581–93, May 2012.

[72] S. Coombs, M. Hastings, and J. Finneran. Modeling and measuring lateral line excitation patterns to changing dipole source locations. *Journal of Comparative Physiology A*, 178(3), 1996.

[73] B. Curcić-Blake and S. M. van Netten. Rapid responses of the cupula in the lateral line of ruffe (*Gymnocephalus cernuus*). *Journal of Comparative Physiology A*, 191(4):393–401, 2005.

[74] S. Coombs and S. M. van Netten. The hydrodynamics and structural mechanics of the lateral line system. *Fish Physiology*, 23:103–139, 2005.

[75] J. Goulet, J. Engelmann, B. P. Chagnaud, J.-M. P. Franosch, M. D. Suttner, and J. L. van Hemmen. Object localization through the lateral line system of fish: theory and experiment. *Journal of Comparative Physiology A*, 194(1):1–17, 2008.

[76] S. Coombs and R. A. Conley. Dipole source localization by the mottled sculpin II. the role of lateral line excitation patterns. *Journal of Comparative Physiology A*, 180(4):401–415, 1997.

[77] J. Engelmann, W. Hanke, and H. Bleckmann. Lateral line reception in still- and running water. *Journal of Comparative Physiology A*, 188(7): 513–26, 2002.

[78] B. P. Chagnaud, H. Bleckmann, and J. Engelmann. Neural responses of goldfish lateral line afferents to vortex motions. *The Journal of Experimental Biology*, 209(2):327–42, 2006.

[79] S. Kröther, J. Mogdans, and H. Bleckmann. Brainstem lateral line responses to sinusoidal wave stimuli in still and running water. *The Journal of Experimental Biology*, 205(10):1471–84, 2002.

[80] D. T. T. Plachta. A hydrodynamic topographic map in the midbrain of goldfish *Carassius auratus*. *Journal of Experimental Biology*, 206(19): 3479–3486, 2003.

[81] J. Engelmann and H. Bleckmann. Coding of lateral line stimuli in the goldfish midbrain in still and running water. *Zoology*, 107(2):135–51, 2004.

[82] S. Künzel, H. Bleckmann, and J. Mogdans. Responses of brainstem lateral line units to different stimulus source locations and vibration directions. *Journal of Comparative Physiology A*, 197(7):773–87, 2011.

[83] G. Meyer, A. Klein, J. Mogdans, and H. Bleckmann. Toral lateral line units of goldfish, *Carassius auratus*, are sensitive to the position and vibration direction of a vibrating sphere. *Journal of Comparative Physiology A*, 2012.

[84] A. J. Ricci, J.-P. Bai, L. Song, C. Lv, D. Zenisek, and J. Santos-Sacchi. Patch-clamp recordings from lateral line neuromast hair cells of the living zebrafish. *The Journal of neuroscience : the official journal of the Society for Neuroscience*, 33(7):3131–4, February 2013.

[85] H. Korn and D. S. Faber. The Mauthner cell half a century later: a neurobiological model for decision-making? *Neuron*, 47(1):13–28, July 2005.

[86] T. M. Szabo, C. A. McCormick, and D. S. Faber. Otolith endorgan input to the Mauthner neuron in the goldfish. *The Journal of comparative neurology*, 505(5):511–25, December 2007.

[87] M. Mirjany and D. S. Faber. Characteristics of the anterior lateral line nerve input to the Mauthner cell. *The Journal of experimental biology*, 214(Pt 20):3368–77, October 2011.

[88] J. Pujol-Martí and H. López-Schier. Developmental and architectural principles of the lateral-line neural map. *Frontiers in neural circuits*, 7: 47, January 2013.

[89] M. Mirjany, T. Preuss, and D. S. Faber. Role of the lateral line mechanosensory system in directionality of goldfish auditory evoked escape response. *The Journal of experimental biology*, 214(Pt 20):3358–67, October 2011.

[90] W. Gnatzy and J. Tautz. Ultrastructure and mechanical properties of an insect mechanoreceptor: Stimulus-transmitting structures and sensory apparatus of the cereal filiform hairs of {G}ryllus. *Cell and Tissue Research*, 213(3):441–463, 1980.

[91] T. Shimozawa and M. Kanou. The aerodynamics and sensory physiology of range fractionation in the cereal filiform sensilla of the cricketGryllus bimaculatus. *Journal Of Comparative Physiology A Neuroethology Sensory Neural And Behavioral Physiology*, pages 495–505, 1984.

[92] T. Kumagai, T. Shimozawa, and Y. Baba. The shape of wind-receptor hairs of cricket and cockroach. *Journal of Comparative Physiology A: Neuroethology, Sensory, Neural, and Behavioral Physiology*, 183(2):187–192, July 1998.

[93] T. Shimozawa and M. Kanou. Varieties of filiform hairs: range fractionation by sensory afferents and cereal interneurons of a cricket. *Journal of Comparative Physiology A: Neuroethology, Sensory, Neural, and Behavioral Physiology*, 155(4):485–493, 1984.

[94] G. A. Jacobs. Detection and Analysis of Air Currents by Crickets. *BioScience*, 45(11):776–785, 1995.

[95] W. Gnatzy and R. Heuß lein. Digger wasp against crickets. *Naturwissenschaften*, 73(4):212–215, April 1986.

[96] I. Weiss. *Untersuchungen zum Windevozierten Fuchtverhalten von Gryllus campestris Linneanus und Gryllus bimaculatus De Geer*. PhD thesis, TU München, 2010.

[97] E. M. Lewandowski. *The Dynamics of Marine Craft: Maneuvering and Seakeeping*. World Scientific Pub Co Inc, 2003.

[98] L. Meirovitch. *Methods of Analytical Dynamics*. Dover Civil and Mechanical Engineering. Dover Publications, 2004.

[99] S. Sosnowski, J.-m. P. Franosch, L. Zhang, Y. Nie, and S. Hirche. Simulation of the underwater vehicle "Snookie": Navigating like a fish. In *1st International Conference on Applied Bionics and Biomechanics*, 2010.

[100] J.-M. Franosch, S. Sosnowski, N. Chami, K. Kuhnlenz, S. Hirche, and J. van Hemmen. Biomimetic lateral-line system for underwater vehicles. In *9th IEEE Sensors Conference*, pages 2212–2217, 2010.

[101] H. Lamb. *Hydrodynamics*. Dover publications, 6th edition, 1945.

[102] J. Bladel. On Helmholtz's Theorem in Finite Regions. Technical report, Midwestern Universities Research Association, U.S. Atomic Energy Commission, 1958.

[103] L. C. Evans. *Partial Differential Equations*. Amer Mathematical Society, 1st edition, 6 1998.

[104] J. D. Jackson. *Klassische Elektrodynamik*. Gruyter, 1 2002.

[105] R. Bouffanais, G. D. Weymouth, and D. K. P. Yue. Hydrodynamic object recognition using pressure sensing. *Proceedings of the Royal Society A: Mathematical, Physical and Engineering Sciences*, 467(2125):19–38, 2010.

[106] W. L. W. George Hsiao. *Boundary Integral Equations*. Springer, (applied m edition, 2008.

[107] A. Leitão and M. M. Alves. Multiple level-sets for elliptic Cauchy problems in three dimensional domains. *Journal of Physics: Conference Series*, 255 (1):012005, November 2010.

[108] Y. Liu. *Fast Multipole Boundary Element Method: Theory and Applications in Engineering*. Cambridge University Press, 1 edition, 2009.

[109] S. Urban. Rekonstruktion stationärer Objekte durch den blinden Höhlenfisch Mexican tetra. Master's thesis, Technische Universität München, 2011.

[110] S. Vogel. Modes and scaling in aquatic locomotion. *Integrative and comparative biology*, 48(6):702–12, December 2008.

[111] R. Full and M. Tu. Mechanics of a rapid running insect: two-, four- and six-legged locomotion. *J. Exp. Biol.*, 156(1):215–231, March 1991.

[112] S. J. Montuelle, A. Herrel, P.-A. Libourel, S. Daillie, and V. L. Bels. Flexibility in locomotor-feeding integration during prey capture in varanid lizards: effects of prey size and velocity. *The Journal of experimental biology*, 215(Pt 21):3823–35, November 2012.

[113] R. Avery and G. Tosini. Dynamics of predation in Lacertidae: the relation between locomotor pattern and prey-capture probability in three contrasted species. *Amphibia-Reptilia*, 16:1–10, 1994.

[114] D. G. Harper and R. W. Blake. Fast-Start Performance of Rainbow Trout Salmo Gairdneri and Northern Pike Esox Lucius. *J. Exp. Biol.*, 150(1): 321–342, May 1990.

[115] M. Muller, J. Osse, and J. Verhagen. A quantitative hydrodynamical model of suction feeding in fish. *Journal of Theoretical Biology*, 95(1): 49–79, March 1982.

[116] A. L. LONGHORN. THE UNSTEADY, SUBSONIC MOTION OF A SPHERE IN A COMPRESSIBLE INVISCID FLUID. *The Quarterly Journal of Mechanics and Applied Mathematics*, 5(1):64–81, January 1952.

[117] D. S. Pavlov and S. N. Tjurjukov. Reactions of dace to linear accelerations. *Journal of Fish Biology*, 46(5):768–774, May 1995.

[118] H. A. D. Underwater sound and fish behaviour. In T. J. Pitcher, editor, *Behaviour of Teleost Fishes*, Fish & Fisheries Series, pages 114–151. Springer US, 2nd edition, 1993.

[119] M. Wahlberg. Sounds produced by herring (Clupea harengus) bubble release. *Aquatic Living Resources*, 16(3):271–275, July 2003.

[120] B. Wilson, R. S. Batty, and L. M. Dill. Pacific and Atlantic herring produce burst pulse sounds. *Proceedings. Biological sciences / The Royal Society*, 271 Suppl(Suppl_3):S95–7, February 2004.

[121] R. Courant and D. Hilbert. *Methods of Mathematical Physics*, volume 1. Wiley-VCH, 1989.

[122] L. M. Milne-Thomson. *Theoretical Hydrodynamics*. Dover Publications, 4 edition, 1962.

[123] F.-L. Yang. A formula for the wall-amplified added mass coefficient for a solid sphere in normal approach to a wall and its application for such motion at low Reynolds number. *Physics of Fluids*, 22(12):123303, December 2010.

[124] R. Folkersma, H. Stein, and F. van de Vosse. Hydrodynamic interactions between two identical spheres held fixed side by side against a uniform stream directed perpendicular to the line connecting the spheres' centres. *International Journal of Multiphase Flow*, 26(5):877–887, May 2000.

[125] V. I. Fernandez, A. Maertens, F. M. Yaul, J. Dahl, J. H. Lang, and M. S. Triantafyllou. Lateral-line-inspired sensor arrays for navigation and object identification. *Marine Technology Society Journal*, 45(4):130–146, 2011.

[126] R. V. Fiorini, O. Akanyeti, F. Visentin, J. Ježov, L. D. Chambers, G. Toming, J. Brown, M. Kruusmaa, W. M. Megill, and Paolo. Hydrodynamic pressure sensing with an artificial lateral line in steady and unsteady flows. *Bioinspiration & Biomimetics*, 7(3):36004, 2012.

[127] F. D. Lagor, L. D. DeVries, K. M. Waychoff, and D. A. Paley. Bio-inspired flow sensing and control: Autonomous rheotaxis using distributed pressure measurements. *Journal of Unmanned System Technology*, 1(3): 78–88, December 2013.

[128] T. Salumae and M. Kruusmaa. Flow-relative control of an underwater robot. *Proceedings of the Royal Society A: Mathematical, Physical and Engineering Sciences*, 469(2153):20120671–20120671, March 2013.

[129] S. P. Windsor, S. E. Norris, S. M. Cameron, G. D. Mallinson, and J. C. Montgomery. The flow fields involved in hydrodynamic imaging by blind Mexican cave fish (*Astyanax fasciatus*). Part I: open water and heading towards a wall. *Journal of Experimental Biology*, 213(22):3819–3831, 2010.

[130] S. P. Windsor, S. E. Norris, S. M. Cameron, G. D. Mallinson, and J. C. Montgomery. The flow fields involved in hydrodynamic imaging by blind Mexican cave fish (*Astyanax fasciatus*). Part II: gliding parallel to a wall. *Journal of Experimental Biology*, 213(22):3832–3842, 2010.

[131] B. Curcić-Blake and S. M. van Netten. Source location encoding in the fish lateral line canal. *The Journal of Experimental Biology*, 209(8):1548–59, 2006.

[132] J.-M. P. Franosch, A. B. Sichert, M. D. Suttner, and J. L. van Hemmen. Estimating position and velocity of a submerged moving object by the clawed frog *Xenopus* and by fish – a cybernetic approach. *Biological Cybernetics*, 93(4):231–8, 2005.

[133] S. D. Pandya, Y. Yang, D. L. Jones, J. Engel, and C. Liu. Multisensor processing algorithms for underwater dipole localization and tracking using mems artificial lateral-line sensors. *EURASIP Journal on Advances in Signal Processing*, pages 1–8, 2006.

[134] V. Isakov. *Inverse Problems for Partial Differential Equations*. Applied Mathematical Sciences. Springer, 1998.

[135] B. Harrach. Recent progress on the factorization method for electrical impedance tomography, 2013.

[136] L. Jaafar Belaid, A. Ben Abda, and N. Al Malki. The cauchy problem for the laplace equation and application to image inpainting, 2011.

[137] G. Alessandrini and E. Sincich. Solving elliptic Cauchy problems and the identification of nonlinear corrosion. *Journal of Computational and Applied Mathematics*, 198(2):307–320, January 2007.

[138] S. G. Sosnowski. *Advances in Social and Underwater Robotics through Biomimetic Design*. PhD thesis, TU München, 2013.

[139] D. Lenz. *Sensory Model for Obstacle Detection with an Artificial Lateral Line System*. PhD thesis, TU München, 2011.

[140] W. Graebel. *Advanced fluid mechanics*. Academic Press, Burlington MA, 2007.

[141] A. N. Vollmayr, S. Sosnowski, S. Hirche, and J. L. van Hemmen. Snookie: an Autonomous Underwater Vehicle with Artificial Lateral Line System. In H. Bleckmann, J. Mogdans, and S. L. Coombs, editors, *Flow Sensing in Air and Water*, chapter 20. Springer Berlin Heidelberg, Berlin, Heidelberg, viii edition, 2014.

[142] M. Stadlmeier. *Simulation von Strömungsfeldern zur neuronalen Rekonstruktion von Information*. PhD thesis, TU München, 2011.

[143] C. Jud. *Gridless Computations of Potential Flows on Arbitrary Geometries*. PhD thesis, TU München, 2012.

[144] D. Derou, J. Dinten, L. Herault, and J. Niez. Physical-model based reconstruction of the global instantaneous velocity field from velocity measurement at a few points. In *Proceedings of the Workshop on Physics-Based Modeling in Computer Vision*, page 63. IEEE Comput. Soc. Press, 1995.

[145] N. E. Murray and L. S. Ukeiley. Estimation of the flowfield from surface pressure measurements in an open cavity. *AIAA Journal*, 41(5):969–972, 2003.

[146] T. Suzuki and T. Colonius. Inverse-imaging method for detection of a vortex in a channel. *AIAA Journal*, 41(9):1743–1751, 2003.

[147] J. P. Miller, G. A. Jacobs, and F. E. Theunissen. Representation of sensory information in the cricket cercal sensory system. I. Response properties of the primary interneurons. *J Neurophysiol*, 66(5):1680–1689, 1991.

[148] F. E. Theunissen and J. P. Miller. Representation of sensory information in the cricket cercal sensory system. II. Information theoretic calculation of system accuracy and optimal tuning-curve widths of four primary interneurons. *J Neurophysiol*, 66(5):1690–1703, 1991.

[149] E. Salinas and L. F. Abbott. Vector reconstruction from firing rates. *Journal of Computational Neuroscience*, 1(1):89–107, 1994.

[150] S. Paydar, C. A. Doan, and G. A. Jacobs. Neural Mapping of Direction and Frequency in the Cricket Cercal Sensory System. *J. Neurosci.*, 19(5): 1771–1781, 1999.

[151] G. A. Jacobs and F. E. Theunissen. Extraction of Sensory Parameters from a Neural Map by Primary Sensory Interneurons. *J. Neurosci.*, 20(8): 2934–2943, 2000.

[152] J. N. Newman. *Marine Hydrodynamics*. MIT Press, 1977.

[153] G. R. Kirchhoff. Über die Bewegung eines Rotationskörpers in einer Flüssigkeit. *Journal für die reine und angewandte Mathematik*, 1870(71):237–262, 1870.

[154] A. I. Korotkin. *Added Masses of Ship Structures*. Fluid Mechanics and Its Applications. Springer, 2010.

[155] G. Kämper and V. Y. Vedenina. Frequency-intensity characteristics of cricket cercal interneurons: units with high-pass functions. *Journal of Comparative Physiology A: Neuroethology, Sensory, Neural, and Behavioral Physiology*, 182(6):715–724, 1998.

[156] I. Vasilescu, C. Detweiler, M. Doniec, D. Gurdan, S. Sosnowski, J. Stumpf, and D. Rus. AMOUR V: A hovering energy efficient underwater robot capable of dynamic payloads. *The International Journal of Robotics Research OnlineFirst*, 29:547–570, 2010.

[157] C. E. Brennen. A review of added mass and fluid inertial forces. Technical report, Department of the Navy, Port Hueneme, CA, USA, 1982.

[158] E. D. Obasaju, P. W. Bearman, and J. M. R. Graham. A study of forces, circulation and vortex patterns around a circular cylinder in oscillating flow. *Journal of Fluid Mechanics*, 196(-1):467–494, 1988.

[159] J. P. Breslin and P. Andersen. *Hydrodynamics of Ship Propellers*. Cambridge University Press, 2008.

[160] J. Feldman. DTNSRDC revised standard submarine equations of motion. Technical report, DTNSRDC, 1979.

[161] T. I. Fossen. *Guidance and Control of Ocean Vehicles*. Wiley, 1994.

[162] M. Motamed and J. Yan. A review of biological, biomimetic and miniature force sensing for microflight. *2005 IEEERSJ International Conference on Intelligent Robots and Systems*, pages 2630–2637, 2005.

[163] N. Izadi, M. J. de Boer, J. W. Berenschot, and G. J. M. Krijnen. Fabrication of superficial neuromast inspired capacitive flow sensors. *Journal of Micromechanics and Microengineering*, 20(8):85041, 2010.

[164] A. Dagamseh, R. Wiegerink, T. Lammerink, and G. Krijnen. Imaging dipole flow sources using an artificial lateral-line system made of biomimetic hair flow sensors. *Interface*, 10(83):20130162, 2013.

[165] F. Li, W. Liu, C. Stefanini, X. Fu, and P. Dario. A novel bioinspired PVDF micro/nano hair receptor for a robot sensing system. *Sensors*, 10 (1):994–1011, 2010.

[166] C. Liu. Micromachined biomimetic artificial haircell sensors. *Bioinspiration & Biomimetics*, 2(4):162–169, 2007.

[167] T.-Y. Hsieh, S.-W. Huang, L.-J. Mu, E. Chen, and J. Guo. Artificial lateral line design for robotic fish. In *Underwater Technology (UT), 2011 IEEE Symposium on and 2011 Workshop on Scientific Use of Submarine Cables and Related Technologies (SSC)*, pages 1–6, April 2011.

[168] A. Qualtieri, F. Rizzi, M. T. Todaro, A. Passaseo, R. Cingolani, and M. De Vittorio. Stress-driven AlN cantilever-based flow sensor for fish lateral line system. *Microelectron. Eng.*, 88(8):2376–2378, 2011.

[169] Y. Yang, A. Klein, H. Bleckmann, and C. Liu. Artificial lateral line canal for hydrodynamic detection. *Applied Physics Letters*, 99(2):023701, 2011.

[170] A. Klein and H. Bleckmann. Determination of object position, vortex shedding frequency and flow velocity using artificial lateral line canals. *Beilstein Journal of Nanotechnology*, 2:276–83, 2011.

[171] A. Klein, H. Herzog, and H. Bleckmann. Lateral line canal morphology and signal to noise ratio. In *SPIE Smart Structures and Materials + Nondestructive Evaluation and Health Monitoring*, pages 797507–797507–6. International Society for Optics and Photonics, 2011.

[172] N. Nguyen, D. L. Jones, Y. Yang, and C. Liu. Flow vision for autonomous underwater vehicles via an artificial lateral line. *EURASIP Journal on Advances in Signal Processing*, 2011(1):806406, 2011.

[173] G. B. Middlebrook and E. L. Piret. Hot wire anemometry-solution of some difficulties in measurement of low water velocities. *Industrial and Engineering Chemistry*, 42(8), 1950.

[174] S. Coombs, R. R. Fay, and J. Janssen. Hot-film anemometry for measuring lateral line stimuli. *The Journal of the Acoustical Society of America*, 85 (5):2185–2193, 1989.

[175] J. Chen, J. Engel, N. Chen, S. D. Pandya, S. Coombs, and C. Liu. Artificial lateral line and hydrodynamic object tracking. In *19th IEEE International Conference on Micro Electro Mechanical Systems*, pages 694–697. IEEE, 2006.

[176] Y. Yang, J. Chen, J. Engel, S. Pandya, N. Chen, C. Tucker, S. Coombs, D. L. Jones, and C. Liu. Distant touch hydrodynamic imaging with an artificial lateral line. *Proceedings of the National Academy of Sciences of the United States of America*, 103(50):18891–5, 2006.

[177] S. Pandya, Y. Yang, C. Liu, and D. L. Jones. Biomimetic imaging of flow phenomna. *IEEE International Conference on Acoustics, Speech and Signal Processing, 2007. ICASSP 2007.*, 2:933–936, 2007.

[178] Y. Yang, N. Nguyen, N. Chen, M. Lockwood, C. Tucker, H. Hu, H. Bleckmann, C. Liu, and D. L. Jones. Artificial lateral line with biomimetic neuromasts to emulate fish sensing. *Bioinspiration & Biomimetics*, 5(1): 16001, 2010.

[179] J. C. Kinsey, R. M. Eustice, and L. L. Whitcomb. A survey of underwater vehicle navigation: recent advances and new challanges. In *IFAC Conference of Manoeuvering and Control of Marine Craft*, Lisbon, Portugal, 2006.

[180] J. W. Nicholson and A. J. Healey. The present state of autonomous underwater vehicle (AUV) applications and technologies. *Marine Technology Society Journal*, 42(1):8, 2008.

[181] W. Felix. Strömungsmessung mit Thermistoren. *Naunyn-Schmiedberg's Arch. exp. Path. u. Pharmak.*, 244:254–269, 1962.

[182] H. Strickert. *Hitzdraht-und Hitzfilmanemometrie.* VEB Verlag Technik, Berlin, 1974.

[183] S. Emsmann and A. Lehmann. Entwicklung eines Thermistoranemometers zur Messung instationärer Wassergeschwindigkeiten. *Fortschrittsberichte der VDI Zeitschriften*, 18(8), 1975.

[184] A. E. Perry. *Hot-wire anemometry.* Clarendon Press, Oxford, 1982.

[185] I. C. Itsweire and K. N. Helland. A high-performance low-cost constant-temperature hot-wire anemometer. *Journal of Physics E-Scientific Instruments*, 16(6):549–553, 1983.

[186] C. G. Lomas. *Fundamentals of hot wire anemometry.* Cambridge University Press, Cambridge, 1986.

[187] U. Eser. *Thermisches Anemometer mit Kugelsonde zur Bestimmung kleiner Geschwindigkeitsvektoren.* PhD thesis, Universität Essen, Essen, 1990.

[188] H. H. Bruun. *Hot wire anemometry.* Oxford Univ. Press, Oxford, 1996.

[189] S. Sharma, S. Coombs, P. Patton, and T. Burt de Perera. The function of wall-following behaviors in the Mexican blind cavefish and a sighted relative, the *Mexican tetra* (*Astyanax*). *Journal of Comparative Physiology A*, 195(3):225–40, 2009.

[190] P. Patton, S. Windsor, and S. Coombs. Active wall following by Mexican blind cavefish (*Astyanax mexicanus*). *Journal of Comparative Physiology A*, 196(11):853–867, 2010.

[191] S. Thrun, W. Burgard, and D. Fox. *Probabilistic Robotics (Intelligent Robotics and Autonomous Agents series)*. MIT Press, 2005.